Multi-scale Analyses of Wildland Fire Combustion Processes in Open-canopied Forests using Coupled and Iteratively Informed Laboratory-, Field-, and Model-based Approaches

Final Technical Report
SERDP Project RC-2641

PI: Dr. Nicholas S. Skowronski

USDA Forest Service

6/18/21

REPORT DOCUMENTATION PAGE

Form Approved
OMB No. 0704-0188

Public reporting burden for this collection of information is estimated to average 1 hour per response, including the time for reviewing instructions, searching existing data sources, gathering and maintaining the data needed, and completing and reviewing this collection of information. Send comments regarding this burden estimate or any other aspect of this collection of information, including suggestions for reducing this burden to Department of Defense, Washington Headquarters Services, Directorate for Information Operations and Reports (0704-0188), 1215 Jefferson Davis Highway, Suite 1204, Arlington, VA 22202-4302. Respondents should be aware that notwithstanding any other provision of law, no person shall be subject to any penalty for failing to comply with a collection of information if it does not display a currently valid OMB control number. **PLEASE DO NOT RETURN YOUR FORM TO THE ABOVE ADDRESS.**

1. REPORT DATE *(DD-MM-YYYY)*	**2. REPORT TYPE**	**3. DATES COVERED** *(From - To)*
10/31/2021	SERDP Final Report	

4. TITLE AND SUBTITLE

Multi-scale Analyses of Wildland Fire Combustion Processes in Open-canopied Forests using Coupled and Iteratively Informed Laboratory-, Field-, and Model-based Approaches

5a. CONTRACT NUMBER

5b. GRANT NUMBER

5c. PROGRAM ELEMENT NUMBER

6. AUTHOR(S)

Nicholas Skowronski et al.

5d. PROJECT NUMBER
RC-2641

5e. TASK NUMBER

5f. WORK UNIT NUMBER

7. PERFORMING ORGANIZATION NAME(S) AND ADDRESS(ES)

USDA Forest Service Northern Research Station
180 Canfield St.
Morgantown, WV 26505

8. PERFORMING ORGANIZATION REPORT

RC-2641

9. SPONSORING / MONITORING AGENCY NAME(S) AND ADDRESS(ES)

Strategic Environmental Research and Program
4800 Mark Center Drive, Suite 17D03
Alexandria, VA 22350-3605

10. SPONSOR/MONITOR'S ACRONYM(S)
SERDP

11. SPONSOR/MONITOR'S REPORT NUMBER(S) RC-2641

12. DISTRIBUTION / AVAILABILITY STATEMENT
DISTRIBUTION STATEMENT A. Approved for public release: distribution unlimited.

13. SUPPLEMENTARY NOTES

14. ABSTRACT

This project, RC-2641, spanned several institutions and objectives, with a focal idea that an interdisciplinary, multi-scale approach is necessary to address the questions that were presented in the original RFP. As we move across these scales of observations, there are benefits and shortfalls that occur. In the laboratory, fuel beds can be deconstructed to the scale of individual particles, and access to the newest laboratory technology and the ability to repeat measures and provide statistical rigor yield new insights.

15. SUBJECT TERMS
Combustion, Computational Fluid Dynamics, Drag Forces, Fuel Structure.

16. SECURITY CLASSIFICATION OF:			**17. LIMITATION OF ABSTRACT**	**18. NUMBER OF PAGES**	**19a. NAME OF RESPONSIBLE PERSON**
a. REPORT	**b. ABSTRACT**	**c. THIS PAGE**			Nicholas Skowronski
Unclass	Unclass	Unclass	UNCLASS	217	**19b. TELEPHONE NUMBER** *(include area code)* 304-285-1507

Standard Form 298 (Rev. 8-98)
Prescribed by ANSI Std. Z39.18

List of Co-authors

Korea University

Seoung-kyun Im – Co-Principal Investigator

Michigan State University

Dr. Sharon Zhong – Co-Principal Investigator

Dr. Michael Kiefer – Post-Doctoral Researcher

Rochester Institute of Technology

Dr. Robert Kremens – Co-Principal Investigator

Tall Timbers Research Station

Alexis Everland – Research Technician

University of Edinburgh

Dr. Zakary Campbell-Lochrie – PhD Student

Dr. Rory Hadden – Co-Principal Investigator

Dr. Eric Mueller – Post-Doctoral Researcher

Carlos Walker-Ravena – PhD Student

USDA Forest Service

Dr. Joseph Charney – Co-Principal Investigator

Xindi Bian - Meteorologist$

Jason Cole – Data Manager

Dr. Kenneth Clark – Co-Principal Investigator

Dr. Michael Gallagher – Co-Principal Investigator

Dr. Warren Heilman – Co-Principal Investigator

John Hom – Co-Principal Investigator

Dr. William Mell – Co-Principal Investigator

Matthew Patterson – Research Technician

Worcester Polytechnic Institute

Dr. Giovanni Di Cristina – PhD Student

Dr. Ali Rangwala – Collaborator

Dr. Albert Simeoni – Co-Principal Investigator

List of Acronyms

AGL	Above Ground Level
ARPS	Advanced Regional Prediction System
ALS	Airborne Laser Scanning
CFD	Computational Fluid Dynamics
DoD	Department of Defense
FFP	Fire Front Passage
FPP	Franklin Parker Preserve
FMC	Fuel Moisture Content
FOV	Field of View
IR	Infrared
JFSP	Joint Fire Science Program
LiDAR	Light Detection and Ranging
MLR	Mass-Loss Rate
NDIR	Non-Dispersive Infrared Sensor
NJFFS	New Jersey Forest Fire Service
PNR	Pinelands National Reserve
RH	Relative Humidity
RMSE	Root Mean Square Error
ROS	Rate of Spread
SERDP	Strategic Environmental Research and Development Program
SLEF	Silas Little Experimental Forest
SODAR	Sonic Detection and Ranging
TKE	Turbulent Kinetic Energy
TLS	Terrestrial Laser Scanner
WFDS	Wildland Fire Dynamics Simulator
WUI	Wildland Urban Interface

Table of Contents

List of Co-authors ii
Korea University ii
Michigan State University ii
Rochester Institute of Technology ii
Tall Timbers Research Station ii
University of Edinburgh ii
USDA Forest Service ii
Worcester Polytechnic Institute ii
List of Acronyms iii
Table of Contents iv
List of Tables viii
List of Figures x
Acknowledgements xix
Abstract 20
Introduction and objectives 20
Technical approach 20
Results 20
Benefits 20
Executive Summary 22
Introduction 22
Objectives 22
Technical approach 23
Results and Discussion 24
Small-scale laboratory investigations. 24
Mid-scale laboratory investigations 27
Small-scale field investigations 27
Management-scale field investigations 28
Management-scale atmospheric modeling 29
Implications for future research and benefits 30
Overview 32
Objective 32
Background 32
Small-scale laboratory investigations 37
Objective 37
Background 37

Thermal decomposition of vegetative fuels 38
Objective 38
Background 38
Materials and Methods 38
Results and Discussion 39
Conclusions and Implications for Future Research/Implications 43
Burning of pine needle and manufactured fuel beds 44
Objective 44
Background 44
Materials and methods 45
Results and discussion 47
Time to ignition 48
Burning rate 49
Conclusions and implications for future research 51
Effect of fuel bed structure in porous flame spread: experimental investigation of heat transfer mechanisms 51
Objective 51
Background 51
Materials and methods 51
Results and discussion 56
Conclusions and implications for future research 72
Towards improved modeling of flow and heat transfer in litter fuels 73
Objective 73
Background 73
Materials and Methods 75
Conclusions and Implications for Future Research/Implications 84
Mid-scale laboratory investigations 85
Objective 85
Overall flame behavior 85
Flame spread behavior characterization 93
Pine needle fuel mass and bulk density 103
Objective 103
Background 104
Materials and methods 104
Results and discussion 109
Small - scale field investigations 116

Objectives....116
Background....116
Materials and methods....117
Site description....117
Experimental design....118
Flow, temperature, and pressure measurements....120
Fire spread....121
Fire radiative power....121
Fuel loads and consumption....122
Ignition....123
Ambient meteorological conditions....123
Transportable analyser for calorimetry outside (TACO)....124
Load cells....125
Results and discussion....126
Ambient meteorological conditions....126
Fuels - Biometric and TLS measurements....129
Flow and temperature measurements....132
Fire spread rates....136
Combustion and energy release....139
Conclusions and implications for future research....142
Flame spread analysis....143
Objective....143
Background....143
Materials and methods....144
Results and discussion....147
Conclusions and implications for future research....151
Management-scale field investigations....152
Objectives....152
Background....152
Materials and methods....153
Results and discussion....158
Conclusions and implications for future research....174
Management-scale atmospheric modeling....176
Objective....176
Background....176
Materials and Methods....177

Results and discussion 186
Conclusions and implications for future research 196
Conclusions and Implications for Future Research 198
Appendices 200
Appendix 1. Supporting technical data: 200
Appendix 2- List of Scientific/Technical Publications 201
Peer Reviewed Publications 201
Conference or symposium proceedings scientifically recognized and referenced 202
Conference or symposium abstracts 202
Literature Cited 206

List of Tables

Table 1. The conversion between mass and porosity for data in Figure 12.....50

Table 2. Needle for Pinus rigida and Pinus rigida x taeda needles species. 52

Table 3. Summary of fuel bed parameters and measured fire behaviour for experiments involving pitch pine needle fuel beds.....58

Table 4. Summary of fuel bed parameters and measured fire behaviour for experiments involving pitch-loblolly pine hybrid fuel beds. 59

Table 5. Summary of fire behaviour results for each fuel bed condition.....65

Table 6. Permeability and Forchheimer coefficient determined by fitting the Forcheimmer equation to experimental data. Goodness of fit is evaluated with root mean squared error (RMSE). 81

Table 7: Results summary.....113

Table 8. Meteorological data collected above canopy (air temperature, RH and windspeed) and at 2.5 to 3.0-meter height above fuel beds during experimental 10 by 10-meter burns. 127

Table 9. Fuel moisture content, windspeed at the height of sonic anemometers above fuel beds and rate of spread of fire fronts (ROS) for 10 by 10-meter experiments.....129

Table 10**.** Comparison of biometric estimates of convective heat flux to sensible heat flux measured at different heights above the flame front during 10 x 10 m burn 7 conducted on May 9, 2018. 142

Table 11. Details of environmental conditions and spread rate for each burn. Ambient temperature and relative humidity come from the 'green tower' data. Wind speed statistics are taken from an average across all sonics during a given burn. Spread rate statistics are taken within a 1m buffer from the plot edges is considered in order to reduce edge effects and the influence of the ignition. 147

Table 12. Spearman's rank correlation coefficient between spread rate and the selected environmental variables. 149

Table 13. Pre-burn and post-burn surface and understory fuel loading in the prescribed burn area and estimated fuel consumption.....159

Table 14. Time periods (LT) for the delineated pre-FFP, FFP, and post-FFP periods at each tower located in the interior of the prescribed burn plot. 161

Table 15. Turbulence statistics at the 3-m, 10-m, and 19-m levels within the pre-FFP, FFP, and post-FFP periods. Brackets indicate an average across all the in situ towers. Overbars indicate temporal means within each period. Units for the tower-averaged temporal mean TKE components (u'^2, v'^2, w'^2), kinematic momentum fluxes ($u'v'$, $u'w'$, $v'w'$), and kinematic heat fluxes ($u't'$, $v't'$, $w't'$) are $m^2\ s^{-2}$, $m^2\ s^{-2}$, and $m\ s^{-1}$ °C, respectively. Anisotropy values (w'^2 $(2 * TKE)^{-1}$) and skewness values for the horizontal and vertical velocity distributions (Sk_u, Sk_v, Sk_w) are unitless. 166

Table 16. Overview of model simulations for SLEF case, where Dx, Dy, and Dz are the grid spacing in the west-east, south-north, and vertical dimensions. 184

Table 17. Summary of sensitivity experiments. VG refers to the vertical grid structure [0: grid stretching beginning at 0 m AGL; 84: grid stretching beginning at 84 m AGL], CD is the canopy drag coefficient (0.2 or 0.3), the heat source is either a vertical profile of vertical

turbulent heat flux (HF) [with an e-folding depth of 4.4 m (Low) or 18 m (High)] or a hotplate (HP), also known as a soil temperature perturbation. No-fire (NF_0) simulation included at bottom of table. 186

List of Figures

Figure 1. Schematic of a backing surface fire (spreading right to left). 33

Figure 2. Schematic of SERDP project RC-2641. 36

Figure 3. TGA (left) and DTG (right) curves for Pinus rigida in air and nitrogen. Dashed vertical lines indicate the temperatures of the onset and maxima of individual reactions. Heating rate 100°C/min. 40

Figure 4. Comparison of TGA (left) and DTG (right) for all Pinus species 41

Figure 5. Temperatures for the onset and maximum reaction rate for Pinus species in nitrogen. R1 is drying and R2 is pyrolysis. 41

Figure 6. Comparison of TGA (left) and DTG (right) for all broad leaf species 42

Figure 7. Temperatures for the onset and maximum reaction rate for broad leaf species in nitrogen. R1 is drying and R2 is pyrolysis. 42

Figure 8. Comparison of the proximate analysis for Pinus species (left) and broad leaves (right) ... 43

Figure 9. Sample preparation for the flammability experiments and the relationship between nominal length scale and porosity 46

Figure 10. Representative stages of experimentation in the FPA. Left-to-right and top-to-bottom: initial exposure, pyrolysis, further pyrolysis, ignition, burning and flameout. 48

Figure 11. Time-to-ignition against global fuel bed porosity. NF00 and NF63 correspond to non-porous and porous sample holders, respectively. 48

Figure 12. Average mass loss rate of repeat tests in shifted time subject to different boundary conditions. Shaded regions show maximum and minimum values for repeat tests. Left shows closed basket cases and right shows open (63%) basket cases. 50

Figure 13. The peak mass loss rate as a function of porosity for porous and non-porous sample holders. 50

Figure 14. Average mass loss rate of repeat tests in shifted time subject to different incident heat fluxes. Shaded regions show maximum and minimum values for repeat tests. Left is 25kW/m2. Middle is 35kW/m2. Right is 50kW/m2. 50

Figure 15. Photograph and schematic of the Table, detailing the position of in-bed bi-directional pressure probes and gas phase thermocouples (all measurements at a height of 0.01 m above the vermiculite substrate surface). 53

Figure 16. Schematic of table instrumentation. 55

Figure 17. Estimated view factor between radiating surface and a heat flux gauge for (a) parallel (b) perpendicular alignment for fuel beds of various height 55

Figure 18. Composite of frames from downward-looking video footage of flame spread experiments displaying variation in flame and front shape between Pitch Pine fuel beds of (Top) 0.2 kg/m^2, 20 kg/m^3 (Middle) 0.8 kg/m^2. 20 kg/m^3 (Bottom) 1.6 kg/m^2, 20 kg/m^3. 57

Figure 19. Flame front position versus time from ignition for pitch pine beds of (a) 20 kg/m^3 bulk density, and (b) 0.8 kg/m^2 fuel loading (avg. of all experiments at each condition). 59

Figure 20. Flame Spread Rate as a function of distance (based on video analysis) for pitch pine fuel beds of different fuel loadings at (a) 10 kg/m^3 bulk density, and (b) 20 kg/m^3 bulk density 60

Figure 21. Comparison of flame spread rate with fuel loading and bulk density for, (a) pitch pine (b) pitch-loblolly pine hybrid needle fuel beds. 61

Figure 22. Correlation between $\alpha\sigma\delta$ and flame spread rate in (a) pitch pine (b) pitch-loblolly pine fuel beds. 62

Figure 23. Comparison of (a) Fuel Loading, (b) Heat Release Rate with mean and max. buoyant flow velocity at a height of 1.2 m above pitch pine fuel bed, in the 10 s after flame arrival. 63

Figure 24. Mean and minimum in-bed flow velocity towards the approaching flame front (50 mm to 10 mm prior to flame arrival), in beds of different fuel loading and bulk density for beds of pitch pine and pitch-loblolly pine hybrid, respectively. 64

Figure 25. (a) Flame Front Position over time for 20 kg/m^3 fuel beds of different fuel loading (b) Flame Front Position over time for 0.8 kg/m^2 fuel beds of different bulk density. 66

Figure 26. Typical normalized mass loss for fuel beds of different $\alpha\sigma\delta$ values. 66

Figure 27. Characteristic total heat flux profiles at each gauge location for fuel beds of 20 kg/m^3 bulk density and different fuel loading. (a) $\alpha\sigma\delta = 98$ and (b) $\alpha\sigma\delta = 197$ 69

Figure 28. Comparison of heat flux to top and bottom surfaces of the fuel bed (5 s Moving Avg. of 10 Hz Data). 69

Figure 29. Comparison of Peak (a) Total and (b) Radiant Heat Flux from the above-bed flame with horizontal heat flux through the fuel beds of various structures. 70

Figure 30. Instantaneous ratio of Radiative: Total Heat Flux relative to flame arrival time for fuel beds of (a) $\alpha\sigma\delta = 98$ and (b) $\alpha\sigma\delta = 197$ (Based on measurements of heat flux transferred horizontally through the fuel bed). 71

Figure 31. Ratio of Instantaneous Heat Flux : Peak Heat Flux at a distance ahead of the flame front of (a) 25 mm (b) 50 mm (c) 100 mm. 72

Figure 32. Schematic of the Wildfire Exposure Ignition Response Device. 75

Figure 33. Example of Pinus rigida needles, which are grouped with three individual needles on one fascicle. b) Example of fuel bed packing for the pressure drop experiments. 76

Figure 34. Test section configuration for the (a) pressure drop and (b) layer flow cases -- for both experiments and simulations. The shaded area corresponds to the region filled with pine needles, and the x-coordinates of measurement locations (filled circles) are given in mm from the leading edge of the needle layer. The measurements in (a) were static pressure taps and in (b) were velocities measured with a hotwire anemometer. 77

Figure 35. Test section configuration for the heating experiments. Dots represent thermocouple locations. 79

Figure 36. Pressure drop as a function of free-stream velocity for bulk densities of (a-f) 10-60 kg m^{-3}. x's represent experimental data points, and the dashed line gives a best-fit 2nd-order polynomial, with the shaded area indicating the 90\% prediction interval. The solid line represents the theory presented in the Background section, and the triangles represent FDS simulations employing the same theory. 81

Figure 37. Development of vertical profiles of velocity in the streamwise direction for the (a) experiments and (b) simulations, for each of the bulk densities tested, taking the case of u0 = 1 m$\cdot$s^{-1}. Error bars represent the standard deviation. The horizontal dashed line represents the

upper surface of the fuel bed, z/h = 1. Note that the experimental profiles only represent a single repeat. 83

Figure 38. Data from a convective heating test of 40 kg/m3 and 1.5 m/s. The shaded regions represent the temperature range recorded in the spanwise measurements.....83

Figure 39. Summary of the numerical optimisation of the Nusselt number for the experimental data (symbols) and the prediction according to the currently implemented model.....84

Figure 40. Diagram of wind tunnel and experimental setup showing edge-to-edge spacing (s = 0.5,0.65,0.75,1,1.15 cm), dowel diameter (d = 3.2 mm), freestream flow (U_∞ = 1,2,3 m/s) and length (l = 26 cm). The dowel position numbering scheme utilizes 0 for the pilot dowel, then 1, 2, up to 9.....87

Figure 41. Critical spacing for 3.2 mm dowel array. The line marks the marginal propagation threshold for which arrays at larger spacings do not see flame spread.....88

Figure 42. Fire spread for (a) 0.50, (b) 0.65, (c) 0.75, (d) 1.00, and (e) 1.15 cm spacings under 1, 2, and 3 m/s freestream flow. The markers are averages of 5 data points with the experimental range shown as the shaded region. The plotted line represents a quadratic regression of the data points.....89

Figure 43. Fire spread rate at dowel positions 3, 5, and 7 for multiple spacings under 1, 2, and 3 m/s freestream flow. 90

Figure 44. Images of early, middle, and late-stage fire spread at 0.75 – 1.15 cm spacings for 2 and 3 m/s. Early-stage images are taken at the ignition of dowel 3. Mid stage images are at the ignition of dowel 5. Late-stage images are taken at the ignition of dowel 7. 92

Figure 45. (a) Schematic of wind tunnel and (b) dowel array setup inside the wind tunnel test section 95

Figure 46. Images and sketches of the continuous (I), discrete (II), and quenching (III) flame spread behaviors observed in a 1 cm spaced array....96

Figure 47. Flame spread regime map showing Continuous (I), Discrete (II), and Quenching/Extinction (III) regimes as a function of flow and spacing of discrete fuel array...98

Figure 48. Schematics (top row) of flame (hollow red line) and ignition location (solid red) and top (middle row) and front (bottom row) view images of dowel 5 ignition for 1 cm spacing at 4 flow speeds Timestamps are relative to pilot ignition. 99

Figure 49. Wake flame width to length ratio (W/L) for a range of flow speeds and array spacings. The filled markers represent discrete flame behavior at those conditions. 100

Figure 50. St vs. Da(d/s) plot comparing the experimental data to a logarithmic regression (a) and zoomed-in plot (b) showing flow-spacing conditions in detail of the current study and from the single cylinder Yang and Tien study that uses the right y-axis (Yang and T'ien 1998).....102

Figure 51. Fire spread experiments conducted in the wind tunnel from left to right; suspended dowel array, pine needle litter layers, and shrub fire. 105

Figure 52. Wind tunnel schematic (top) and image (bottom). 106

Figure 53. Diverging section sub-division (left) with cut lines shown for each piece. On the right is the entire diverging section broken down onto a shipping pallet. 107

Figure 54. Test section in the laboratory (left) and collapsed onto a custom shipping pallet (right). 108

Figure 55. Experimental setup from a pine needle fire spread campaign. Instrumentation was mainly thermocouples embedded within the fuel package, and heat flux gauges on the fuel layer surface. A load cell was installed in the back half of the setup. 109

Figure 56. A pine needle litter layer ready for ignition (left). The experimental platform showing the instrumentation embedded within the pine needle fuel package (right). 109

Figure 57. Mass loss (blue) and total heat flux (red) plots for pine needle layer fuel beds at a loading and bulk density of 0.8 kg/m^2 and 60 kg/m^3, respectively. The images on the right correspond to snapshots at the black dotted lines. 111

Figure 58: Temperature results from the fuel surface thermocouple. The solid lines show the 40 kg/m^3 and dashed are the 60 kg/m^3 bulk density. 114

Figure 59. Temperature results for the embedded thermocouples at the top, middle, and base of the fuel. Results shown are for a 0.8 kg/m2 fuel loading subject to a flow speed of 3 m/s. 114

Figure 60. Experiment site in pitch/loblolly pine plantation at the Silas Little Experimental Forest, New Lisbon, NJ. 118

Figure 61. Idealized rendering of equipment locations for 10 x 10m field experiments. 119

Figure 62. Trusses and instrumentation used to quantify fire behavior during 10 x10- meter burns at Silas Little Experimental Forest. (a) tower mounted IR camera and sonic anemometer, trusses with sonic anemometers, thermocouples, pressure gauges, and spectral sensors/digital cameras. (b) closer view of instruments mounted on a single truss for burns 7 and 8 conducted in May 2018. 121

Figure 63. Radiometer and visible spectrum camera pair mounted on truss. 121

Figure 64. FARO TLS Scanner. 122

Figure 65. Typical linear ignition using 10 m cord soaked in accelerant 123

Figure 66. Location of the 10 by 10-meter plots and meteorological towers at the Silas Little Experimental Forest, New Lisbon, New Jersey. The 10-meter and 3-meter towers located near the center of the plot are in the pitch and loblolly pine plantation where all experiments were conducted. 124

Figure 67. Transportable Analyser for Calorimetry Outside (TACO). 125

Figure 68. (a) Estimated consumption of fine fuels as a function of initial fuel mass, corrected for moisture content for warm season 10 by 10-meter experiments. Data are from burns 20-36. (b) The relationship between initial fuel loading and mean flame heights was curvilinear (right panel) across experiments at the three fuel loadings (1x, 2x and 3x). 130

Figure 69. (a) Estimated consumption of fine fuels as a function of initial fuel mass, corrected for moisture content for warm season 10 by 10-meter experiments. Data are from burns 20-36. (b) Fine fuel loading and estimated consumption during 10 by 10-meter burns and management scale prescribed fires conducted in the New Jersey Pinelands National Reserve. Prescribed fire data are from Clark et al. 2020. 130

Figure 70**.** Pre- and post-burn LiDAR scans provide fine-scale information on fuel consumption during 10 by 10-meter burns. 131

Figure 71. Overhead FLIR camera time series captured at 25 Hz were resampled at 0.1 Hz to estimate flame arrival times, here estimated as time to reach ≥ 300 °C, during the 10 by 10-meter burns. Data are from a fire ignited with the wind using 2x fuel loading on March 17, 2018. 131

Figure 72. Overhead FLIR camera time series captured at 25 Hz were resampled at 0.1 Hz to estimate residence times of pixel temperatures ≥ 300 °C during the 10 by 10-meter burns. Data are from a fire ignited with the wind using 2x fuel loading on March 17, 2018. 132

Figure 73. An example of 1 Hz wind velocity and direction calculated from 16 sonic anemometers mounted at 2.5 meters over fuel beds during a 10 by 10-meter burn in March 2018. Size of the arrow and color of the box is proportional to wind velocity (m sec^{-1}), and arrow direction shows direction, with mean wind direction from west to east. 133

Figure 74. Temperature data from two sets of thermocouples mounted at the 0 cm height (lower panel) and 100 cm height (upper panel) above fuel beds mounted along seven thermocouple arrays on a center truss. The fire was lit with the wind and progressed from west to east along the seven arrays. "A" indicates each array by color. Note the different temperature ranges on the y-axis. 134

Figure 75. Fire line progression from bottom to top illustrated using the FLIR camera mounted at 10-meter height above a 10 by 10-meter burn conducted on March 17, 2018 (side panel). The first panel (bottom of figure) shows the linear ignition using a line soaked in accelerant. The following panels show a typical behavior where the center of the plot burned more rapidly than the north and south edges. Colored circles indicate sonic anemometer positions along one of the trusses. 10 Hz sonic anemometer air temperature data indicating tilt of the convective plume with the wind (upper panel). 135

Figure 76. (a) The relationship between air temperature and vertical wind velocity at different heights above flame fronts during 10 by 10 m burn 8 conducted in May 2018. Yellow symbols are temperature values ≥ 5 °C above ambient air temperature measured at 10 Hz. (b) Slopes of the relationship between air temperature and vertical wind velocity at different heights above flame fronts during the management-scale burn at Silas Little Experimental Forest in March 2019 (top panel) and 10 by 10 m burn 8 in May 2018 (bottom panel). 136

Figure 77. Sensible heat fluxes measured during 10 by 10-meter burn 20 on May 20, 2019 demonstrates patterns of peak 1-minute and integrated sensible heat flux progress with fire line progression. Average maximum 1-minute sensible heat fluxes are shown on the left axis, with peak values for a sonic anemometer at each position indicated with a yellow triangle, and integrated total sensible heat flux is shown on the right axis and approximates total convective heat flux (MJ m^{-2}). The burn was ignited on the western edge with the wind and burned east (side panel). 139

Figure 78. Fire line progression and sensible heat fluxes values at each sonic anemometer for 10 by 10-meter burn 13 conducted on May 11, 2018. Fire line progression from bottom (western edge) to top (eastern edge) illustrated using the FLIR camera mounted at 10-meter height above the 3x fuel bed. Peak 1-minute sensible heat flux (KW m^{-2}; middle panel) and integrated total sensible heat flux (MJ m^{-2}; right panel) are shown for each sonic anemometer as the fire line progressed. Average maximum 1-minute sensible heat flux and integrated total sensible heat flux for each row of sonic anemometers along the trusses is shown on the right of each panel. The burn was ignited on the western edge with the wind and burned east. 140

Figure 79. Sensible heat fluxes measured during 10 by 10-meter burns 23 and 25 conducted on May 21, 2019 demonstrate how fire behavior (ROS) affects convective heat fluxes at each sonic position. a) Average maximum 1-minute sensible heat flux are shown, with peak values for a sonic anemometer at each position indicated with a yellow triangle. b) Integrated 1-minute sensible heat fluxes during the fire used to estimate total convective heat flux (MJ m^{-2}). Burns were ignited on the western edge and burned east. 141

Figure 80. Steps for processing the overhead IR data, for Burn 20. (a) Example of a single frame from the raw IR data. (b) Image of fire arrival times, based on temperature threshold criteria. (c) Arrival time matrix rotated and scaled to match real-world (TLS) coordinates, and sub-sampled at a 10 cm resolution. 145

Figure 81. Example of wind and spread rate calculation for Burn 20. (a) The computed vectors of spread rate, overlaid on a contour plot of arrival time, which are used together to create a time-history of plot-average spread. Note that the outer-most meter on either flanking edge is neglected in the analysis, and for clarity, only every 5th vector is shown. (b) The time history of plot-average spread vectors. (c) The 10-second average wind vectors and the total magnitude (U), as compared with the wind magnitude projected in the direction of average spread (u). 146

Figure 82. Fire progression for each of the 10x10 fires 148

Figure 83. Burn success (spread across the whole plot), as a function of relative humidity and average wind. Filled circles correspond to successful spread and x's to unsuccessful. 149

Figure 84. (a) Summary of dynamic spread (R) versus aligned wind (u) for all burns. (b) Data corresponding to concurrent flow ($u > 0$), with spread rate normalized by a zero-wind value, estimated for each burn based on an exponential fit. An exponential best-fit for the entire dataset is shown, where b = 0.77 150

Figure 85. The locations of observed data for the 13 March 2019 SERDP management-scale prescribed burn experiment conducted at the Silas Little Experimental Forest in southern New Jersey. 154

Figure 86. Pre- and post-burn fuel loading and estimated consumption from 24 0.5 m^{-2} plots at the March 13, 2019 management scale burn. Additional sampling was conducted in forest census plots within 100 m of the main flux tower (see Clark et al. (2018)for details). Energy partitioning was calculated from consumed fuels and moisture contents, following Kremens et al. (2012). 159

Figure 87. Fireline progression for the management scale burn conducted on March 13, 2019. The fireline is shown in orange, and timestamps for each image are shown in white in the lower left corner of each image. 160

Figure 88. Time series of (a) temperature (T), (b) zonal wind velocity (U), (c) meridional wind velocity (V), (d) vertical wind velocity (W), and (e) turbulent kinetic energy (TKE) at 3 m, 10 m, and 19 m AGL before, during, and after fire-front-passage at the west tower. 162

Figure 89. Mean (a) temperatures (T), (b) zonal wind velocities (U), (c) meridional wind velocities (V), (d) vertical wind velocities (W), and (e) turbulent kinetic energy (TKE) at 3 m, 10 m, and 19 m AGL during the pre-FFP, FFP, and post-FFP periods, computed from all five in situ towers. 164

Figure 90. Mean fractional number of sweep, ejection, outward interaction, and inward interaction events during the (a) pre-FFP, (b) FFP, and (c) post-FFP periods at 3 m, 10 m, and 19 m AGL, computed from all five in situ towers. 167

Figure 91. Mean contributions of sweep, ejection, outward interaction, and inward interaction events to the average vertical turbulent momentum fluxes during the (a) pre-FFP, (b) FFP, and (c) post-FFP periods at 3 m, 10 m, and 19 m AGL, computed from all five in situ towers. Average vertical turbulent momentum flux values (m^2 s^{-2}) at each height level are indicated with labeled yellow vertical lines....168

Figure 92. Mean fractional number (lines) and contributions (bars) of sweep, ejection, outward interaction, and inward interaction events to the average vertical turbulent momentum fluxes during the (a) pre-FFP, (b) FFP, and (c) post-FFP periods at 3 m, 10 m, and 19 m AGL at the control tower and the flux tower. Average vertical turbulent momentum flux values (m^2 s^{-2}) at each height level are indicated with labeled yellow vertical lines. 169

Figure 93. (a) Average slopes and (b) correlation coefficients for the relationship between air temperature and vertical wind velocity at different heights above flame fronts during the large-scale burn at Silas Little Experimental Forest conducted on March 13, 2019. Average maximum 10 Hz air temperatures (mean ± 1 SD) at each height are indicated to the right of each bar. 171

Figure 94. (a) 1-minute peak sensible heat flux and (b) integrated total `sensible heat flux measured at different heights above flame fronts during the large-scale burn at Silas Little Experimental Forest conducted on March 13, 2019. Red lined triangles indicated values for the west tower, and green lined triangles indicated values for the other towers in the burn area. 172

Figure 95. (a) Maximum 1-minute sensible heat flux and (b) total sensible heat flux at different heights above flame fronts during four instrumented burns in the New Jersey Pinelands. Values are means ± 1 SD, and values from the west tower at the SERDP management scale burn are indicated with yellow stars. 173

Figure 96. Convective heat flux calculated from fuel consumption measurements and above-canopy Δ sensible heat flux for low-intensity backing fires (blue symbols) and high-intensity head fires (yellow symbols).....174

Figure 97. Plant area density profiles at the nearest grid point to the six SLEF flux towers: TWR C (control), TWR E (east), TWR F (flux), TWR S (south), TWR N (north), and TWR W (west). 178

Figure 98. One-minute mean vertical turbulent heat fluxes during 15–20-minute fire period at each tower (markers), and profiles at time of peak heat flux (lines): TWR C (control), TWR E (east), TWR F (flux), TWR S (south), TWR N (north), and TWR W (west). At TWR S there was no 10-m sonic anemometer; a dashed line is used to indicate the heat flux profile there.180

Figure 99. Maximum FireTracker temperatures observed during the SLEF 2019 prescribed fire..181

Figure 100. FireTracker fire front position (thick line), ARPS-CANOPY grid cells in which the heat source is applied (black squares), and 1-min mean vertical turbulent heat flux at the six flux towers [see legend for height above ground level (AGL) of observations; heat flux values less than 1 K ms^{-1} are unshaded], at 15:28 EDT 13 Mar 2019. Towers are named as follows: TWR C (control), TWR E (east), TWR F (flux), TWR S (south), TWR N (north), and TWR W (west). At TWR S there was no 10-m sonic anemometer; gray shading is used to denote the absence of heat fluxes at this level. 182

Figure 101. Google Earth images depicting nesting strategy for SLEF case, at two zoom levels: (a) outer zoom with domains D1-D5, (b) inner zoom with domains D3-D5. See Table 16 for details of each domain. Burn block denoted by red polygon in center of domain D5.....184

Figure 102. 90th percentile values of 1-min mean wind speed [m s^{-1}] during each FPP simulation, at 9.8 m AGL, where Hf refers to the surface value of the vertical turbulent heat flux profile representing the fire sensible heat source. Contours of Ap [m^2 m^{-3}] are overlaid on each panel, and the ambient wind direction (236.5 deg) is indicated in the left panel. 187

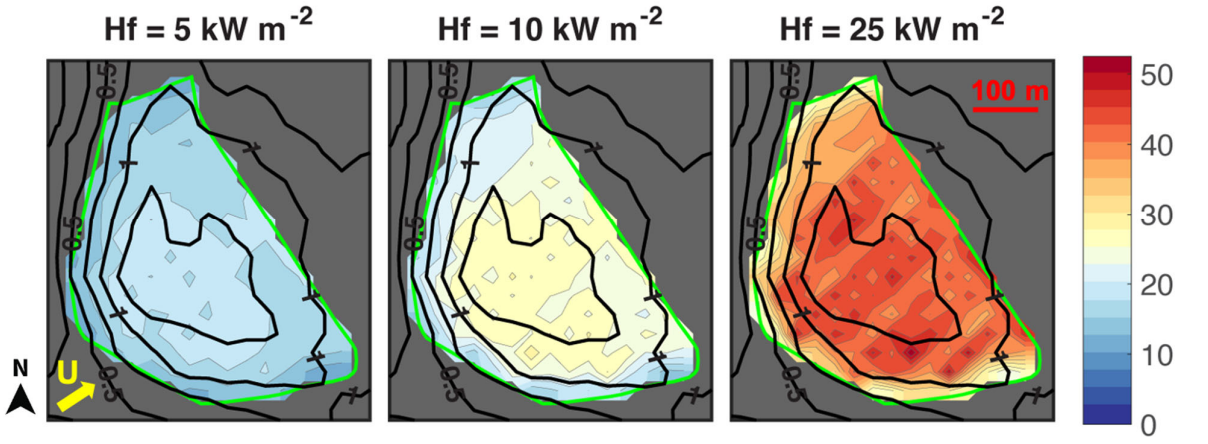


Figure 103. As in Figure 102, but for temperature [ºC] at 1 m AGL. 187

Figure 104. Schematic depicting possible configuration of 20-m flux towers for hypothetical FPP case, based on ARPS-CANOPY simulations, overlaid on Google Earth image. 188

Figure 105. Vertical profiles of time-averaged simulated variables interpolated to tower coordinates, for the ARPS-CANOPY simulation $HP_{400}VG_{84}CD_{0.2}$ (Table 16). Towers are named as follows: TWR C (control), TWR E (east), TWR F (flux), TWR S (south), TWR N (north), and TWR W (west). Averaging period is indicated below tower name; for all towers except TWR C, this period corresponds to the fire period subjectively determined from time series of observed vertical turbulent heat flux; for TWR C, this period corresponds to the one-hour period immediately prior to sea breeze passage. Lines denote the model simulation and markers denote the tower observations; see legend below figure [M: model; Os: observation (sonic anemometer); Ot: observation (thermocouple)].....190

Figure 106. Timeseries of 1-min mean simulated variables interpolated to tower coordinates, for the ARPS-CANOPY simulation $HP_{400}VG_{84}CD_{0.2}$ (Table 16). Towers are named as follows: TWR C (control), TWR E (east), TWR F (flux), TWR S (south), TWR N (north), and TWR W (west). For all towers except TWR C, the magenta lines denote the beginning and end of the fire period subjectively determined from time series of observed vertical turbulent heat flux; for TWR C, the magenta lines denote the one-hour period immediately prior to sea breeze passage. Lines denote the model simulation and markers denote the tower observations; see legend below figure [M: model; Os: observation (sonic anemometer); Ot: observation (thermocouple)].....191

Figure 107. Three-dimensional model surface plot of 1-min mean TKE at 3, 10, and 20 m AGL, for the ARPS-CANOPY simulations (a) $HP_{400}VG_{84}CD_{0.2}$ and (b) $NF_0VG_{84}CD_{0.2}$ (no-fire) (Table 17). Towers are named as follows: TWR C (control), TWR E (east), TWR F (flux), TWR S (south), TWR N (north), and TWR W (west). For TWR S the 10-m marker is omitted since there was no 10-m sonic anemometer on that tower.....192

Figure 108. Fire-period average profiles of temperature, wind speed, wind direction, and TKE, for heat source sensitivity tests, at the flux tower (TWR F). Averaging period is 15:25-15:40 EDT. See Table 17 for experiment details. Lines denote the model simulation and markers denote the tower observations; see legend below figure [M: model; Os: observation (sonic anemometer); Ot: observation (thermocouple)]. 194

Figure 109. As in Fig. 107, but for vertical turbulent heat flux profile sensitivity tests. 194

Figure 110. As in Fig. 107, but for vertical grid structure sensitivity tests. 195

Figure 111. As in Fig. 107, but for canopy drag coefficient sensitivity tests. 196

Acknowledgements

There are many that need acknowledged for their contributions to this project. First, we would like to thank the New Jersey Forest Fire Service for facilitating the field studies, particularly Greg McLaughlin, Jeremy Webber, Michael Achey, Shawn Judy, Tom Gerber, John Earlin, and Ben Brick. We also broadly thank the administrative and support staffs at each of the Co-Investigator Institutions and specifically Jerry Elian of the USDA Forest Service Northern Research Station for his assistance and diligence in processing the vast number of sub-agreements through the five years of this project. We thank the SERDP program office for working with our team through several unforeseen circumstances and supporting us as we moved forward. This work was funded by the Department of Defense Strategic Environmental Research and Development Program through award RC-2641.

Abstract

Introduction and objectives

This project, RC-2641: "Multi-scale Analyses of Wildland Fire Combustion Processes in Open-canopied Forests using Coupled and Iteratively Informed Laboratory-, Field-, and Model-based Approaches," spanned several institutions and objectives, with a focal idea that an interdisciplinary, multi-scale approach is necessary to address the questions that were presented in the original RFP. As we move across these scales of observations, there are benefits and shortfalls that occur. In the laboratory, fuel beds can be deconstructed to the scale of individual particles, and access to the newest laboratory technology and the ability to repeat measures and provide statistical rigor yield new insights. These experiments, however, are typically undertaken under simple, idealized conditions to allow study of individual phenomena. While this is advantageous in many cases, these studies need to be contrasted with those undertaken at larger scales. Conversely, while a prescribed fire (tens of hectares) provides an opportunity to study the phenomenon at an operational scale, it is impossible to account for, or measure, the myriad of factors, many of which exhibit strong couplings, that are interacting in the field and to make sense of the fundamental phenomenon that are driving the fire. Rectifying the reality of the field with the simple elegance of the laboratory was the challenge of this project.

Technical approach

Our specific technical approach was to:

1) Use a combination of integrated laboratory and field measurements to quantify particle-scale and fuel-bed-scale based combustion and transport processes to support the development of a mechanistic description of surface and ground fire behavior.
2) Conduct a series of small-scale, highly instrumented prescribed burn experiments in the field to quantify the interactions among fuel-bed structure, moisture content, and meteorological factors (e.g. wind, humidity, temperature) driving variability in fire behavior and fuel consumption.
3) Conduct two management-scale field experiments during operational prescribed burns to quantify how larger-scale atmospheric dynamics, including ambient, fire-induced, and forest canopy-induced turbulence regimes within and near the fire environment affect fire propagation, energy exchange, and fuel consumption.
4) Augment the management-scale field experiments with numerical model simulations of coupled fire-atmosphere dynamics under varying environmental conditions to further understanding of how those dynamics affect management-scale fire propagation and heat transfer.

Results

The multiple sub-studies of this project have resulted in a a range of new findings that span broad scales of processes related to improving our understanding of fire spread. For example, when investigating heat transfer implications for flame spread in the laboratory, we found that varying the structure of porous fuel beds, both the fuel loading and bulk density were observed to independently influence the flame spread rate and fire behavior. At the field scale, in the buoyant atmospheric layers above fire fronts within forested areas, the downward turbulent flux of higher horizontal momentum air from aloft can still occur throughout the vertical extent of the overstory vegetation and thereby potentially introduce high momentum air (i.e., wind gusts) into combustion zones and affect fire spread.

Benefits

The benefits of this project are rooted in the original request for proposals that emphasized investigating fundamental physical processes of fire dynamics. Our project provides insights at numerous scales that will help to underpin future wildland fire modeling for both wildland and prescribed fires. Additionally, we have been careful to document and curate our data products for future interrogation and use as a benchmark for future models.

Executive Summary

Introduction

This project, RC-2641: "Multi-scale Analyses of Wildland Fire Combustion Processes in Open-canopied Forests using Coupled and Iteratively Informed Laboratory-, Field-, and Model-based Approaches," spanned several institutions and objectives, with a focal idea that an interdisciplinary, multi-scale approach is necessary to address the questions that were presented in the original RFP. Thus, our project team has worked to span the idea of "scale" in this project with the aim of leveraging these different approaches to drive forward understanding of the processes that control fire behavior. We have also worked with a project team that spans several areas of expertise in engineering, remote sensing, ecology, and fire management and atmospheric science. The interaction between these varied specialties allows for several approaches and different insight to the common objectives of the project.

As we move across scales of observations, there are benefits and shortfalls that occur. In the laboratory, fuel beds can be deconstructed to the scale of individual particles, and access to the newest laboratory technology and the ability to repeat measures and provide statistical rigor yield new insights. These experiments, however, are typically extremely idealized and not representative of field conditions, nor do they provide an opportunity to examine and tease apart some of the complex interactions between the fire and the fire environment. Conversely, while a prescribed fire (tens of hectares) provides an opportunity to study the phenomenon at an operational scale, it is impossible to account for, or measure, the myriad of factors that are interacting in the field and to make sense of the fundamental phenomenon that are driving the fire. Rectifying the reality of the field with the simple elegance of the laboratory was the challenge of this project.

Objectives

Many DoD facilities utilize low intensity prescribed fire to manage hazardous fuels, restore ecological function and historic fire regimes, and encourage the recovery of threatened and endangered species in the forests they manage. Current predictive models used to simulate fire behavior during low-intensity prescribed fires (and wildfires) are empirically-based, simplistic, and fail to adequately predict fire outcomes because they do not account for variability in fuel characteristics and interactions with important meteorological variables. We are using a suite of measurements at the fuel particle, fuel bed, field plot, and stand scales to quantify how variability in fuel characteristics and key meteorological factors interact to drive fire behavior during low intensity prescribed burns. Our experiments were designed to inform the development and evaluation of mechanistic, physics-based models that explicitly account for combustion, turbulent transfer, and energy exchange by coupling and scaling individual component processes. These will improve our understanding of, and ability to accurately predict, fire behavior under a wide range of management scenarios. The objectives of our proposed research and the specific SERDP RCSON-16-02 research needs they address are shown below:

Objective 1) Improve our understanding of the processes driving heat transfer, ignition, thermal degradation, flaming and smoldering combustion, mass consumption, and fire propagation at the scale of individual fuel particles and fuel layers in low-intensity surface fires.

Objective 2) Develop an understanding of how fuel consumption is affected by spatial variability in fuel particle type, fuel moisture status, bulk density, and horizontal and vertical arrangement of fuel components in low-intensity surface fires.

Objective 3) Increase our understanding of the effects of multi-scale atmospheric dynamics, including ambient and fire- and forest overstory-induced turbulence, on fire spread and convective heat transfer in low-intensity surface fires.

Objective 4) Ensure that the measurements undertaken support the development and validation of physics-based fire behavior models using an iterative approach consisting of laboratory, field, and model simulations.

Our research is aimed at measuring key factors controlling fire behavior across multiple spatial and temporal scales. To accomplish our goals, we have developed a suite of laboratory and field experiments which account for relevant variation in fuel characteristics and meteorological factors at several scales and with replication, when possible. Our research efforts are focused on open-canopy, pitch pine (*Pinus rigida* Mill.)-dominated stands, with shrub-form oaks, ericaceous shrubs and herbaceous vegetation in the understory. These forests 1) have a relatively simple forest structure, 2) are directly relevant to DoD installations throughout the NE US, and 3) are adjacent to large population centers in the NE US.

Technical approach

Our specific technical approach was to:

1) Use a combination of integrated laboratory and field measurements to quantify particle-scale and fuel-bed-scale based combustion and turbulent transfer processes to support the development and testing of a mechanistic description of surface and ground fire behavior.

2) Conduct a series of small-scale, highly instrumented prescribed burn experiments in the field to quantify the interactions among fuel-bed structure, moisture content, and meteorological factors (e.g. wind, humidity, temperature) driving variability in fire behavior and fuel consumption.

3) Conduct two management-scale field experiments during operational prescribed burns to quantify how larger-scale atmospheric dynamics, including ambient, fire-induced, and forest canopy-induced turbulence regimes within and near the fire environment affect fire propagation, energy exchange, and fuel consumption.

4) Augment the management-scale field experiments with numerical model simulations of coupled fire-atmosphere dynamics under varying environmental conditions to further understanding of how those dynamics affect management-scale fire propagation and heat transfer.

This approach spans scales with an ensemble of interactive and complementary studies: particle-based combustion experiments in the laboratory; fuel-bed scale combustion and flow-field experiments in the laboratory and the field; a series of small-scale, highly instrumented prescribed burn experiments in the field during dormant and growing season conditions; and management-scale field experiments conducted during two operational prescribed burns. One of the strengths of our research is the iterative approach employed, which has allowed initial experimental findings and model simulations to feedback and sharpen the focus of further measurements, both within and among experimental components, and at different scales and levels of control on the experimental conditions. A second strength is the commonality of

measurements, instrumentation, and methods employed across spatial scales, allowing us to transfer the detailed understanding of wildland fuel combustion gained at small-scale to management-scale prescribed burn conditions. Our approach is to address these objectives using a multi-scale approach of experimentation and modeling.

Results and Discussion

In the following section, we point out important conclusions that have arisen from our investigations. This section is organized as follows; i) small-scale laboratory investigations, ii) mid-scale laboratory investigations, iii) small-scale field investigations, and iv) management-scale field investigations and atmospheric modeling."

Small-scale laboratory investigations.

Thermal decomposition of vegetative fuels and fuel bed flammability

- The decomposition of a range of dead vegetation typically forming litter layers was characterized by a pyrolysis temperature in the relatively narrow region of 320—360°C. Given that ignition occurs soon after the onset of pyrolysis (at or close to the lower flammability limit) this narrow range means that the differences in structure of the fuel bed will contribute significantly to any inter-species variation in flammability due to the resulting changes in the heat and mass transfer processes.

Burning of pine needle and manufactured fuel beds.

- The flammability of fuel beds is a strong function of the structure of the fuel bed. This arises due to the effects of flow through the porous fuel which acts to cool the fuel bed prior to ignition. However, once ignited the burning rate was shown to increase due to increased oxygen availability This highlights the complex interactions at the heart of the burning of wildland fuels. The implications of this work again point to the fuel bed structure as a controlling property in wildfire dynamics.
- Flame spread through porous natural fuel beds in quiescent conditions (no wind, no slope), flame spread rate (along with the energy release rate and flame height) was found to increase with independent increases in fuel loading or decreases in bulk density (Figure ES 1). Yet in terms of linking these bulk parameters to the physical processes driving flame spread, neither parameter alone can sufficiently explain the observed changes in fire behavior. A better correlation is observed with a dimensionless fuel bed parameter, $\alpha\sigma\delta$, incorporating terms for porosity, α, surface-to-volume ratio, δ, and fuel bed height , σ, similar to previous studies involving wood cribs and engineered fuel beds.

0.2 kg/m^2, 20 kg/m^3



t = 191 s (Probe 1)



t = 342 s (Probe 2)



t = 494 s (Probe 3)

0.8 kg/m^2, 20 kg/m^3



t = 136 s (Probe 1)



t = 248 s (Probe 2)



t = 363 s (Probe 3)

1.6 kg/m^2, 20 kg/m^3



t = 92 s (Probe 1)



t = 159 s (Probe 2)



t = 241 s (Probe 3)

Figure ES 1. Composite of frames from downward-looking video footage of flame spread experiments displaying variation in flame and front shape between Pitch Pine fuel beds of (Top) 0.2 kg/m^2, 20 kg/m^3 (Middle) 0.8 kg/m^2. 20 kg/m^3 (Bottom) 1.6 kg/m^2, 20 kg/m^3.

- Independent changes in bulk density and fuel loading were observed to result in variations in the buoyancy induced flows. In the buoyancy-controlled regime explored in this study, this buoyant flow drives lateral entrainment towards the fire front. Variations in the entrainment flow profile through the porous fuel bed were observed as this buoyant flow profile changed, with an overall trend of increasing mean entrainment velocity towards the approaching flame front as the fuel loading was increased.
- Study of the heat transfer mechanisms controlling the flame spread process, highlighted the dominant role of “in-bed” heat transfer i.e. heat transfer from the smouldering combustion region behind the flame front to the unburnt fuel. The significance of heat transfer from the flame generally increased with increasing $\alpha\sigma\delta$ value of the fuel bed Comparison of a simple thermal model with the experimental

observations of spread rate, indicated a maximum variation in predicted ROS of 29 % where only radiative transfer from the in-bed combustion region was considered, with closer agreement at lower $\alpha\sigma\delta$ values. Where the contributions of both the in-bed and above-bed heat transfer mechanisms were considered, the need to incorporate additional heat loss terms into this thermal model were apparent. Similarly, the importance of understanding the short-range heat transfer mechanisms involved in the flame spread process is emphasized, with this approach embracing the concept of a surface of fire inception within the fuel bed.

Towards improved modeling of flow and heat transfer in litter fuels

- The importance of the fuel bed structure in controlling the magnitude of the transport processes associated to flame spread was further explored through studies of drag and convective heat transfer in porous fuel beds. The results of these experiments indicated that fuel bed drag under relevant conditions is represented well by a Forchheimer equation (i.e. dominated by inertial rather than viscous effects). This finding allowed for improved predictive capability compared to existing models of drag in wildland fuels. Convective heat transfer in fuel layers was evaluated and Nusselt number correlations for fuel beds with randomly oriented fuel particles were developed. These allow alternative descriptions of the fuel bed heat transfer compared to those currently implemented in numerical models (Figure ES 2).

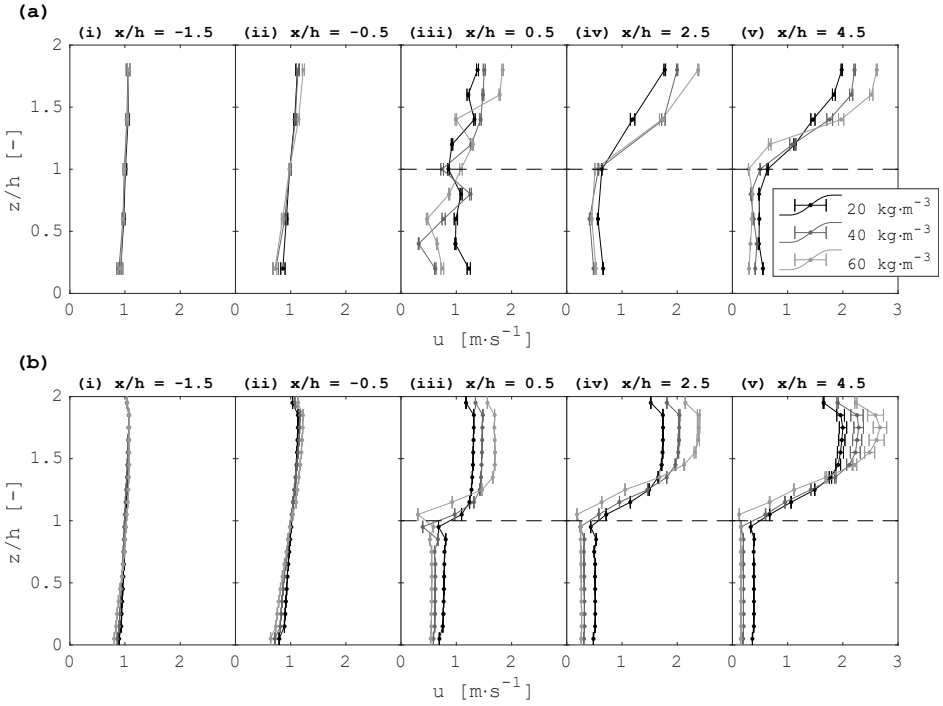


Figure ES 2. Development of vertical profiles of velocity in the streamwise direction for the (a) experiments and (b) simulations, for each of the bulk densities tested, taking the case of u_0 = 1 m·s^{-1}. Error bars represent the standard deviation. The horizontal dashed line represents the upper surface of the fuel bed, z/h = 1. Note that the experimental profiles only represent a single repeat.

Mid-scale laboratory investigations

- The fire spread behavior along a suspended array of wooden dowels was investigated for a range of spacings (0.5, 0.65, 0.75, 1, and 1.15 cm) and wind speeds (1, 2, and 3 m/s). At fixed spacings, the spread rate generally increases with faster flow speeds. However, deviations from expected propagation behavior occur. Namely, at the 1 cm spacing conditions, faster spread is observed when subjected to a flow of 2 m/s rather than 3 m/s, in contrast to the other spacing conditions. Furthermore, increasing the spacing between dowels does not always lead to slower ignition times, with the 0.75 cm spacing cases showing spread rates comparable to those of 0.5 cm at 2 and 3 m/s flow speeds.
- Flame visualization showed smaller discrete flames formed in the 1 cm spacing array when subjected to a 3 m/s flow. The higher frequency vortices measured with pitot probes developed from each dowel cylinder are changing the gaseous mixing conditions as well as stretching or constricting the flame in a way that fluctuates the heat transfer. Consequently, there exists a shift in the spread rate trend between the 0.75 cm and 1 cm spacings. Flow effects seemed to be minimal for the spacings below 0.75 cm. At 0.75 cm spacing the mixing and flow conditions are such that an optimal combination is achieved leading to fire propagation as fast as the 0.5 cm spacing cases. Once past 0.75 cm spacing, the fire spread was slowed down significantly.

Small-scale field investigations

- 10 by 10-meter experiments were designed to "bridge the gap" between small-scale laboratory experiments conducted under controlled conditions, and large, management-scale prescribed fire experiments conducted under a finite set of meteorological and fuel loading and moisture contents, yet are essentially uncontrolled experiments. Employing much of the instrumentation and information collected at smaller and larger scales during 10 by 10-meter experiments has contributed to an improved understanding of combustion processes and fire behavior during prescribed fires, but has also identified some limitations to this approach and highlighted a number of areas to be pursued in future research efforts.
- Sampling of fine-scale pre- and post-fuel structure for consumption utilized both biometric and LiDAR-based approaches. Instrumentation including thermocouple arrays to estimate gas temperatures and arrival times of flame fronts, sonic anemometers to estimate turbulence statistics and sensible heat fluxes, and custom multispectral radiometers to measure radiative heat flux have been used during small-scale laboratory investigations and large-scale prescribed burns.
- This analysis has shown the challenge in correlating observed fire behavior with environmental variables. This is due to the time-dependent nature of the fire spread phenomena and in particular challenges associated with accounting for the effects of wind hence reinforcing the need for multi scale investigation of the phenomena. Despite this, some observations regarding the effects of variables such as relative humidity on the success (or otherwise) of a burn have been identified.

Management-scale field investigations

- Even in the buoyant atmospheric layers above fire fronts within forested areas, the downward turbulent flux of higher horizontal momentum air from aloft can still occur throughout the vertical extent of the overstory vegetation and thereby potentially introduce high momentum air (i.e., wind gusts) into combustion zones and affect fire spread (Figure ES 3). The extent to which this downward turbulent momentum transfer can occur, of course, is partially dependent on fire intensity, but also related to the plant-area-density characteristics of the overstory vegetation, with denser overstory vegetation leading to enhanced dissipation of turbulence energy via the breakdown of large turbulent eddies to smaller turbulent eddies by forest structural elements.

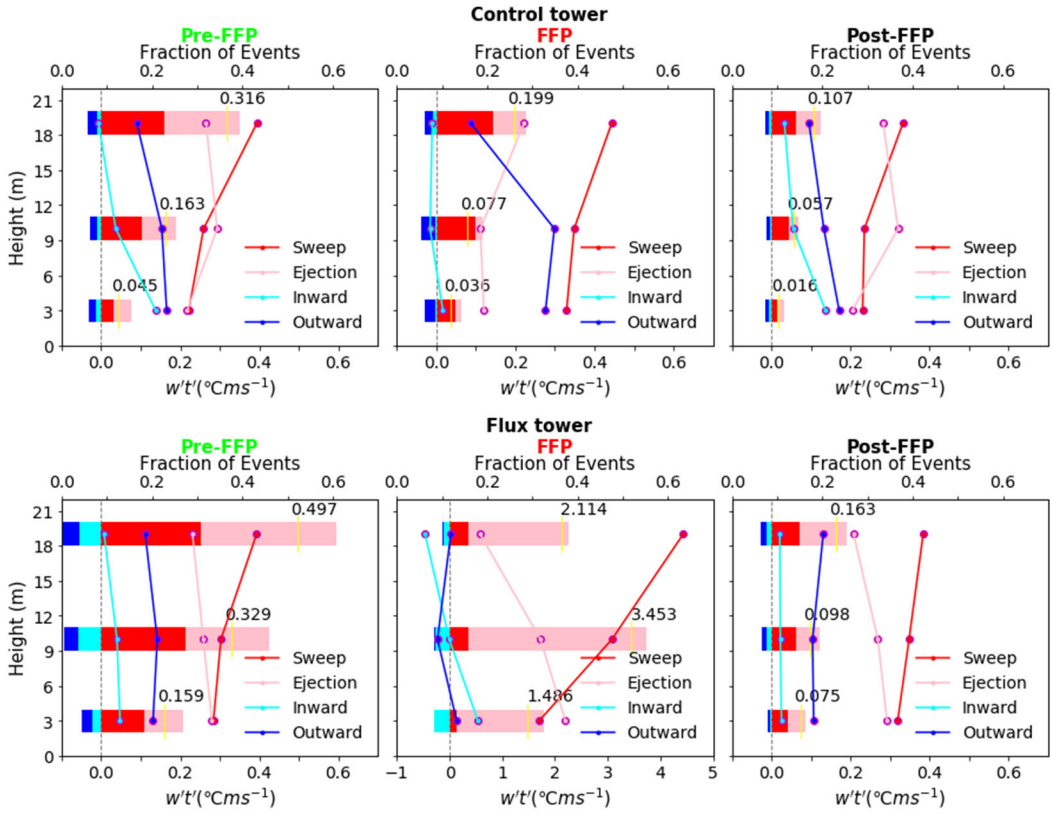


Figure ES 3 Mean fractional number (lines) and contributions (bars) of sweep, ejection, outward interaction, and inward interaction events to the average vertical turbulent momentum fluxes during the (a) pre-FFP, (b) FFP, and (c) post-FFP periods at 3 m, 10 m, and 19 m AGL at the control tower and the flux tower. Average vertical turbulent momentum flux values (m^2 s^{-2}) at each height level are indicated with labeled yellow vertical lines.

- Convective heat flux calculated from fuel consumption and sensible heat flux calculated from sonic anemometer data during the passage of fire fronts compared favorably, as has been demonstrated in previous large-scale prescribed fires.

Management-scale atmospheric modeling

- The pre-burn modeling framework developed herein shows promise for informing instrumentation deployment strategy for future prescribed fires. Preliminary results suggest one or more linear arrangements, with clustering where simulated gradients are overall strongest. However, deployment recommendations may depend on the specific variables of interest (e.g., wind speed, turbulent kinetic energy or TKE, relative humidity). Furthermore, the actual deployment strategy is subject to late adjustments based on weather forecasts, and above all, on-the-ground expertise.
- The post-burn model evaluation exercise and sensitivity experiments have provided useful insights into the strengths and weaknesses of the atmospheric model and the fire sensible heat source representation in the model. The model simulated mean wind and temperature structure and evolution were in good agreement with the measurements by the instrumented tower array and the model also captured the observed TKE at half of the six instrumented towers (Figure ES 4).

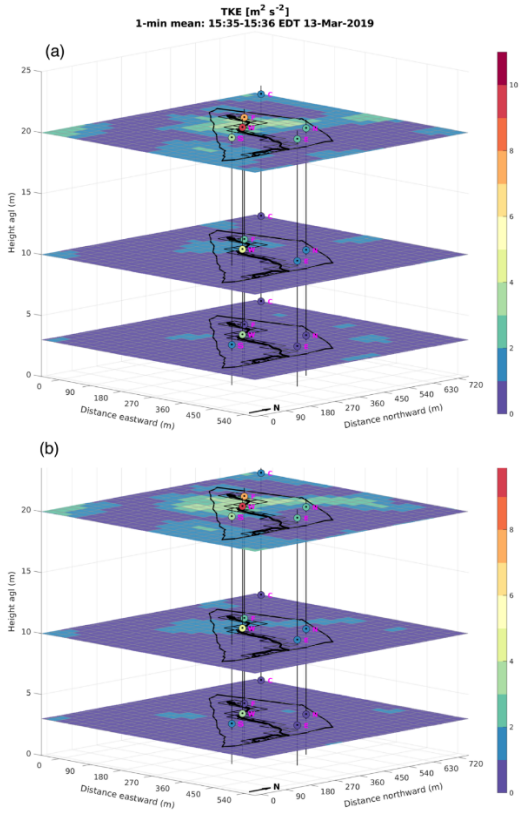


Figure ES 4.Three-dimensional model surface plot of 1-min mean TKE at 3, 10, and 20 m AGL, for the ARPS-CANOPY simulations (a) $HP_{400}VG_{84}CD_{0.2}$ and (b) $NF_0VG_{84}CD_{0.2}$ (no-fire) (Table 17). Towers are named as follows: TWR C (control), TWR E (east), TWR F (flux), TWR S (south), TWR N (north), and TWR W (west). For TWR S the 10-m marker is omitted since there was no 10-m sonic anemometer on that tower.

- At the remaining towers, overstory Turbulent Kinetic Energy (TKE) was grossly underestimated. None of the fire heat source approaches used in the model yielded the quantity of TKE observed at these towers. Possible reasons for the TKE underestimation include (1) orientation of the ambient wind normal to the fireline as it passed beneath the towers, yielding a relatively short residence time for air parcels crossing the one-grid-point-wide model fireline, compared to other periods during the burn when the ambient wind was oriented at an oblique angle to the fireline; and (2) the absence in the model of smoldering heat release behind the fireline that may have contributed to the larger TKE values observed at the towers.

Implications for future research and benefits

This work has provided an immense amount of information regarding combustion process and fire behavior but has also indicated that there are significant gaps in our understanding of the effects of fuel bed structure on the combustion process driving flame spread. The complex and coupled nature of fluid mechanics and heat transfer within structured fuels requires further investigation, particularly when considering understory and canopy fuels in addition to the surface fuels that we focused on here. For example, it has been shown that flow in porous fuels can lead to cooling due to convection but also increased combustion due to the enhanced flow of oxygen. These sensitivities require further investigation to allow improved prediction of fire phenomena, and this type of tradeoff creates uncertainties that will require further investigation. Overall, an improved understanding of combustion processes and the interactions between environmental variables and fuel attributes have resulted from our project, and this will improve our ability to predict the fire spread and fuel consumption in the future.

Our findings have highlighted the role of fuel structure in the burning of fuel layers. The structure cannot be adequately described by commonly used terms of fuel load and bulk density. Investigations of fuel flammability suggest that an optimal fuel structure exists for a given fuel type due to the controlling (and competing) processes which govern burning. Future assessments of wildland fuel flammability should seek to quantify these effects in more detail.

In addition, the effects of fuel structure on the mean entrainment flow and radiative heat transfer through the fuel bed require further investigation. Resolving the flow will allow better evaluation of the convective heat transfer ahead of the flame region and the oxygen mass flux available for combustion in the flaming and smoldering regions. The heat transfer from this trailing, smoldering region, and the factors on which it depends, also needs to be better quantified. Understanding these processes will allow for improved understanding of low-intensity fire spread. region and the overall flame spread process.

An important outcome of the modeling effort of the management-scale fire experiment is the knowledge gained regarding the fire heat source representation in ARPS-CANOPY. The turbulent heat flux profile approach used successfully in Kiefer et al (2014) performed poorly in this study. It is critical to note that none of the one-way heat source approaches applied in previous ARPS and ARPS-CANOPY studies (exponentially decaying vertical turbulent heat flux profile, surface turbulent heat flux, or soil temperature perturbation) has been adequately validated. Furthermore, the need for a fire behavior sub model in ARPS-CANOPY is underscored by the shortcoming of the one-way heat source representation used in this study.

Efforts are ongoing external to this project to implement the wildland fire spread model DEVS-FIRE in ARPS-CANOPY, as was done with ARPS in Dahl et al. (2015).

Because capturing the spatial and temporal distribution of ambient, fire, and forest overstory-induced mean and turbulent flows has relevance to prediction of, for example, fire behavior, smoke dispersion, and tree mortality, the analyses of the model results have been focused on (1) identifying turbulence processes present during management-scale fire but not captured by the model, and (2) improving the representation of the fire sensible heat source in the model. Overall, these studies serve to explore the dynamic effects of wind in the field and serve to contrast with the quiescent conditions studied in the laboratory. The data sets generated will inform future studies and provide an evidence base for future numerical model development.

An important benefit of the work completed in this project is the vast amount of data that will be available for future modeling. We have paid particular attention to experimental design, replication, and data consistency in the outdoor 10x10 fire spread experiments. Meta-data and carefully quality-checked data files for these experiments will be available as citable data products housed at the USDA Forest Service Research Data Archive. In addition, our data has been selected as pilot data for the ESS-Dive demonstration project.

Overview

Objective

Many DoD facilities throughout the eastern United States utilize low intensity prescribed fire to manage hazardous fuels, restore ecological function and historic fire regimes, and encourage the recovery of threatened and endangered species in the forests they manage. Current predictive models used to simulate fire behavior during low-intensity prescribed fires (and wildfires) are empirically-based, simplistic, and fail to adequately predict fire outcomes because they do not account for variability in fuel characteristics and interactions with important meteorological variables. We propose to use a suite of measurements at the fuel particle, fuel bed, field plot, and stand scales to quantify how variability in fuel characteristics and key meteorological factors interact to drive fire behavior during low intensity prescribed burns. We have designed these experiments to inform the development and evaluation of mechanistic, physics-based models that explicitly account for combustion, turbulent transfer, and energy exchange by coupling and scaling individual component processes. These will improve our understanding of, and ability to accurately predict, fire behavior under a wide range of management scenarios.

The objectives of our proposed research and the specific SERDP RCSON-16-02 research needs they addressed are shown below:

Objective 1) Improve our understanding of the processes driving heat transfer, ignition, thermal degradation, flaming and smoldering combustion, mass consumption, and fire propagation at the scale of individual fuel particles and fuel layers in low-intensity surface fires (Addresses Research needs 1, 2, and 3).

Objective 2) Develop an understanding of how fuel consumption is affected by spatial variability in fuel particle type, fuel moisture status, bulk density, and horizontal and vertical arrangement of fuel components in low-intensity surface fires (Addresses Research needs 2 and 4).

Objective 3) Increase our understanding of the effects of multi-scale atmospheric dynamics, including ambient and fire- and forest overstory-induced turbulence, on fire spread and convective heat transfer in low-intensity surface fires (Addresses Research need 4).

Objective 4) Ensure that the measurements undertaken support the development and validation of physics-based fire behavior models using an iterative approach consisting of laboratory, field, and model simulations (Addresses Research needs 1-4).

Background

Current operational models for fire intensity, fuel consumption, gas-phase emissions, and ecological effects of fire are largely empirically based and fail to capture the physical processes that regulate variability in combustion and fire spread (Andrews 2014). To-date, the goal of most measurement studies of wildland fire has been to create datasets to support the empirical models. This does not advance a fundamental understanding of the physics underlying wildland fire behavior, which is the only way to substantially improve our ability to predict fire behavior. In this project, we propose an integrated multi-scale approach to collect and analyze data that will support the further development of physics-based models, and support the assumptions needed to develop simpler models that would be more accurate at the landscape scale.

Mechanistic, physics-based models explicitly account for the processes driving fire behavior by coupling and scaling individual component processes. Important component processes (see Fig. 1) include thermal degradation (drying, pyrolysis, and smoldering) at the fuel particle scale; momentum drag, and convective and radiant heat transfer at the fuel bed and fire scales; and interactions between ambient wind fields, forest structure, heat release rate from gas-phase combustion, and buoyancy- and shear-induced turbulence on the scale of a fire's plume.

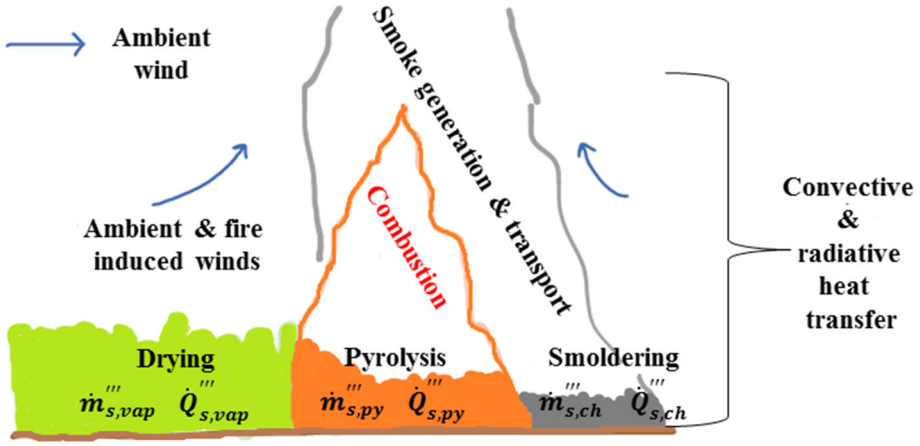


Figure 1. Schematic of a backing surface fire (spreading right to left).

An example of a detailed physics-based fire-spread model is the Wildland-urban interface Fire Dynamics Simulator (WFDS), which is one of the models in which our experimental databases and simulations of fire spread/behavior are based. The WFDS model numerically solves the equations governing transient three-dimensional fluid flow and thermal radiation. Model equations for the thermal degradation of the vegetation are coupled to the gas-phase through mass and heat generation associated with the thermal degradation of the vegetation. Large-eddy simulation (LES) methods are used to model the turbulent flow and the gas-phase turbulent combustion.

The governing equations in WFDS are listed below. Figure 1 is a schematic showing the processes modeled in WFDS and terms found in the model equations. These include mass generated (kg s^{-1} m^3) in the form of water vapor during vegetation drying ($\dot{m}'''_{s,vap}$) and fuel vapor during pyrolysis ($\dot{m}'''_{s,py}$). The terms for heat sources (or sinks; kW kg^{-1} m^{-3}) are also shown: endothermic drying ($\dot{Q}'''_{s,vap}$), pyrolysis ($\dot{Q}'''_{s,py}$), exothermic smoldering or char oxidation ($\dot{Q}'''_{s,ch}$). These processes of thermal degradation are driven by the radiative heat transfer generated by combustion and the convective heat transfer generated by the interacting ambient and buoyancy-induced flows.

The main balance equations of WFDS are (Mell et al. 2009); nomenclature is provided in Appendix 1:

Gas Phase:

$$\frac{\partial \rho}{\partial t} + \nabla \cdot (\rho \boldsymbol{u}) = \dot{m}'''_{s,vap} + \dot{m}'''_{s,py} \quad \text{(Total mass)}$$

$$\frac{\partial (\rho Y_i)}{\partial t} + \nabla \cdot (\rho Y_i \boldsymbol{u}) = \nabla \cdot (\rho D_i Y_i)_{LES} + \dot{m}'''_i + \dot{m}'''_{s,i} \quad \text{(Mass of gas species i)}$$

$$\frac{\partial(\rho \boldsymbol{u})}{\partial t} + \nabla \cdot (\rho \mathbf{u}\mathbf{u}) = -\nabla p - (\nabla \cdot \boldsymbol{\tau})_{LES} + \rho \boldsymbol{g} + \boldsymbol{F}_D \quad \text{(Momentum: Navier-Stokes equations)}$$

$$\rho \frac{\partial h}{\partial t} + \rho \boldsymbol{u} \cdot \nabla h = \frac{Dp_o}{Dt} - (\nabla \cdot \boldsymbol{q})_{LES} - (\nabla \cdot \dot{\boldsymbol{q}}''_r)_{LES} + \nabla \cdot \dot{\boldsymbol{q}}''_{sr} + \nabla \cdot \dot{\boldsymbol{q}}''_{sc} + \dot{h}'''_s \quad \text{(Energy)}$$

Solid Phase:

$$\beta_s \rho_s c_{p,s} \frac{\partial T_s}{\partial t} = -\nabla \cdot \dot{\boldsymbol{q}}''_{sr} - \nabla \cdot \dot{\boldsymbol{q}}''_{sc} - \dot{Q}'''_{s,vap} - \dot{Q}'''_{s,py} - \dot{Q}'''_{s,ch} \quad \text{(Energy)}$$

The balance equations represent the Navier-Stokes equations applied to a multiphase radiative and reactive medium for the gas phase and an energy balance for the solid phase. The different phases are the solid phase, representing vegetation with its different classes of fuel and particles (denoted by an *s* subscript in the equations above), and the gas phase. Some of the sub-models, such as the LES model for turbulence are adapted from other fields (in this case fluid mechanics and turbulent transfer theory) and directly applied to the problem of wildland fire spread. However, in order to make this model mathematically tractable ("close" the model), sub-models have to been established to describe the source terms, from the drying and burning of the vegetation, in the balance equations and the coupling between phases. This is where a fundamental gap occurs, which is very specific to wildland fires and cannot be obtained from other fields: we need to describe the fuel and its interaction with the gas phase. This covers several aspects that need to be treated separately.

The first aspect is to describe what gas species are formed by the thermal degradation of the fuel and converted to the gas phase to support the flames (see $\dot{m}'''_{s,i}$ terms in gas phase total mass conservation equation); this aspect is fundamentally linked to the convective and radiative heat transferred from the fire front to the unburned and burning fuel (see $\dot{q}''_{sc}$ and $\dot{q}''_{sr}$ in solid phase energy equation, respectively), which represents another aspect. It is also linked to the way vegetation dries, ignites, and burns (see $\dot{Q}''_{s,vap}$, $\dot{Q}''_{s,py}$, and $\dot{Q}''_{s,ch}$ in the solid phase energy equation), which is the main aspect linked to the description of vegetation as a fuel. Another very important aspect is the interaction between the vegetation layer and the wind. The friction between the vegetation layer and the gas flow is represented by the drag forces (see $\boldsymbol{F}_D$ in gas phase momentum equation) and this drives the wind profile in the fuel layer which in turn influences the heat transfer within the fuel. Drag forces also influence the turbulent transfer between the fuel layer, the fire plume, and the atmosphere. All of these aspects strongly depend on the particle and fuel bed properties, which are explicitly formulated (Mell et al. 2009). However, particle and fuel bed properties are difficult to discriminate and need to be decoupled using well-designed and well-controlled laboratory experiments (Bartoli et al. 2011b). It is then possible to reintroduce them in steps to better understand and describe their coupling. This is what we propose to do by conducting small-scale laboratory experiments (most decoupled phenomena), laboratory fire spread experiments (wind tunnel for controlled wind, fuel, and ambient conditions), controlled field experiments (for controlled wind conditions) and open field experiments (for uncontrolled but more realistic conditions).

To date, most lab and field measurements of fires in vegetation have been collected with the purpose of developing and evaluating empirical models that predict only net outcomes of the coupled physical processes (e.g., spread rate, total fuel consumption) under idealized or limited

conditions (Rothermel 1972; Stocks et al. 2004). These measurements, and the resulting empirical models, are significantly restricted in their ability to clarify the relevance of variability in vegetation, soil, and meteorological factors to the behavior of a fire (e.g., rate of fuel consumption or heat fluxes). Alternatively, inter-connected laboratory, field measurement and modeling studies focused on fundamental fire processes can provide a basis for both understanding and predicting the behavior and outcome of wildland fire as influenced by local variability in the vegetation and the ambient atmospheric conditions, and also move forward the understanding of scale as related to fire propagation and behavior.

To improve our understanding of fire behavior, it is necessary to consider the processes outlined above across a range of scales. For example, the response, or thermal degradation, of individual fuel elements (e.g., pine needles, leaves, branches, etc.) to the net surface heat flux determines if ignition, sustained flaming, and smoldering will occur in a given wind environment. Thermal degradation is complex, and both measurements and physics-based models are far from complete in capturing important processes accurately, as discussed above (Finney et al. 2013). In addition, variation in fuel bed properties surrounding individual fuel elements (e.g., pine needle) may be present, creating variability in bulk properties and spatial arrangements relevant to heat transfer and wind flow (e.g., pine needle bed on the forest floor versus pine needles in a tree crown, (Simeoni et al. 2011)). Finally, the behavior of the fire plume, which is a major source of heat and turbulence, depends on the interaction of the combustion-generated buoyant flow with the ambient wind and canopy drag forces (Kiefer et al. 2014; Mueller et al. 2014).

Currently, measurements are limited for quantifying and linking the relevant processes outlined above across scales. Laboratory experiments, which allow controlled and repeatable environmental conditions, are essential to advance our understanding of the response of fuel elements to a given net heat flux environment (Santoni et al. 2014). Idealized, but representative, laboratory experiments of fuel beds also provide measurements for advancing models for momentum drag, heat transfer via convection and radiation, wind flow in and around spatially complex fuel beds, and fire propagation across horizontal and vertical gaps separating fuel beds. When possible, these laboratory measurements should reproduce environmental conditions that are representative of conditions in the field for the problem of interest and should cover a wide range of the studied parameters. This requires appropriate field measurements of the ambient wind fields, vegetation structure, and soil characteristics. Finally, replicated field experiments with fire are needed in an environment that is as controlled as possible and instrumented with sufficiently high density sensor arrays that the influence of the spatial distribution of vegetation and atmospheric conditions (wind, temperature, and humidity) on fire behavior can be accounted for. In addition to these quantities, measurement of temperature and heat fluxes will also support validation of a physics-based modeling system (as opposed to validation of the component sub-models).

Our specific technical approach was to (Figure 2):

1) Use a combination of integrated laboratory and field measurements to quantify particle-scale and fuel-bed-scale based combustion and turbulent transfer processes to support the development and testing of a mechanistic description of surface and ground fire behavior.
2) Conduct a series of small-scale, highly instrumented prescribed burn experiments in the field to quantify the interactions among fuel-bed structure, moisture content, and meteorological factors (e.g. wind, humidity, temperature) driving variability in fire behavior and fuel consumption.

3) Conduct two management-scale field experiments during operational prescribed burns to quantify how larger-scale atmospheric dynamics, including ambient, fire-induced, and forest canopy-induced turbulence regimes within and near the fire environment affect fire propagation, energy exchange, and fuel consumption.
4) Augment the management-scale field experiments with numerical model simulations of coupled fire-atmosphere dynamics under varying environmental conditions to further understanding of how those dynamics affect management-scale fire propagation and heat transfer.

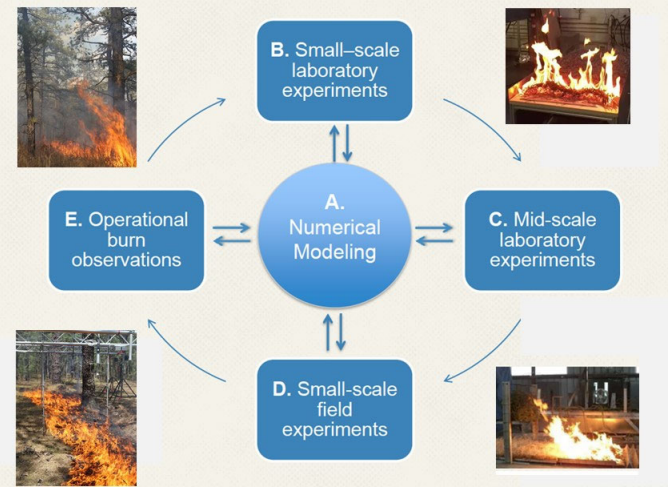


Figure 2. Schematic of SERDP project RC-2641.

The following sections of this report divide our project into representative sections to best explain the investigations that were undertaken at the multiple scales.

Small-scale laboratory investigations

Objective

The objective of this package of work is to explore observations made during the field scale experimental program and explore at higher resolution, and in a systematic way free from the influence of environmental variables, the transport processes which dominate the burning of structured fuel beds.

The structure of the fuel bed will control the heat transfer and oxygen flow to the combustion zone. However, the nature of these interactions may be competing, or complimentary. In either case, the interactions are strongly coupled and so a program of experimental work is required to quantify the influence of fuel bed structure on the processes which control the flame spread. As such the aims of this activity are:

- To test the hypothesis that fuel structure is more significant in determining the flammability of vegetative fuels than fuel chemistry.
- To evaluate the effect of fuel structure on the flammability of pine-needle beds.
- To quantify the heat transfer mechanisms during flame spread in porous fuels.
- To measure the buoyancy induced flow in a porous fuel bed.
- To determine an appropriate relationship between the fuel bed structure and the fuel bed drag.
- To determine an appropriate form of the heat transfer coefficient accounting for the fuel bed structure.

Background

The flammability of wildland fuels has been widely studied yet there remains no complete theory to describe the ignition and burning of wildland fuels. The problem is complicated with many variables and strong sensitivity to the boundary conditions, determining how the fuel elements respond to heating, undergo thermal decomposition (pyrolysis) and react with oxygen from the air to burn. The primary processes of interest are:

- Heat transfer – the rate at which a wildland fuel will heat up upon exposure to an external heat source is determined by the mode of heat transfer (conduction, convection or radiation), the shape of the fuel element, the structure of the fuel layer, the thermophysical properties of the fuel and the moisture content.
- Pyrolysis – understanding the processes by which vegetation thermally decomposes to produce flammable gases (which burn as a flame) and char (which burns through a heterogeneous oxidation process).
- Oxygen mass transfer – the transport of oxygen to the zone containing either flammable pyrolysis gases or hot char will determine the rate of the reaction and therefore the energy release from the fuel.

Of these three processes, the heat transfer and mass transfer are strong functions of the shape of the fuel elements and the fuel bed structure as this will describe: a) the air flow around and through the fuel which governs the convective heating/cooling and oxygen mass transfer, and hence energy release; b) the radiative exchange through the configuration factors; and c) element to element conductive heat transfer.

The chemical composition of the fuel, and hence the pyrolysis reactions are deemed to be of second order importance in determining the flammability and flame spread within wildland fuels. The work presented in the following sections therefore seeks to explore the effect of fuel structure on flammability and flame spread.

The effects of fuel chemistry are not however completely irrelevant to the study of wildland fuels. The composition will determine (along with the burning conditions) the species that are emitted from burning vegetation and hence the hazards associated to smoke, water run-off and post-fire soil stability.

In simple terms, it is often *how* something is burning that is important not *what* is burning.

The combustion processes which dominate low intensity fire spread were explored in the laboratory. This work compliments the work undertaken in the field, specifically the low intensity fires in litter-dominated fuel systems.

The activities carried out at this scale were:

- Evaluation of the thermal decomposition of vegetative fuels
- Assessment of the flammability of vegetation as a function of fuel bed structure
- Assessment of the effect of fuel bed structure on the processes governing opposed flow flame spread on porous fuels
- Development of fuel bed structure-dependent drag
- Development of fuel bed structure-dependent convective heat transfer coefficient

Thermal decomposition of vegetative fuels

Objective

This section therefore seeks to characterize the thermal decomposition (pyrolysis) of different vegetation species. The specific focus is to identify the pyrolysis characteristics relevant to the ignition of fuels which typically comprise litter layers. Consequently, all the specimens tested are dead and conditioned in the laboratory prior to testing. The objective is to identify the significance of pyrolysis chemistry on the ignition of fuels such that this can be assessed in the context of the fuel structure in the following sections.

Background

The flammability of fuel particles derived from plants is frequently linked to their species (Varner et al. 2015). However, the exact characteristics of a species which may lead to increased flammability are often not well articulated. From the perspective of assessing the effect of ‘species’ on flammability there are three main components: 1) chemical composition of the species; 2) moisture content, and 3) structure. It is hypothesised that the latter of these will dominate species flammability.

Materials and Methods

The fuels used in this study are litter (dead litter) from the following species:

- *Pinus rigida*
- *Pinus taeda*
- *Pinus echinata*
- *Pinus halepensis*

- *Pinus pinea*
- *Quercus marilandica*
- *Quercus alba*
- *Quercus stellata*
- *Vaccinium pallidum*

Prior to testing, fuels were stored and conditioned in the laboratory (approximately 15 °C, 40-60 % RH).

Prior to testing the 1-5 g samples were ground into a powder. The results presented here are for unsieved sub-samples on the order of 15 mg.

To explore the thermal decomposition behavior, Thermogravimetric Analysis (TGA) is used. This technique records the mass of a small specimen (~10 mg) upon heating in a temperature-controlled chamber. The composition of gas flowing through the chamber can also be changed to allow pyrolysis and oxidation reactions to be studied separately using nitrogen and air environments, respectively.

Using the mass loss rate the Differential Thermogravimetric data can be presented (DTG) as a function of temperature which allows study of the material thermal decomposition reactions. In this work we are concerned primarily with the onset of pyrolysis reactions as this determines the temperature at which flammable gases are emitted from the samples.

Results and Discussion

A typical TGA and DTG data for *Pinus rigida* tested at a heating rate of 100°C/min are shown in Figure 3. The TGA data show that the thermal decomposition proceeds in a similar manner in both oxidative and inert environments. At temperatures greater than ~500°C the decomposition rate in air decreases and the residual mass is approximately 20% of the initial mass. This residue comprises primarily char and mineral content. In the air case, the char is oxidised and the residual mass at 900°C is less than 5%. The DTG data indicates that the reaction is continuing.

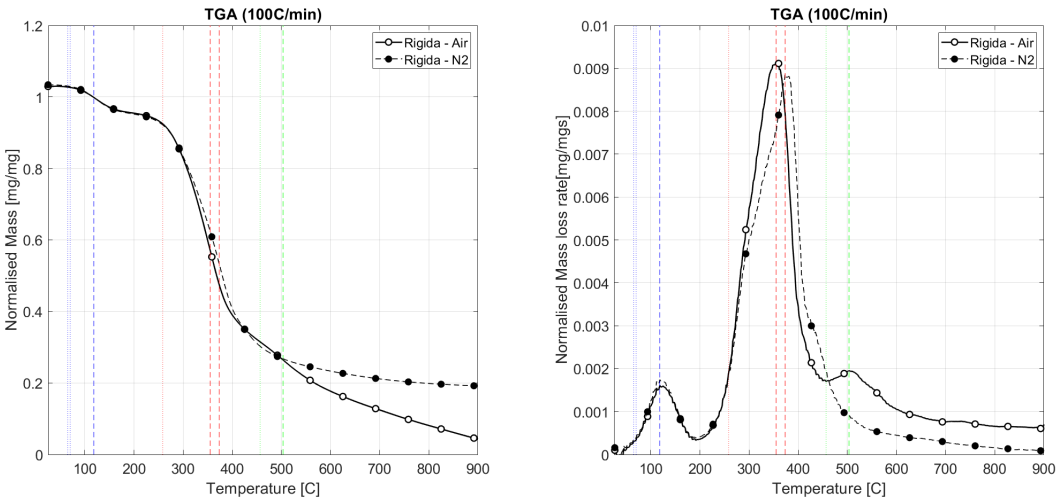


Figure 3. TGA (left) and DTG (right) curves for Pinus rigida in air and nitrogen. Dashed vertical lines indicate the temperatures of the onset and maxima of individual reactions. Heating rate 100°C/min.

In addition to the observation of the oxidative processes, these data also indicate the onset temperatures for the reactions. The reactions are characterised by a drying at 50—200°C, pyrolysis starting at 260°C and reaching a maximum around 350°C. Char oxidation is observed to start around 450°C reaching a maximum at 500°C. The onset temperatures of the reactions define the hazard associated with a fuel as this is when the fuel will produce flammable gases and/or undergo char oxidation thereby contributing to the energy release from the fire.

The following section explores the behaviour of commonly studied wildland fuels used in this project to evaluate the differences between different fuels. First comparison between *Pinus* species is made before comparing these to broad leaved species. The principal focus is on assessing the onset of pyrolysis for these species, as this will define the onset of flaming ignition for these fuels.

Pinus species

The TGA and DTG results from the five *Pinus* species tested in nitrogen are given in Figure 4 (note that the mass is normalised to the dry mass). There is a high degree of similarity between the TGA curves resulting in a final mass of between 20 and 30% of the dry mass. The vertical lines indicate the onset (dotted) and maximum (dashed) of each reaction for each species. The species follow very similar pyrolysis processes (as shown on the DTG) with the onset of the pyrolysis reaction between 210—250°C and the maximum reaction rate for each species is between 350 and 370°C. These temperatures are presented in Figure 5.

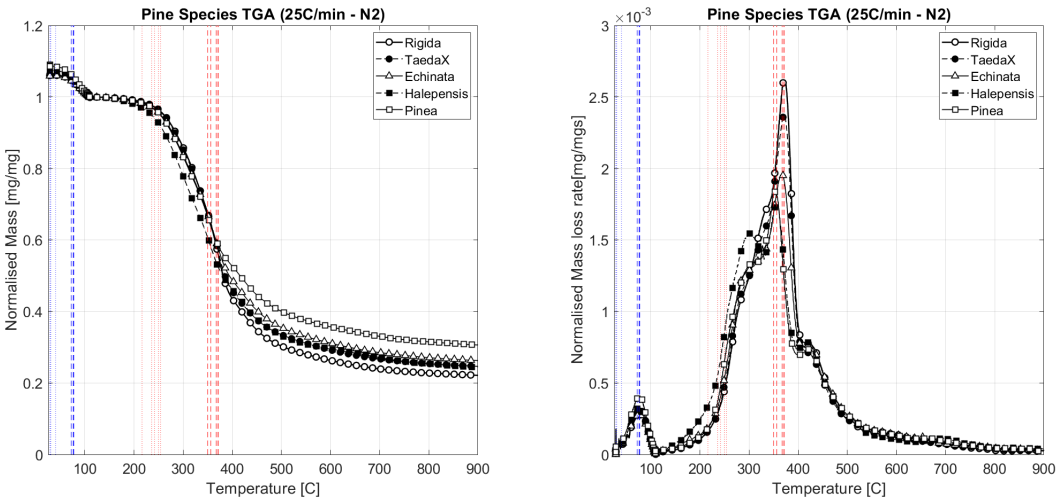


Figure 4. Comparison of TGA (left) and DTG (right) for all Pinus species

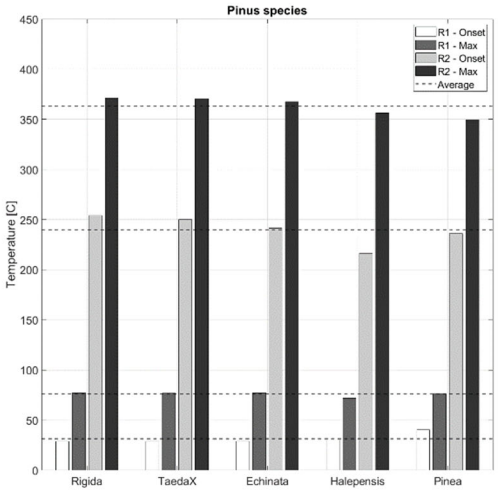


Figure 5. Temperatures for the onset and maximum reaction rate for Pinus species in nitrogen. R1 is drying and R2 is pyrolysis.

Broad leaf species

The TGA and DTG data for the broad leaf species are show in Figure 6. As with the *Pinus* species, there is a high degree of similarity between the TGA curves resulting in a final mass of between 30 and 45% of the dry mass. The vertical lines indicate the onset (dotted) and maximum (dashed) of each reaction for each species. The species follow very similar pyrolysis processes

(as shown on the DTG) with the onset of the pyrolysis reaction between 210—250°C and the maximum reaction rate for each species is between 300 and 360°C. These temperatures are presented in Figure 7.

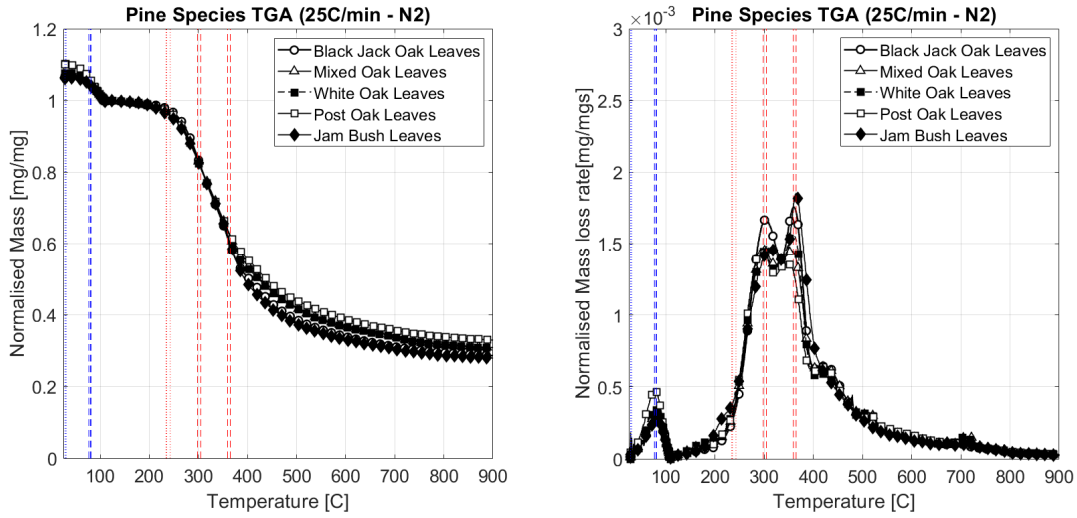


Figure 6. Comparison of TGA (left) and DTG (right) for all broad leaf species

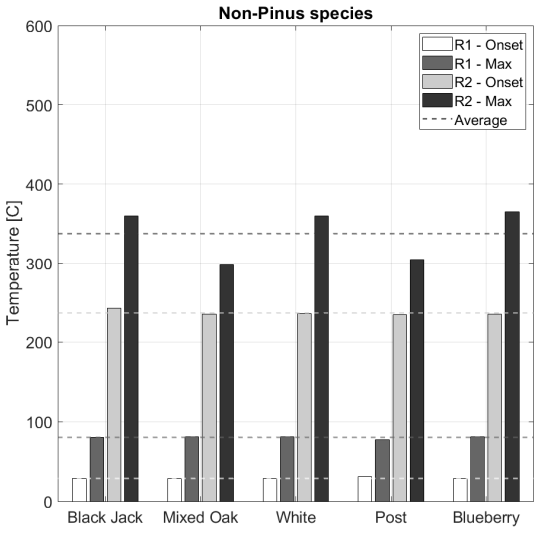


Figure 7. Temperatures for the onset and maximum reaction rate for broad leaf species in nitrogen. R1 is drying and R2 is pyrolysis.

The primary difference between the *Pinus* and broad leaf species is the prominence of a secondary peak in the pyrolysis of the broad leaf species. This suggests that the decomposition is

characterized by (at least) two reactions which, if they occur in the *Pinus* species, are much less distinct. This is likely attributed to the different ratios of the structural polymers which make up the different forms of the leaves (needles vs broad leaf).

Proximate analysis

The temperature data defined above with the mass lost during the pyrolysis, and oxidation reactions can be combined– this is alternatively referred to as proximate analysis. These data are shown in Figure 8. For all species, the proximate analysis shows that 67-77% of the mass is lost during the pyrolysis process as volatiles. The average value is slightly higher for the *Pinus* species than the broadleaf species. The fraction of each species that remains as char is approximately 22% for the *Pinus* species and 36% for the broad leaf species. In both cases, around 4% of the mass is ash.

If it is assumed that the products of pyrolysis have a similar heat of combustion (i.e. are dominated by the conversion of carbon monoxide to carbon dioxide) then this indicates that for all species there is an approximately even split between the potential energy release in the flaming and char oxidation phases of burning.

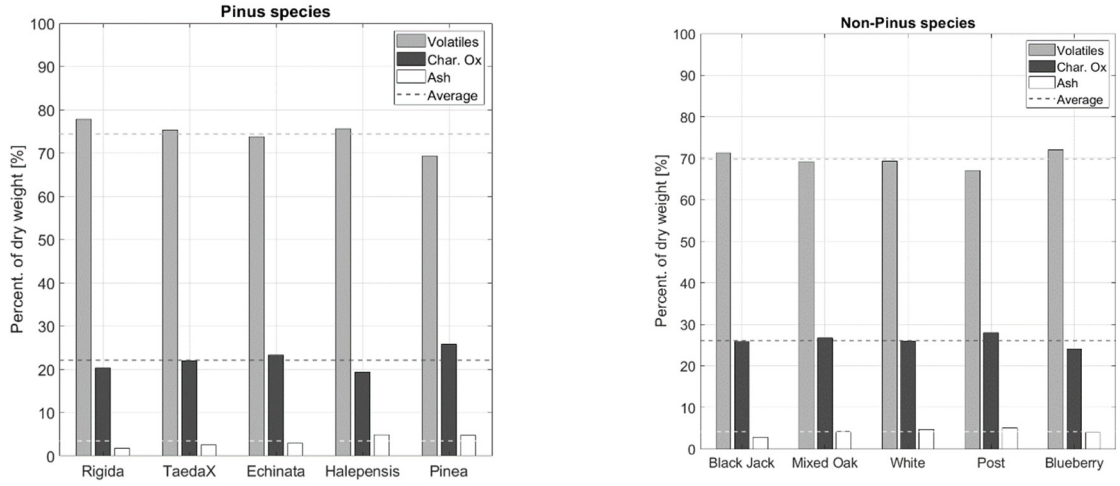


Figure 8. Comparison of the proximate analysis for Pinus species (left) and broad leaves (right)

Conclusions and Implications for Future Research/Implications

The primary conclusion from this study is that in the context of material flammability, the decomposition of dead vegetation typically forming litter layers is broadly similar. The onset temperature for pyrolysis does not vary by a significant degree, with an onset temperature in the region of 320—360 °C. This means that in determining the ignition of wildland fuels, the heating of the fuel to this pyrolysis temperature, and the processes that control that heating will be significant in determining the relative flammability of species.

There are several important caveats to the data presented in this section. Namely, that the results are sensitive to the heating rate and the heating rate presented here is much lower than

typically found in wildfire scenarios (where heating rates in excess of 100°C/min may be found). The effect of increased heating rate is to make the reactions less distinct and to shift the onset temperatures to higher values. This is due to limitations in the assumptions required to interpret the TGA results and is not further discussed here.

Nevertheless, the TGA studies conducted as part of this project indicate that, in terms of fuel flammability, and by extension flame spread, there is relatively little difference in the pyrolysis characteristics for fuels spanning a wide range of species. To allow for more detailed interpretation of thermal decomposition data, it is essential to understand the processes which control the heating (temperature) of the fuel elements. Therefore, in the subsequent sections, we focus on the effects of fuel structure on the burning and flame spread of vegetative fuels and the heat transfer and fluid mechanic representations of these phenomena.

Burning of pine needle and manufactured fuel beds.

Objective

This objective of this section is to evaluate the effect of fuel bed structure on the ignition and burning of porous fuel beds. The fuel bed structure will affect the mass and energy transport processes that control ignition (radiative heating and convective cooling, mass transport of pyrolysis gases) and therefore quantifying these relationships is essential in understanding the burning dynamics. To avoid the effects of changes in chemistry, one species of needle is selected and this is mechanically modified by cutting and grinding to change the fuel bed structure, for which porosity is used as a surrogate.

Background

The flammability of a material is determined by two factors: the time to ignition and the heat release rate. The time to ignition is a measure of the ease of ignition of a specimen while the heat release rate characterizes the burning of the sample. Together these can be used to create an assessment of the flammability of a specimen.

Assessment of material flammability is typically undertaken using standardized apparatus. In this study, we use the FM Global Fire Propagation Apparatus (FPA). The FPA is a bench-scale calorimeter that allows control of the thermal boundary conditions and the environment in which the burning takes place (oxidative or inert).

There are many studies using the FPA (or similar apparatus) to evaluate the flammability of wildland fuels. These have provided valuable insights into the burning of vegetation. One key difference in this work is that the specimens were created specifically to explore the effect of fuel structure while maintaining a constant fuel composition (i.e. chemistry). This allowed the effects of fuel structure on ignition to be explicitly explored.

Ignition is a gas phase phenomenon where a sustained exothermic oxidation reaction occurs in a gaseous fuel/oxidizer system. Ignition occurs when a sufficient rate of gaseous fuel is supplied to, and mixed with, sufficient gaseous oxidizer. This is governed by mass transfer.

However, often the fuel is not initially in the gaseous state and must undergo a phase transformation. The phase transformation is thermal in origin. In liquids this may be solely evaporation whilst in solids pyrolysis often takes place. Evaporation is the change from liquid to gas phase of a material. Pyrolysis is the breaking of a material into smaller parts, leading to the

production of liquid and gaseous fractions. This is governed by heat transfer and the degradation chemistry.

When the fuel in question is porous it affects both the mass and heat transfer. Porous fuels are often permeable, allowing gaseous components to move more freely within and around the fuel. This can be beneficial to ignition as the mixing of fuel and oxidizer can occur more easily. On the other hand, it can be detrimental as the gaseous fuel is diluted by excess oxidizer.

Additionally, the heat transfer process is altered due to the increase in gas movement and decrease in the conductivity. Consequently, the relative importance of convection as a heat transfer mechanism is increased. Similarly, the heat transfer process is influenced by the changes in radiative heat transfer owing to the changes in exposed material. This differs from non-porous fuels, where conduction is the main heat transfer mechanism within the material, and the exposed material is the uniform top surface.

A ubiquitous example of porous fuels are wildland fuels, in which fuel beds are composed of vegetative fuel elements. To understand the ignition process, we characterize the fuel bed and alter its mass transfer, heat transfer and thermal degradation. Hence, we can analyses each of these processes within the ignition response.

The fuel bed can be characterized using global parameters, such as density, but also by local parameters such as the dimensions of the fuel element. Altering the fuel element will change the packing efficiency of the fuel bed. As such, the fuel element will change the mass transfer and heat transfer in the fuel bed. This can be done by choosing a different material or species, however, this not only alters the fuel element dimensions but also the thermal degradation.

Materials and methods

Materials

The materials used in this study were *Pinus rigida* needles. Samples were prepared by cutting needles to a desired length to change the packing efficiency and hence the porosity of the samples. The relationship between the nominal fuel element length and the sample porosity of the prepared samples are shown in Figure 9. The porosity was calculated using the method below [1]

$$\phi = \frac{\rho_{needle} - \rho_{bulk}}{\rho_{needle} - \rho_{air}}$$

Before testing samples were conditioned in an oven at 60°C for 24 hours.

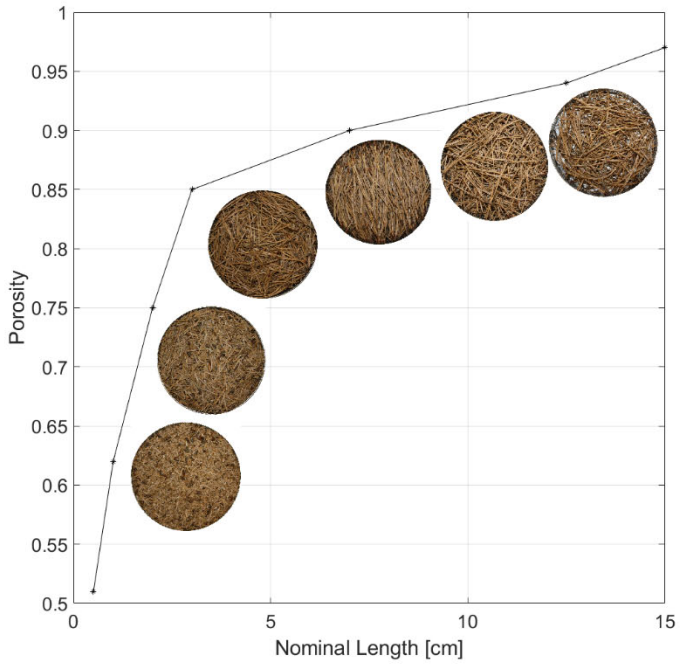


Figure 9. Sample preparation for the flammability experiments and the relationship between nominal length scale and porosity

Methods

The FM Global Fire Propagation Apparatus (FPA) is a small-scale calorimeter used to test the flammability of materials subject to external heating by radiation, and in an environment which allows the flow of oxidizer to be varied.

The sample holder used is cylindrical with a diameter of 126 mm and height of 30 mm and is made of circularly perforated steel with an open area of 63%. For the non-permeable test condition, the sample holder was covered with aluminum foil and thus had an open area of 0%.

Most samples were subjected to a radiant heat flux of 25 kW/m^2 from the FPA. However, to see if the results follow the trend seen in literature, where the effects of structural differences are minimized at high heat flux, a subset of permeable samples (φ = 0.64; 0.86; 0.94) were subjected to 35 and 50 kW/m^2. An ethylene/air pre-mixed flame was used as a pilot and was positioned 20 mm above the sample surface to induce piloted ignition.

Time to ignition was recorded using visual observation during the test and later confirmed through analysis of video footage after the experiment. Sample mass and concentrations of O_2, CO_2 and CO in the exhaust duct were measured at a frequency of 1 Hz. These measurements were processed to obtain the mass loss rate (MLR) and the heat release rate (HRR).

Study samples were prepared using porous and non-porous sample holders. The use of non-porous sample holders allowed the effect of flow through the porous media to be isolated form the effects of the porous layer alone. This also better represents the scenario in which flow to a litter layer is blocked by the soil underneath.

During these experiments, the time to ignition and the mass loss rate of the samples are recorded to characterize the ignition and burning processes.

Results and discussion

Figure 10 shows a series of snapshots from a typical flammability experiment. The sample is exposed to a heat flux and begins to pyrolyze. The rate of pyrolysis increases until the lower flammability limit of the gas-air mixture is reached and then ignition occurs (bottom row, left). The sample then burns with a flame until the rate of pyrolysis drops below that required to sustain burning and char oxidation of the needles occurs (bottom row, right).

The following sections characterize the effects of the boundary conditions and the fuel bed structure on the ignition and burning of pine needle fuel beds.

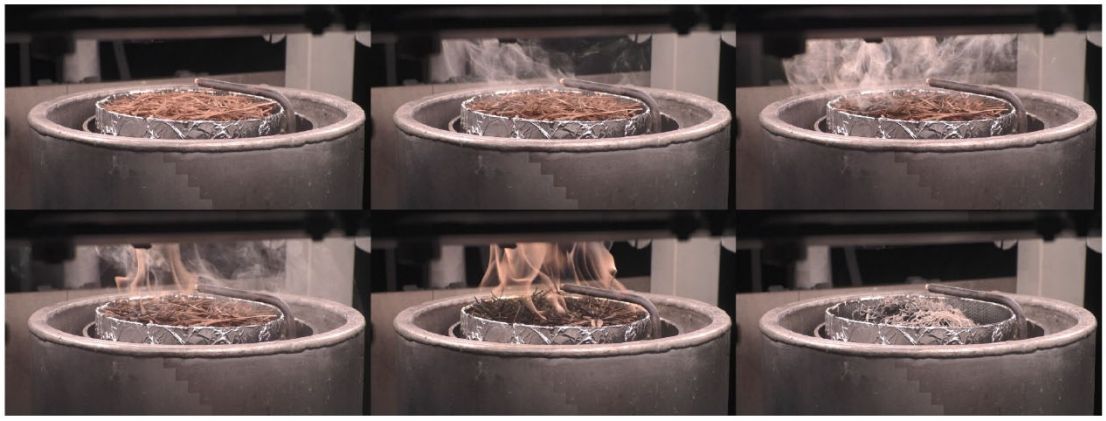


Figure 10. Representative stages of experimentation in the FPA. Left-to-right and top-to-bottom: initial exposure, pyrolysis, further pyrolysis, ignition, burning and flameout.

Time to ignition

The time to ignition, as a function of fuel bed porosity, is presented in Figure 11 for both porous and non-porous sample holders. Time to ignition is longer for samples with porous sample holders. This suggests that convective cooling of the fuel is significant in the heating of the samples. The convective cooling will be larger in the porous sample holders as buoyancy-induced air flow can be established throughout the sample. A second possible cause is that the pyrolysis products are diluted by the larger buoyant flow induced in the sample. This hypothesis is discussed later.

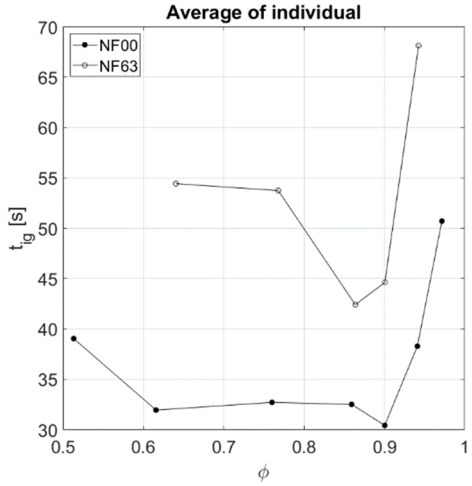


Figure 11. Time-to-ignition against global fuel bed porosity. NF00 and NF63 correspond to non-porous and porous sample holders, respectively.

The time to ignition data are non-monotonic functions of porosity. This suggests that the phenomena controlling the heating of the surface fuel bed elements varies as a function of porosity. At low porosities the time to ignition is high and as the porosity is increased, this stabilizes or reaches a minimum around 0.85—0.90 before rapidly increasing again. At low

porosities, there is more mass present at the 'surface' and increased particle contact. As a result, these samples result in increased rates of heat transfer from the surface to the depths of the sample. However, convective losses are relatively low, resulting in long times to ignition. As the porosity is decreased, there is less mass at the surface but the convective losses remain low. This results in a minimum of the time to ignition. Finally, the porosity becomes so low that a large convective flow can be established and effectively cool the sample resulting in longer times to ignition. Again, this relies on the assumption that the dilution of the pyrolysis gases is negligible.

Burning rate

The burning (mass loss) rate of the fuel allows further insights into the effect of controlling transport mechanisms on the burning of porous fuel beds. The data shown in Figure 12 are the mass loss rate for samples of porosities ranging from 0.51 to 0.97 (see Table 1 for conversion to porosity).

Independent of the sample holder and sample mass, the overall time series behavior was similar for the different porosity cases. The mass loss rate increases rapidly at ignition to a peak value and then decays as the fuel is consumed. The fuel consumption makes it challenging to interpret the period after the peak as the whole depth of the fuel bed is burning and therefore the mass loss rate is dependent on the fuel remaining.

Nevertheless, these data are useful in highlighting the importance of the mass transfer processes in the burning of these materials. Even shortly after ignition (t = 0), the peak mass loss rate is shown to be much higher for the porous baskets than the non-porous baskets. This is particularly pronounced for the low mass (high porosity) cases. This is shown more clearly in Figure 13. Again, this indicates the importance of the mass transport processes on the flammability of the porous fuel beds. In this case, the increased porosity allows an enhancement of the burning rate by providing additional oxygen to support char oxidation at the same time as the thermal decomposition of the fuel to sustain flaming. These higher burning rates are most noticeable at the highest porosity resulting in an approximately 90% increase in the burning rate at the highest porosity case.

Figure 14 additionally shows the effect of varying incident heat fluxes on different porosity fuel.

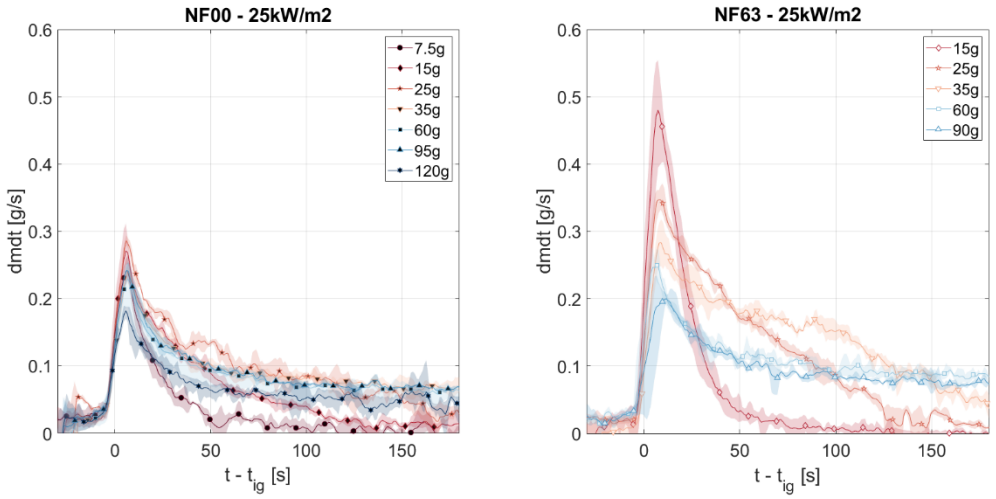


Figure 12. Average mass loss rate of repeat tests in shifted time subject to different boundary conditions. Shaded regions show maximum and minimum values for repeat tests. Left shows closed basket cases and right shows open (63%) basket cases.

Table 1. The conversion between mass and porosity for data in Figure 12

Mass, m [g]	Porosity, [-]
120.0	0.51
95.0	0.62
60.0	0.75
35.0	0.85
25.0	0.90
15.0	0.94
7.5	0.97

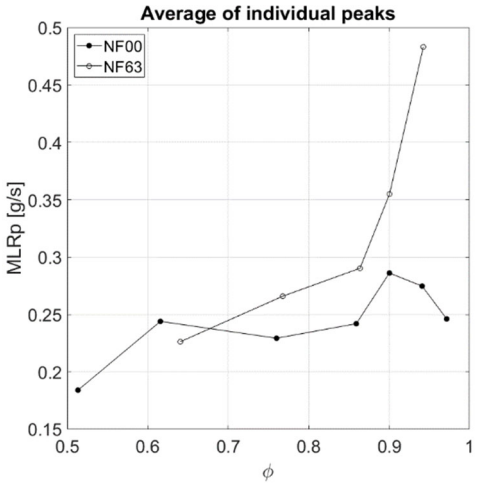


Figure 13. The peak mass loss rate as a function of porosity for porous and non-porous sample holders.

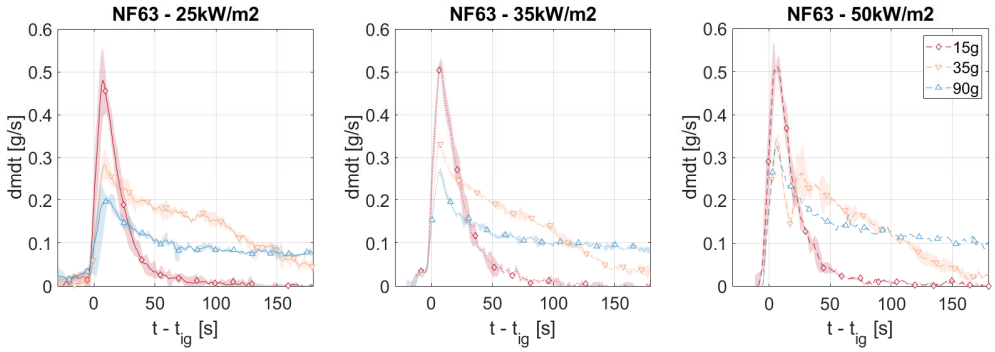


Figure 14. Average mass loss rate of repeat tests in shifted time subject to different incident heat fluxes. Shaded regions show maximum and minimum values for repeat tests. Left is 25kW/m2. Middle is 35kW/m2. Right is 50kW/m2.

Conclusions and implications for future research

This section has quantified the effects of flow through the porous fuel on the flammability of vegetative fuel beds. The results indicate that the flow through fuel beds can act to delay ignition due to the increased convective cooling of the fuel particles. However, the burning rate is shown to increase for porous fuel beds once these have been ignited. This highlights the complex interactions at the heart of the burning of wildland fuels.

Future assessment of wildland fuel flammability should seek to quantify these effects in more detail. Particularly the influence of the effects of dilution on achieving the lower flammability limit of the pyrolysis gas-air mixture.

The implications of this work again point to the fuel bed structure as a controlling property in wildfire dynamics. In the following section this is explored in more detail in the context of fire spread.

Effect of fuel bed structure in porous flame spread: experimental investigation of heat transfer mechanisms

Objective

This objective of this study is to determine the effect of fuel bed structure on the flame spread rate in reduced scale experiments. Quantifying the dominant heat transfer processes and the magnitude of the buoyancy-induced flows during the flame spread process will allow better identification of the relevant structural characteristics of the fuel bed. Fuel beds are prepared by independently modifying the bulk density and fuel loading however, this has been recognized to not provide an adequate description of the fuel bed so the use of a dimensionless parameter $\alpha\sigma\delta$ which captures the fuel bed height, porosity and the surface to volume ratio of the fuel elements is explored.

Background

Experimentally observed effects of fuel bed structure have varied, with several studies observing a positive relationship between fuel loading and spread rate (Dupuy 1995; Morandini et al. 2013). Fang and Steward (1969) however observed the fire spread rate to be independent of fuel loading (for excelsior fuel beds of constant fuel bed voidage). This was assumed to indicate that, for the range of cases studied, the radiative heat flux from the above-bed flame was negligible and that the in-bed burning region was of sufficient thickness to be considered as a black radiator. The fuel loadings studied by Fang and Steward were however relatively high: involving a minimum fuel loading of around 0.7 kg/m^2.

Similarly, the relatively large fuel loading (2.44 kg/m^2) and fuel height (7.6 cm) used during the radiation shielding experiments of Rothermel and Anderson should be considered. Particularly as Thomas had previously suggested that the significance of flame heating may be greater in shallower fuel beds, given the scaling laws involved (Thomas 1967).

Materials and methods

Properties of the fuel beds

The fuel beds for each experiment consisted solely of dead pine needles, with two separate experimental series completed, each using a different needle species. The two needle types used were *Pinus rigida* (Pitch Pine) and *Pinus rigida x taeda* (Pitch - Loblolly Pine hybrid). Both

needle species were collected at the Silas Little Experimental Forest, New Lisbon, New Jersey (Clark et al. 2014).

Needles were air-dried in a storage room and otherwise unconditioned prior to experiments. The fuel moisture content (FMC) was measured for each experiment by drying ~20 g samples of pine needles in an oven for 24 hours at 60 °C (Marcelli et al. 2004). The bomb calorimeter was used to measure the high heat of combustion of each species as given in Table 2. The individual needle geometrical properties, including the surface-to-volume ratio (σ) were measured through random sampling, using the methods outlined by Thomas *et al* (2017a). The average FMC (dry basis) for each needle type is also given, with the FMC higher across the pine-loblolly hybrid series, than those involving the pitch pine needles.

Table 2. Needle for Pinus rigida and Pinus rigida x taeda needles species.

Species	Mean Density, ρ [kg/m^3] (SD)	Mean Needle Diameter [mm] (SD)	Mean Surface to Volume Ratio, σ [m^{-1}] (SD)	Average Fuel Moisture Content [% Dry] (SD)	High Heat of Combustion [kJ/kg] (± Max-Min)
Pinus rigida (Pitch Pine)	706 (71)	1.31 (0.15)	5063 (640)	10.1 (0.8)	19669 ± 422
Pinus rigida x taeda (Pitch-Loblolly Pine)	725 (33)	1.34 (0.12)	4899 (446)	16.0 (0.9)	19672 ± 346

The fuel bed was constructed by randomly dropping (without controlling the orientation or final needle position) the needles on to the Table. To achieve a uniform fuel loading and bed height, the Table was divided into 10 equally sized segments and 10 % of the total fuel load was loaded onto each segment. After the fuel bed was constructed, the average height was randomly measured at ten locations, to ensure the desired average height was achieved.

Across tests, the fuel loading of the fuel bed was varied (0.2 kg/m^2, 0.4 kg/m^2, 0.6 kg/m^2, 0.8 kg/m^2, 1.2 kg/m^2, 1.6 kg/m^2) on a wet basis. The fuel bed bulk density (ρ^*) was altered (10 kg/m^3, 20 kg/m^3, 40 kg/m^3) by varying the fuel bed height (δ) for fuel beds of constant fuel loading. Replicate experiments were conducted for each fuel bed case, given the potential for heterogeneity within the fuel bed structure.

For the highest bulk density tests (40 kg/m^3), compression of the fuel bed was required to achieve the desired fuel bed height. The fuel bed porosity, α was calculated using the packing ratio β,

$$\alpha = 1 - \beta \qquad (3)$$

The porosities of the fuel beds for the different experimental conditions are given in Table 2 and Table 3, along with the average FMC for each case.

The dimensionless structural parameter $\alpha\sigma\delta$ incorporates three terms that describe different aspects of the structure: α is the overall fuel bed porosity, σ is the surface-to-volume ratio of individual fuel element, and δ is the fuel bed height. This parameter is similar to those suggested by previous authors for various porous fuel beds (Rothermel and Anderson 1966; Thomas 1967; Wilson 1990), but these past parameters have not always allowed for independent effects from bulk density and fuel loading. The fuel bed structure ($\alpha\sigma\delta$) was deliberately varied by altering the fuel loading (0.2 kg/m^2 to 1.6 kg/m^2), bulk density (10 kg/m^3, 20 kg/m^3, 40 kg/m^3), and fuel bed height (10 mm to 80 mm). Controlling the fuel bed height allows variation of the fuel loading without altering the bulk density, or similarly the bulk density can be varied by maintaining a constant fuel loading.

Flame spread table

Fuel beds were constructed on a 1.5 m x 0.67 m flame spread table (the Table), with a vermiculite substrate base. Steel sidewalls, covered with alumina-silica fibre, were adjusted to a height of 0.03 m above the fuel bed surface. This limits lateral entrainment into the fuel bed which has been shown to promote formation of a linear flame front (Dupuy and Maréchal 2011). The Table was situated under a furniture calorimeter allowing the energy release rate to be measured using oxygen consumption calorimetry (Janssens 1991), assuming an energy release value per unit of O_2 consumed of 14.15 kJ/gO_2, as determined for forest fuels by Bartoli (2011a).

Flow measurement

The Table was instrumented in three locations (0.5 m, 0.8 m and 1.1 m from the ignition line, in the direction of the fire spread) as shown in Figure 15. Flow in the bed was measured at a height of 10 mm above the base of the Table. Flow measurements were derived from measurements using bi-directional pressure probes (20 mm probe diameter) and a gas phase thermocouple (0.25 mm, K Type) (McCaffrey and Heskestad 1976).

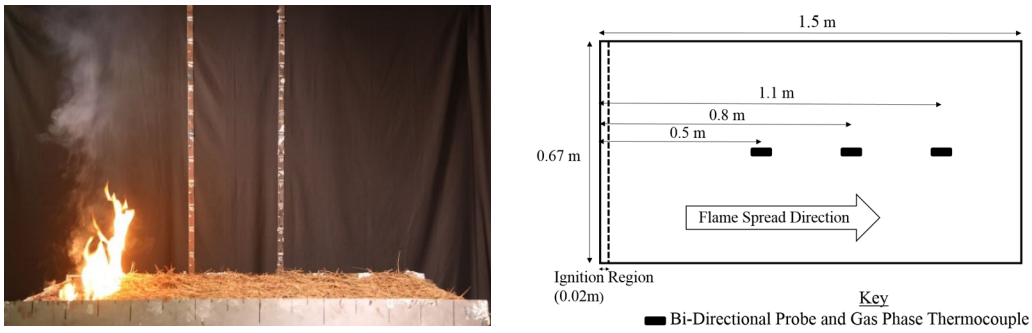


Figure 15. Photograph and schematic of the Table, detailing the position of in-bed bi-directional pressure probes and gas phase thermocouples (all measurements at a height of 0.01 m above the vermiculite substrate surface).

For a subset of experiments, additional pressure probes (and accompanying gas phase thermocouples) were also positioned vertically at a height of 1.2 m above the fuel bed at the first

two measurement locations (0.5 m and 0.8 m from the ignition line) to measure the upward (buoyant) velocity above the fuel bed.

For every experiment, ignition was in the form of a line ignition at one short edge of the table using a 0.67 m long strip of alumina-silica fibre, on which 10 ml of acetone was distributed. This was observed to result in the formation of a linear front immediately after ignition in all but the lowest fuel loadings (0.2 kg/m^2). The average burning duration of this ignition line was 61 seconds (maximum 69 seconds). Both overhead and side-on (perpendicular to flame travel direction) video footage was recorded throughout the experimental duration.

The in-bed temperatures were used to calculate the residence time at each thermocouple location, using a temperature threshold of 300 °C. The same threshold value was used to calculate the arrival time of the flame front at each pressure probe. The flame spread rate was calculated through video analysis of the flame front position over time. An arrival time was determined, based on the leading edge of the front centreline, at 0.1 m distances from the ignition line. Regression analysis was used to determine the spread rate, with the standard deviation in spread rate across all 0.1 m table segments also calculated.

Flame heights were determined through video analysis, with a vertical length scale (0.05 m divisions) aligned with the measurement locations, as shown in Figure 15. The flame height was defined as the distance between the fuel bed surface and the peak of the continuous flame region (Morandini et al. 2006). Additional analysis of the visual imagery allows additional qualitative analysis of the flame front shape and depth, and the smouldering combustion region.

Heat Flux measurements

Heat fluxes (both radiant and total) were measured using water-cooled heat flux gauges calibrated up to 100 kW/m^2. For radiative heat flux measurements, sapphire windows were added to the gauges to prevent convective heat transfer. These windows have a spectral transmission range of 0.2 – 5.5 μm compared to 0.2 – 50 μm for the un-windowed gauges.

Heat flux measurements were recorded at a minimum of 5 Hz (24 out of 27 experiments at 10 Hz), however higher frequency fluctuations in heat flux may occur. The focus of this study is the overall contributions of different heat transfer terms, rather than detailed analysis of any intermittent heating (which in any case is limited by the response time of the gauges). A maximum random error of ± 0.12 kW/m^2 was observed during the background period prior to ignition.

To enable a thorough investigation of the heat transfer from both the flame and the in-bed reaction zone, two different experimental setups were employed. In the first set of experiments, four heat flux gauges were vertically oriented and positioned in two pairs (radiant and total gauge in each pair). One pair was positioned flush to the table surface while the second pair were positioned flush with the fuel bed surface. All four gauges were located near the fuel bed centreline, at a distance of 1.3 m from the ignition line,

In the second set of experiments, only two heat flux gauges (radiant and total) were used. These gauges were horizontally oriented and located within the fuel bed, with the midpoint of the positioned at a height of 12.7 mm above the table surface and 0.9 m from the ignition line. Both

setups are shown in Figure 16, and together allow measurement of both the heat transfer from the above-bed flame and in-bed combustion region, including the effect of fuel bed attenuation.

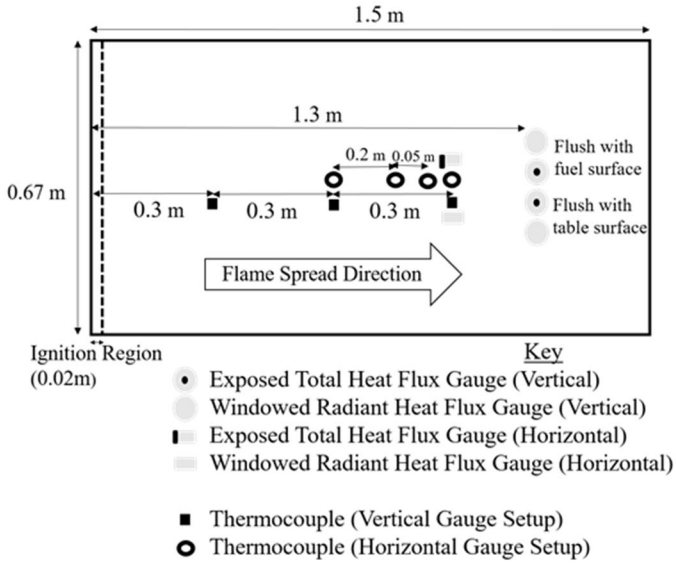


Figure 16. Schematic of table instrumentation.

The view factor between the radiator (either the flame or the combustion region) and the gauge must also be considered. It was assumed that the radiator is well-approximated by a rectangle, and the view factor to was estimated for both a parallel and perpendicular discrete element (representing each of the heat flux gauge orientations) (McGuire 1952). The calculated view factor is shown in Figure 17 as a function of the distance between the radiator and the receiving element. While the peak view factor is lower in the case of perpendicular alignment, the parallel case may be more appropriate at the time of arrival for all gauge configurations, given the presence of the flame or burning fuel bed directly in front of the gauge surface.

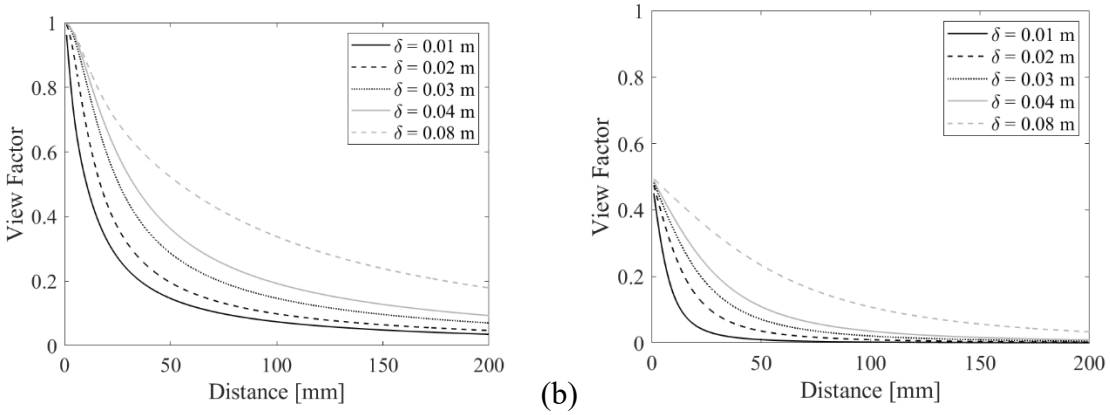


Figure 17. Estimated view factor between radiating surface and a heat flux gauge for (a) parallel (b) perpendicular alignment for fuel beds of various height

Temperature measurements

As indicated in Figure 16, the location of the thermocouples varied between both experimental setups (in-bed and above-bed respectively). In both cases, 0.25 mm diameter thermocouples measured temperatures, at a minimum frequency of 5 Hz (21 out of 27 experiments at 10 Hz). The random error was also estimated over a 30 s period prior to ignition and, while the use of small diameter thermocouples reduces the radiation exchange, the remaining radiation error must be considered.

Silvani and Morandini (2009) estimated the maximum error for a 0.25 mm thermocouple, both when located ahead of the fire front and when positioned within the flame front, estimating a maximum error of < 10 % in both cases. This radiative error has been incorporated into the error treatment within this study.

Results and discussion

Effects of fuel bed structure on buoyancy driven airflow flow

Significant variations in fire behavior were observable as the fuel loading and bulk density of the fuel bed were varied. Figure 18 shows the fire front characteristics and times of flame front arrival at each measurement location for pitch pine fuel beds. It can be observed that the spread rate and flame height increased with increasing fuel load and for decreasing bulk density. At fuel loadings of 0.4 kg/m^2 or higher, the flame front was observed to be continuous across the width of the fuel bed. At the lowest fuel loading (0.2 kg/m^2) the flame front became discontinuous with flame spread between individual needles and clusters appearing to dominate.

0.2 kg/m^2, 20 kg/m^3



t = 191 s (Probe 1)



t = 342 s (Probe 2)



t = 494 s (Probe 3)

0.8 kg/m^2, 20 kg/m^3



t = 136 s (Probe 1)



t = 248 s (Probe 2)



t = 363 s (Probe 3)

1.6 kg/m^2, 20 kg/m^3



t = 92 s (Probe 1)



t = 159 s (Probe 2)



t = 241 s (Probe 3)

Figure 18. Composite of frames from downward-looking video footage of flame spread experiments displaying variation in flame and front shape between Pitch Pine fuel beds of (Top) 0.2 kg/m^2, 20 kg/m^3 (Middle) 0.8 kg/m^2. 20 kg/m^3 (Bottom) 1.6 kg/m^2, 20 kg/m^3.

Key fire behavior measurements for all experiments are summarized in Table 3 for the pitch pine fuel beds and in Table 4 for those involving pitch-loblolly pine hybrid needles. For these measurements, the mean values across repetitions are reported for each fuel bed case. The mean spread rate was calculated based on continuous 0.1 m segments in all experiments, while the mean of the HRR was calculated based on the steady state period across all experiments at a given fuel bed condition. The mean residence time for all in-bed thermocouples was calculated, with the average for each fuel bed condition reported.

For both species, the flame spread rate, peak HRR and flame height increased with independent increases in fuel loading or decreases in bulk density, in agreement with the previously discussed trends in the existing literature (Dupuy 1995; Morandini et al. 2013; Rothermel 1972).

The importance of the small scale (inter-needle) variations in structure was also observed in the pitch-loblolly pine hybrid experimental series. For this needle species, fuel beds of 0.2 kg/m^2 and 16.6 % moisture content were unable to sustain flame spread across the entire Table, however the distance from the ignition line at which extinction occurred varied between repeat experiments.

While a positive linear trend was observed between fuel loading and residence time for the hybrid needles (R^2 = 0.99 for 20 kg/m^3 fuel beds), in the case of the pitch pine needles, following an initial linear correlation, a peak residence time was observed at 1.2 kg/m^2 (for 20 kg/m^3 cases) and 0.6 kg/m^2 (for 10 kg/m^3 cases). Significant variations in residence times were however observed at specific fuel bed conditions, which may be due to the complex interaction of both the smoldering and flaming phases given the in-bed location of the temperature measurement. Within the fuel bed, neighboring regions of smoldering and flaming combustion are often observed simultaneously along with transition between these phases. Based on qualitative visual analysis, at the lowest fuel loading (0.2 kg/m^2) there was a notable absence of the smoldering region behind the flame front, shown in the higher fuel loading cases in Figure 18.

Table 3. Summary of fuel bed parameters and measured fire behavior for experiments involving pitch pine needle fuel beds.

Fuel Loading (kg/m^2)	Bulk Density, $\boldsymbol{\rho}^*$ (kg/m^3)	Fuel Bed Height, $\boldsymbol{\delta}$ (m)	Porosity, $\boldsymbol{\alpha}$	Fuel Moisture Content (% ± Std. Dev.)	Flame Spread Rate (mm/min ± Std. Dev.)	Steady State HRR (kW ± Std. Dev)	Residence Time (s ± Std. Dev.)	Flame Height (m ± 0.025 m)
0.2	10	0.02	0.986	10.1 ± 1.1	108 ± 31	12.2 ± 3.1	17 ± 9	0.10
0.2	20	0.01	0.972	10.0 ± 1.2	114 ± 24	1.1 ± 1.1	18 ± 10	0.05
0.4	10	0.04	0.986	9.6 ± 0.8	144 ± 20	15.4 ± 1.6	20 ± 11	0.23
0.4	20	0.02	0.972	9.6 ± 0.6	126 ± 17	10.5 ± 1.5	29 ± 9	0.16
0.6	10	0.06	0.986	10.9 ± 2.1	180 ± 28	24.1 ± 3.6	30 ± 10	0.43
0.6	20	0.03	0.972	9.8 ± 0.7	132 ± 19	18.6 ± 1.8	33 ± 14	0.29
0.8	10	0.08	0.986	10.1 ± 0.5	210 ± 26	39.4 ± 2.0	27 ± 15	0.57
0.8	20	0.04	0.972	10.2 ± 0.7	162 ± 16	28.9 ± 3.6	46 ± 14	0.42
0.8	40	0.02	0.943	10.1 ± 0.9	126 ± 37	N/A	38 ± 24	0.33
1.2	20	0.06	0.972	11.3 ± 0.3	174 ± 33	N/A	64 ± 52	0.65
1.6	20	0.08	0.972	12.3 ± 1.7	246 ± 39	N/A	49 ± 23	0.93

Table 4. Summary of fuel bed parameters and measured fire behaviour for experiments involving pitch-loblolly pine hybrid fuel beds.

Fuel Loading (kg/m2)	Bulk Density, $\boldsymbol{\rho}^*$ (kg/m3)	Fuel Bed Height, $\boldsymbol{\delta}$ (m)	Porosity, $\boldsymbol{\alpha}$	Fuel Moisture Content (% ± Std. Dev.)	Flame Spread Rate (mm/min ± Std. Dev.)	Steady State HRR (kW ± Std. Dev.)	Residence Time (s ± Std. Dev.)	Flame Height (m ± 0.025 m)
0.2	10	0.02	0.986	16.6 ± 1.9	Unsustained	N/A	N/A	N/A
0.2	20	0.01	0.972	16.6 ± 1.9	Unsustained	N/A	N/A	N/A
0.4	10	0.04	0.986	15.3 ± 1.2	114 ± 25	9.3 ± 2.0	28 ± 18	0.21
0.4	20	0.02	0.972	15.5 ± 0.3	90 ± 21	6.6 ± 2.1	15 ± 14	0.10
0.6	10	0.06	0.986	15.6 ± 0.3	156 ± 39	18.1 ± 2.9	37 ± 17	0.35
0.6	20	0.03	0.972	17.1 ± 0.7	114 ± 18	13.1 ± 2.5	23 ± 13	0.28
0.8	10	0.08	0.986	15.9 ± 0.6	162 ± 28	28.9 ± 3.0	45 ± 7	0.48
0.8	20	0.04	0.972	15.7 ± 2.4	126 ± 21	17.5 ± 1.6	45 ± 31	0.4
0.8	40	0.02	0.945	16.0 ± 0.8	96 ± 11	11.9 ± 1.4	29 ± 14	0.28

Spread Rate

The position of the flame front from the ignition line (x = 0), versus the time from ignition was determined from video analysis. This flame front position over time is plotted in Figure 19 for pitch pine fuel beds of different fuel loading and bulk density.

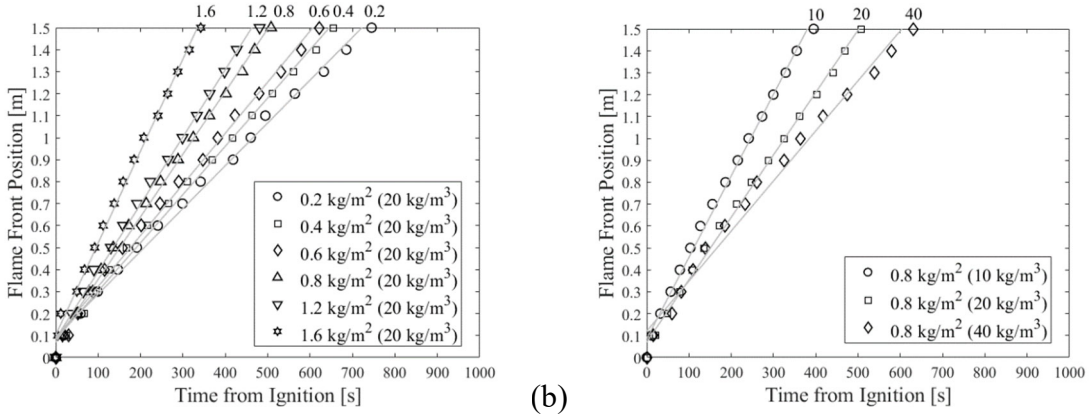


Figure 19. Flame front position versus time from ignition for pitch pine beds of (a) 20 kg/m^3 bulk density, and (b) 0.8 kg/m^2 fuel loading (avg. of all experiments at each condition).

There is an apparent reduction in flame spread rate after the initial post-ignition time period (during the first 0.3 m from the ignition line) which is likely due to the influence of the ignition source. The length of this ignition affected region is similar to the maximum burning duration of the ignition source (69 s) multiplied by the maximum flame spread rate (246 mm/min) which

results in a maximum flame propagation distance of 0.28 m while the ignition source is present, which is well before the first measurement location is reached.

This initial 0.3 m region was therefore not considered when deriving the flame spread velocity for each fuel bed condition using a least squares regression, with the calculated correlation coefficient (R^2) providing an indication of the degree of linearity of the observed flame spread. The correlation coefficient was greater than 0.99 in all cases, which, in line with previous studies (Rossa and Fernandes 2018) was assumed to indicate flame spread of a quasi-steady nature.

In reality, the instantaneous flame spread rate may vary across the table due to heterogeneity in both the combustion region and the fuel bed properties. This variability is demonstrated in Figure 20, where the flame spread rate is plotted as a function of distance from the ignition line, for each 0.1 m segment of the flame spread table (starting with the spread rate between 0.3 m and 0.4 m from the ignition line).

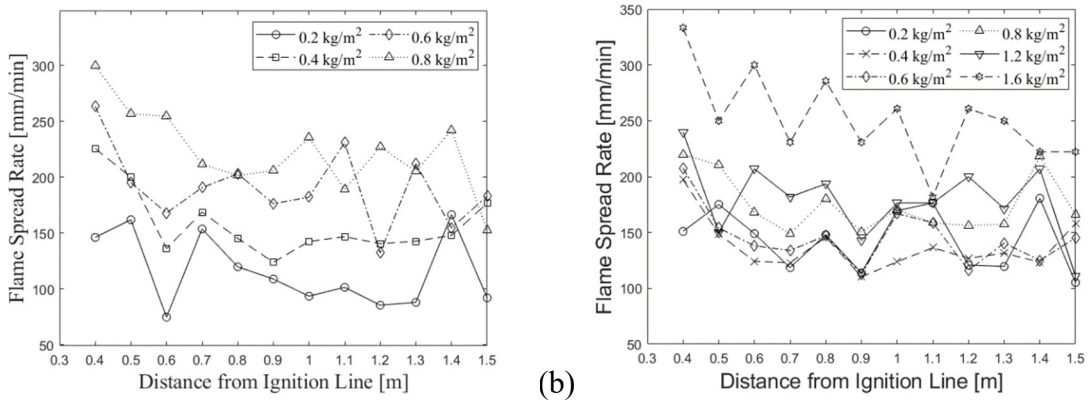


Figure 20. Flame Spread Rate as a function of distance (based on video analysis) for pitch pine fuel beds of different fuel loadings at (a) 10 kg/m^3 bulk density, and (b) 20 kg/m^3 bulk density.

In Table 3 and

Table 4, a trend of increasing flame spread rate with increasing fuel load or decreasing bulk density respectively is observed. Neither the fuel loading nor the bulk density alone adequately describe the variation in flame spread rate, with both parameters having an influence, as shown by the variation in spread rate for fuel beds at consistent fuel loading but differing bulk density in Fig. 19. For 0.8 kg/m^2 pitch pine fuel beds, the spread rate increased from 126 ± 37 mm/min for 40 kg/m^3 fuel beds to 210 ± 26 mm/min for 10 kg/m^3 fuel beds. The variation in spread rate with independent changes in either bulk density or fuel loading is also demonstrated in Fig. 21.

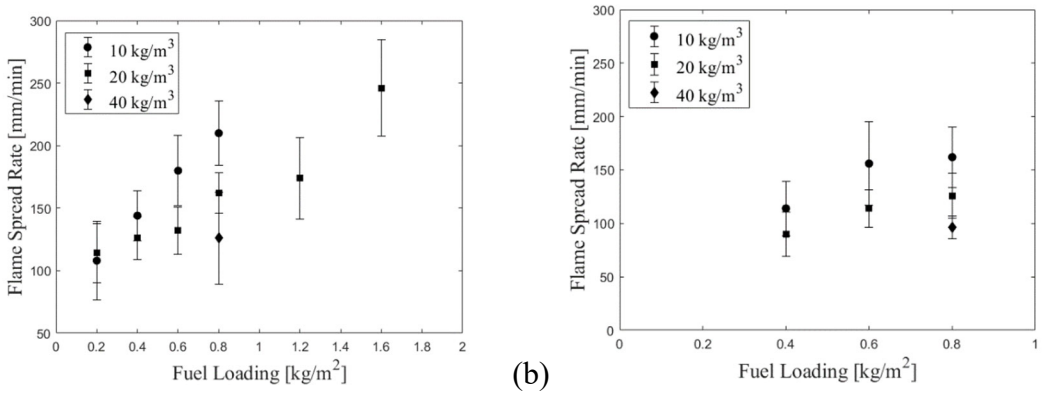


Figure 21. Comparison of flame spread rate with fuel loading and bulk density for, (a) pitch pine (b) pitch-loblolly pine hybrid needle fuel beds.

Examining instead the effect of fuel bed height (Rossa 2017; Rossa and Fernandes 2018), demonstrates a greater correlation with spread rate with a smaller observable impact of changes in either fuel loading or bulk density. This suggests that other aspects of the fuel bed structure, not adequately described by fuel loading and bulk density parameters, are significantly influencing the flame spread rate.

Comparison of the spread rate with the dimensionless fuel bed parameter $\sigma\lambda$ (proposed by Rothermel and Anderson (1966)) displays a strong correlation only once normalised with respect to fuel loading. The fuel loading therefore has a multiplier effect on the original parameter $\sigma\lambda$, similar to the way in which wind loading was originally included (Rothermel and Anderson 1966). Normalisation in this manner however loses the dimensionless property inherent in this original descriptor.

Given that the Rothermel and Anderson term for porosity λ, is defined as the ratio of void volume to surface area of fuel in the bed, the parameter $\sigma\lambda$ can also be considered in terms of packing ratio as $\frac{1-\beta}{\beta}$, therefore multiplication by the packing ratio (β), surface-to-volume ratio of fuel elements (σ), and the fuel bed height (δ) results in an alternative dimensionless parameter $\alpha\sigma\delta$, where α is the fuel bed porosity. The correlation of $\alpha\sigma\delta$ with flame spread rate is shown in Figure 22, and this parameter can be considered in terms of a porosity factor.

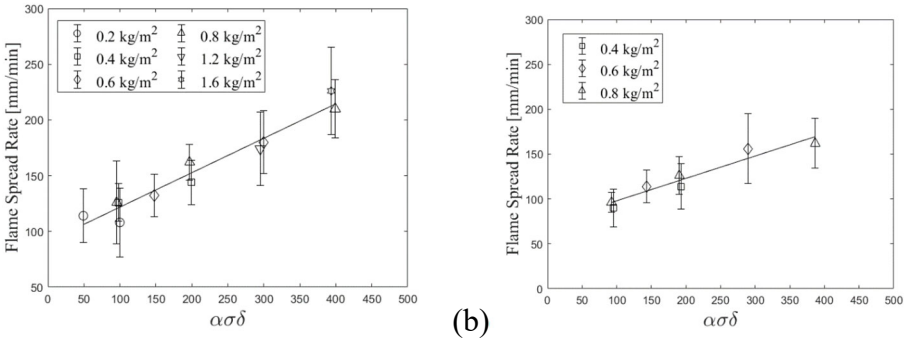


Figure 22. Correlation between ασδ and flame spread rate in (a) pitch pine (b) pitch-loblolly pine fuel beds.

The $\alpha\sigma\delta$ term is similar to the bed descriptor $\beta\sigma\delta$ introduced by Wilson (1990), and later Anderson (1990), based on the optical depth term $\sigma\beta$. Using that parameter, a constant value can be obtained for fuel beds of identical fuel loading but different bulk density, where the height is altered (due to cancellation of the β and δ terms). In this study however variation in spread rate and fire behavior were observed for fuel beds of equal fuel loading but differing bulk density.

Additionally, the porous fuel beds described in this study are quite different structurally to excelsior and wooden cribs. The fuel beds used by Anderson, for example were significantly less porous than those here, however this is due to differing element properties (σ,ρ) in addition to changes to the pore structure, the combined effect of which must be further explored to understand the relative merit of different structural parameters in a given scenario.

Used in this study, the proposed $\alpha\sigma\delta$ allows independent influences from both bulk density and fuel loading changes to be incorporated. As with past studies however, this parameter has been investigated only at the range of structural conditions described in this study. Further investigation of the effect of variation in σ using different fuel types should be explored.

To understand these changes in flame spread, the role of the fuel bed properties within the feedback loop between the increasing HRR, flame height (and the associated changes to the buoyant flow regime) and the resulting entrainment profile into the combustion region must be investigated.

Flows

At quiescent conditions (and in the absence of a slope), the buoyant plume above the combustion zone is expected to result in entrainment towards the combustion region. The entrainment flow profile will rely not only on the magnitude of the buoyant flow but also on the internal porous fuel bed structure, which may alter the drag and flow regimes. The effect of this structure on entrainment into the combustion region will modify the heat transfer and oxygen supply in both the flaming and smouldering phases.

Buoyant Flow

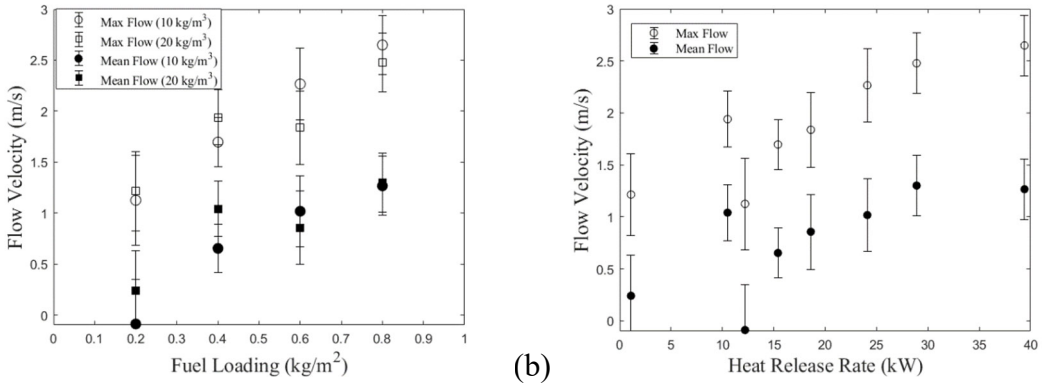
The buoyant flow profile above the flame fronts of different fuel beds was compared across a 10 s window following the arrival of the flame front underneath the above-bed pressure probe. This interval was chosen to allow proper characterisation of the average plume features, while

avoiding periods in which the flame front was no longer present (based on the minimum measured residence time of 17 s).

The pressure probes were at a height of 1.2 m above the table surface. While this height is constant with respect to the table surface, the height relative to the flame tip varies. Although the measurement is always upstream of the flame tip (in the buoyant plume region) with the focus on comparison of the overall buoyant system. The velocity is reported relative to the average pre-experiment velocity (measured in the 1 minute period prior to ignition) which characterises the background velocity profile.

During the post-flame arrival period, an increased maximum buoyant flow above the fuel bed was observed with increasing fuel load as shown in Figure 23, with the peak buoyant flow increasing from 1.3 m/s to 2.6 m/s, as the fuel loading was increased from 0.2 kg/m^2 to 0.8 kg/m^2.

Fig. 23 also shows that a slight variation in maximum buoyant flow velocity as the bulk density decreases from 20 kg/m^3 to 10 kg/m^3 at a fuel loading of 0.6 kg/m^2. The opposite effect however is observed for fuel beds of fuel loading of 0.4 kg/m^2 or lower.



(a) (b)

Figure 23. Comparison of (a) Fuel Loading, (b) Heat Release Rate with mean and max. buoyant flow velocity at a height of 1.2 m above pitch pine fuel bed, in the 10 s after flame arrival.

The increasing maximum buoyant flow velocity with increasing fuel loading matches the observed trend in past Particle Image Velocimetry (PIV) based studies of the buoyant flow profile above excelsior fuel beds (no wind, no slope conditions (Silvani et al. 2018)). As expected, there is also largely a positive trend between HRR and both the mean and maximum vertical flow magnitudes as shown in Fig. 23b. The lowest HRR values in Fig. 23b correspond to the 0.2 kg/m^2 fuel beds and for these cases increased variation may be expected given the discontinuous, non-linear nature of the flame front.

Buoyancy Induced Flows

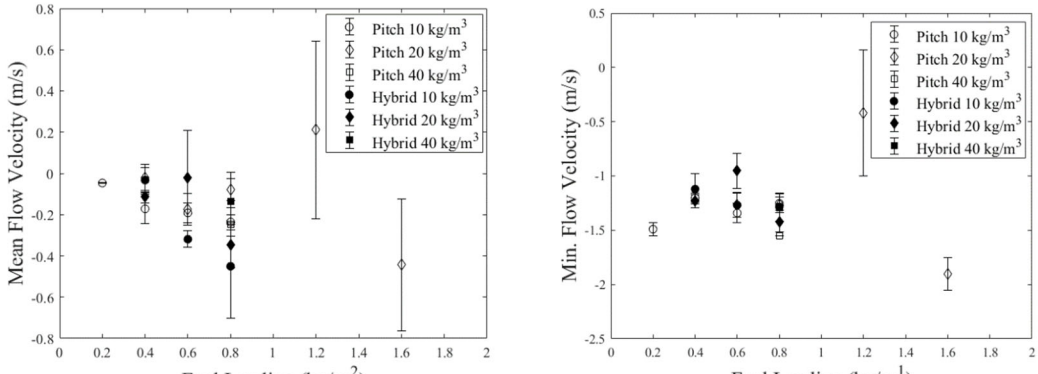
The buoyant upward flow results in lateral entrainment of air, and as such, an opposed flow flame spread regime. This pattern of entrainment, firstly towards the approaching flame front and then reversing towards the departing flame front is observed in this study, in a similar manner to studies of above bed, lateral flow (Anderson et al. 2010).

The magnitude of the entrainment towards the approaching flame front, through the intact, unburned fuel structure, was compared across fuel bed types. This was calculated by investigating the flow profile over a distance of 50 mm to 10 mm between the probe and the approaching flame front, prior to flame arrival.

This period was chosen through observation of the flow profile across all tests, where the onset of the measurable entrainment occurred at a distance of around 50 mm ahead of the flame. The use of a 10 mm cut-off reduces the influence of any local flame impingement, structural changes in the fuel bed, or flow reversal ahead of the recorded flame arrival time. During this period negative flow indicates flow towards the approaching flame front, and therefore characterises the fire-induced entrainment.

Both the minimum and mean flow velocities were calculated, and as shown in

Figure 24 an overall trend of increasing mean entrainment velocity is observed with increasing fuel loading (and hence HRR), however the 1.2 kg/m^2 pitch pine fuel bed is an exception to this observed trend. At the highest fuel loadings (1.2 kg/m^2 and 1.6 kg/m^2) greater variation in both mean and peak entrainment velocity values were recorded, as demonstrated by the larger (max-min) error bars in Fig. 24. Additionally, at these highest fuel loadings, the peak velocity (in the opposite direction to the flame travel direction) was in some cases observed after flame arrival (and was therefore outside of the window considered in Fig. 23). Further investigation is required to separate the influence of the increased spread rate from the possible physical effects based of the flame dynamics and fuel bed structure. Bulk density also appears to affect the entrainment flow, with variation in mean entrainment flow observed for fuel beds of equal fuel loading. The increase in bulk density is, as shown earlier, accompanied by a decrease in HRR.



(a) (b)

Figure 24. Mean and minimum in-bed flow velocity towards the approaching flame front (50 mm to 10 mm prior to flame arrival), in beds of different fuel loading and bulk density for beds of pitch pine and pitch-loblolly pine hybrid, respectively.

Interestingly, these observed trends are less clear for the minimum flow velocities, which may reflect the highly transient nature of the flow. As well as the effect of both local fuel structure variations and fine scale variations in the local buoyant flow profile as a result of variations in bed structure (pore size, connectivity and permeability varies).

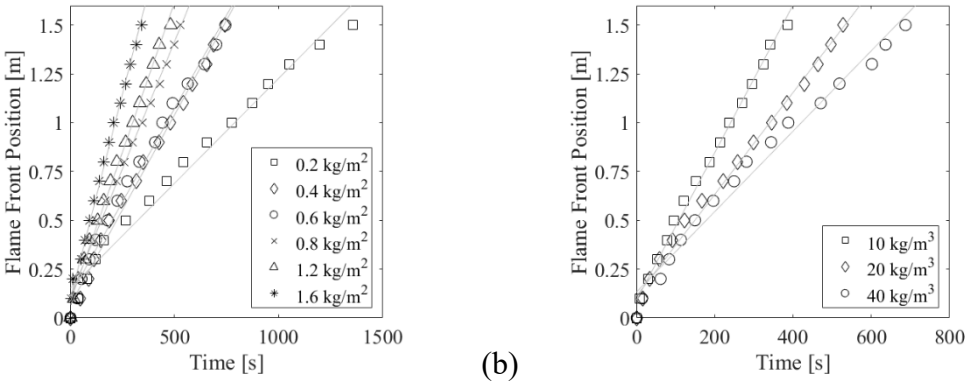
If the air being entrained towards the approaching flame front is assumed to be ambient air, then any increase in entrainment velocity could affect both convective heat transfer and species transport. Particularly for thin fuel elements, this would alter the convective heat transfer coefficient and the resulting cooling during the pre-heating period. Similarly, the effect on oxygen supply and mixing within the combustion region requires further investigation, particularly given the observed variation in buoyant flow profiles because of changes in the fuel bed structure.

Heat transfer mechanisms driving flame spread in porous fuel beds: General flame spread characteristics

Table 5 and Figure 25 summaries the results from this study. The rate of flame spread was found to have a positive correlation with fuel loading and a negative correlation with bulk density. These trends are in agreement with those identified in several past studies where positive trend with fuel loading (Dupuy 1995; Morandini et al. 2013) and porosity (Fang and Steward 1969; Rothermel and Anderson 1966) (Curry and Fons 1940), and a negative trend with bulk density (Fang and Steward 1969) were observed independently. Although Fang and Steward observed no independent effect from fuel loading on spread rates through excelsior fuel beds (Fang and Steward 1969).

Table 5. Summary of fire behaviour results for each fuel bed condition.

Fuel Loading [kg/m^2]	Bulk Density [kg/m^3]	α	δ [mm]	$\alpha\sigma\delta$	N	Flame Spread Rate [mm/min ± Max/Min]	Flame Height [m ± 0.05 m]	Peak HRR [kW ± Max/Min]
0.2	20	0.996	10.0	49.2	2	82 ± 17	0.05	4.5 ± 2.4
0.4	10	0.998	40.0	200	2	168 ± 16	0.23	24.5 ± 5.0
0.4	20	0.996	20.0	98.4	4	114 ± 24	0.13	15.6 ± 1.7
0.6	20	0.996	30.0	148	2	139 ± 20	0.29	19.5 ± 5.0
0.8	10	0.998	80.0	399	4	195 ± 37	0.55	38.3 ± 1.0
0.8	20	0.996	40.0	197	5	149 ± 30	0.36	31.7 ± 1.8
0.8	40	0.992	20.0	95.5	4	122 ± 47	0.34	20.7 ± 1.0
1.2	20	0.996	60.0	295	1	200 ± 20	0.65	69.2 ± 6.9
1.6	20	0.996	80.0	394	3	232 ± 41	0.81	120.3 ± 12.3



(a) (b)

Figure 25. (a) Flame Front Position over time for 20 kg/m^3 fuel beds of different fuel loading (b) Flame Front Position over time for 0.8 kg/m^2 fuel beds of different bulk density.

The normalized mass loss exhibited extended periods of constant mass loss rate, characteristic of steady state flame spread (Viegas et al. 2018), as shown in Figure 26. Using a least squares regression, a characteristic burning rate was obtained for this linear region. The mass loss observed in Figure 26 was positively correlated with the $\alpha\sigma\delta$ value of the fuel bed, and linear in nature.

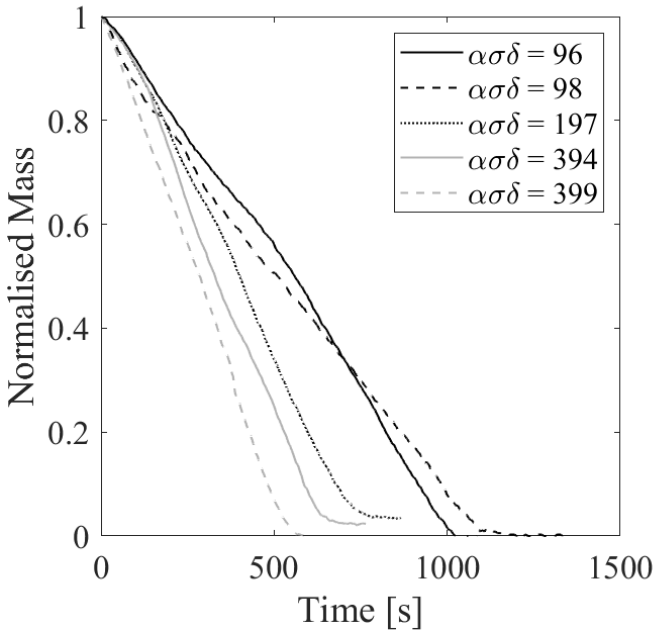


Figure 26. Typical normalized mass loss for fuel beds of different ασδ values.

The lowest $\alpha\sigma\delta$ case ($\alpha\sigma\delta = 49.2$) did not exhibit quasi-steady flame spread behavior. Instead the flame front was highly discontinuous with large local variations in spread rates. It is likely that in this case the flame spread is largely controlled by the interaction between individual needles due to the larger spacing between particles. In all other cases, the continuous flame front width was equal to the fuel bed width (0.67 m) and therefore the flame shape was a function of flame height only.

Visual observations highlighted the lack of a smoldering region behind the flame front at the lowest $\alpha\sigma\delta$ condition ($\alpha\sigma\delta = 49.2$). This region is present in all other cases, suggesting the existence of a limiting condition for the emergence of a smouldering region behind the flame front. Past studies of smouldering in different fuel types have highlighted the existence of a critical dimension for sustained smoldering propagation (Palmer 1957). This condition is excluded from further analysis.

Defining fuel bed structure

To explore the relationship between the fuel bed characteristics and the flame spread, it is necessary to move beyond global descriptors of fire behavior and bulk structural descriptors (fuel loading and bulk density). The direct link between these global structural terms and the physical processes which control the flame spread are often unclear. To explore these in more detail, it is necessary to look at the processes leading to the heating of the fuel bed using a single dimensionless parameter $\alpha\sigma\delta$, to describe the fuel bed structure.

The surface-to-volume ratio (β) and porosity (since $\alpha = 1 - \beta$) is a key parameter in defining the characteristics of the fuel bed as this will determine the in-bed radiation attenuation and the magnitude of convective cooling/heating of the fuel elements. The convective cooling is dominated by the velocity of the air entrained through the fuel layer and hence the drag force exerted by the fuel matrix. This drag force is reduced as the porosity of the fuel bed increases, and inclusion of the fuel bed depth ensures that comparisons of porosity are independent of fuel loading (since the fuel bed area is fixed). Finally, as the porosity is varied the combustion dynamics may be altered (due to a variation of the supply rate of oxidizer to the combustion region) affecting both the flaming and smoldering combustion dynamics.

The variation in fire behavior, and resulting combustion feedback effects, are clearly observed in this study given the correlation between spread rate and the $\alpha\sigma\delta$ value. Although the overall fuel loading still strongly influences the energy release rate and the resulting flame height. This observation may explain the differences in behavior observed for fuel beds with similar $\alpha\sigma\delta$ but very different fuel loadings. For example, the two highest $\alpha\sigma\delta$ cases ($\alpha\sigma\delta = 394$ and $\alpha\sigma\delta = 399$), where both the bulk density and the fuel loading vary by a factor of two, but the greater rate of spread is observed for the lower fuel loading case. This may increase the available fuel loading which can be consumed in the flaming combustion phase, perhaps explaining the increase in HRR by a factor of 2.4 in the greater fuel loading case. The overall mass consumption is high in all cases, yet it remains unclear what proportion of the additional available fuel is actually consumed in the flaming phase as opposed to being consumed in the trailing smoldering region.

The combustion mode in which fuel consumption occurs may have important implications if there is a significant difference in the efficiency of heat transfer to the unburnt fuel from the combustion region compared to the above-bed flame. This dependence may have important implications for the development, and limits of applicability, of a flame spread model and in particular accounting for the identification of dominant heat transfer modes. This is particularly relevant given that past authors have suggested the existence of varying heat transfer regimes across different fuel loadings in porous fuels (Fang and Steward 1969; Thomas 1967).

General Heat Transfer Characteristics

The heat flux measured at each of gauges, varied between fuel beds of different fuel structure, both in terms of onset distance and magnitude. In all cases, the typical heating profile consisted of an initial steady growth period as the flame front approached the gauge, with a subsequent sharp rate of increase followed by characteristic peak-decay behavior as shown in Figure 27. Generally, higher peak flux magnitudes (both radiant and total) occurred at higher fuel loadings for all measurement locations. At each measurement location, the peak total heat flux was generally greater than the peak radiant heat flux.

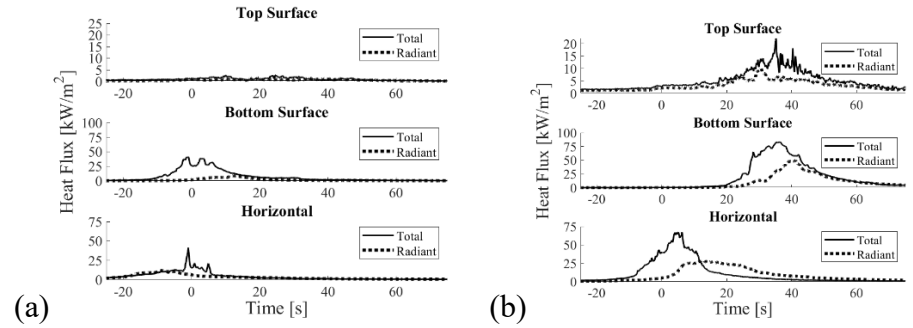


Figure 27. Characteristic total heat flux profiles at each gauge location for fuel beds of 20 kg/m^3 bulk density and different fuel loading. (a) $\alpha\sigma\delta = 98$ and (b) $\alpha\sigma\delta = 197$.

From Figure 27, it is also clear that the peak heat flux measured at the top surface of the fuel bed is significantly lower than at either of the other two measurement locations. This suggests that the heat flux from the flame to the unburnt fuel is significantly less than the heat flux transferred from the combustion region within the fuel bed. As shown in Figure 28, the ratio of peak heat flux at the bottom surface to that at the top fuel bed surface, ranged from 3.0 to 20.4.

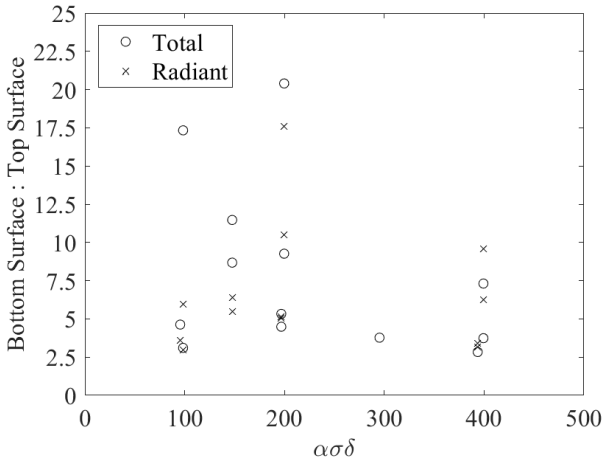


Figure 28. Comparison of heat flux to top and bottom surfaces of the fuel bed (5 s Moving Avg. of 10 Hz Data).

The heat flux transferred to the gauges at the bottom surface might be affected by deposition of burning fuel elements onto the gauge sensor. However, a similar trend, of greater heat flux from the combustion region, is also observed when comparing heat flux from the flame to the heat flux measured horizontally through the fuel bed, as shown in Figure 29. Given the orientation of these gauges (perpendicular to the fuel bed surfaces) accumulation of burning fuel elements does not play a role.

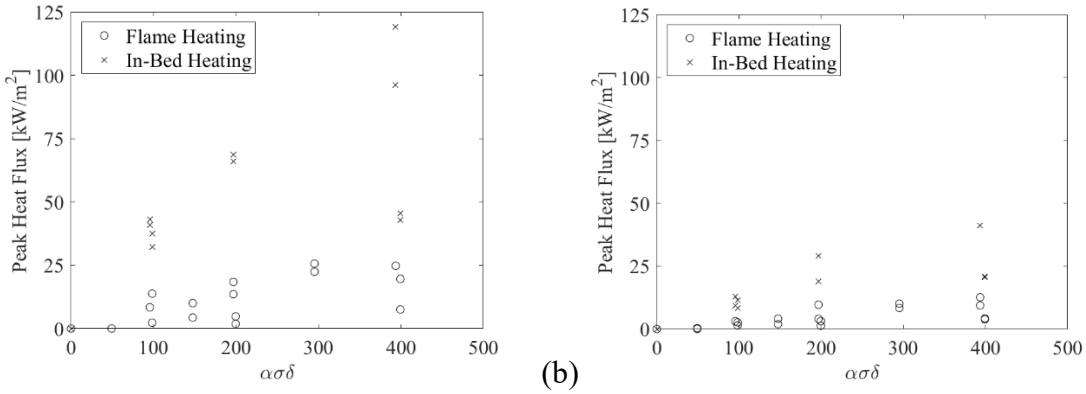


Figure 29. Comparison of Peak (a) Total and (b) Radiant Heat Flux from the above-bed flame with horizontal heat flux through the fuel beds of various structures.

In Figure 29, where the peak total heat flux was greater than the maximum of the calibration range (100 kW/m^2), its absolute value should be interpreted with caution. In general, a positive relationship between $\alpha\sigma\delta$ and the (radiant or total) heat flux is observed at each location, with greater heat flux magnitudes measured within the fuel bed than at the top surface. Similarly, the ratio between the horizontal heat flux magnitude and the flame heat flux generally increases with increasing $\alpha\sigma\delta$ value. Again, the importance of fuel loading at similar $\alpha\sigma\delta$ values is observed in the two highest $\alpha\sigma\delta$ cases, with significant variation in heat flux magnitudes occurring between these cases. This variation is greater for total heat flux measurements which may be as a result of an increased combustion rate (and hence energy release rate) and/or increased convective cooling due to the greater porosity in the $\alpha\sigma\delta = 399$ case.

While the dominant heat transfer path appears to be heat transfer through the fuel bed (from the combustion region), it is also important to understand the relative significance of radiative and convective heating associated with this heat transfer path. A qualitative indication of convective cooling or heating effects is given by calculating the ratio of radiative to total heat flux, as shown in Figure 30. A radiative flux ratio of less than 1.0 indicates convective heating, while a ratio of greater than 1.0 indicates convective cooling.

When the heat flux gauge is located far from the flame front, then some convective heating would be expected since the gauges are water-cooled. At the low heat flux values typical of these far-field measurements, significant noise is also present due to both natural fluctuations and random error, the frequencies of which may vary.

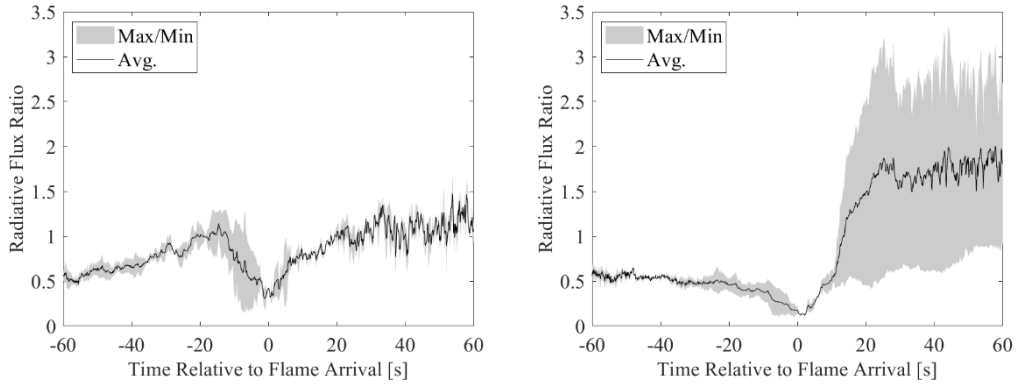


Figure 30. Instantaneous ratio of Radiative: Total Heat Flux relative to flame arrival time for fuel beds of (a) $\alpha\sigma\delta = 98$ and (b) $\alpha\sigma\delta = 197$ (Based on measurements of heat flux transferred horizontally through the fuel bed).

From Figure 30, a minimum radiative flux ratio is observed near the flame arrival time (t = 0 s), followed by an increase in radiative flux ratio after flame arrival. This general trend is observed across all the fuel bed structures studies, however some variation in the time at which the minimum value occurs is observed.

The measured heat flux profiles allow detailed investigation of the effect of fuel bed structure on the heat transfer mechanisms involved in the flame spread process and identification of the dominant heat transfer paths. The flux density distribution ahead of the flame front can also be calculated since the flame front position over time is known.

Dominant Heat Transfer Mechanisms

For both heat-transfer mechanisms, the maximum pre-heating distance was less than 250 mm. The peak heat flux however occurred after the arrival of the vaporization front. This is partly due to an extended heating duration after the passage of the vaporization front, when the trailing flaming and smoldering regions continue to propagate over the gauges. It is also difficult to determine a single arrival time given the discontinuous flame structure within the bed and therefore it may be useful to consider the peak flux values within the framework of a surface of fire inception. As shown in Figure 29, these peak total heat fluxes demonstrate a similar trend of significantly greater heat transfer from the in-bed combustion region than from the overhead flame.

The heat transfer from the combustion region, through the fuel bed is therefore the dominant heat transfer path in this flame spread scenario. This agrees with previous qualitative observations in pine needle beds (Fang and Steward 1969; Rothermel and Anderson 1966) and wood cribs (Rumpf 1990).

Given the dual influence of view factor and fuel bed attenuation, the radiant heat flux transferred through the fuel bed to the gauge varies as a function of the distance from the flame front. As shown in Figure 31, the radiant heat flux (normalized by the peak radiant flux) at a distance ahead of the flame front varied with both bulk density (and hence porosity) and fuel loading. This alters the effective heating distance within the fuel bed, which must be specified (along with the heat flux at the fire inception surface) within a thermal model.

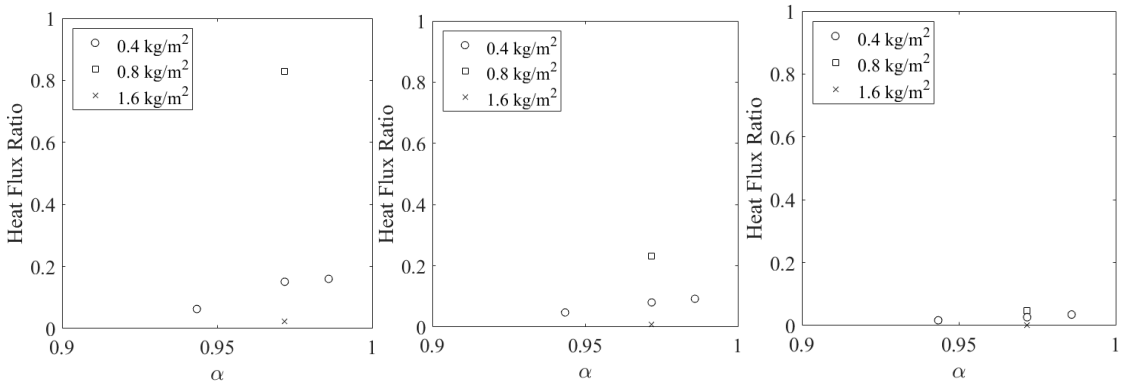


Figure 31. Ratio of Instantaneous Heat Flux : Peak Heat Flux at a distance ahead of the flame front of (a) 25 mm (b) 50 mm (c) 100 mm.

Conclusions and implications for future research

Flow effects on flame spread

As in previous studies, for flame spread through porous natural fuel beds in quiescent conditions (no wind, no slope), flame spread rate (along with HRR and flame height) was found to increase with independent increases in fuel loading or decreases in bulk density. Yet in terms of linking these bulk parameters to the physical processes driving flame spread, neither parameter alone can sufficiently explain the observed changes in fire behavior. A better correlation is observed with a dimensionless fuel bed parameter $\alpha\sigma\delta$ in a similar manner to previous studies, particularly those involving cribs and engineered fuel beds.

Independent changes in bulk density and fuel loading were observed to result in variations in the buoyant flow profile. In the buoyancy-controlled regime explored in this study, this buoyant flow drives lateral entrainment towards the fire front. Variations in the entrainment flow profile through the porous fuel bed were observed as this buoyant flow profile changed, with an overall trend of increasing mean entrainment velocity towards the approaching flame front as the fuel loading (and hence HRR and buoyant flow velocity) increased. Variations in mean entrainment flow for fuel beds of different fuel loading, along with the variation between the mean and minimum entrainment velocity towards the approaching flame front, indicate the need to further quantify the role of bulk and local fuel bed structure and the subsequent changes in oxygen supply and convective heat transfer on the combustion region and the overall flame spread process.

Heat transfer implications for flame spread

By varying the structure of porous fuel beds (fuel loading, bulk density, fuel bed height), both the fuel loading and bulk density were observed to independently influence the flame spread rate and fire behavior (flame height, Heat Release Rate, Burning Rate). It was found that the overall effect of fuel structure on the flame spread rate was well-described by a single parameter $\alpha\sigma\delta$ (incorporating terms for porosity (α), surface-to-volume ratio (σ) and fuel bed height (δ)), similar to those suggested in earlier flame spread studies.

Examining further the underlying physical mechanisms controlling the flame spread process, highlighted the dominant role of in-bed heat transfer (from the combustion region in the fuel

bed) across all the range of fuel beds studied ($\alpha\sigma\delta$ = 49.2 to $\alpha\sigma\delta$ = 399). While the significance of heat transfer contributions from the overhead flame generally increased with increasing $\alpha\sigma\delta$ value of the fuel bed, in contrast with some past predictions regarding heat transfer mechanisms in shallow fuel beds. Direct measurement of the heat flux magnitude and effective heating distance allowed the development of a simple thermal model considering only the radiative heating contributions. Comparison with experimental observations of spread rate indicated a maximum variation in predicted ROS of 29 % where only radiative transfer from the in-bed combustion region was considered, with closer agreement at lower $\alpha\sigma\delta$ values. Where the contributions of both the in-bed and above-bed heat transfer mechanisms were considered, the need to incorporate additional heat loss terms into this thermal model were apparent. Similarly, the importance of understanding the short-range heat transfer mechanisms involved in the flame spread process is emphasized, with this approach embracing the concept of a surface of fire inception within the fuel bed. The range of fuel loadings and fuel structure studied should be considered when interpreting these results, given that previous authors have highlighted the potential for regime changes as the fuel loading (and or fuel bed height) vary, with the potential for optimal fuel loadings or bulk density for a given fuel type.

Implications for future research

This work has indicated that there are significant gaps in the understanding of the effect of the structure of a fuel bed on the combustion process driving flame spread. The complex nature and the coupled nature of the fluid mechanics and heat transfer within a structured fuel requires much more investigation particularly when moving into shrub fuels or canopy fuels particularly since the effect of flow in porous fuels can lead to cooling due to convection but also increased heating due to enhancing the flow of oxygen. This is a fine balance which requires further investigation. Improved understanding of the combustion process is in these scenarios will lead to a better ability to predict the fire spread the fuel consumption and the interactions between the environmental variables and the fuel variables.

Towards improved modeling of flow and heat transfer in litter fuels

Objective

Having shown that induced flows flow through the fuel bed are significant, it is necessary to ensure that these are adequately resolved in numerical models. The objective of this section is to evaluate current approaches used in CFD modeling and, where necessary, to propose alternative formulations for the drag and convective heat transfer coefficients.

Background

Having previously shown the importance of flow through and around porous fuel layers to be critical in understanding the heat and mass transfer, it was necessary to evaluate how these are currently understood (and modelled) and whether there was an opportunity, or need, to improve this to allow better prediction of the processes which underpin fire behavior.

Fuel bed drag in pine forest litter

The flow through porous fuel layer has been shown to be significant in controlling the oxygen mass transfer and hence flame spread and also the convective component of the energy balance ahead of the combustion region. Current approaches to predicting the flow in a porous layer of wildland fuels (e.g. (Mell et al. 2010)) are based on modelling vegetation at the subgrid

scale using a multiphase approach. In such an approach, it is necessary to provide an adequate representation of the drag forces exerted by the vegetation. This is commonly assumed to be represented by a body force on bluff bodies (typically cylinders). The most commonly used formulation is that of a cylinder in cross flow:

$$F_d = \frac{1}{2}\sigma\beta c_s c_d \rho u^2$$

where σ is the surface volume ratio of a single particle, β is the solid volume fraction in the control volume, c_d is the particle drag coefficient, c_s is the shape factor of the fuel element, ρ is the fluid density and u is the fluid velocity. For a circular cylinder in cross flow the drag coefficient has been assumed to be dependent on the particle Reynolds number in various empirical relationships (Schlichting and Gersten 2016). The terms σ and β can be measured or estimated for common wildland fuels however the shape factor (c_s) is likely to be different as particles in natural fuel beds are not aligned in cross flow and the pore structure, fuel element flexibility (and associated elastic storage of energy) have been suggested to be significant (Cao et al. 2012; Kyan et al. 1970; Rudnicki et al. 2004; Vollsinger et al. 2005).

Given these significant assumptions, and the importance of fluid flow through the fuel bed in determining the convective heat transfer and the mass transfer, it is necessary to evaluate the ability of this formulation to adequately predict the flow through porous wildland fuel beds.

In many porous media applications, the drag force is dominated by viscous dissipation. This leads to the formulation of drag force known as Darcy's Law

$$F_d = \frac{\mu}{k}u$$

where k is the Darcy permeability. This holds well for low Reynlods numbers (O(1)) in circumstances where the Reynolds number becomes greater than ~2, inertial effects must be considered (Holdich 2020). These can be incorporated with an addition quadratic term, resulting in the Forchheimer equation

$$F_d = \frac{\mu}{k}u + \frac{Y}{\sqrt{k}}\rho u^2$$

where Y is an empirical coefficient and k is the permeability (which can be considered separate from the Darcy permeability. It is suggested that for the conditions encountered in wildland fires this formulation will better represent the drag force in the fuel layer.

Convective heat transfer in pine litter beds

Convective heating of wildland fuels has been shown to be a key mechanism in fire spread under some conditions (Finney et al. 2013) and as shown above, the convective cooling of particles ahead of the flame front can be significant. Therefore, accurately representing the convective heat transfer in porous fuels is an essential step in predicting the spread of wildland fires. Accurately representations of all modes of heat transfer is required to avoid seeding biases as to the dominant mechanism(s) and therefore to develop.

There are a number of analogues in the heating of porous wildland fuels to other engineering applications such as heat exchanger design (El Houssami et al. 2016) and convective heating studies in porous media have been carried out under a wide range of flow conditions. However, most of these conditions involve porosities and Reynolds numbers outside the ranges typically encountered in wildland fuels. The validity of such studies is also challenged as the characteristic particle length-scale and particle to particle interactions (connectivity) can compound the analysis of convective heating. Additional challenges around the thermophysical properties of wildland fuels, moisture migration and chemical reaction present further challenges to the analysis.

Materials and Methods

To explore these issues a bespoke apparatus was designed and constructed: the Wildfire Exposure and Ignition Response Device (WEIRD) at the University of Edinburgh.

The experiments were carried out in a stainless-steel wind tunnel, designed to generate heated flows characteristic of conditions encountered in wildland fires. The general design of this apparatus, named the Wildfire Exposure and Ignition Response Device (WEIRD), is shown in Figure 32. Air is drawn from the surrounding environment and an associated pressure increase supplied by a blower (Leister Silence). This air is then forced through a process heater (Leister LHS 61L) capable of elevating the temperature up to 650 °C. Air is then passed through a divergence section, a settling chamber with a honeycomb straightener, and a contraction section which was designed following a 3rd-order polynomial matched with a 7th-order polynomial for the outlet (Morel 1975; Su 1991). An enclosed test section, with dimensions of 750 mm x 150 mm x 100 mm is attached to the contraction outlet.

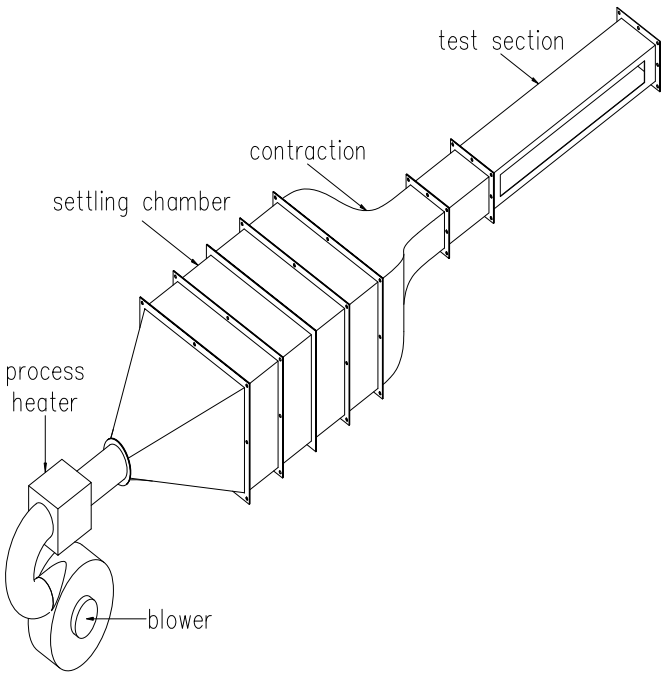


Figure 32. Schematic of the Wildfire Exposure Ignition Response Device.

Within the test section, porous fuel beds were comprised of dead pine needles of the species *Pinus rigida* (pitch pine). These have been the focus of a number of previous studies on the mechanisms of fire spread in forest litter e.g. (Campbell-Lochrie et al. 2018; El Houssami 2016) and the particle properties have been extensively characterized (Thomas 2016). The surface-to-volume ratio for a single needle was taken to be σ = 4661m^{-1} (giving an equivalent cylindrical diameter of $d = 4/\sigma = 0.86$ mm), and the effective material density (assuming a moisture content of 10%) was $\rho_e = 650$ kgm^{-3}. Figure 33 shows the typical appearance of individual particles. Note that pine needles are clasped together, in species-specific quantities, on one end by a thin structure known in botany as a fascicle. In the case of *Pinus rigida* there are 3 needles per fascicle, however, most species have between 2 and 5 needles per fascicle (Thomas 2016). In all cases, the fuel beds tested were 300 mm in length and filling the entire area of the test section. Bed bulk densities of 20, 40, and 60 kg m^{-3} were tested. A very fine steel wire mesh was placed just below the mid-height of the test section in order to support fuel structure and ensure equal distribution along height (particularly in the low bulk density case of 60 kg m^{-3}). The mesh was positioned in such a way as to avoid interference with any intra-bed measurements.

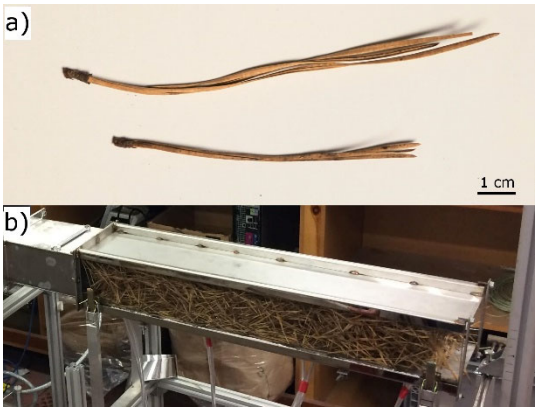


Figure 33. Example of Pinus rigida needles, which are grouped with three individual needles on one fascicle. b) Example of fuel bed packing for the pressure drop experiments.

Pressure drop experiments

For the first set of experiments, a 700 mm length of the test section was filled completely with pine needles and static pressure was measured at four locations along the bed (see Figure 34a). For this basic configuration, the conservation of momentum can be reduced to:

$$F_d = -\frac{\Delta P}{\Delta x},$$

enabling the drag force to be determined directly from the measured pressure gradient.

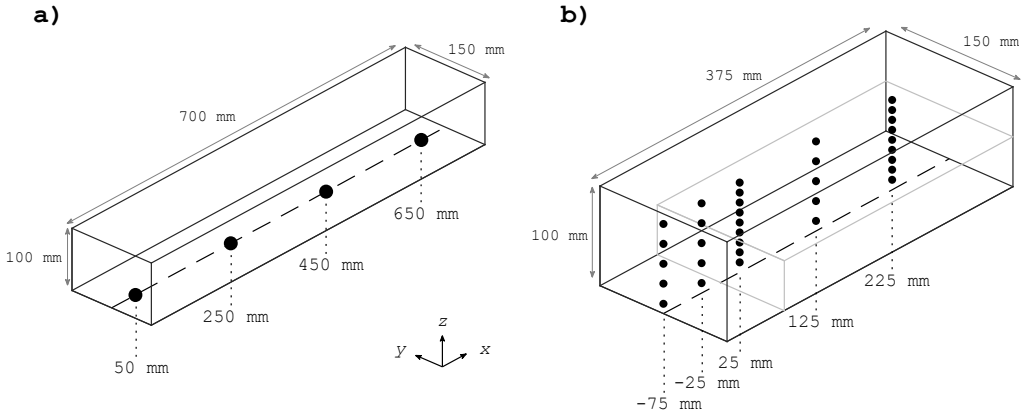


Figure 34. Test section configuration for the (a) pressure drop and (b) layer flow cases -- for both experiments and simulations. The shaded area corresponds to the region filled with pine needles, and the x-coordinates of measurement locations (filled circles) are given in mm from the leading edge of the needle layer. The measurements in (a) were static pressure taps and in (b) were velocities measured with a hotwire anemometer.

Static pressures were recorded with digital pressure transducers (Sensirion SDP800-125). These cover a range of ±125 Pa, with span accuracy of 3% and a zero-point accuracy of 0.08 Pa. The superficial velocity (i.e. the bulk velocity neglecting local variations within bed pores) was measured upstream at the tunnel centerline with a diameter of 7.9 mm S-type pitot tube (Dwyer 160S-18), connected to the same type of pressure transducer. The combination of pitot tube and transducer was calibrated in an open tunnel for the range of velocities investigated.

For a given packing of the test section, pressure drop was recorded at eight different superficial velocities, nominally at 0.25 m s^{-1} intervals between 0.25 m s^{-1} and 2.0 m s^{-1}. At a given velocity, pressure data was recorded at 10 Hz for 120 s to ensure a steady state was captured.

The pine needles were distributed in the test section in a quasi-random manner, while attempting to maintain macro-scale homogeneity in the test section volume. The total mass of vegetation within this volume was adjusted to achieve a range of bulk densities (ρ_b)from 10-60 kg m^{-3}. For ρ_b <30 kg m^{-3} a loose steel-wire supporting mesh was inserted at the mid-plane height of the test section in order to help maintain a quasi-uniform distribution of fuel across the full 100 mm depth. This range was selected both to cover the range of beds which could reasonably be constructed in the test section with homogeneous structure and to overlap with conditions studied previously (Fehrmann et al. 2017). Data on realistic values for *Pinus rigida* litter density are limited, though values on the order of 10—40 kg m^{-3} can be inferred from measurements of loading and height (Gallagher et al. 2017; Mueller et al. 2017).

Four repetitions were carried out at each bulk density (with a complete re-packing of the test section) in order to capture any variability in bed packing technique. Fehrmann (2017) identified the fact that the arrangement and orientation of the fuel elements can have an impact on permeability, with manufactured litter layers behaving differently from natural ones. Thus, it is acknowledged that in-situ pine litter may yield slightly different results, but this technique for

creating the bed structure closely matched that which has been used for flame spread experiments in the same fuel (Campbell-Lochrie et al. 2018), and so the results are still highly relevant.

For the second set of experiments, the test section was filled only to a height of 50 mm, over a length of 300 mm (see Figure 34b). Tests were run with superficial velocities at 0.5 m s^{-1} increments between 0.5 m s^{-1} and 2.0 m s^{-1}. The local velocity was measured at 33 points, distributed along five different vertical transects in the tunnel centerline. The measurements were made with a 8 mm diameter hotwire anemometer (Kimo CTV 210-R), which has an accuracy of 3%±0.03 m s^{-1} up to 3 m s^{-1}, and 3%±0.1 m s^{-1} beyond this. The probe was moved to each point sequentially and left to record for 60 s at 10 Hz. In this case, the bulk densities tested were 20, 40, and 60 kg m^{-3}, and these packings were repeated twice. In all cases, a loose-steel wire mesh was placed at the mid-plane height to help create a well-defined upper surface to the fuel bed.

Pressure drop simulations

CFD simulations, mirroring the experimental configurations, were carried out using the National Institute of Standards and Technology (NIST) Fire Dynamics Simulator (FDS), version 6.7.3 (McDermott et al. 2008). This employs a Large Eddy Simulation (LES) approach to solving a low-Mach number formulation of the Navier-Stokes equations. It includes additional numerical models for incorporating gas-phase combustion, thermal radiation, solid fuel degradation, particle transport, etc. Subgrid-scale vegetation is incorporated with through a continuum approach via source and sink terms in the gas-phase conservation equations, and the focus of this work is on the momentum sink term associated with drag.

Simulations of the experiments were conducted using 3-dimensional domains with the same dimensions indicated in Figure 34. In the case of the pressure drop simulations, the numerical grid resolution was $\Delta x = \Delta y = \Delta z = 10$ mm. For the layer flow simulations, the resolution was $\Delta x = \Delta y = \Delta z = 10 = 5$ mm. The upwind yz-boundary was set to maintain a fixed flow, using either the target superficial velocities for the pressure drop cases or the experimental values from the upwind-most velocity profile for the layer flow cases. The downwind yz -boundary was set to a zero pressure gradient (open outflow), and the lateral boundaries were set to solid surfaces. For solid boundaries, FDS employs a wall model to approximate the viscous stress when the boundary layer is unresolved (McDermott et al. 2008). The walls were treated as smooth, with the wall model following the work of Werner and Wengle (1993). A preliminary investigation indicated that implementing a wall roughness, following Pope (2001), did not significantly alter the results, with the fluid mechanics dominated by the presence of the fuel bed.

Vegetation, in the form of a bulk drag force, was incorporated in all grid cells corresponding to the shaded volume in Figure 34. The one exception was the case of $\rho_b = 60$ kg m^{-3} in the layer flow configuration. The high density of needles used in the experiment pushed up against the wire mesh at the upper surface of the fuel bed, resulting in a bed depth of 55 mm. Thus, this more realistic value was used in the corresponding simulations.

Convective heating experiments

In each test, the fuel beds were instantaneously exposed to a high-temperature air stream (100 - 125°C) at seven velocities, covering a range of nominally 0.5 - 2.0 m s^{-1}. The test section

was initially detached from the rest of the wind tunnel, with the air diverted upwards by a shutter. When a quasi-steady temperature was attained at the desired velocity, the test section was attached and the data logging was started. After a period of recording initial values, the shutter was open and the sample exposed for a duration of 50 s. After each experiment, the test section was removed and cooled to ambient before repeating at the next velocity set-point. To repeats (involving a full re-packing of the bed) were tested for each combination of velocity and bulk density for each of the two experimental configurations (as described below). In a related study on the flow through these types of fuel beds, it was determined that random variability introduced by manually packing the bed did not dominate over the effect of varying overall bulk density.

In all tests, exposure wind speed was measured with a Dembio blade, a type of averaging pitot tube, connected to a digital differential pressure transducer. This was positioned between the exposure shutter and the sample at the centerline of the tunnel. Gas-phase temperatures were measured with very fine gauge (0.08 mm) K-type thermocouples. These were chosen in order to minimize response times and radiative effects and characterize true gas-phase temperature more accurately. Thermocouple positioning varied based on the test (see Figure 35). Intra-bed thermocouples were initially protected by a sheath entering from the base of the test section, and the fuel bed was packed around them. The sheath was then lowered to expose the bare tip of the thermocouple. This was done in order to create a small air pocket around the thermocouple and avoid direct contact with pine needles, which would skew the measurement from the true gas-phase value.

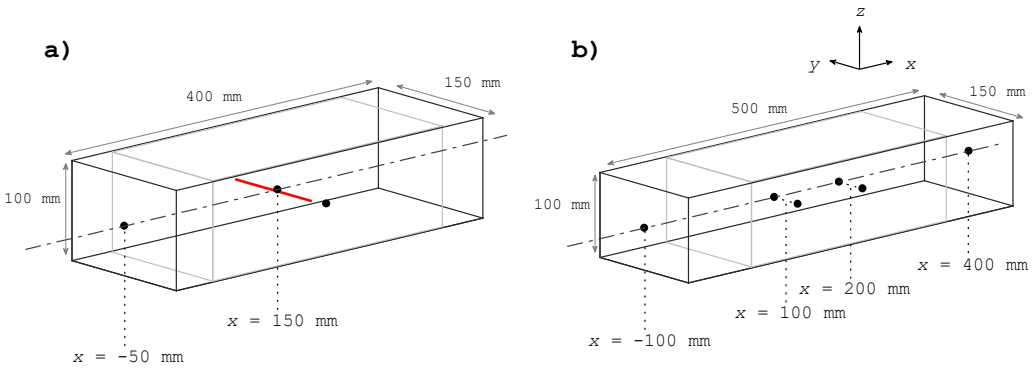


Figure 35. Test section configuration for the heating experiments. Dots represent thermocouple locations.

Convective heating modelling

To represent the gas- and solid-phase responses in the WEIRD, a simple 1-D advection-diffusion model of the gas-phase is proposed:

$$\rho_g c_{p,g} \frac{\partial T_g}{\partial t} + u \rho_g c_{p,g} \frac{\partial T_g}{\partial x} = k_g \frac{\partial^2 T_g}{\partial x^2} + \sigma \beta h_c (T_s - T_g)$$

The second term on the LHS, the convective heat transfer between phases, is obtain by modeling the solid-phase temperature as:

$$\rho_b c_{p,s} \frac{\partial T_s}{\partial t} = \sigma \beta h_c \left(T_g - T_s\right)$$

This coupled model involves a number of key simplifying assumptions. The gas phase is treated as a single, incompressible species, with constant properties representative of dry air). The use of a constant density is necessitated in order to conserve mass, due to the simple (incompressible) treatment of the flow. The use of a constant thermal conductivity is considered acceptable as the ratio of advective transport to diffusive transport, known as the Peclet number ($Pe = Lu\ \rho c_p/k$), is in the range of ~4000-20000. Thus, a simplified treatment of the thermal conductivity should not significantly impact the results. These constants also ignore any effects of moisture; however, the ambient lab air has a water vapor mass fraction of <1.0\%, and the impact on effective properties is deemed negligible here.

The velocity is assumed constant along distance. Changes in velocity at the inlet are experienced instantaneously at any downstream location $u(x,t) = u(0,t) = f(t)$, with the function $f(t)$ obtained from the experimental data.

The pine needle specific heat, c_p, is locally updated as a function of temperature. Thermal radiation and solid-phase conduction are neglected. These assumptions are related, in that they should tend to add a diffusive component to the solid phase temperature profile. In previous models of pine needles beds it was assumed that the high porosity (above 0.9 in our case) makes solid-phase conduction negligible; however, intra-bed radiation was included with through effective conduction coefficient, using the Rosseland approximation (Simeoni et al. 2012). For simplicity, we do not include solid-phase radiation here, as we assume intra-bed transfer will be low due to the relatively low temperatures (<150°C) and the local similarity in temperature of neighboring fuel elements. It is recognized that some of these assumptions may be significant over-simplifications. However, the focus is more-so on understanding how the selection of h_c impacts the solution. Further, by comparing to the more detailed CFD simulation, which includes many of these effects, their impact can be explored.

Results and Discussion

Pressure drop

The time-average pressure drop values are shown for all experiments in Figure 36. The data has been fit with a 2nd-order polynomial, which is forced to zero at u=0, giving the same form as the Forchheimer relationship. The results again demonstrate high repeatability for given bulk densities (the 90% prediction intervals for the polynomial fit are shown as a shaded area). Deviation from the fit can most likely be attributed to the upstream measurement of superficial velocity, which had more noise than the static pressure measurements. A Forchheimer-type formulation gives a good representation of the velocity dependence on bed-drag for these pine needle layers under the range of Reynolds numbers considered. This can be seen in the small error values shown in Table 6Table 6. Permeability and Forchheimer coefficient determined by fitting the Forcheimmer equation to experimental data. Goodness of fit is evaluated with root mean squared error (RMSE) as compared with the range of pressure drops measured.

Table 6. Permeability and Forchheimer coefficient determined by fitting the Forcheimmer equation to experimental data. Goodness of fit is evaluated with root mean squared error (RMSE).

ρ_b [kg·m^{-3}]	ε [-]	k [m^2]	Y [-]	RMSE [Pa·m^{-1}]
10	0.984	1.01×10^{-5}	0.024	1.1
20	0.969	3.63×10^{-6}	0.030	0.9
30	0.954	2.18×10^{-6}	0.037	1.8
40	0.937	1.23×10^{-6}	0.037	1.2
50	0.923	6.35×10^{-7}	0.035	8.5
60	0.908	6.84×10^{-7}	0.044	9.3

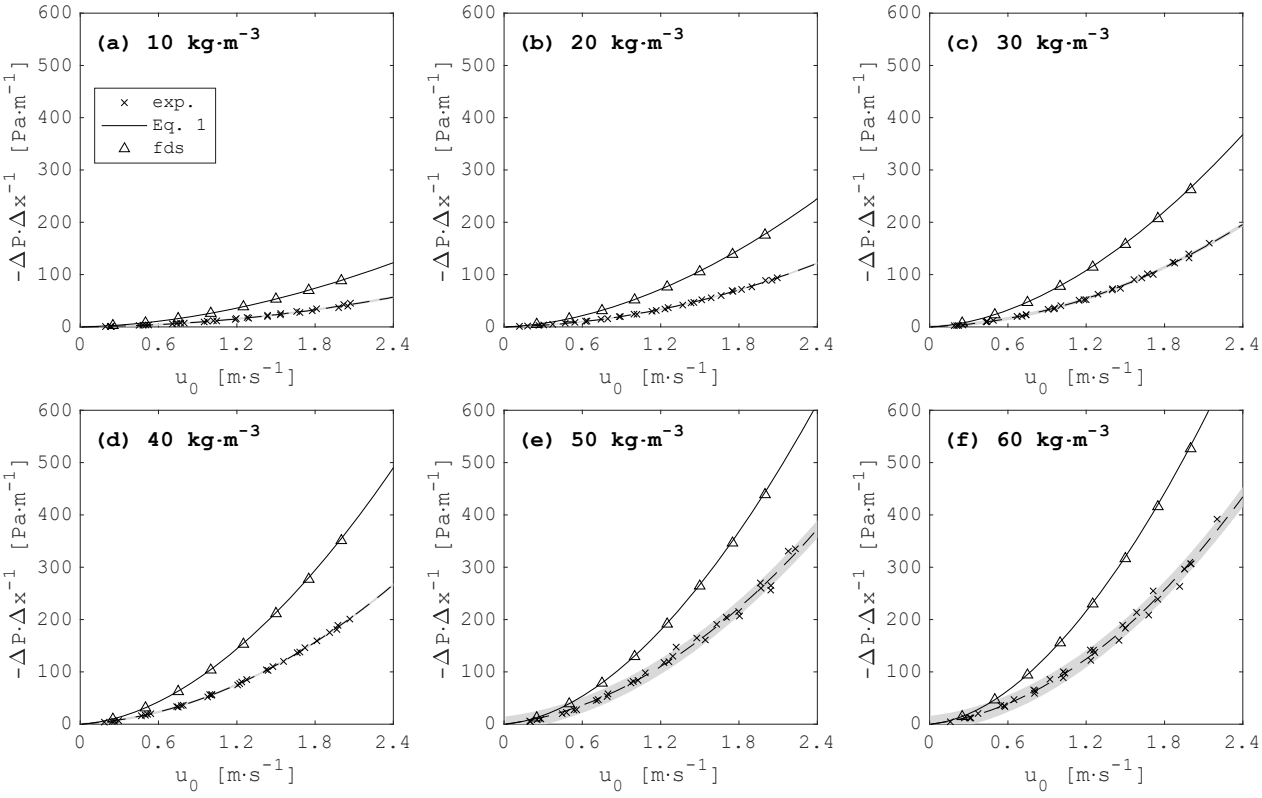


Figure 36. Pressure drop as a function of free-stream velocity for bulk densities of (a-f) 10-60 kg m^{-3}. x's represent experimental data points, and the dashed line gives a best-fit 2nd-order polynomial, with the shaded area indicating the 90\% prediction interval. The solid line represents the theory presented in the Background section, and the triangles represent FDS simulations employing the same theory.

The values in Table 6 appear to give an improved representation of the flow through porous fuel layer. To test this, a series of simulations using a fixed height fuel bed as shown in Figure 34b) was undertaken. The results from these simulations are shown in Figure 37 for the three different bulk densities. In the context of this discussion, the bed height (5 cm) is referred to as h.

As the flow approaches the leading edge of the fuel layer (x/h = -0.5), a marginal adjustment can be observed, with decreasing velocity below layer height and increasing above, particularly for increasing bulk density. Just downwind of the leading edge (x/h = 0.5), the flow profile becomes very irregular as a function of height. This can be attributed to the adjustment of the flow and the fact that the layer does not actually have a well-defined upwind face due to its highly porous nature. Further downstream, the flow establishes into a classic profile for flow over a porous canopy (such as a forest) (Finnigan 2000). A clear influence of bulk density (and correspondingly, porosity) can be identified, particularly at x/h = 4.5, with higher intra-bed velocities for low bulk density and vice versa above the layer.

The simulations show a very similar development of the velocity profiles. It is expected that upstream-most profiles match, as the experimental data at this point was used to define the numerical boundary condition. As the simulated flow establishes within and above the fuel bed (e.g. x/h = 4.5), it adopts the same qualitative profile as the experiments. An exception is the region of flow adjustment just downwind of the leading edge (x/h = 0.5). As opposed to the experiment, the profiles appear more established at this point (there is a clear relationship between local velocity and bulk density), though they are still developing in the downstream direction. This can be traced to the fact that, unlike the experiments, the simulations have well-defined edges to the fuel layer, with vegetation becoming suddenly and uniformly present for all grid cells located at x/h>0 and y/h<1.

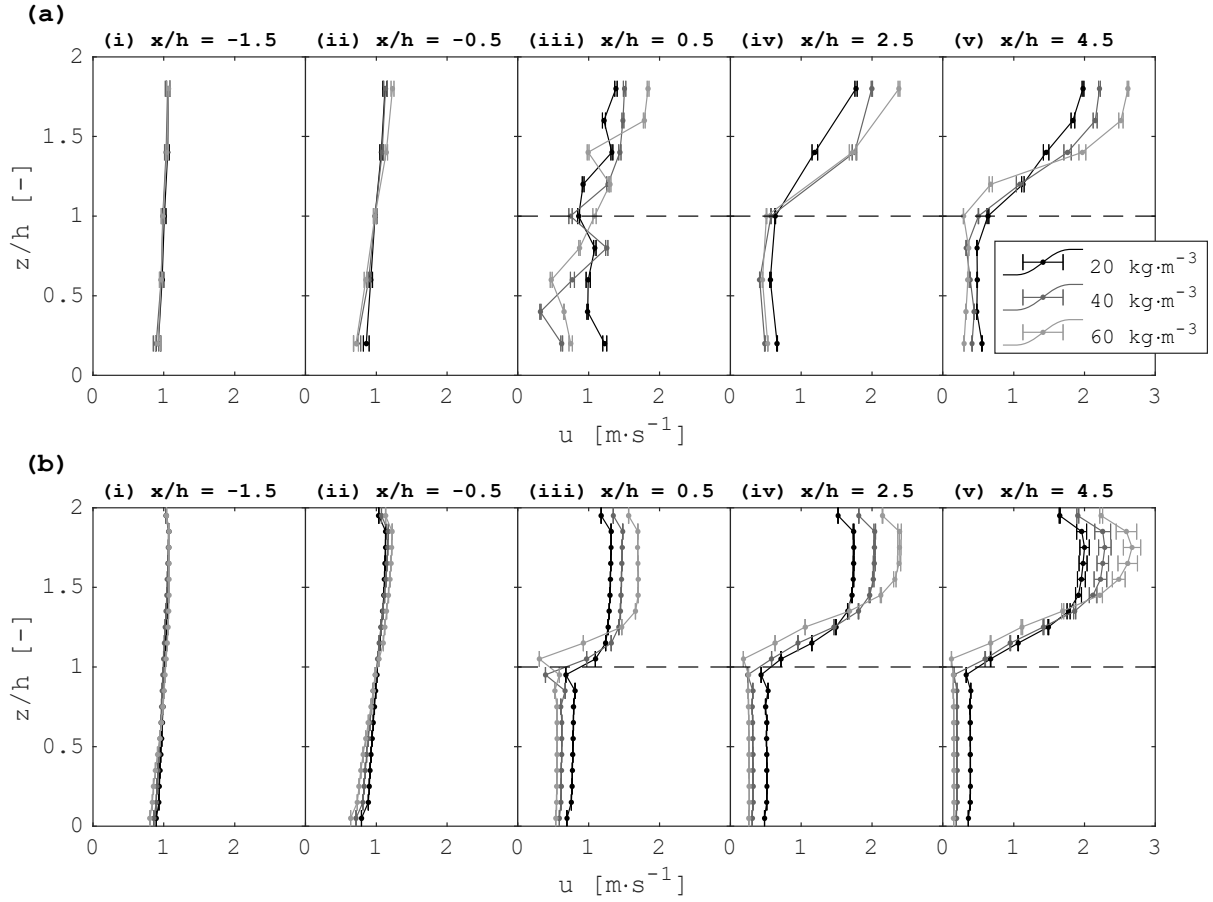


Figure 37. Development of vertical profiles of velocity in the streamwise direction for the (a) experiments and (b) simulations, for each of the bulk densities tested, taking the case of $u_0 = 1$ $m \cdot s^{-1}$. Error bars represent the standard deviation. The horizontal dashed line represents the upper surface of the fuel bed, z/h = 1. Note that the experimental profiles only represent a single repeat.

Convective heating

Data from a typical convective heating experiment are shown in Figure 38. The exposure is shown to be pseudo-instantaneous and a temperature gradient through the porous bed in the flow direction is apparent. There is a small scatter between spanwise measurements indicating the importance of thermocouple placement, and local fuel bed structures.

Using these data with the 1-D model presented in the background section, the value of the Nusselt number can be optimized against the experimental results. The result of this optimization is presented in Figure 39. It is shown that the current formulation over predicts the Nusselt number.

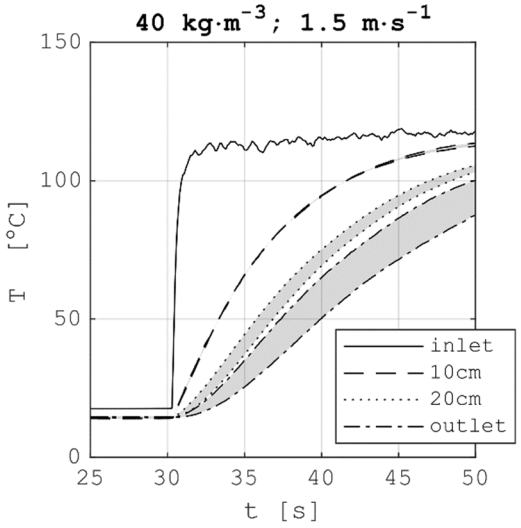


Figure 38. Data from a convective heating test of 40 kg/m3 and 1.5 m/s. The shaded regions represent the temperature range recorded in the spanwise measurements.

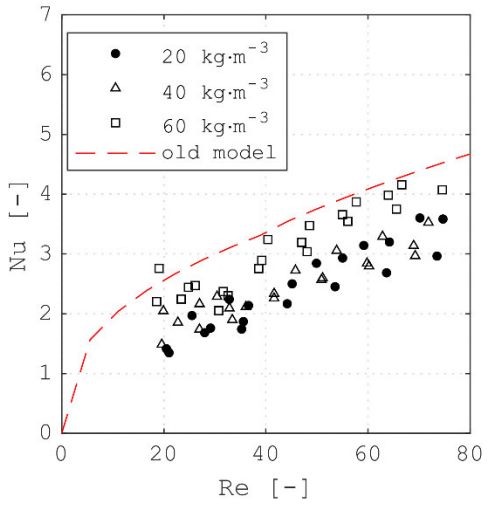


Figure 39. Summary of the numerical optimisation of the Nusselt number for the experimental data (symbols) and the prediction according to the currently implemented model.

These data suggest a new relationship between the Nusselt and Reynolds number could be presented in the form

$$Nu = CRe^n$$

This has not been proposed as there appears to be some dependency on the fuel bulk density that requires further analysis and interpretation of the data.

Conclusions and Implications for Future Research/Implications

The prediction of flow and associated phenomena in porous media has been studied under the conditions relevant to wildland fire. These conditions (high porosity, high Reynolds number) have not been subject of significant precious study. These new insights can be incorporated into state-of-the-art fire models and will serve to increase our ability to model and understand the dynamics of wildland fire spread. They key highlights are:

- Development of a small-scale heated wind tunnel suitable for exploration of the interactions of air flow with wildland fuels.
- Fuel bed drag found to be represented well by a Forchheimer equation i.e. dominated by inertial rather than viscous effects.
- Improved predictive capability compared to existing models of drag in wildland fuels.
- Development of Nusselt number correlations for fuel elements orientated perpendicular to the flow, and fuel beds.

It is acknowledged that the results here pertain to one fuel type and a relatively narrow range of testing conditions. Future research should consider the generality of these conclusions by testing alternative fuel types e.g. broadleaf litter and seek to include the effects of fuel decomposition. as this has been shown to be significant in Section 7.1. Furthermore, future research at this scale should consider evaluating the pore-scale velocity as this may be used to explain observed underprediction of the velocities in the porous fuel layer.

Mid-scale laboratory investigations

Objective

A study focused on examining wind driven fire spread was designed to provide an increased understanding of the convective effects on flame spread and flame behavior. Conducting such studies in the field under realistic conditions is problematic due to the changing atmospheric conditions. The proceeding experiments can be organized into two categories. The first examines the flame behavior and spread rate of fire propagation along an array of discrete fuel elements. Here, the focus is on the flow-flame interactions within fine scale fuels and the processes by which flame propagates and ignition occurs under a forced convection. The second part begins to bridge the in-situ field experiments to the laboratory. By replicating the instrumentation and particular fuel conditions, comprehensive data sets can be brought together from the various experimental scales to examine the effects of increasing complexity of experiments from the small benchtop conditions all the way to the field burns. Finally, the wind tunnel pine needle experiments can serve as the basis of computational model validation data set due to the known boundary conditions of the flow and fuel, as well as rigorous instrumentation throughout the experiments.

Overall flame behavior

Objective

The effect of freestream flow on fire spread behaviors of a discrete wooden fuel array were studied. The spacing between fuel elements was varied and the flame spread behavior under 1,2, and 3 m/s forced flow velocities was investigated. Unexpectedly, the fastest spread rate was not observed for the smallest spacing. Furthermore, increasing spacing did not necessarily lead to a slower spread, as seen with the flame spread along the 0.75 cm spaced array which was as fast or faster than the 0.5 cm spacing condition. Likewise, a unique flame behavior at a spacing of 1 cm was found, which exhibited fragmented flames at wind speeds of 3 m/s that coincided with a slower spread rate than the 2 m/s wind conditions. It seems that a coupling between the combustion and fluid dynamics of flow around the dowel cylinders under certain conditions strongly affects the fire spread behaviors.

Background

A variety of flame spread scenarios, such as wildland fires, urban structure fires, and interior fires, can be thought of as complex systems of discrete fuel flame spread. Researchers have often used arrays or fuel beds of wooden sticks, paper strips, cardboard or other simple fuels to simplify the study of these complex fire scenarios (Beer 1995; Emmons and Shen 1971; Fons 1946; Gollner et al. 2012; Jiang et al. 2019; Miller and Gollner 2015; Prahl and Tien 1973; Vogel and Williams 1970; Weise and Biging 1994; Wolff et al. 1991). Generally, since the fine fuels are the first to ignite and therefore have an important contribution to the rate of spread, researchers have focused on using small-scale fuels.

Early work by Fons (1946) and Emmons (Emmons 1965; Emmons and Shen 1971) took steps to model the consecutive ignitions of fuel elements in arrays and fuel beds to represent nonhomogeneous forest fuel beds. Vogel and Williams (1970) examined the spread along short matchsticks (with the head removed) mounted on a plate at different spacing conditions and found that the spread can be approximated using a linear geometric model and 1-dimensional

approximations to represent heat transfer. Further studies investigated similar fuels under slow constant wind (Prahl and Tien 1973). Some research, for example Emmons (1965) and Kosdon et al. (1969), explored the dynamics of the downward propagation along single wooden dowels and the effect of different environmental conditions on the spread rate. More recently, Jiang et al. (2019) examined vertical spread of buoyancy driven convection along multiple configurations of 2D arrays, using a convective heat transfer model to predict upward flame spread. Past studies have featured differing degrees of convective flow ranging from buoyancy driven natural convection to flows up to 1 m/s.

Experiments with no imposed flow field (Vogel and Williams 1970) show a linear flame spread that is successfully modeled with 1-D thermal physics or geometric arguments. These models have also been shown to extend to sloped arrays, imposing a flame angle, which has been argued to also represent the tilting effect of wind on the flame plume (Beer 1995). Vertically arranged array flame spread provides a slight flow (assumed to be the induced buoyancy velocity) as the convective flow parameter, however, because there is no overall flow field but rather slowly increasing hot gasses from the combustion, the flow effects are minimal and each element is treated as unaffected by upstream flow disturbances (Gollner et al. 2012; Jiang et al. 2019; Miller and Gollner 2015). Furthermore, the approximated maximum speed of the gasses is around 1.5 m/s. Lastly, horizontally arranged forced flow studies have shown that convection and turbulent diffusion are primary heat transfer mechanisms in these systems (Wolff et al. 1991), but few past studies have examined flows greater than 1 m/s, where the buoyancy effects are still comparable to momentum from the imposed flow field (Prahl and Tien 1973).

The developed models to predict fire spread in these past studies do not consider any coupling between the wind and flame, but rather the wind serves to only increase flame contact and heat transfer as a laminar flame. In order to bolster the accuracy of these models, the interactions between flame and flow need to be investigated. The presented research bases its premise on the past works mentioned above, with a few key distinctions. In contrast to past studies, wooden dowels are suspended to avoid boundary effects from a flat surface and use round instead of square cross sections. The array of wooden dowels is then subject to flow speed ranges higher than previously studied. It has been reported that at relatively high flow speeds (around 3 m/s) fire spread around the 2.5 mm diameter scale becomes unsteady. Also, studies of cylinders in non-reacting cross-flow have found that the inter-cylinder region turbulence and mixing is highly dependent on the vortex shedding behavior of the upstream cylinder (Carmo et al. 2010a; Harimi and Saghafian 2012; Khan et al. 2005).

Materials and methods

Figure 40 shows the experimental setup and relevant parameters. For this study, 3.2 mm diameter pine wooden dowels cut to 26 cm in length were used. The thickness chosen is similar to prior studies (Gollner et al. 2012; Miller and Gollner 2015; Prahl and Tien 1973; Vogel and Williams 1970) examining fire spread in discrete elements, which are also representative of the small-scale fuels that dive fire spread. Prior to testing, the dowels were dried until they reached 5% moisture content. The dowels were placed in a linear array suspended on both ends approximately 12 cm above the wind tunnel floor. By suspending the dowels, interference effects from the wind tunnel wall boundaries could be eliminated. Furthermore, the test conditions could

more closely represent suspended twigs and small branches on trees. The suspended dowels were placed 3 m downstream of the test section inlet of a wind tunnel (Figure 40). The tunnel is composed of a 5 m long diverging section and two fans capable of providing uniform flows up to 8 m/s and a turbulence intensity up to 20% at the test section inlet. The test section, with a flow cross sectional area of 1.5 m x 2.26 m, has a total length of 6 m and features large transparent windows capable of enduring direct flame contact with temperatures up to 1200 K for an hour. The transparent windows allow optical access to the test section for flame visualization and optical measurements.

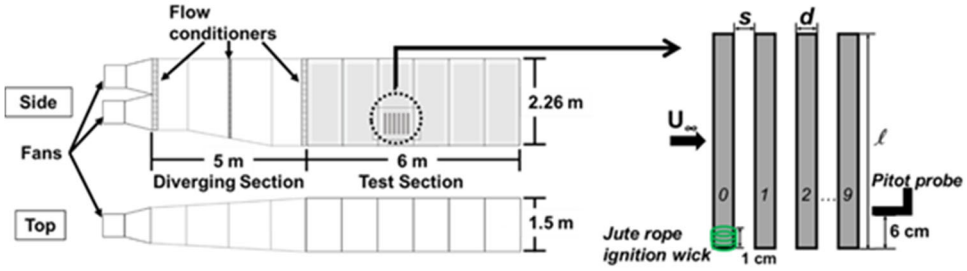


Figure 40. Diagram of wind tunnel and experimental setup showing edge-to-edge spacing (s = 0.5,0.65,0.75,1,1.15 cm), dowel diameter (d = 3.2 mm), freestream flow (U_∞ = 1,2,3 m/s) and length (l = 26 cm). The dowel position numbering scheme utilizes 0 for the pilot dowel, then 1, 2, up to 9.

The first dowel in the array was wrapped with a jute rope coil soaked with 0.3 ml of Kerosene to provide a pilot ignition. The freestream flow was blocked during pilot ignition for 30 seconds to ensure that the kerosene was burned away and interference from transient flow features during tunnel fan start up were eliminated. The flame propagation of the 10-element dowel array was studied for five spacings (0.5, 0.65, 0.75, 1, and 1.15 cm) at three freestream flow conditions (1, 2, and 3 m/s). fire spread was captured using a GoPro Hero5 camera at 60 frames/sec. A pitot probe was used to measure pressure fluctuations in non-reacting flow behind the dowel array approx. 6 cm above the bottom attachment point. The probe was connected to an Omega PX-275 differential pressure transducer sampling at 1 kHz.

Results and discussion

Critical spacing

For horizontal flame propagation along discrete fuels under no freestream velocity, the fire spread from element to element has been found to be linear (Beer 1995; Prahl and Tien 1973; Quintiere 2006; Vogel and Williams 1970; Zhang et al. 2013) in other words the fire spread velocity is constant, relying on the flame from one element to make contact with the next element to initiate ignition. The increasing spacing between elements only serves to slow down the fire spread due to the reduced flame contact with the next element. However, when a freestream velocity is applied, the most immediate effect is to tilt the flame causing much earlier impingement on the adjacent fuel elements, leading to faster forward flame propagation. In addition, spacings where flame propagation is not possible under natural conditions (zero free stream velocity) can now sustain flame spread as shown in Figure 41 where regions that flame

does and does not propagate with varying spacing and flow velocity are depicted. As spacing is increased a higher free stream velocity is needed to sustain continuous flame spread.

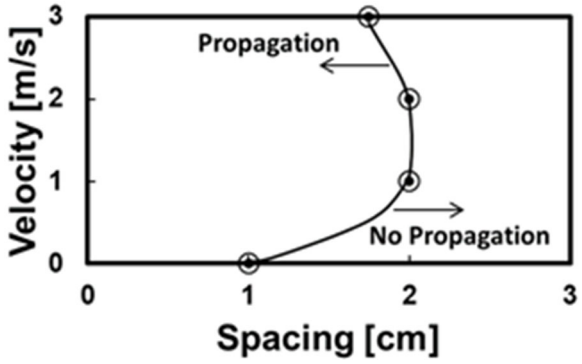


Figure 41. Critical spacing for 3.2 mm dowel array. The line marks the marginal propagation threshold for which arrays at larger spacings do not see flame spread.

The spacing beyond which the adjacent element fails to ignite and thereby stopping forward propagation is defined as the critical spacing. At the no flow conditions, the flame is purely buoyant, and the flame front extends to a limited distance. Thus, conduction and radiative heat transfer are the main heat transfer modes for pyrolysis and ignition of downstream dowels, and the critical spacing for the no flow conditions is less than those with a freestream flow. When a freestream velocity is applied, the flame tilts and contacts downstream dowels. In this manner, flame buoyancy is decreased by the effects of a convective flow on the fire spread. Furthermore, because of the increased flame contact and flow advection, the rate of heat transfer increases as both convective and conductive effects from flame are increased in addition to the radiative heating. Consequently, the critical spacing increases in the presence of the cross-flow.

At low velocities, the convective flow and the flame's buoyancy have comparable influence on the flame shape forming a steep angle. At an intermediate velocity, the convective flow plays a dominant role in the flame angle, forming a shallower angle, but overall, the flame retains a similar shape as the 1 m/s case. Eventually the flow speed becomes strong enough to flatten the top of the flame, and the flame takes on a different shape than the slower speeds. Based on the changes in the flame shape and tilt angle, it can be assumed that the convective heat transfer could be significantly changed compared to a no flow scenario. Heat could be gained or lost to the freestream flow through convective heating or cooling, respectively. Additionally, the flame impingement area is increased due to a wind. Therefore, there could exist a competing effect between flame and the flow. Lastly, the fluid dynamics induced by the interactions between the flow and the array elements subsequently affect combustion. Initially and up to 2 m/s the addition of a wind allows the flame to spread at higher spacings when compared to a no flow condition. However, increasing the flow speed to 3 m/s leads to a hindering effect as the overall flame size becomes smaller, flame fluttering increases, and convective cooling plays a greater role which decreases the critical spacing seen in Figure 41.

Fire spread rate

The ignition times for each spacing and velocity case was extracted from the fire spread video data. Each experimental case was repeated five times to ensure repeatability. The averaged

ignition times for each dowel position in the array are plotted in Figure 42. The shaded regions indicate the range of the experimental results, although some cases have overlapping regions, such a wide range is unavoidable and is seen in similar studies (Gollner et al. 2012; Jiang et al. 2019). The data is arranged such that the t = 0 s corresponds to the ignition of the dowel following the pilot dowel.

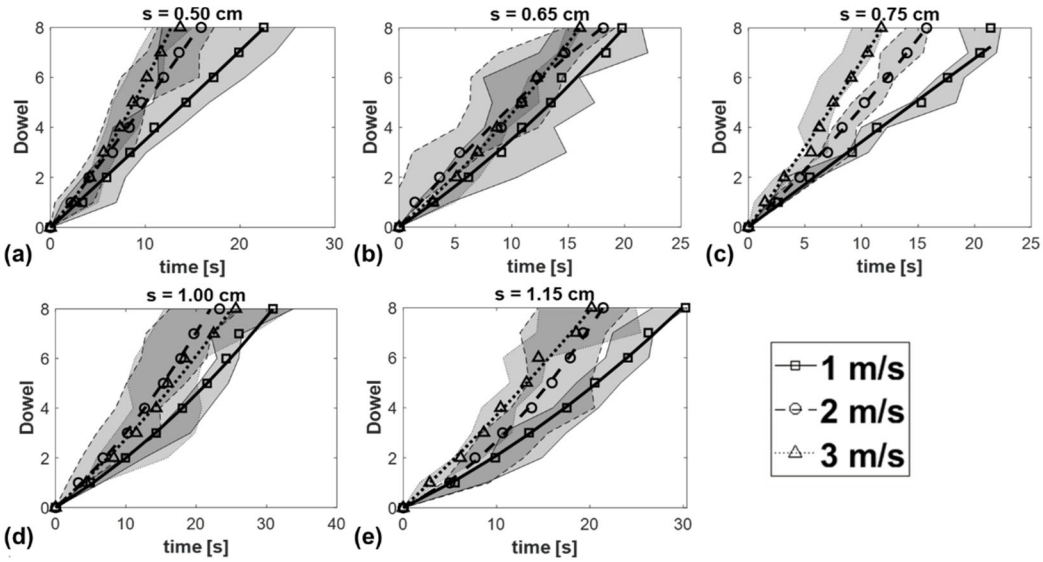


Figure 42. Fire spread for (a) 0.50, (b) 0.65, (c) 0.75, (d) 1.00, and (e) 1.15 cm spacings under 1, 2, and 3 m/s freestream flow. The markers are averages of 5 data points with the experimental range shown as the shaded region. The plotted line represents a quadratic regression of the data points.

Due to observed non-linearities in the results, especially in the later stages of the spread and in larger spacing configurations, a quadratic regression was fit to the data in order to compare the results. The minimum regression R^2 value for all the cases was .98. Taking the derivative of the regression equations, the average rate of spread at the time of specific dowel positions can be evaluated. The spread rates for dowel positions 3, 5, and 7 are shown in Figure 43. These three dowel positions represent the early, mid, and late stages of fire spread along the array.

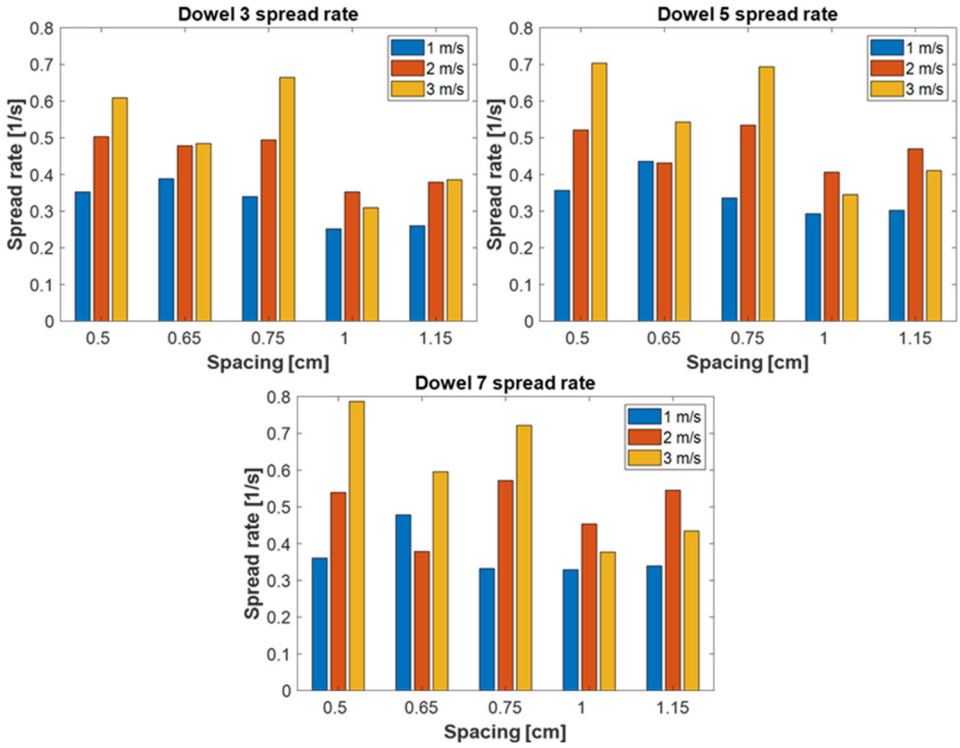


Figure 43. Fire spread rate at dowel positions 3, 5, and 7 for multiple spacings under 1, 2, and 3 m/s freestream flow.

It is expected that increasing the flow speed will increase the spread rate due to increased flame tilting and convective heat transfer. However, Figure 43 shows this is not always the case. Specifically, the cases of 1 and 1.15 cm spacing show faster spread rate under a 2 m/s freestream velocity compared with 3 m/s. It should be noted that although 1 and 1.15 cm spacings have a faster spread rate at 2 m/s, only the 1 cm case has an overall faster fire spread at 2 m/s than 3 m/s as seen in Figure 43. It would also be expected that smaller spacings between dowels result in faster flame spread because of reduced distance that the flame must overcome to contact the next array element. Indeed the 0.5 cm spacing condition exhibits the fastest spread rates, but the 0.75 cm spacing spread rates under 2 and 3 m/s wind conditions are comparable to the 0.5 cm case, at most within 8-9% of the 0.5 cm rates despite the increased distance between dowels. Similar trends are seen in the flame propagation under a 1 m/s wind, which seems to be only slightly affected by the increasing spacing, as compared to higher flow speeds. Higher flame buoyancy effects at 1 m/s coupled with the slow flow speed create the biggest flame area of the three velocities, which could contribute to the decreased effects spacing has on flame spread. However, a large part of the flame is directed upwards in contrast to the other two flow speeds leading to slower spread overall when compared to faster flow speeds. There is a consistent drop in the spread rates throughout the three stages of fire spread when the spacing is increased to 1 cm or greater. Note that 1 cm is the critical spacing for the no flow condition, or where marginal flame propagation is observed as shown in Figure 41.

Studies on the fluid mechanics of tandem cylinders in cross flow show the existence of various wake flow regimes, and it could be used to explain the observed fire spread rate behavior

(Carmo et al. 2010a; Papaioannou et al. 2006; Sewatkar et al. 2012; Zhou and Yiu 2006). When cylinders are placed in a tandem array, the wake and corresponding vortical structures are dictated by cylinder spacing and Reynolds number (*Re*). The spacing and Re used in this study correspond to the conditions outlined in literature (Carmo et al. 2010a), in which a significant change in the vortex shedding pattern was observed. The increased spacing between cylinders and faster flow speed leads to the wake vortex shedding affecting the inter-cylinder region rather than extending past the downstream cylinder. The size and fluctuations of the wake and vortex structures could act to inhibit or hinder fresh air entrainment and mixing from the surrounding freestream flow into the reaction zone. Under favorable fire spread conditions, air entrainment results in partially premixed conditions leading to a higher flame temperature. The increased flame temperature enhances heat transfer and compensates the convective cooling due to the entrained cold air. At unfavorable conditions, the induced vortical structures block fresh air entrainment to the reaction zone. Consequently, combustion reactions occur at rich conditions reducing the flame temperature. Furthermore, increased velocity accompanies convective cooling from the surrounding cold air. The reduction in flame temperature from less partially premixed conditions and increased convective cooling could hinder the flame spread and lead to longer ignition times. More discussion will be provided in the later sections by analyzing flame visualization.

Flame visualization

Although the spread rate analysis gives some insight into the fire spread behavior, the deviations from expected behaviors need further explanation. These deviations are mainly the drop off in spread rate at spacings greater than 0.75 cm and the subsequent acceleration of the fire propagation under 2 m/s flow that generates faster fire spread than the 3 m/s case. To provide further understanding, direct flame images were compared. Figure 44 shows representative images from the fire spread experiments at the time of ignition of dowel positions 3, 5, and 7 representing the early, middle, and late stages of fire spread along the array, respectively. It should be noted that the early, middle, and late stages are not the same for each spacing and flow speed condition. They represent stages of the fire spread for each tested condition. Actual time of ignition are marked in each picture in Figure 44. Images of the 0.75, 1, and 1.15 cm spacing arrays are presented for 2 and 3 m/s.

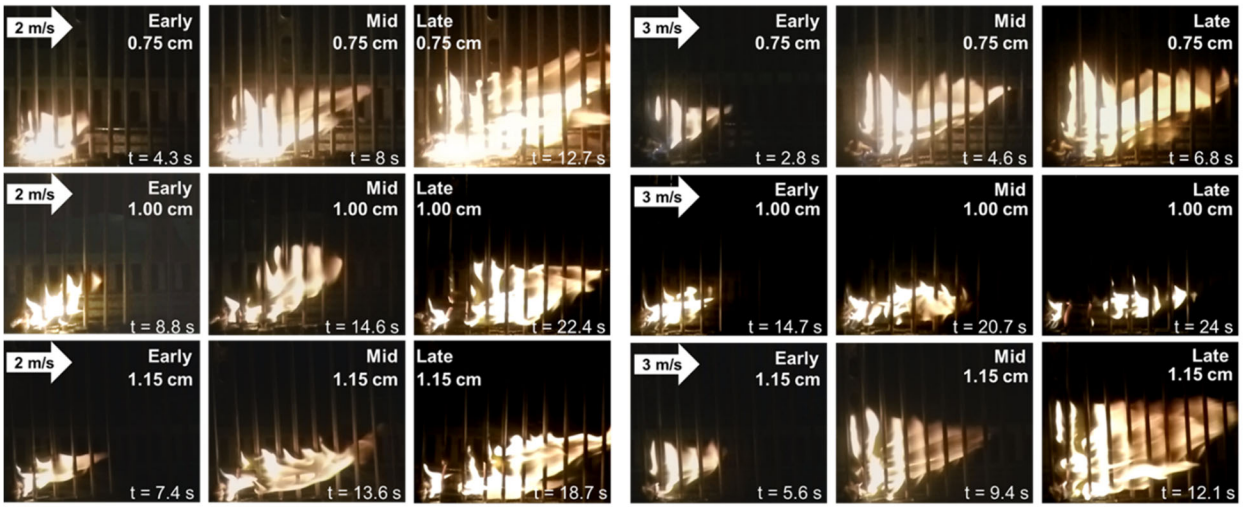


Figure 44. Images of early, middle, and late-stage fire spread at 0.75 – 1.15 cm spacings for 2 and 3 m/s. Early-stage images are taken at the ignition of dowel 3. Mid stage images are at the ignition of dowel 5. Late-stage images are taken at the ignition of dowel 7.

At 1 cm spacing, it seems that the fire spread at 2 m/s is the more vigorous spreading case than that at 3 m/s. At 2 m/s, the flame is slightly segmented by each dowel, but the flame is largely merged. As the flame spreads downstream, the flame grows and engulfs multiple dowels simultaneously (mid stage). Eventually a large, merged flame is observed in the late stage, with the earliest dowels burned through. In contrast, at 3 m/s, early in the fire spread the flames are like the 2 m/s but markedly slower, suggesting that the effects of the flow are present in the 2 m/s case but not as prevalent. The flame structure becomes more fragmented instead of merging as the flames move to the middle stages of the array. Towards the end of the array, the flames remain small and almost seem to burn independent of each other. In contrast, at the 2 m/s case the fire includes 6 burning dowels contributing to the overall flame. At 3 m/s, it seems that the flow confines the flame close to each ignited dowel instead of aiding the flame to contact the next unignited dowel. The flame confinement then slows down the overall fire spread. Although most prevalently seen in the 1 cm case, the flame confinement may be present for all spacings at 3 m/s since the upward flame spread along each dowel at other spacings is greater compared to 2 m/s, suggesting a longer residence time at each dowel position.

Flame images also show a significant flame behavior changes from 0.75 cm to 1.15 spacings. As discussed in the previous section, a spacing change from 0.75 cm to 1 cm causes a significant decrease in spread rate, and at 1.15 cm spacing the flame spread is comparable or faster than those at 1 cm spacing. It would be expected that the 3 m/s behavior would be similar to that of the 1 cm case at 1.15 cm. However, the flame at 1.15 cm spacing resembles the 0.75 cm case instead, as seen in Fig. 5.

From the flame images (Figure 44), the 1 cm spacing case shows unique flame behavior in response to the higher flow speed of 3 m/s. At 2 m/s the flame created at the 1 cm condition resembles that of the other spacings. The flow tilts the flame and creates an oblong shape stretching in the downstream direction. In contrast, at a flow speed of 3 m/s the flame shape is completely changed for the 1 cm condition in comparison to the flames at other spacings.

Additionally, the 0.75 cm cases have the most intense flames in comparison. It seems that the flow has multiple effects; tilting the flame and increasing the flame contact surface to dowels and inducing the vortex shedding around the dowel cylinders which change the mixing conditions (air entrainment) in the inter-cylinder region. The vortices also are interacting with the flame itself to either confine or stretch the flame and increasing or decreasing the heat delivered to unignited dowels. Although it is not the focus of the current study, flow field measurements could provide further details for the vortex shedding effects on the fire spread behaviors.

Conclusions and implications for future research

The fire spread behavior along a suspended array of wooden dowels was investigated for a range of spacings (0.5, 0.65, 0.75, 1, and 1.15 cm) and wind speeds (1, 2, and 3 m/s). The spread rate for all cases was modeled with quadratic regressions due to slight flame spread acceleration. At fixed spacings, the spread rate generally increases with faster flow speeds. However, deviations from expected propagation behavior occur. Namely, at the 1 cm spacing conditions, faster spread is observed when subjected to a flow of 2 m/s rather than 3 m/s, in contrast to the other spacing conditions. Furthermore, increasing the spacing between dowels does not always lead to slower ignition times, with the 0.75 cm spacing cases showing spread rates comparable to those of 0.5 cm at 2 and 3 m/s flow speeds. Flame visualization showed smaller discrete flames formed in the 1 cm spacing array when subjected to a 3 m/s flow. The higher frequency vortices measured with pitot probes developed from each dowel cylinder are changing the gaseous mixing conditions as well as stretching or constricting the flame in a way that fluctuates the heat transfer. As a consequence, there exists a shift in the spread rate trend between the 0.75 cm and 1 cm spacings. Flow effects seemed to be minimal for the spacings below 0.75 cm. At 0.75 cm spacing the mixing and flow conditions are such that an optimal combination is achieved leading to fire propagation as fast as the 0.5 cm spacing cases. Once past 0.75 cm spacing, the fire spread was slowed down significantly. In the future, flow field measurements around the cylinder array will be performed to further investigate the confined fire behaviors at 1 cm spacing at 3 m/s and reduced spread rates at 1 cm spacing. A more refined study of the flame behavior at fixed spacings with gradually increased flow speeds should identify clearer trends in the flame propagation behavior need to be conducted. Additionally, turbulence intensity measurements at select points in the array should characterize the changes in the mixing behavior as flow speed is varied. Lastly, experiments with arrays of more fuel elements will be conducted in order to fully characterize the non-linearities observed in the fire spread.

Flame spread behavior characterization

Objective

The large wind tunnel experiments revealed the existence of discretized flame behavior. However, due to the velocities tested, it could only be said that the onset of discrete flames occurred between 2 and 3 m/s. Due to operational limitations in the flow settings of the large wind tunnel, flow speed resolution was limited to 0.5 m/s. To better characterize the flame behavior as it propagates along dowel arrays, a smaller wind tunnel with more precise flow control was employed. In addition to the finer flow control (down to 0.2 m/s) the smaller wind tunnel also decoupled the freestream turbulence from the array induced flow structures due to the lower turbulence intensity (5%).

In the smaller wind tunnel, the forced flow driven flame spread behavior along an array of discrete wooden fuel elements was experimentally investigated, which could be an important step to understanding the flow-flame interactions that govern fire spread. Fuel arrays with five different spacings (0.75, 0.875. 1.00, 1.125, and 1.25 cm) were subject to flow speeds ranging from 2.2 to 4.3 m/s at approximately 0.2 m/s intervals. For each spacing-flow speed conditions tested, the flame spread behavior was categorized into three different regimes, continuous, discrete, and quenching, and the regimes were presented in a flammability map. Visual analysis of top and front view video data was used to describe the changing flame behavior and increasing discretization of the overall flame structure as the flow speed increases. An analysis of the fluid mechanics and heat transfer conditions revealed a correlation between the Stanton number (*St*), the Damkohler number (*Da*), and the onset of flame instabilities and quenching.

Background

Small-sized wooden sticks or dowels have been used to represent the initiation and early buildup of a forest fire, where the first vegetation involving initial ignition processes are the small leaves, pine needles, and branches. Early fire spread research by Fons (1946) and Emmons (Emmons 1965; Emmons and Shen 1971) modeled the consecutive ignitions of fuel elements in arrays and simple fuel beds to represent non-homogeneous forest fuel beds. Since then, researchers have used arrays or fuel beds of wooden sticks, paper strips, cardboard or other simple fuels to simplify the study of complex fire scenarios (Beer 1995; Emmons and Shen 1971; Fons 1946; Gollner et al. 2012; Jiang et al. 2019; Miller and Gollner 2015; Prahl and Tien 1973; Vogel and Williams 1970; Weise and Biging 1994; Wolff et al. 1991).

Vogel and Williams (1970) examined the spread along square dowels mounted on a plate at different spacing conditions and found that the spread can be accurately approximated using a 1-dimensional conduction model. Prahl and Tien (1973) expanded on the work of Vogel and Williams (1970) by subjecting a similar setup to convective flows of up to 0.9 m/s. While (Prahl and Tien 1973) predicted the spread rate of their wind-driven experiments, they could not accurately predict the onset of no propagation for the higher wind speed conditions. Beer (1995) developed a purely geometric model for fire spread of arrays subject to flow or slope by using similar assumptions from Vogel and Williams (1970). In Beer's model, the flow (or slope) only serves to tilt the flame but does not account for other effects of the flow, such as quenching from high wind speeds.

Although the previous works have demonstrated predictions and modelling of fire spread behaviors under a flow with a relatively low speed (below 1.5 m/s), studies for the fire spread behaviors were relatively rare for the flow conditions above 1.5 m/s, where the buoyancy effects on the flame are still comparable to the effects of momentum from the imposed flow. Furthermore, it has been reported that fire spread around the 2.5 mm diameter scale becomes unsteady and highly variable at relatively high flow speeds (around 3 m/s) (Wolff et al. 1991). The propagation and flame behavior changes at extinction conditions in fuel arrays have not been studied previously. Studies for unsteady flames near extinction have been conducted for single cylinders (Yang and T'ien 1998) and tandem spheres (Raghavan et al. 2009) but not for cylinder arrays. Extensive studies on fluid mechanics of single cylinders, tandem cylinders (Carmo et al. 2010a; Carmo et al. 2010b; Sumner 2010), and cylinder arrays and banks (Bao et al. 2012)

inform how the convective flow may interact with the cylinders. Such interactions alter the convective heat transfer depending on the separation distance and flow speed. For a reacting flow, the flame-flow coupling can cause unique flame dynamics and spread behaviors. (Finney et al. 2015) suggested that unsteady flame convection is strongly dictated by buoyant and inertial interaction, and the findings could contribute to advancing physics-based modeling.

The current study seeks to provide further discussion on the flame-flow coupling, arguing that the common assumptions of continuous increase in flame contact or convective heat transfer with an increasing freestream flow speed should be adjusted if the flow and fuel setting lead to discretized flame behavior. The flame-spread behavior of discrete solid fuels was characterized at flow speeds above 2 m/s for multiple spacing conditions. The systematic classification and corresponding analysis of the flow conditions are used to generate a flammability map for flame spread on discrete fuels under forced flow. For example, in an array of dowels, the ignition of the dowel at position *n* will depend on the flame heat transfer of upstream dowels at positions (*n-1*, *n-2*, etc.) that further depend on the upward and downward spread rates on each dowel based on the flow velocity, separation distance, and material properties. The problem is further complicated by the flame-flow instabilities triggered at certain flow speed-array spacing conditions. The ability to predict the onset of such flame instabilities due to convective conditions could be the first step in extending the accuracy of flame spread models.

Materials and Methods

Wooden dowels with a diameter (d) of 3.2 mm and a length of 14 cm were arranged into in-line arrays. Mounting plates with drilled holes at the desired spacings were manufactured, and the dowels were press-fit to the holes. The mounting plate was then placed in a small wind tunnel with a test section that has a cross-sectional area of 15.25 cm by 15.24 cm and length of 81.28 cm, as schematically illustrated in Figure 45a. Flow conditioning screens were utilized to achieve a uniform flow profile across the height of the wind tunnel and minimize fluctuations to less than 5% of the mean flow. A pilot ignition using a small cotton wick soaked in 0.1 ml of dodecane initiated the fire 1 cm ahead of the first dowel as shown in Figure 45b. The pilot was ignited after turning the flow on to avoid flow unsteadiness from the fan startup. Because the pilot ignition could affect the flame propagation, the ignition method was kept consistent for all experiments.

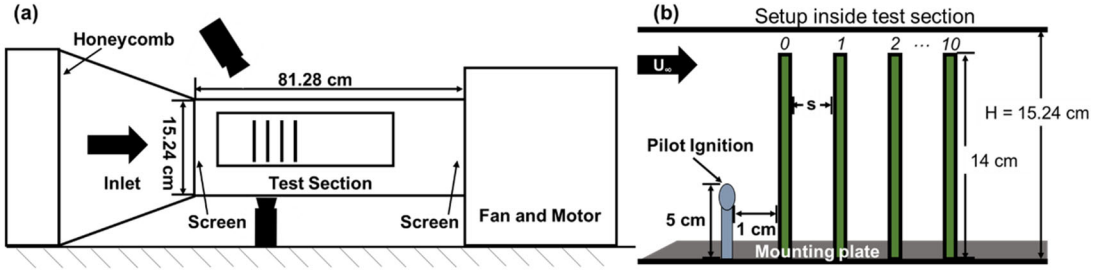


Figure 45. (a) Schematic of wind tunnel and (b) dowel array setup inside the wind tunnel test section

Flame propagation was measured with two cameras, a GoPro camera facing the dowel array and a Sony DSCIII facing downward. The side camera visualized the flame propagation behavior while the downward-facing camera captured the flame wake. The flame propagation behavior

was studied for 5 spacings (s = 0.75, 0.875, 1.00, 1.125, and 1.25 cm) under freestream flows of 2.2 to 4.3 m/s at approximately 0.2 m/s increments. The smallest spacing (0.75 cm) was selected based on the flame size without wind, at which the flame barely touches the next dowel. The buoyancy currents exit the test section before they impact the ceiling with the flow speeds chosen in the current study. Thus, minimizing ceiling effects. For each spacing-velocity combination, the experiments were repeated 3 times. In addition to the flame spread experiments, a hot-wire anemometer was utilized to measure the mean flow speed and turbulent intensity behind dowel 5 of the array in cold flows. Measurements were taken approximately 6 cm above the base of the tunnel at the centerline of the cylinder longitudinal axis. Flow data was collected at a half-spacing distance away from dowel 5 at all spacing conditions.

Results and Discussion

Flame propagation behavior characterization

From the time the pilot is ignited, the very first dowel is in contact with the flame. The first dowel will then begin to char and eventually ignite. The ignition kernel is observed in the wake of the dowel. Subsequent ignition of downstream dowels then depends on contact from the upstream ignited fuel elements. As the flame propagates through the array and more dowels are burning simultaneously, the flame spread accelerates and reaches a steady-state around the 4th dowel position. By the time the last dowel position ignites, upstream dowel positions in the early stages of spread have been consumed and are no longer flaming.

At each spacing-velocity test condition, the flame propagation behavior was classified into three regimes: continuous flame spread (I), discrete flame spread (II), and no propagation (III). Figure 46 depicts the key differences of each regime classification for various flow speeds at a fixed spacing of 1 cm. It should be noted that dowel bending does occur, affecting the dowel spacing. However, dowel bending typically occurs at the later stages of flame propagation. When bending is observed, the flame has already reached a few dowels downstream, and it would have a minimal effect on the quantities reported.

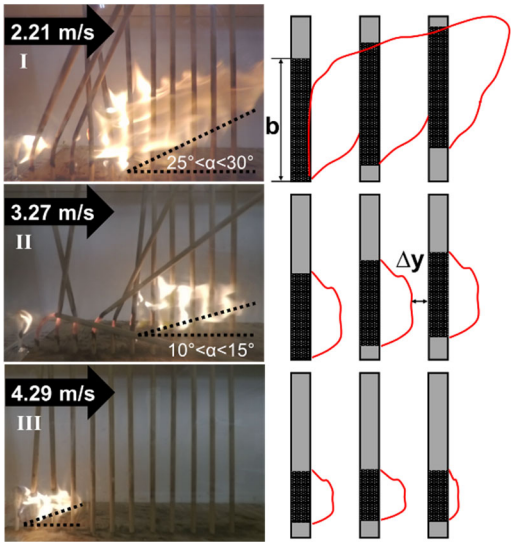


Figure 46. Images and sketches of the continuous (I), discrete (II), and quenching (III) flame spread behaviors observed in a 1 cm spaced array

In the continuous regime (I), each flaming dowel contributes to an overall flame that encompasses the array. The largest flame areas are seen in this regime, and typical flame angles are in the range of 25° to 30°, lower than Prahl and Tien (Prahl and Tien 1973b) who observed 40° to 70°. As the wind speed increases, the large flame brush breaks down into discrete flames (II) attached to each dowel, and the discrete flames do not combine into one flame structure. The flame length is also reduced. The increased flow momentum causes the flame angle to decrease from approximately 25 degrees to 10 degrees. As evidenced by the shorter char height (b), the overall flame contact area is also reduced compared with the continuous regime (I). For regime II, the flame length around each dowel shortens to an extent, and a noticeable gap (Δy) is observed between the flame and the adjacent dowel. With further increase in the flow speed, the flame length is further reduced, and Δy increases. The increase in Δy results in reduced heat transfer from one dowel to the next which reduces the global flame spread rate. The flame also flickers laterally. The combination of the reduced flame length, high flickering, and reduced flame area leads to an arrest of flame propagation past the first few dowels after the pilot and eventually quenching. The velocity-spacing condition leading to quenching is classified as the quenching regime (III).

Each flow-spacing condition was categorized into the corresponding regime based on the flame behavior visualized by the side-view camera, and the results are shown in Figure 47. Experimental results from Vogel and Williams (1970) and Prahl and Tien (1973) are also plotted. In Figure 47, each regime is delineated by hand-drawn lines to qualitatively describe the trend of the boundary change for various normalized spacing (s/d) and Reynolds number (Re) based on the dowel diameter (d). It should be noted that transition conditions (solid grey circle) between the continuous and discrete flame spread regimes are also shown in Figure 47, at which both continuous and discrete flame spreads were observed within 3 repetitions of the experiments.

When the flow speed and spacing are low, the flame spread is in the continuous regime (I), where the flow tilts the flame, thereby touching the next fuel elements. When the spacing is comparatively small (s/d < 4.15), continuous flame spread persists even at high flow speeds (greater than 3 m/s) known to cause instabilities in flame spread at larger spacings (Steward et al. 1977; Wolff et al. 1991). Once the spacing is increased greater than approximately s/d = 4.15 (1 cm spacing), continuous flame spread is difficult to sustain above Re = 500 (2.5 m/s). Further increase in the flow speed or spacing causes the flame on each element to shrink, such that it no longer touches the adjacent dowel, and discrete flame behavior (regime II) is observed. Note that the discrete regime can also occur at low flow speeds with larger spacings. Thus, it is reasonable to presume that at a large enough spacing the only possible sustained flame spread would be discrete. Likewise, at a small enough spacing only continuous flame spread would be observed for all flow speeds below the blow-off limit. When the flow speed or spacing becomes sufficiently large, sustained propagation in the array becomes impossible (III).

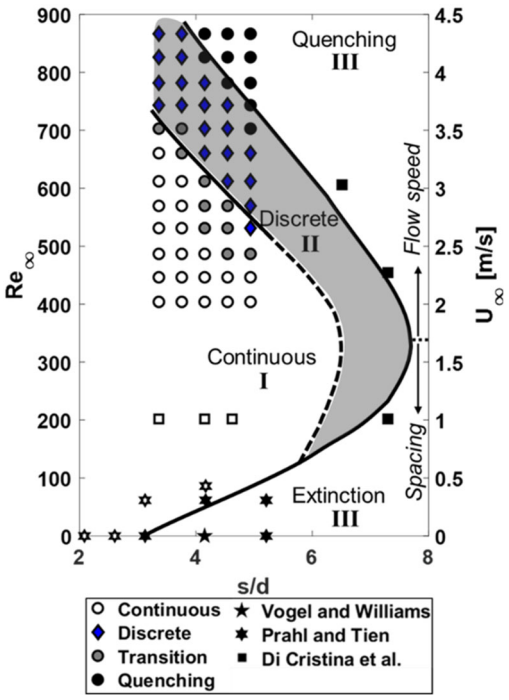


Figure 47. Flame spread regime map showing Continuous (I), Discrete (II), and Quenching/Extinction (III) regimes as a function of flow and spacing of discrete fuel array.

The current experimental data combined with data from the literature suggests that the threshold boundary for quenching seems to take on a hyperbolic shape, with the vertex approximately at s/d ~ 7.5 and between 1.5 and 2 m/s. Within regime III for flow slower than 2 m/s, the quenching is because of spacing being too large for the upstream flame to overcome and ignite the next fuel element, which is more akin to extinction. For flow speeds above 2 m/s, the flow introduces flame instabilities and highly fragmented flames, and here the propagation cessation is more akin to blow-off. It would be natural to assume that the discrete propagation boundary, similar to the quenching boundary, would also follow a hyperbolic trend (dashed-line) although further investigation is needed to delineate the boundary.

Flame structure

Each flame propagation regime has a distinct flame structure, and both the flame shape and propagation are strongly affected by the flow and spacing. In order to analyze the effects of increasing flow on the flame shape, images of the front and top view are compared. Figure 48 shows schematics of the flames and flame images of the front and top views at the time of ignition of dowel 5 for a constant spacing (1.00 cm) and 4 flow conditions, 2.42, 2.82, 3.27, and 3.63 m/s (*Re* = 486, 570, 660, and 740).

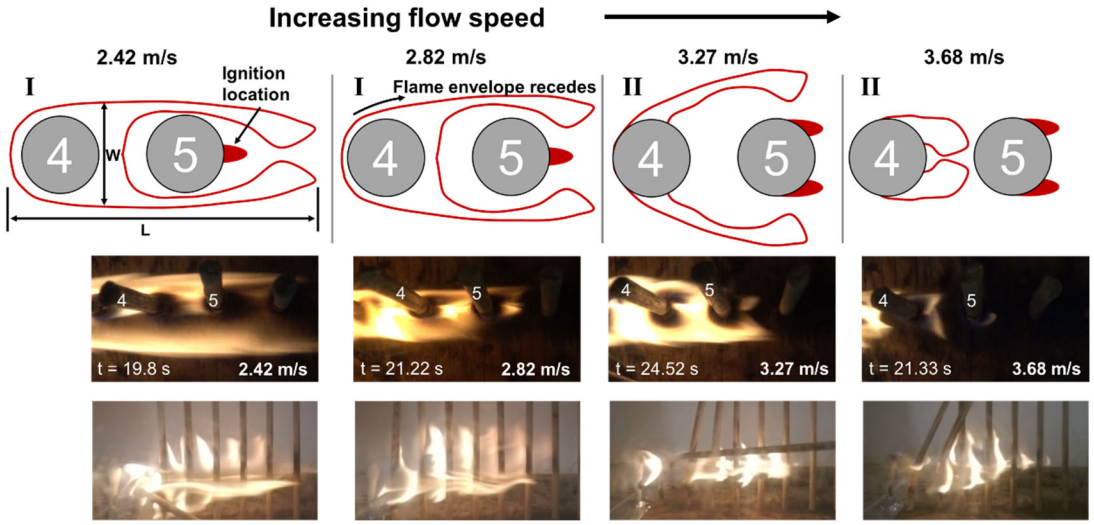


Figure 48. Schematics (top row) of flame (hollow red line) and ignition location (solid red) and top (middle row) and front (bottom row) view images of dowel 5 ignition for 1 cm spacing at 4 flow speeds Timestamps are relative to pilot ignition.

The schematics in Figure 48 illustrate the behavioral trends of the flame from dowel 4 as it interacts with, and ignites, dowel 5 for increasing flow speeds. At flow speeds of 2.42 and 2.82 m/s, within the continuous flame spread regime (I), the flame attaches on the leading edge of the upstream cylinder (dowel 4 in Figure 48) forming a flame envelope that extends past the downstream cylinder (dowel 5) through the wake region and impinges on the leading edge of the downstream cylinder. As the flow speed increases from 2.42 to 2.82 m/s, the wake width (W) increases while the length (L) decreases, similarly observed in other forced convection studies (Fernandez-Pello and Law 1982; Prahl and Tien 1973). Additionally, the standoff distance in front of the upstream dowel reduces, and the flame envelope begins to recede. For the discrete flame spread (regime II, 3.27 m/s), the wake is widened significantly. Also, the length of flame is further decreased, barely passing the downstream cylinder, and the standoff distance reaches zero attaching onto the leading edge of the cylinder. The length of the flame fluctuates, but the wake flame remains in the inter-cylinder region rather than going past the downstream cylinder. As the velocity continues to increase, the length continues to decrease until it is only sustained in the inter-cylinder region. The length will keep decreasing correspondingly with the increasing flow speed. The most fragmented flames are present at the flow speeds just below the quenching (regime III) threshold, the flame envelope previously observed transitions into a wake flame as seen in the far right images under a flow of 3.68 m/s in Figure 48. The changes in wake width and length are further described in Figure 49 which shows the width to length ratio of the wake flame (W/L) around dowel 4 at the time when dowel 5 is igniting. It should be noted that the effect of spacing on the flame shape does not seem to be linear. However, in general, W/L increases and reaches an asymptotic value as the wind speed increases. A high W/L is indicative of highly discretized flame behavior.

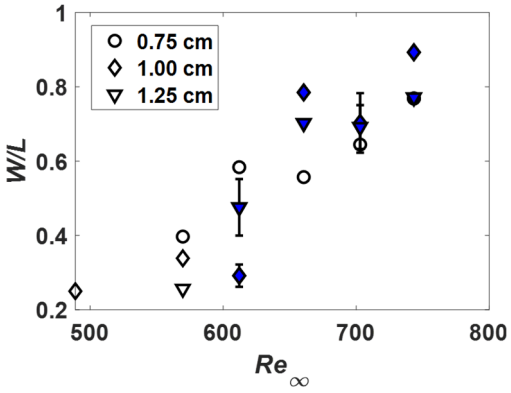


Figure 49. Wake flame width to length ratio (W/L) for a range of flow speeds and array spacings. The filled markers represent discrete flame behavior at those conditions.

For fire spread in the continuous flame regime (I), although the cylinder leading edge shows some charring, ignition occurs at the trailing edge of the cylinder where the local flow speed is slowest, resulting in the maximum residence time. In contrast, for regime II, the ignition typically occurs near the two flow separation points of the dowel cylinder, as shown in Figure 48. At this location, the flow is at an intermediate speed between the faster freestream and slower wake region, and the surface temperature would be higher as the upstream flame shortens. Similar ignition location behavior has been observed in droplet combustion by Fernandez-Pello and Law (1982).

It is important to note that the regime classification was based on the front view flame images. The drastic change in flame shape between 2.82 and 3.27 m/s is evident from Figure 48. The discrete flame cases have little to no cohesion in the overall flame, with each dowel burning independently, along with a significant decrease in the flame contact area. The decrease in the flame contact area is also in contradiction with some fire propagation models (Beer 1995; Prahl and Tien 1973) that are based on the assumption that faster flow speeds increase the contact area. Thus, there may be a limit to the applicability of the assumption that faster flow leads to greater flame contact. Although not shown, at a constant flow speed, increasing the spacing has the same effect on the overall flame shape as increasing the flow speed for a fixed spacing.

Regime boundary prediction

Ignition of a solid fuel requires sufficient heating to be pyrolyzed such that the pyrolyzates mix with an oxidizer to create a flammable mixture. Then, the mixture can be ignited. Because the pyrolyzing process is the slowest process, the pyrolysis time scale could be regarded as the time scale for ignition. In the current study, by considering the size of the flame and flow settings (Gollner et al. 2012; Vogel and Williams 1970; Wolff et al. 1991), it is assumed that convection is the dominant source of heat transfer and radiative heat transfer is much smaller than the convective heat transfer. For a forced flow environment, enough heat must penetrate the boundary layer along the surface to increase temperature of the solid fuel, which also needs accounting for ignition prediction. The heat transfer through a boundary layer is typically quantified by using the Nusselt number (*Nu*). The Nusselt number (and correspondingly the heat transfer coefficient) was calculated by using an empirical correlation for cylinder banks in crossflow shown as Eq. (1),

$$Nu = 1.367\left[0.25 + e^{(-0.55(s/d))}\right](s/d)^{0.212}Re^{1/2}Pr^{1/3} = \frac{hd}{k} \quad , \quad (1)$$

where, *Re*, *Pr*, *h*, and *k* are Reynolds number, Prandtl number, convective heat transfer coefficient, and thermal conductivity, respectively. *Pr* was assumed to be 0.7, and *k* of 2.624 x 10^{-5} kW/mK was used similar to other studies with the same fuel (Gollner et al. 2012; Vogel and Williams 1970). The values of *h* calculated from Eq. (1) were used to estimate the boundary layer length (δ_{BL}) by following the method outlined in Quintiere (2006), as shown in Eq. (2). In this study, the local mean flow velocity behind dowel 5, as measured with a hot-wire anemometer, was utilized instead of the freestream velocity for calculations of the boundary layer. The boundary layer length is then used to approximate the mixing time (t_{mix}) from Eq. (3). The mass diffusivity (D) was assumed to be the value of CO at 600 K since CO would be the dominant gas species in combustion products, and 600 K is typical fuel pyrolysis surface temperature (Quintiere 2006).

$$h \approx \frac{k}{\delta_{BL}} \quad , \qquad (2)$$

$$t_{mix} \approx \frac{\delta_{BL}^2}{D} \quad . \quad (3)$$

Although the Nusselt number (more specifically *h*) gives an idea of how much convective heat transfer is delivered to the dowel surface, it cannot account for convective cooling at higher flow speeds. Therefore, the Stanton number (*St*) is utilized, which can be thought of as a modified Nusselt number, the ratio of convective heat transfer to the heat capacity of the fluid shown as Eq. (4),

$$St = \frac{Nu}{RePr} = \frac{h}{\rho U_\infty c_p} = \frac{h/U_\infty}{\rho c_p} \quad , \qquad (4)$$

where ρ and c_p are density and specific heat of the gas, respectively. Therefore, when the flow velocity increase, the amount of heat that the fluid can absorb instead of transferring to the solid fuel also increases. Note that the Stanton number (St) was identified by Quintiere (2006) as a pertinent dimensionless quantity and can be defined as $St = h/\rho c_p(gl)^{1/2}$ when buoyancy is dominant.

Pyrolysis alone does not dictate the ignition of the solid fuel and flame propagation along the array. Therefore, using *St* alone may not be sufficient for prediction. As seen in Figure 46, Figure 47, and Figure 48, quenching occurs although the pilot flame still provides the necessary heat to pyrolyze. Therefore, other transport phenomena could also play a role in ignition and flame propagation. The mass transport of the flammable mixture with respect to chemical reactions also affects ignition and flame propagation. Therefore, the Damkohler number (*Da*) is used to predict the flame propagation boundary in addition to *St*. In the current study, the mixing time scale is used to represent the mass transport time scale. Equations (5) and (6) presents the Damkohler number definition and chemical time scale, with Eq. (3) used as the mixing time scale.

$$Da = \frac{t_{mix}}{t_{chem}} \quad , (5)$$

$$t_{chem} = \frac{0.623kT}{\alpha[E/(RT)]A\Delta h_c e^{-E/(RT)}} \quad . (6)$$

Here, α (1.25×10^{-7} m^2/s), Δh_c (16.3 kJ/g) , T (1600 K), E, R ($E/RT = 16$), A (10^{13} g/m^3s) are the thermal diffusivity, heat of combustion, flame temperature, activation energy, gas constant, pre-exponential Arrhenius constant, respectively. For the chemical time, estimates for the constants were taken from literature for wood (Gollner et al. 2012; Quintiere 2006). In the current study, the chemical time is constant. Thus, *Da* is changed due to the changes in the mixing time. *Da* is multiplied by d/s to account for the effects of spacing on ignition and flame propagation. Figure 50 shows a plot of the Stanton number (*St*) vs. scaled Damkohler number (*Da(d/s)*) similar to a functional *St – Da* relationship used by Quintiere (2006) in describing flame propagation on a solid block. A full range from St = 0 to 0.1, is shown in Figure 50a, with a zoomed-in view of the current experiments shown in Figure 50b (Quintiere 2006).

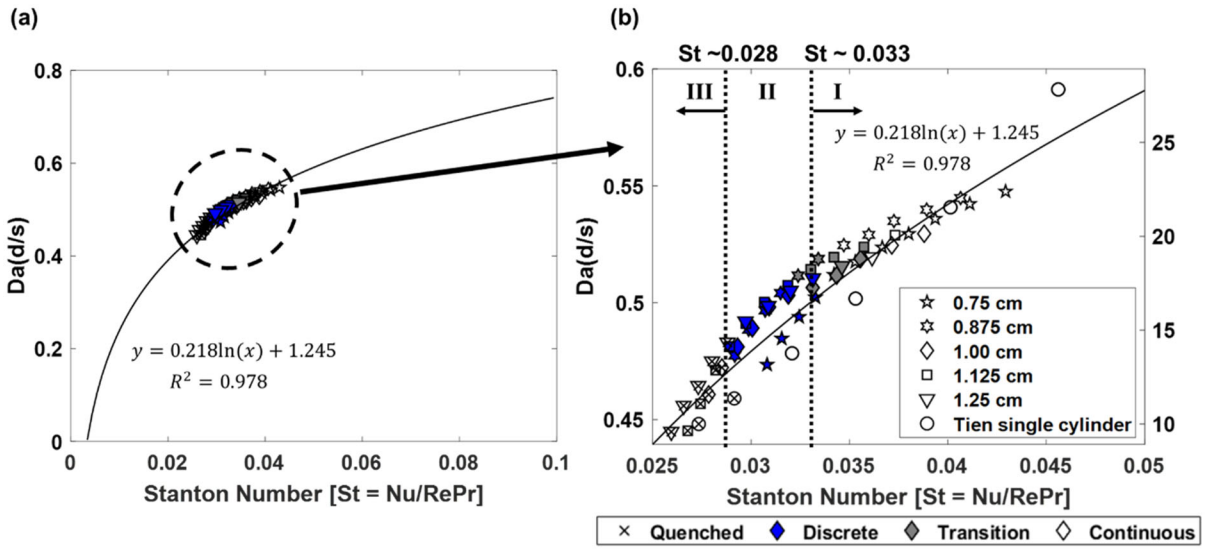


Figure 50. St vs. Da(d/s) plot comparing the experimental data to a logarithmic regression (a) and zoomed-in plot (b) showing flow-spacing conditions in detail of the current study and from the single cylinder Yang and Tien study that uses the right y-axis (Yang and T'ien 1998).

The flow-spacing conditions used in this study collapse reasonably onto a fitted logarithmic regression line (Figure 50a). *Da(d/s)* decreases as either flow speed increases or spacing increases. Thus, quenching could occur at low enough *Da(d/s)* values. It seems that *Da(d/s)* approaches an asymptote as *St* increases. At lower wind speeds, mixing would generally be weak and not sensitive to the flow speed. By manually inspecting flame images, it was observed that there is less fluctuation of the flame, which indicated less mixing as flow speed decreases. Since flow speed decreases as *St* increases, the mixing or *Da(d/s)* becomes less sensitive to the flow speed. Also, when the spacing becomes small enough, the discrete solid fuel array would behave like a continuous fuel. Thus, the flame propagation behavior also becomes less sensitive to the flow as the spacing decreases, especially when *St* is higher.

The boundaries of the onset of both discrete flames (regime II) and flame spread quenching (regime III) are reasonably well captured by *St* (Figure 50b). A lower *St* corresponds to faster flow speeds and ultimately flame quenching due to insufficient heat delivered to the next unignited dowel. For the current experiments, *St* below 0.028 and over 0.033 correspond to the quenching regime (III) and the continuous regime (I), respectively. For a comparison, numerical data of a single PMMA cylinder in crossflow by Yang and T'ien (1998) is shown alongside the experimental data. The flame blowoff conditions found by (Yang and T'ien 1998) agree with the *St* threshold for quenching of the current experiments. As *St* increases, between approximately *St* values of 0.028 and 0.033, the convective cooling effects decrease such that propagation is sustained but in a discrete regime (II). When *St* is greater than 0.033, the flow is slow enough that flame propagation is in the continuous regime (I). Further experiments are needed to validate the applicability of the shown regression at both larger and smaller *St* values.

Conclusions and Implications for Future Research/Implications

Three fire spread behavior regimes were identified for a fuel array under a range of flow and element spacing conditions. These regimes correspond to how each individual flaming dowel contributes to the overall flame spread, whether the flame is continuous (regime I), discretized (regime II) about each dowel, or propagation is unsustained (regime III). The flame shapes within the propagating regimes showed how initially the upstream flame extends past the downstream cylinder. As the flow speed is increased, the flame begins to encroach and lie in the inter-cylinder region. The ignition location also shifts from directly in the wake where the mixing time is longest due to slower flow speed to the flow separation points along the cylinder where the surface temperature is higher. The front view showed how the overall flame shape changes and the contact area is reduced with increasing flow speed. The analysis of the time scales, fluid dynamics, and heat transfer revealed a correlation between the Stanton number and Damkohler number. The correlation exhibits a threshold that corresponds to the onset of the three flame spread regimes. Further work is required to fill in the gaps and solidify the assumed boundaries of the flame spread map (Figure 48). Additionally, the scaling of the flow regimes for other dowel diameters and orientations needs to be explored. However, this study suggests that assumptions of continuous increase in flame contact or convective heat transfer with increasing free stream flow should be adjusted if the flow and fuel setting lead to a discretized flame behavior.

Pine needle fuel mass and bulk density

Objective

The wind tunnel discussed here was designed to conduct experimental campaigns alongside field experiments of similar composition. The wind tunnel serves as the keystone between the smaller bench-top scale experiments and the 10 m x 10 m field experiments. That is experiments of fire spread along forest litter vegetation and primarily pine needle fuel beds. Additionally, the two testing approaches (field and laboratory) would coalesce with the wind tunnel's portability, allowing for the use of a controlled, steady freestream flow for field experiments. In this section, the large-scale experiments conducted in the wind tunnel are exhibited. These experiments will eventually inform a comprehensive database for future researchers to compare against model predictions.

Background

The increasing severity and risk induced by wildland fires recently have further emphasized the need for improved operational scale, field deployable, fire spread models in order to mitigate the risk posed to wildland-urban interface (WUI) communities as well as fire managers and rescue personnel. Wildland fire spread prediction poses a multi-dimensional problem due to the variability in fuel characteristics and interactions with important meteorological and ambient variables. Current predictive models used to simulate fire behavior are to some extent based on data collected during low-intensity prescribed fires (Cruz et al. 2017; Finney et al. 2013; Sullivan 2009). To this end, the models are empirically based and fail to adequately predict fire outcomes. Although there have been improvements to predictive models, including the use of computational fluid dynamics (CFD), empirical relationships within modern wildland fire spread models are still in use. One such variable which has a large impact on the fire spread behavior is the wind.

Early work approximated the wind as a forcing agent which increased the flame angle, driving the flame plume closer to the ground and increasing heat transfer (Albini 1981; Rothermel 1972). Wind tunnels provide a steady, controllable source of wind and are a powerful tool for fire researchers to study the effects of wind (Catchpole et al. 1998; McAllister and Finney 2016; Sullivan et al. 2013; Sullivan et al. 2018; Weise and Biging 1994). Wind tunnel experiments have shown that the effects of wind are still largely underestimated. Furthermore, convective effects play a significant role in not only fire front propagation (Catchpole et al. 1998; Finney et al. 2015), but ember and firebrand dispersal (Koo et al. 2010), as well as fire whirl formation (Finney et al. 2015). Despite the findings, a disconnect still exists between most wind tunnel research and wildland fire dynamics due to the use of idealized fuels, such as wooden cribs or excelsior. Although these simplified fuels help identify convective effects on fire spread and flame behavior, ultimately more experiments are needed.

The experiments presented here are designed as a step to link laboratory and field experiments. As field experiments begin to adopt more precise and accurate instrumentation, it becomes paramount to establish how results from each domain (laboratory and field) translate to the other. The wind tunnel allows for experiments at a relatively large scale to be conducted in the laboratory mimicking the vegetation and fuel package utilized in the field. In addition, the instrumentation used is similar such that measurement can be directly compared between the two domains. Furthermore, the wind tunnel is designed to be portable.

Materials and methods

In the three years that the wind tunnel has been operational (since 2018), a comprehensive set of experimental campaigns has been carried out. Figure 51 shows a sampling of these experiments; small-scale fire spread along suspended dowel arrays (Figure 51 left), forest surface (litter) fuels fire spread along pine needle layers (Figure 51 center), and shrubbery (Figure 51 right). Results of these experiments have found unique flame behaviors in discrete fuel arrays (Di Cristina et al. 2021) and will contribute to an overall experimental campaign combining field and laboratory experiments (Clark et al. 2020). The limitations to experimental setups are determined mainly by the physical dimensions of the test section and safety constraints by the

extraction hood in the laboratory. However, it has been successfully demonstrated that the wind tunnel is capable of experiments at wide-ranging scales.



Figure 51. Fire spread experiments conducted in the wind tunnel from left to right; suspended dowel array, pine needle litter layers, and shrub fire.

However, the initial primary mission was to study wind-driven fire spread along pine needle beds. These experiments are in conjunction with studies conducted in situ (Clark et al. 2020; Mueller et al. 2017; Mueller et al. 2021). As such, testing matrix parameters represent fuel conditions (fuel loading and bulk density) and wind speeds encountered in the field. Parts of the studies examined how changes in fuel compaction, represented by higher bulk densities, altered the flame spread and fuel consumption.

Wind tunnel design

Conventional wind tunnels use a variety of techniques and devices to achieve the desired flow characteristics. Generally, fans or blowers produce highly turbulent and variable flows. In order to transform the flow from the fans, the geometry of the wind tunnel itself is utilized. A typical wind tunnel may be comprised of a diffuser or diverging section, a settling or straightening portion, followed by a contracting section (Cattafesta et al. 2010; Mehta and Bradshaw 1979). The diffuser slows down the flow from the fans and distributes the energy contained within the flow over a larger volume. The settling or straightening section typically contains screens and honeycombs to further align the turbulent flow along the streamwise direction and diminish fluctuations in the other directions. Finally, the contracting section accelerates the flow while keeping the turbulence and fluctuations to a minimum (Comte-Bellot and Corrsin 1966). The contracting section then connects to the test section such that the flow exiting the contraction is at the desired state.

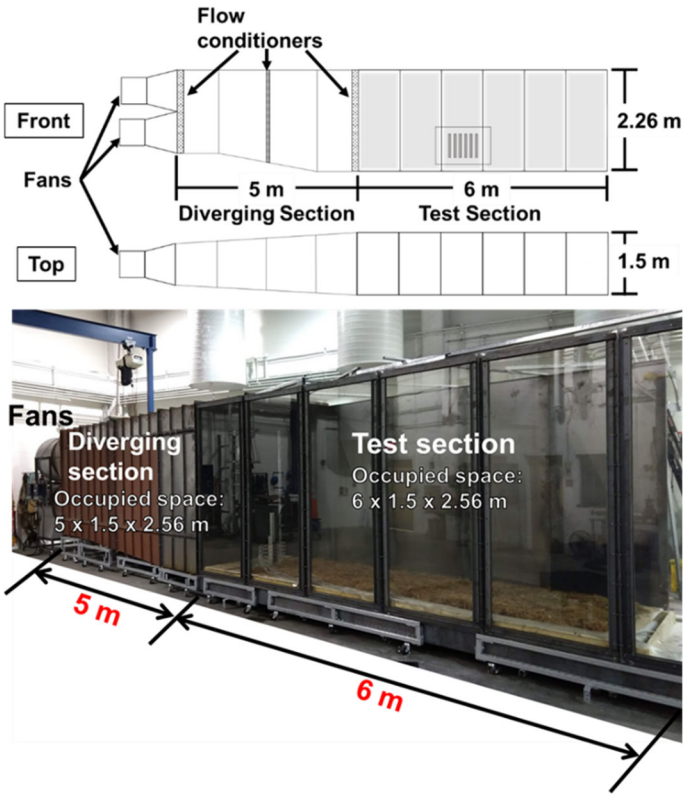


Figure 52. Wind tunnel schematic (top) and image (bottom).

A diagram of the wind tunnel is shown in Figure 52. Three main sections comprise the wind tunnel: the fan assembly, diverging section, and test section. Conspicuously, there is no converging section. The main objective of the wind tunnel is to link laboratory experiments to in situ wildland fire experiments conducted in the field. Specifically, the tunnel was formulated to be portable. However, the tunnel must also fit within the physical confines of a laboratory. The laboratory building which would house the wind tunnel constrained the total length. Therefore, to maximize the cross-sectional flow area and limit the size both for portability and laboratory space, a contracting section was omitted.

Diverging section and fans

The fans and proceeding diffuser together are approximately 1 m long. Composed of two Cincinnati Fans, they are each rated to provide a flow rate of 5.55 m^3/s at 1770 revolutions per minute. At the rated flow rate, each fan can sustain a static pressure of approximately 600 Pa. Following the fan assembly, is the main body of the wind tunnel, the diverging section. A total of 5 m long, the diverging section is composed of four sub-divisions that further break down into top, bottom, and wall pieces. A representative drawing of one of the sub-divisions is shown in Figure 53. The tunnel width at the inlet of the diverging section at the fans is 1 m and expands throughout the diverging section to a total width of 1.5 m at the entrance to the test section. The resulting lateral expansion angle is approximately 2.9°. The height of the tunnel also expands but asymmetrically. The top of the diverging section remains flat, with the second and third sub-divisions expanding downward 10 cm each such that the total height of the tunnel expands from 2.06 m at the fans to 2.26 m at the test section. The expansion can be seen in Figure 52.

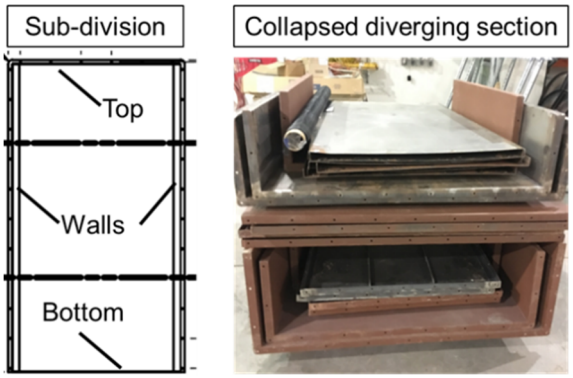


Figure 53. Diverging section sub-division (left) with cut lines shown for each piece. On the right is the entire diverging section broken down onto a shipping pallet.

As the wind tunnel walls diverge, an adverse pressure gradient is created (Schlichting et al. 1955). The adverse pressure gradient and the omission of a contracting section could result in boundary layer separation and non-uniform flow across the exit of the diverging section. A mix of honeycomb panels, mesh screens, and perforated metal plates were placed throughout the diverging section to remedy the non-uniformities in the flow. These flow conditioners are a common tool to enhance the flow of test sections. Honeycomb panels function as flow straighteners, forcing the flow through small channels which reduce the flow swirl and turbulence in the lateral directions. The mesh screens and perforated plates serve to impose a pressure drop proportional to the flow speed, creating a more uniform flow profile. Screens and to a lesser extent honeycombs reduce the turbulence by breaking the large-scale turbulent eddies into smaller eddies that decay faster (Cattafesta et al. 2010; Mehta and Bradshaw 1979)

Test section

Attaching to the end of the diverging section, the test section features a constant cross-sectional flow area of 2.26 m x 1.5 m at a length of up to 6 m. The test section is composed of wall, window, and roof panels and features an 8 cm deep fuel pan along with a removable floor and platform that is flush with the diverging section exit. The walls of the test section are composed of a mix of blank metal panels and window panels. Figure 54 shows the standard configuration of the test section, with one side composed of all window panels. However, the panels are interchangeable. If optical access is required from both sides, the test section can be assembled such that windows are on either wall. The viewing area on each window is 2.16 m x 0.88 m. Due to the high-intensity heating that the windows are exposed to, traditional glass could not be utilized. Instead, the windows of the test section were fitted with FireLite glass ceramic. The glass ceramic is rated to withstand direct flame contact for up to 60 minutes and can withstand direct impact from a fire hose if one is needed for extinguishing an experiment. Furthermore, the glass ceramic is rated at 88% visible transmission facilitating access of optical diagnostics.

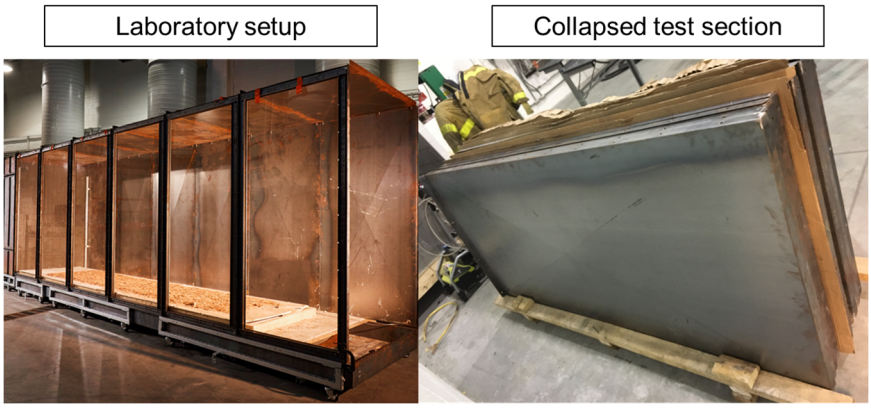


Figure 54. Test section in the laboratory (left) and collapsed onto a custom shipping pallet (right).

As with the diverging section, the test section also breaks down. The window and wall panels fit on a custom-made pallet for shipping to field experiments. Figure 54 shows a close-up of the test section assembled for laboratory testing (left) and collapsed for shipping (right). The fuel pans are designed for laboratory use only, as the bottom of the wall and window panels would be flush with the ground. The entire wind tunnel, from the fans to the test section, sits on stands with wheels. The stands allow for the movement of the wind tunnel within the laboratory space.

Experimental setup

The instrumentation and experimental setup used for these studies are shown in Figure 55. The measurements and instrumentation are designed to facilitate direct comparisons with field data. Mimicking field instrumentation is key to furthering the main goal of the wind tunnel, to study the effects of scaling on fire behavior and fire spread results. The pine needles were laid uniformly on gypsum panels. This allowed for a non-flammable surface that was reusable between tests. To ensure uniformity of the fuel distribution, the pine needles were disbursed on grids along the testbed. The testbed measured 1 m wide by 5 m in length, and fuel was placed on 1 m^2 squares. Measurements of the fuel height (d) were taken throughout the bed once all the fuel was placed. Embedded within the fuel were thermocouples (K type, 0.5-mm wire size). In the first half, the thermocouples were placed at the fuel layer base and surface, while the second half featured additional thermocouples embedded at the mid-height. Additionally, the second half of the testbed was on a load cell to measure mass loss. Heat flux gauge pairs (total and radiative) on the fuel surface measure the heat delivered to the fuel from the flame.

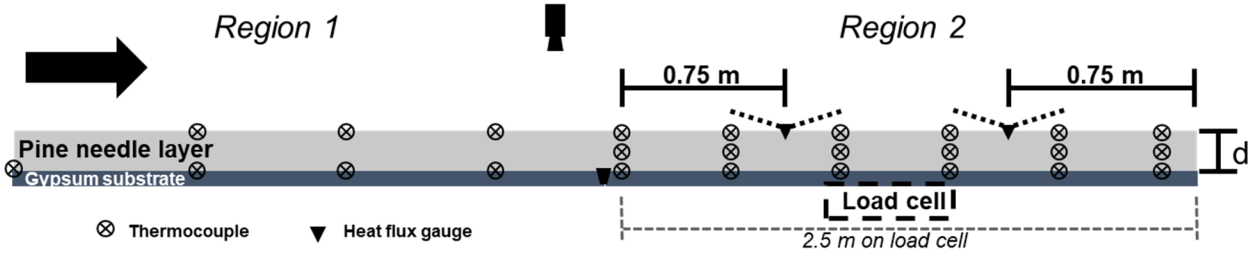


Figure 55. Experimental setup from a pine needle fire spread campaign. Instrumentation was mainly thermocouples embedded within the fuel package, and heat flux gauges on the fuel layer surface. A load cell was installed in the back half of the setup.

Figure 56 shows images of the setup with the pine needle fuel package (left) and without. In the images can be seen the heat flux gauges, load cell location beneath the gypsum board substrate, and the thermocouples before placement within the fuel. Ignition was achieved by laying some isopropyl alcohol at the leading edge of the testbed and remotely triggering an electrical spark. The flame spread was recorded with cameras placed on the side (Sony DXIII, 60 fps) looking through the test section windows and from above (GoPro Hero 5, 60 fps).

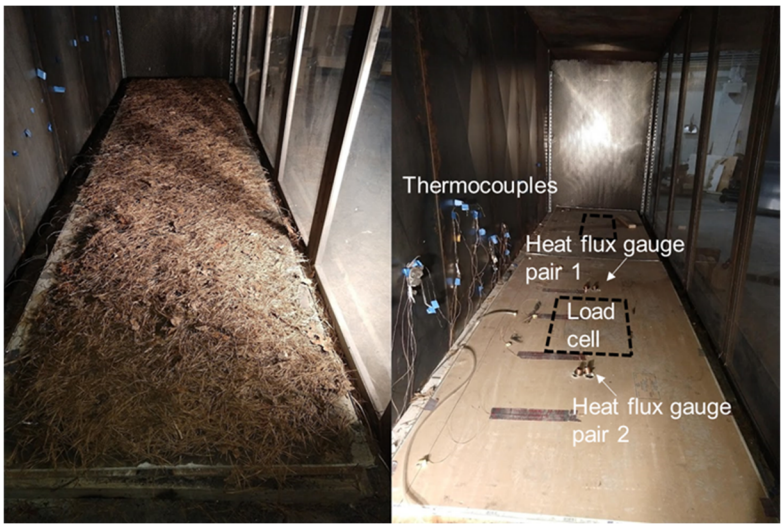


Figure 56. A pine needle litter layer ready for ignition (left). The experimental platform showing the instrumentation embedded within the pine needle fuel package (right).

Results and discussion

Due to the wide range of test conditions conducted in the field, the fuel loadings tested range from 0.5 kg/m^2 to 1.5 kg/m^2. The full list of fuel conditions tested is shown in

Table 7. For a subset of the fuel conditions, the bulk density was modulated in order to examine the effects of fuel porosity on the fire spread. Flow speeds reflect input from the field researchers and generally are a baseline no flow, low, and high wind speeds. The fuel consumption measured as a percent of the fuel mass remaining was observed to be independent of fuel amount, but sensitive to bulk density. For higher bulk densities, the fuel is more compactly packed hindering the amount of fresh air available for the combustion reaction. However, flow speed accelerated the flame spread. Because of the acceleration in fuel consumption, mass loss rates were observed to increase as flow speed was increased. Similarly, the peak total heat flux

Snapshots from the top-view camera are featured in Figure 57. The data and images are from pine needle fuel beds at a fuel loading and bulk density of 0.8 kg/m^2 and 60 kg/m^3, respectively. On the left are plots of the mass loss and total heat flux, the two heat flux plots correspond to positions 1 and 2 in Figure 56, which are separated by 0.75 m. The top-view snapshots on the right correspond to when the flame front reaches the first heat flux gauge position, the same time is indicated by the vertical dotted line on the plots. The mass loss data has been normalized by the initial mass, and overall, the wind speed does not change the fuel percent consumed. However, the mass-loss rate increases drastically with flow speed, as can be noted by the time axis on each plot. From the images, the changes in flame behavior are apparent. As the flow speed increases, the flame front takes a pronounced curvature. Due to the faster flame spread at faster flow speeds, the smoldering region behind each flame front is more prominent. In some cases, such as the 3 m/s, the region shown behind the flame front is still flaming. Peak heat fluxes observed were on the order of 20 kW/m^2 irrespective of the flow speed.

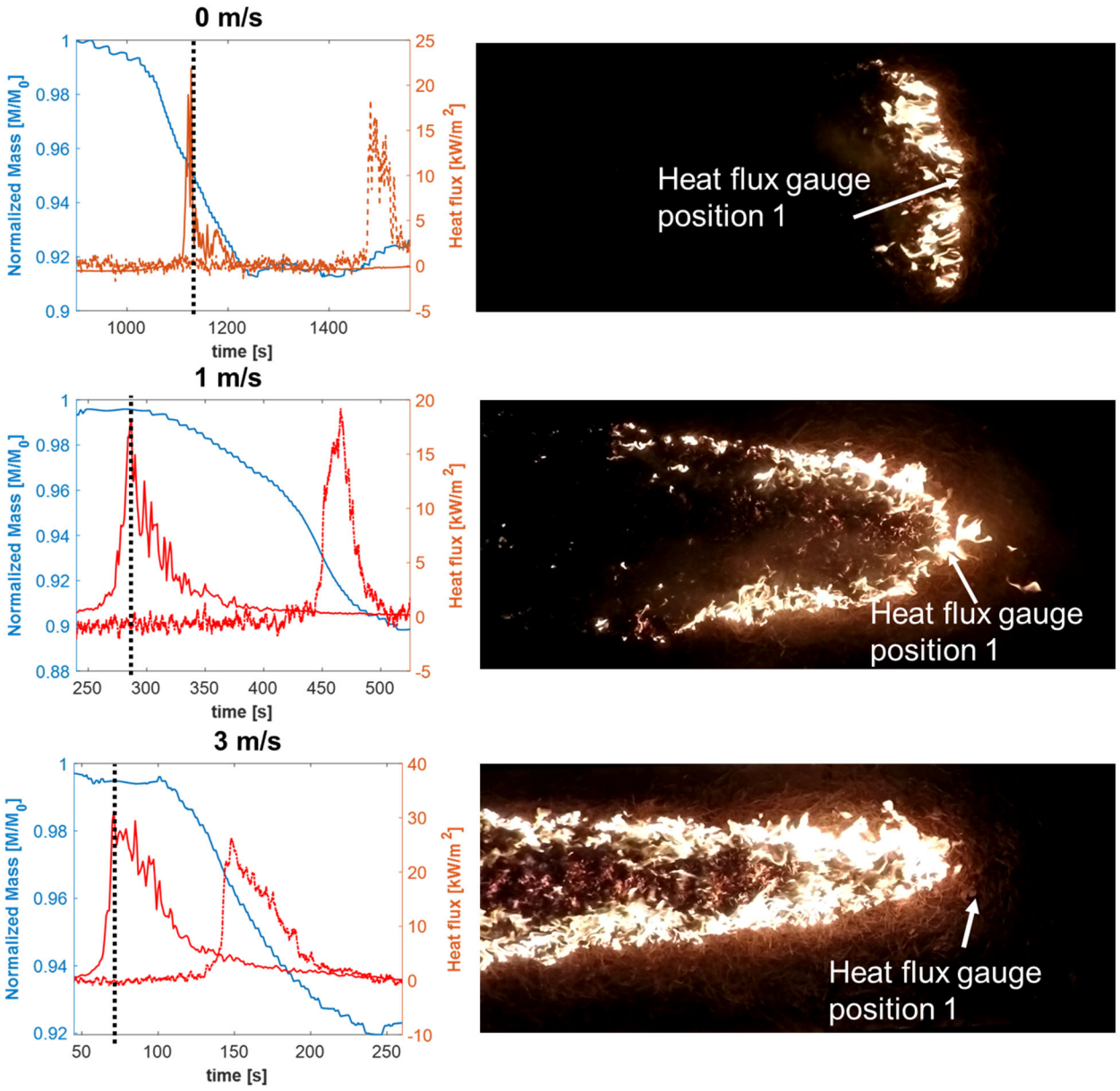


Figure 57. Mass loss (blue) and total heat flux (red) plots for pine needle layer fuel beds at a loading and bulk density of 0.8 kg/m^2 and 60 kg/m^3, respectively. The images on the right correspond to snapshots at the black dotted lines.

The heat flux, mass loss, and mass rate results for other fuel conditions are summarized in

Table 7. Changes in the bulk density (porosity) are found to affect mass consumption, rather than flow speed or fuel loading. The higher compaction (lower porosity) shows lower mass consumption as less oxygen penetrates the fuel matrix, limiting the depth at which flaming reaction can occur. This is confirmed by preliminary measurements from O_2 sampling at the base of the fuel matrix. For a 0.8 kg/m^2 fuel load subject to 1 m/s flow, the O_2 measured at flame front passage dropped from 16% for a 40 kg/m^3 bulk density to 12% for the 60 kg/m^3 case.

Table 7: Results summary.

Fuel Loading [kg/m^2]	Bulk Density [kg/m^3]	Flow speed [m/s]	Mass Remaining	Peak MLR [g/s]	Peak Heat Flux [kW/m^2]	Spread Rate [mm/s]
0.5	40	0	88%	2.8	20	2.1
		1	87%	6.4	22	14.9
		4	90%	7.6	49	42.2
0.8	40	0	72%	2.5	25	2.4
		1	70%	6.5	22	6.8
		3	62%	10	50	19.5
	60	0	91%	1.2	20	2.1
		1	90%	2	19	4.3
		3	92%	1.5	30	9.8
1	40	0	85%	3.85	25	3.0
		1	87%	6.2	31	18.9
		4	77%	7.9	41	48.5
1.2	40	0	76%	2.5	25	2.6
		1	71%	5	25	6.9
		3	70%	10	–	14.2
	60	0	85%	1	15	2.5
		1	90%	1.5	20	5.6
		3	87%	3	30	12.3
1.5	40	0	82%	4.75	27	3.1
		1	80%	7.5	38	30.0
		4	79%	17	42	43.5

Although the fuel consumed appears to be largely insensitive to flow speed, the mass-loss rate (MLR) drastically increases due to the same amount of fuel being consumed on a shorter time interval. The increased MLR is coupled with increases in heat transfer as evidenced by the higher heat fluxes at faster flow speeds. The increased heat transfer then results in a faster flame spread.

The temperature results are shown in Figure 58 and Figure 59. Peak temperatures were around 600 C, recorded on the surface. Additionally, changes in fuel loading or bulk density did not affect the temperature results significantly. However, the changing flow speeds widen or narrow the length of time that high temperatures were observed. Figure 58 shows the fuel surface measurements for the different bulk densities and flow speeds tested, with 0.8 kg/m^2 fuel loading on the left and 1.2 kg/m^2 on the right.

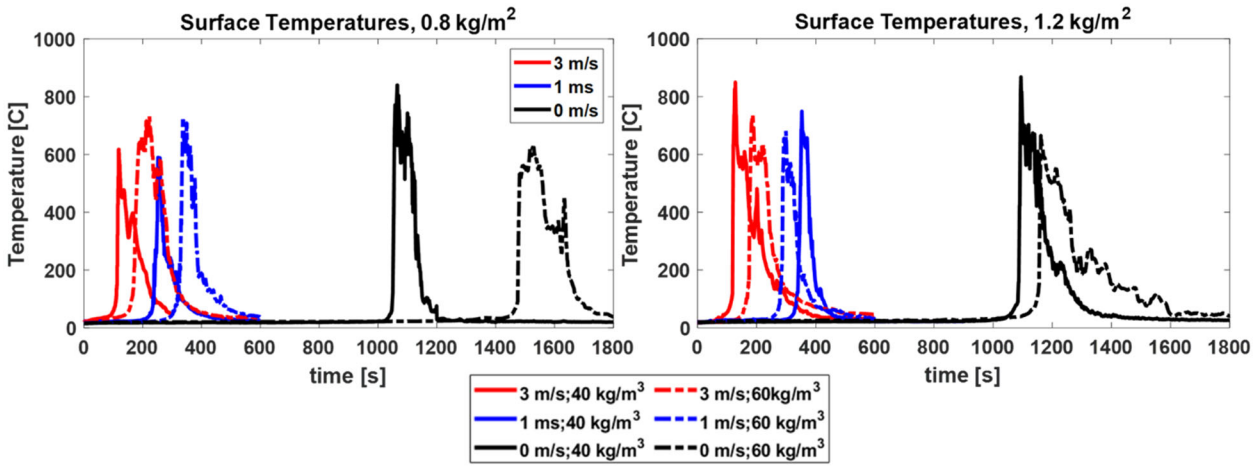


Figure 58: Temperature results from the fuel surface thermocouple. The solid lines show the 40 kg/m^3 and dashed are the 60 kg/m^3 bulk density.

The temperature penetration can be seen in Figure 59, from measurements taken by the embedded thermocouples at the top, middle, and base of the fuel matrix. A substantial decrease in peak temperatures is observed deeper into the fuel, with the base temperatures reading approximately 30% lower than the surface. The middle thermocouple measurements resemble the surface readings shifted by some time delay. The lag corresponds to the time it takes the flames to penetrate deeper into the fuel matrix.

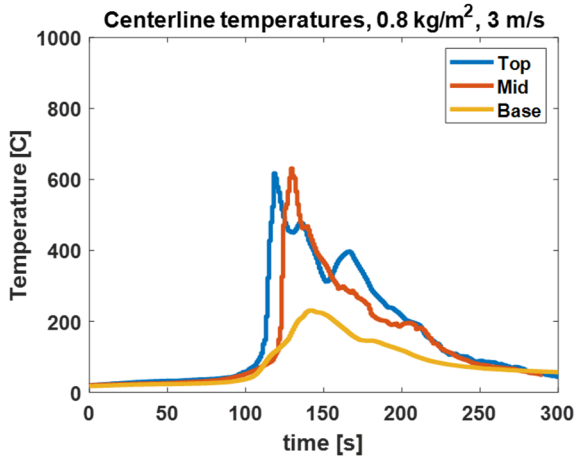


Figure 59. Temperature results for the embedded thermocouples at the top, middle, and base of the fuel. Results shown are for a 0.8 kg/m2 fuel loading subject to a flow speed of 3 m/s.

Conclusions and Implications for future research

The results from pine needle flame spread experiments are presented. These results serve as the basis of a larger study examining the effect of scale across wildland fire experiments conducted in the laboratory and field. The current instrumentation and measurement suite can collect heat flux, temperature, and mass data. In addition, dedicated cameras capture the flame spread and allow for comparison of the other data against flame images. The parametric nature of the experiments builds an excellent database for the validation of fire spread simulations. Thus

far, the wind tunnel has proven an asset in wildland fire research, and the experimental results presented here validate the full capabilities of the wind tunnel.

Small - scale field investigations

Objectives

Our understanding of combustion processes and fire behavior during prescribed fires is derived primarily from measurements made at two separate scales: small-scale laboratory experiments and large-scale experimental and operational prescribed burns. To provide a better understanding of combustion processes and fire behavior across spatial scales, we designed and conducted a series of intensively instrumented experiments on replicated 100 m^2 plots, contrasting cool, dormant season vs. warm, growing season conditions, and natural vs. augmented fuel loads. Through making comprehensive, spatially explicit quantifications of critical properties of the fire's physics domain (e.g. fuels and ambient conditions) and processes associated with combustion (e.g. heat transfer, flame propagation, flow) during these outdoor experiments, we were able to link observed patterns and processes to those observed in other modules of this project, which were focused on indoor and outdoor fire experimentation at both smaller and larger scales.

Instrumentation consisted of a network of IR cameras to measure flame arrival times, intensity, and radiative heat fluxes, dense arrays of thermocouples to measure gas temperatures, sonic anemometers to measure turbulence and convective heat fluxes at multiple heights above the flame fronts, and high-speed pressure sensors. Fuel loading, moisture contents, and consumption were estimated from a combination of LiDAR and harvest measurements.

Background

Our understanding of combustion processes and fire behavior during prescribed fires in pine-dominated and pine-oak ecosystems is derived primarily from measurements made at two separate scales; small-scale laboratory experiments (Campbell-Lochrie et al. 2021; El Houssami et al. 2018; El Houssami et al. 2016) and large-scale operational prescribed fires (Clark et al. 2020; Heilman et al. 2017; Mueller et al. 2017; Mueller et al. 2021). Synthesis and integration of experimental results across scales using physics-based fire behavior models have highlighted the benefits and limitations of both approaches and have revealed several uncertainties that remain to be resolved (Mueller et al. 2021). At the smallest scale, burn table experiments in the laboratory have quantified key processes controlling flammability and fire propagation across fuel beds under well-controlled conditions. However, important factors such as variability in ambient weather conditions, spatial variation in fuel loading, arrangement and moisture contents, or interactive processes influencing fire-induced turbulence and heat transfer cannot be addressed adequately at this scale.

At the scale of operational prescribed burns, surface and tower-based measurements across a range of fire intensities have quantified ambient and fire-induced effects on turbulence and heat fluxes and how these in turn affect overall fire behavior, fuel consumption and ember production (Clark et al. 2020; Heilman et al. 2017; Heilman et al. 2015; Mueller et al. 2017). These efforts have quantified patterns of fire-induced circulation within and above the canopy, and have documented greater enhancement of horizontal turbulence than vertical components associated with buoyant plumes, and the occurrence of horizontal inflow and downdrafts of cooler air behind flame fronts during more intense fires, typically with some torching behavior, but less frequently during low intensity fires. However, while measurements made during large-scale

operational burns can be used to evaluate the overall performance of fire behavior models, they typically integrate so many complex phenomena that disentangling the underlying relationships controlling fire behavior is nearly impossible, limiting their utility. In addition, while these experiments have quantified turbulence and heat fluxes in the fire environment simultaneously (Heilman et al. 2017; Heilman et al. 2015; Mueller et al. 2017; Mueller et al. 2018), fuel consumption measurements were relatively coarse in scale, and the majority of large-scale experiments are limited by a lack of comprehensive fine-scale fire behavior measurements.

Important questions that have evolved during prior investigations include which key relationships or phenomena occur consistently across scales? Or do "emergent behaviors" occur at the larger scale that that may not occur or at least are undetected at smaller scales? As an example, is the influx of cool air from aloft flowing into the backs of passing flame fronts that has been observed during more intense flanking and head fires, but not during relatively low intensity backing fires, related to enhanced rates of spread that occurs as pulses, or to transitions from surface to crown fires? Understanding when and under what conditions more intense fires set up larger-scale circulations is critical to accurately predicting fire behavior. A second important issue revolves around our ability to synthesize and predict fire propagation during prescribed fires. This has been a major limitation of empirically-based models, which are unable to adequately represent the complex ignitions standardly used during prescribed burning or backing and flanking fire progression types that dominate prescribed burns. While enabling these capabilities represents one of the important benefits of physics-based fire behavior models (e.g., WFDS, FIRETEC, and QUIC-Fire), their use for prescribed fire planning remains limited by a need for greater model validation and the availability of data to initialize, parameterize and evaluate model simulations.

Here we describe a series of highly instrumented, intermediate-scale experiments conducted on 100 m^2 plots at the Silas Little Experimental Forest, New Lisbon, New Jersey. Experiments were designed to investigate how contrasting fuel conditions (e.g. fuel load, particle type, bulk density), fire spread type (e.g. heading vs. backing), and ambient conditions (e.g. seasonality, moisture, flow, temperature) influenced physical processes associated with combustion (e.g. heat transfer, flame propagation, flow) and the scale-dependent coupling of these processes, and to provide 1) a linkage between small-scale laboratory combustion experiments and large-scale operational prescribed fires, and 2) archived datasets for further model development and evaluation. Our experimental design incorporates complementary approaches, methods, and instrumentation employed at these other scales, to quantify critical properties of the experimental fires' physics domains (e.g. fuels and ambient conditions) and processes associated with combustion (e.g. heat transfer, flame propagation, flow). Our experiments were conducted between March of 2018 and September of 2019 under a mix of dormant and growing season conditions.

Materials and methods

Site description

Small-scale field experiments were conducted at the United States Department of Agriculture Forest Service Northern Research Station Silas Little Experimental Forest, located in New Lisbon, NJ at approximately 39.917740 north latitude -74.596422 west longitude within the New

Jersey Pinelands National Reserve (Figure 60). The Pinelands National Reserve occupies approximately 380,000 ha in southern New Jersey and is predominantly occupied by pure pitch pine forests (*Pinus rigida* Mill.) or mixed oak (*Quercus spp.*) and pine forests with a pitch pine component. Pine and oak forests in the Pinelands are compositionally similar to other pine and oak forests of the Atlantic Coastal Plain such as those comprised of *Pinus taeda,* loblolly pine. This range is also home to multiple Department of Defense installations (e.g. Warren Grove, NJ; Camp Edwards, Massachusetts; Eglin Airforce Base, Florida) where prescribed burning for safety and ecological reasons (e.g. heterogeneity, threatened and endangered species and ecosystems) is recognized as a key forest management need. The experimental area used at the Silas Little Experimental Forest was a 5-acre plantation containing mature *Pinus rigida*, and *P. taeda* planted in 1971 and 1972 (Little and Trew 1979).

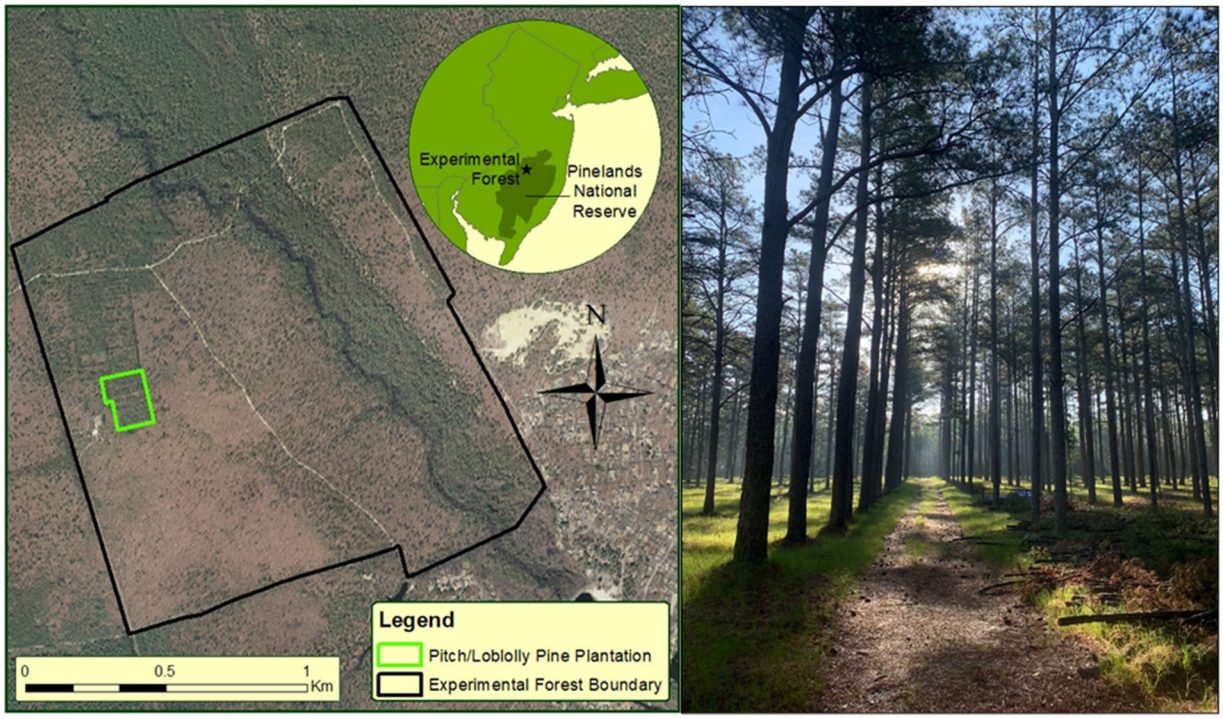


Figure 60. Experiment site in pitch/loblolly pine plantation at the Silas Little Experimental Forest, New Lisbon, NJ.

Experimental design

Experimental burns were conducted in 10 x 10m units delineated within the Experimental Forest's pitch/loblolly pine plantation. A total of 35 burns were conducted between March 2018 and June 2019. Burns 1-10 were conducted in unique units within the plantation, however, burns 11 – 35 were conducted using the same unit repeatedly (this was accomplished by clearing burnt fuel following experiments and refueling the plot for subsequent burns). Plot infrastructure consisting of 4 aluminum trusses suspended by steel tripods outside of the unit to enable instrumentation and wiring of sensor equipment (see *Flow and Temperature Measurements* and *Fire Radiative Power*) where it would be less impactful on fire behavior and fuel conditions. Trusses were oriented east-west and were labeled sequentially as truss "A", "B", "C", or "D",

with “A” being the northern-most truss and “D” being the southern-most truss (Figure 61). Sensor locations were denoted by truss designator (e.g. A-D) and a position number, beginning with “1” in the western side of the plot and ending with “4” at the eastern side of the plot. In addition to the trusses, a portable aluminum tower was located in the center of each burn to support additional instrumentation (see *Fire Spread Rates*). Further, in a limited number of later experiments, additional measurements of 1 - 2 load cells (see *Load Cells*) collected fuel load and consumption data under trusses “B” and “C”, as were fire emissions data at Truss B (see *TACO*). Data were recorded by dataloggers and computers outside of the burns.

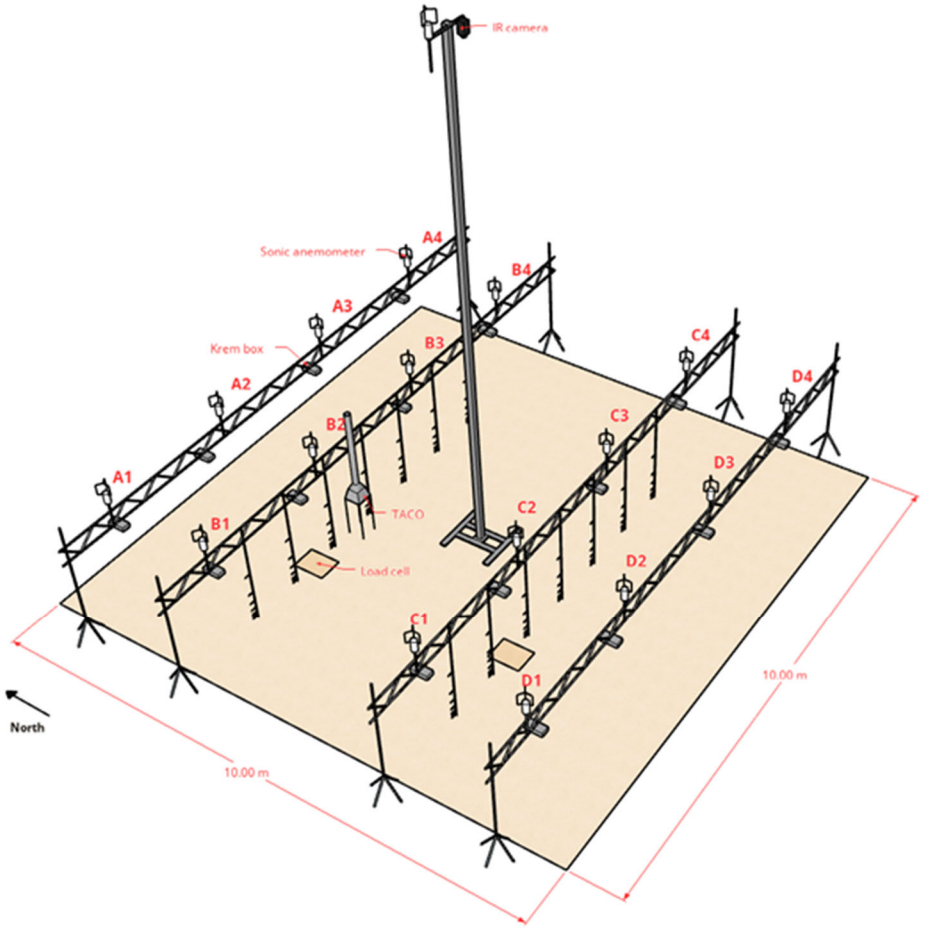


Figure 61. Idealized rendering of equipment locations for 10 x 10m field experiments.

Flow, temperature, and pressure measurements

Sonic anemometers, thermocouples, and high-speed pressure sensors were used to measure spatially explicit flow, temperature, and air pressure variations within and above flame fronts during experiments, as well as ambient conditions prior to experiments. Sensors were deployed in unique locations on the trusses, which were subtly changed for certain groups of experiments in response to the unique research questions posed through the iterative experimentation process of this project.

Sonic anemometers (81000V, R.M. Young Inc.) were mounted on the aluminum trusses at 2.5 to 3.0 m heights (depending on the specific experiment) in a 4 by 4 grid over fuel beds for all experiments (Figure 61 and Figure 62a) except two (Burns 7 and 8 conducted in May 2018), when sonics were mounted only on Trusses B and C at two heights (1.5 m and 3.5 m) to explore fine-scale patterns of vertical turbulence above flame fronts. Sonic anemometers were logged at 10 Hz using CR3000 dataloggers (Campbell Scientific), and pre-fire data were used to quantify ambient wind conditions before and after fire front passage, and turbulence and sensible (convective) heat fluxes above flame fronts during fires.

Thermocouples were deployed as 9-14 vertical arrays on Trusses B and C, with each array consisting of seven K-type thermocouples (KMTXL-IOM25G-150, Omega Engineering Inc., Norwalk, CT) mounted in a vertical profile at 0, 5, 10, 20, 30, 50 and 100 cm heights above fuel beds (Figure 61). For experiments 1-6 conducted in March 2018, four thermocouple arrays mounted on the two center trusses were used, and these were mounted adjacent to each sonic anemometer, for a total of 8 arrays. For experiments 7-36 conducted in May and September 2018 and May 2019, three additional thermocouple arrays were added to each truss, which halved the distance between arrays to 1.5 m, for a total of 14 arrays. Thermocouples were logged at 10 Hz using CR3000 dataloggers, and data were used to estimate arrival times, persistence, and height and tilt of flame fronts.

Air pressure data was collected using Bosch BMP 180/ BMP 280 air pressure sensors collecting at 10 Hz for burns 1-19 to measure fine-temporal resolution variation in atmospheric pressure associated with the passage of fire fronts (Figure 62). Each pressure sensor is associated with a sonic anemometer. The pressure sensor was placed directly below a sonic anemometer in all except for two experiments. For Burns 7 and 8 conducted in May 2018 the pressure sensor was associated with the eight center sonics. And where mounted above the sonics that where mounted at 1.5m and below the sonics mounted at 3.5m (Figure 9). Pressure sensors were logged at 10 Hz using CR6p dataloggers (Campbell Scientific).

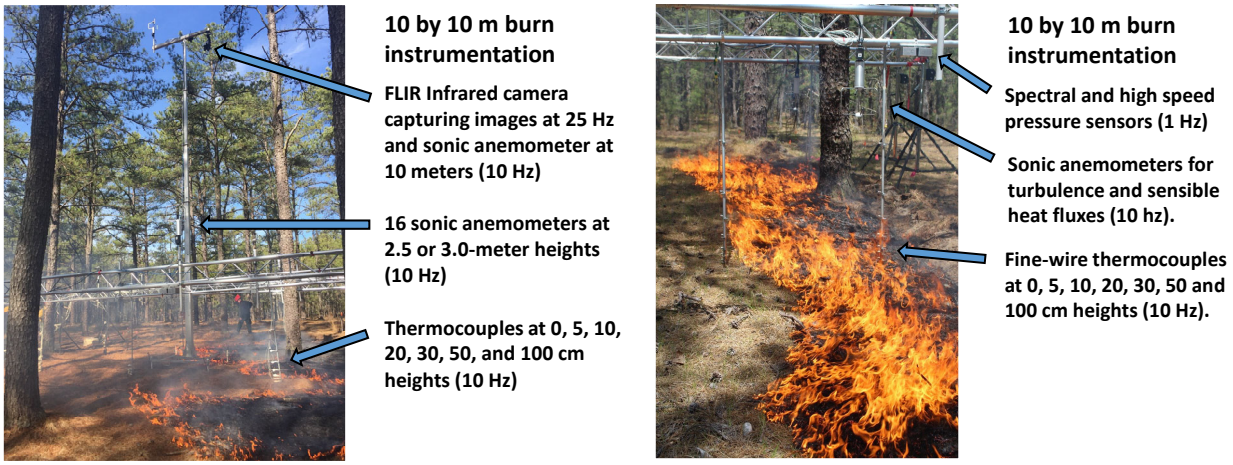


Figure 62. Trusses and instrumentation used to quantify fire behavior during 10 x10- meter burns at Silas Little Experimental Forest. (a) tower mounted IR camera and sonic anemometer, trusses with sonic anemometers, thermocouples, pressure gauges, and spectral sensors/digital cameras. (b) closer view of instruments mounted on a single truss for burns 7 and 8 conducted in May 2018.

Fire spread

Spatially explicit observations of fire spread were created for each burn using an overhead FLIR infrared video-camera (A655SC, FOL6 100.0-650.0 C lens; FLIR Systems Inc., Wilsonville, OR) mounted at a height of 10-meters in the center of the plot on the. The camera recorded data as infrared images at a rate of 25 Hz and were time-stamped using vendor software. From these observations, rate of spread was calculated throughout the fire, as was pixel temperature, pixel residence time, and time to pixel ignition relative to the experiment ignition.

Fire radiative power

Radiometer and visible spectrum camera pairs (Kremens et al. 2012; Kremens et al. 2017) were mounted adjacent to each sonic anemometer at 2-meter height to measure radiative heat fluxes and flame arrival times and persistence (Figure 63). Multispectral radiometers captured data at 1 Hz, and digital cameras at 1 image per second.



Figure 63. Radiometer and visible spectrum camera pair mounted on truss.

Fuel loads and consumption

Remote sensing, complemented by additional physical approaches, were used to characterize fuel load properties of experimental burns. Terrestrial scanning LiDAR (TLS) was used estimate fuel bed depth, loading and consumption, and fine-scale variation in fuel consumption, and fuel moisture contents. Plots were scanned from each of the 4 corners and from a height of approximately 2m before fuels were laid down, after fuels were laid down, and after each burn was conducted using a Faro Focus 3D X330 HRD (Faro Technologies, Lake Mary, FL).



Figure 64. FARO TLS Scanner

For experiments 1-8, pre-existing litter on the plantation floor was used to fuel each experiment. This fuelbed was dominated of pitch and loblolly pine needles, with a minimal component of sedge and fine woody material and was estimated to be 480g/m2 ± 192 (mean ± standard deviation) from random destruction sampling across the plantation. For burns 9-35, plots were fueled with senesced pitch pine or loblolly pine from the plantation or nearby, oak foliage (mix of *Q. alba, montana, and coccinea)*, or as a mix of these foliage types as necessitated by the given experiment. Fuels for burns 9-35 were weighed out pre-fire to fuel burns at the rate of 480g/m2 or multiples of that according to experimental needs.

Fuels were primarily pitch pine needles (88 ± 6% of loading in pine-only experiments) and pine-oak foliage mixes. Target fresh (field) weight loadings averaged 480 g m^{-2} (1x), 960 g m^{-2} (2x), and 1440 g m^{-2} (3x).

Biometric measurements: Field weight of added fuels was measured with a Pesola scale (50 kg maximum weight). Target fuel loadings were then spread evenly over the 10 by 10-meter plots by hand. Dry fuel mass was then corrected using the average fuel moisture content estimated from 5 to 20 subsamples collected immediately before each burn. Fuel moisture samples were stored in separate plastic zip-lock bags and stored in a cooler at the site until

weighed, typically within 24-hours of collection. Samples were then dried at 70 °C and weighed when dry. Post-fire measurements of the remaining uncombusted material was collected in three to five 0.5-m^2 subplots. These were dried at 70 °C, sorted into pine needles, oak leaves when present, stems, and reproductive material, and weighed.

Ignition

Fires were ignited as either a linear backing or head fire, depending upon ambient wind conditions and experiment. A single 10-meter cord was soaked in accelerant, stretched across one end of the 10 x10 m plot, ignited and then dropped on the fuel bed quickly and evenly to produce a linear ignition.



Figure 65. Typical linear ignition using 10 m cord soaked in accelerant

Ambient meteorological conditions

Ambient meteorological variables were measured from 3-, 18- and 20-meter towers surrounding the 100 m^2 plots (Figure 66). Measurements included air temperature and relative humidity (HMP45C, Vaisala Inc., Woburn MA), windspeed and direction (05013, R.M. Young, Traverse City, MA) above canopy and at 2-meter height, and 10-hour fuel moisture (CS505, Campbell Scientific, Logan UT) at 0.3-meter height.

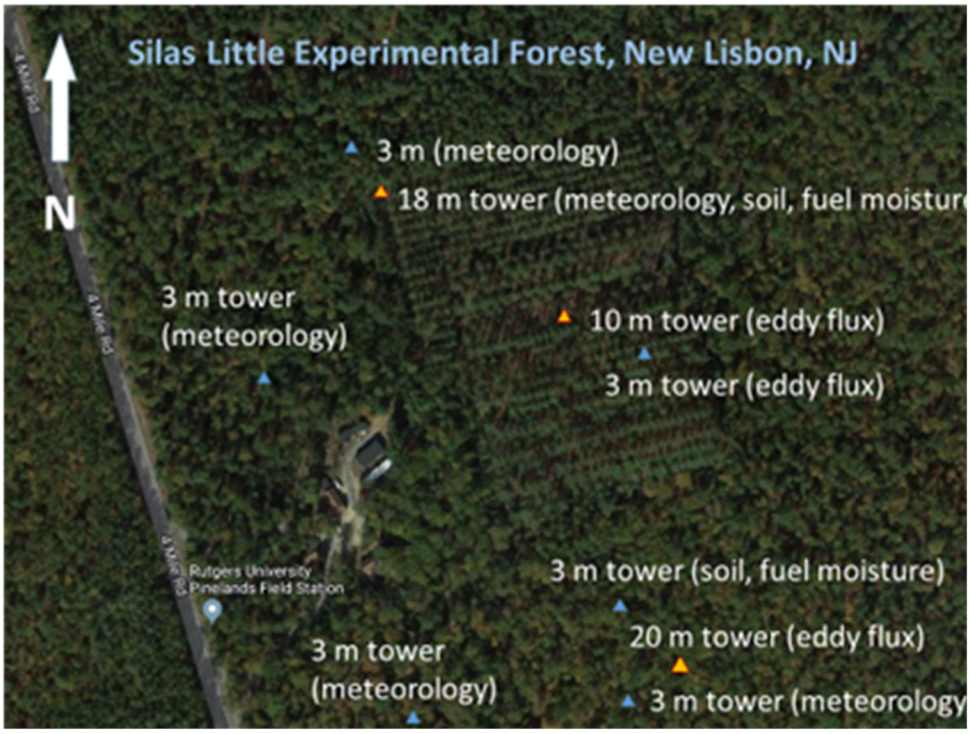


Figure 66. Location of the 10 by 10-meter plots and meteorological towers at the Silas Little Experimental Forest, New Lisbon, New Jersey. The 10-meter and 3-meter towers located near the center of the plot are in the pitch and loblolly pine plantation where all experiments were conducted.

Transportable analyser for calorimetry outside (TACO)

A custom-built field calorimetry hood, the TACO, with an inlet oriented over a portion of the fuel bed was used to sample gas concentrations of O_2, CO_2, and CO in buoyant plumes during experiments conducted during September 2019 and May 2019. TACO measurements were conducted at a single measurement location within the plot. The TACO system consists of an exhaust collection hood and duct, with a gas sample line extracting from the duct. The TACO exhaust duct was altered after Burn 13, so for Burns 8 – 13 the exhaust duct radius was 0.1016 m and for Burns 14 – Burns 35 the duct radius was 0.0508 m.

The exhaust duct pressure difference was measured using a 25 mm diameter bi-directional pressure probe connected to a Sensiron SDP810-125Pa air pressure sensor. The exhaust gas temperature was measured using a 0.25 mm K-Type Thermocouple. Oxygen concentration was measured using an AO2 Citicel oxygen cell, while CO2 and CO concentrations were measured using a Non-Dispersive Infrared Sensor (NDIR) on the Crestline Instruments 7911 Automotive Gas Analyzer (Crestline NDIR 7911, Crestline, Livermore, CA). Flow velocity was measured using a pressure sensor (SDP 810-125, Sensirion AG, Switzerland) and gas temperature was measured using a thermocouple sensor (AD8495, Analog Devices, Wilmington, MA). The data was collected at 1 Hz.

The presented data was subject to the following processing steps. The absolute value of the measured pressure difference in the exhaust duct has been presented, such that it is non-

directional, as the flow channels were unintentionally reversed for some burns. Some negative concentrations are recorded for CO and CO2 since the NDIR analyzer was zeroed at ambient air conditions, and additionally some drifting may occur.



Figure 67. Transportable Analyser for Calorimetry Outside (TACO)

Load cells

Load cells estimated fuel loading and consumption at specific locations in the fire under either Truss B, Truss C, or both, depending on the specific experiment. For experiments 21 – 26 one load cell was under Truss B and C each, for experiments 27 – 35 two load cells were located under Truss B.

Combustion and energy release

Biometric measurements and TLS estimated total fuel consumption, while load cell data collected during burns in September 2018 and May 2019 provided time series of mass loss of fuels during combustion. Biometric measurements of fuel consumption were used to estimate total energy release during fires, while load cell data provided time-resolved estimates of combustion and energy release.

Data processing

Fuels - biometric and TLS measurements:

Biometric measurements of fresh field weights were corrected for initial dry mass using averaged fuel moisture contents measured for each burn. Average consumption for each burn was estimated by subtracting post-burn fuel mass from initial mass.

TLS data were processed using the following methods. Raw Scans were preprocessed using Scene (version 2019.0.1.1653) software. Artificial reference points were detected (Corner points,

Rectangle, Sphere, and Plane), individual scans were manually aligned, and a final aligned point cloud was created for each burn for before fuels were laid down, after fuels were laid down, and for after each burn. Output point clouds were then cropped to the 10x10m extent using Cloudcompare (version 2.9.1) software and converted to Laz files. Finally, X, Y and Z coordinates were rotated and shifted to create 10m x 10m grid with the south west corner of plot representing (0,0,0) using LasTools las2las tool. For each output file the Cloud Compares Cloth Simulator Filter (csf filter) was used to separate the ground points from non-ground points. Then the Volume/Compute 2.5D tool was used to subtract pixel z values for un-fueled point clouds from their respective pre-burn fuel point clouds, and for post-burn point clouds from their respective pre-burn point clouds, to obtain rasters that reflected volumes of pre-burn fuel, post-burn fuel, and volume consumed for each burn.

Flow and temperature measurements:

Raw sonic anemometer data streams collected at 10 Hz captured u, v, and w wind speeds (m s^{-1}), air temperature (°C) and an error code to detect erroneous values. All raw thermocouple and sonic anemometer data are archived. Further data processing of the sonic anemometer data streams to date includes: 1) calculation of average horizontal and vertical wind vectors to relate to fire behavior (fire type and ROS), 2) an evaluation of relationships between horizontal and vertical turbulence and convective heating in buoyant plumes (Heilman et al. 2017, in press, Clark et al. 2019, 2020), an analysis of sweep, ejection and inward and outward interactions (e.g., Heilman et al. in press), and 4) estimation of sensible heat flux from sonic anemometers to explore relationships between fire behavior and convective heat fluxes above flame fronts (e.g., Clark et al. 2020).

Sensible heat flux during fires was calculated using coordinate-rotated vertical wind velocities and sonic air temperature measured at 10 Hz to calculate covariances of turbulence and temperature from 1-minute block averages using $H = \rho_{air} c_p \overline{w'T'}$. We then reported peak, 1-minute values of sensible heat flux (KW m^{-2}) and total sensible heat flux (MJ m^{-2}) during the duration of the fire or when flame fronts are nearby. Flux values approximate convective heat fluxes. Parallel analyses have been conducted on data sets collected during management-scale prescribed fires (e.g., Heilman et al. 2017; Clark et al. 2020).

Thermocouple data were processed to estimate average ROS using a cutoff of 300 °C for arrival times and persistence of flame fronts.

Results and discussion

A total of 35 burns were conducted. 30 burned completely while 6 burns were either very low intensity or fuel beds were too wet for flame fronts to carry and were omitted from further analyses.

Ambient meteorological conditions

Experiments were conducted over a wide range of ambient air temperature and humidity conditions, ranging from 2.3 to 31.3 °C and 22.1 to 89.2 % RH (Table 8). Dormant season burns conducted in March 2018 contrasted with warm, growing season burns in May 2018 and May 2019, which were characterized by higher temperatures but lower windspeeds during most

experiments. Highest RH values occurred during September 2018 experiments, when some of the lowest rate of spreads of flame fronts were observed.

Table 8. Meteorological data collected above canopy (air temperature, RH and windspeed) and at 2.5 to 3.0-meter height above fuel beds during experimental 10 by 10-meter burns.

Date	Air temp °C	RH (%)	Windspeed m sec^{-1}	Peak wind m sec^{-1}
March 2018	6.0 ± 2.1	34.5 ± 8.2	3.3 ± 1.4	8.1 ± 2.8
May 2018	21.6 ± 1.8	46.9 ± 12.1	2.5 ± 0.4	6.5 ± 0.8
September 2018	21.5 ± 1.3	69.5 ± 15.5	1.8 ± 0.3	5.1 ± 1.2
May 2019 pine	23.5 ± 5.7	34.7 ± 5.6	3.3 ± 0.9	7.9 ± 2.1
May 2019 p/oak[1]	23.5 ± 1.4	34.2 ± 18.5	2.0 ± 0.6	4.6 ± 0.6
May 2019 comp[2]	26.3 ± 1.2	64.2 ± 2.1	2.2 ± 0.4	5.5 ± 1.0

[1] Pine/oak mixed fuels; 1:1 ratio

[2] Compressed pine needles at 3x loading

During warm weather burns conducted in May 2018 through May 2019, wind velocities at approximately 2.5 to 3.0 meters directly above fuel beds averaged 1.3 ± 0.3 m s^{-1} and wind gusts averaged 5.4 ± 1.6 m s^{-1} (mean ± 1 SD;

Table 9). Maximum wind gusts were 8.0 m s^{-1} during burn #23 conducted on May 21, 2019.

Table 9. Fuel moisture content, windspeed at the height of sonic anemometers above fuel beds and rate of spread of fire fronts (ROS) for 10 by 10-meter experiments.

Time	FMC	Windspeed	Peak wind	ROS	Peak ROS
	%	m sec^{-1}		cm sec^{-1}	
March 2018	27.1 ± 7.1				
May 2018	11.3 ± 2.0	1.3 ± 0.2	5.2 ± 1.5	4.3 ± 1.1	11.2 ± 3.5
September 2018	13.7 ± 1.6				
May 2019 pine	6.3 ± 1.2	1.4 ± 0.3	6.0 ± 1.6	4.9 ± 1.5	13.4 ± 4.1
May 2019 p/oak[1]	5.9 ± 0.7	1.0 ± 0.0	3.4 ± 0.1	3.4 ± 1.9	7.8 ± 2.3
May 2019 comp.[2]	8.3 ± 1.5	1.2 ± 0.3	5.2 ± 1.7	1.3 ± 1.0	4.7 ± 2.7

[1.] Pine/oak mixed fuels; 1:1 ratio

[2.] Compressed pine needles at 3x loading

Fuels - Biometric and TLS measurements

Fuel moisture content was generally highest during the March 2018 burns when naturally occurring fuels in 10 by 10-meter fuel beds were ignited. Added fuels, initiated during the May 2018 burns, typically had lower moisture contents, and more closely reflected moisture contents of pine needles used during laboratory investigations. Across the range of "natural" fuel loadings (1x ~ 0.5 kg m^{-2}) to augmented fuel loadings (2x ~ 1.0 and 3x ~1.5 kg m^{-2}), fuel consumption estimated from initial pre-burn dry mass was significantly related to pre-burn loading (consumption = 0.871 * initial loading – 114.1; r^2 = 0.909, F = 130.0; Figure 68a). The percent of fuels consumed increased with initial dry mass, and averaged 61.5 ± 23.1%, 74.4 ± 5.9% and 8.5 ± 11.7% at 1x, 2x and 3x fuel loadings, respectively. The relationship between initial fuel loading and mean flame heights estimated from the thermocouple arrays was curvilinear (Figure 68b).

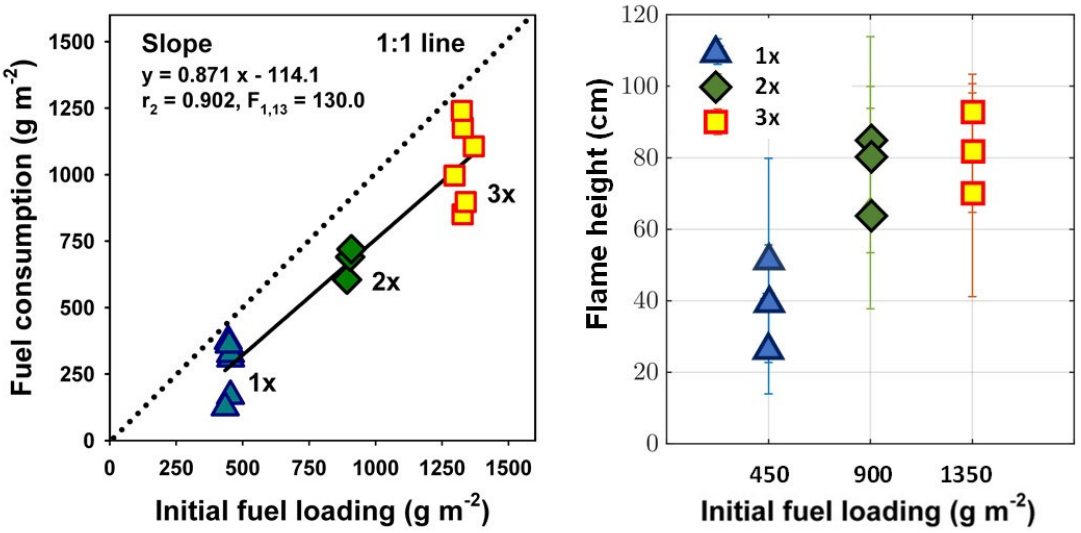


Figure 68. (a) Estimated consumption of fine fuels as a function of initial fuel mass, corrected for moisture content for warm season 10 by 10-meter experiments. Data are from burns 20-36. (b) The relationship between initial fuel loading and mean flame heights was curvilinear (right panel) across experiments at the three fuel loadings (1x, 2x and 3x).

Fuel loading and consumption estimated during 10 by 10-meter experiments encompassed the much of the range of fine surface fuel loading and consumption measured previously during operational prescribed fires conducted by the NJFFS (Figure 69b; Clark et al. 2015, 2020, Gallagher et al. 2017).

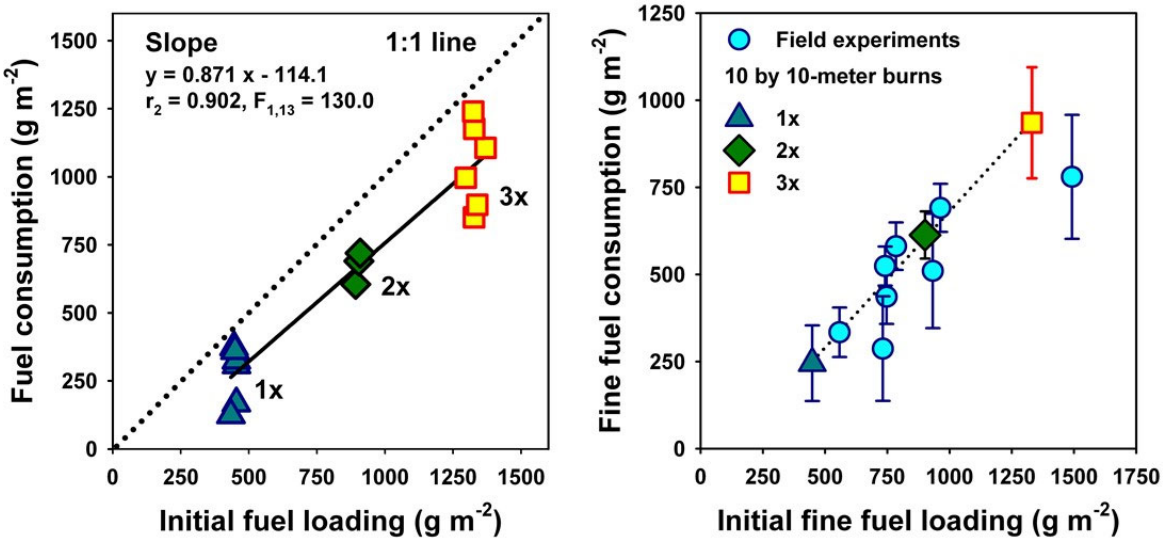


Figure 69. (a) Estimated consumption of fine fuels as a function of initial fuel mass, corrected for moisture content for warm season 10 by 10-meter experiments. Data are from burns 20-36. (b) Fine fuel loading and estimated consumption during 10 by 10-meter burns and management scale prescribed fires conducted in the New Jersey Pinelands National Reserve. Prescribed fire data are from Clark et al. 2020.

Pre- and post-burn Terrestrial LiDAR Scanning allowed us to link fuel bed depth with flame residence time, and to evaluate fine scale patterns of fuel consumption. Figure 70 is an example of fine scale fuel reduction derived from the height difference between pre- and post-burn LiDAR scans.

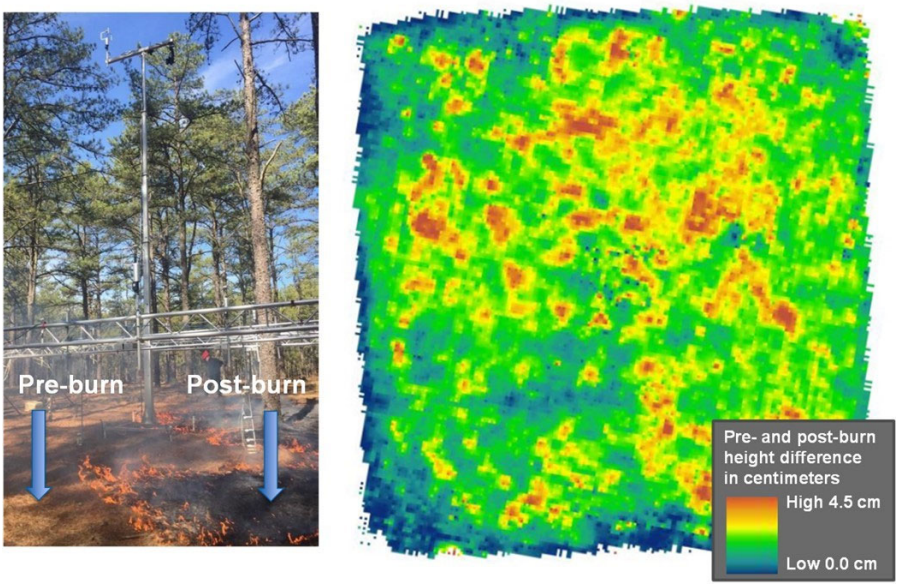


Figure 70**.** Pre- and post-burn LiDAR scans provide fine-scale information on fuel consumption during 10 by 10-meter burns.

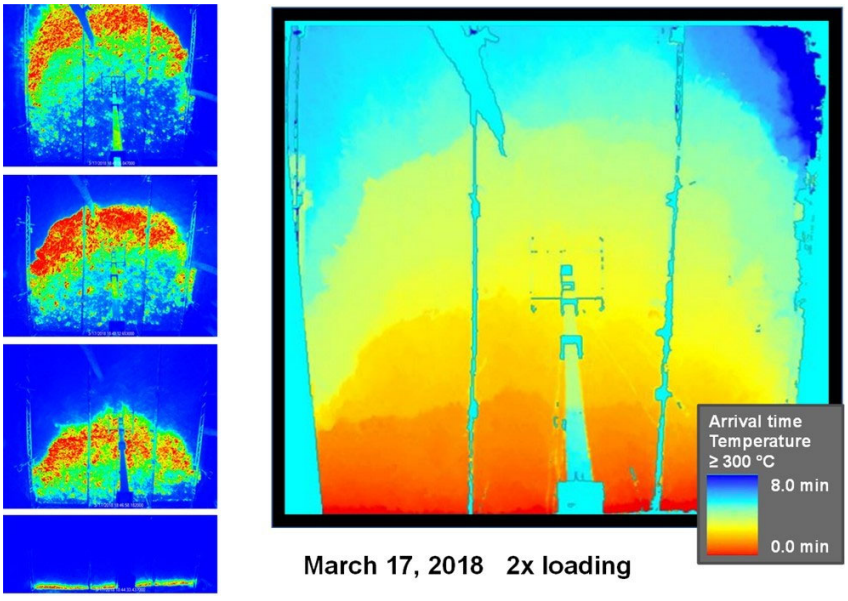


Figure 71**.** Overhead FLIR camera time series captured at 25 Hz were resampled at 0.1 Hz to estimate flame arrival times, here estimated as time to reach ≥ 300 °C, during the 10 by 10-meter burns. Data are from a fire ignited with the wind using 2x fuel loading on March 17, 2018.

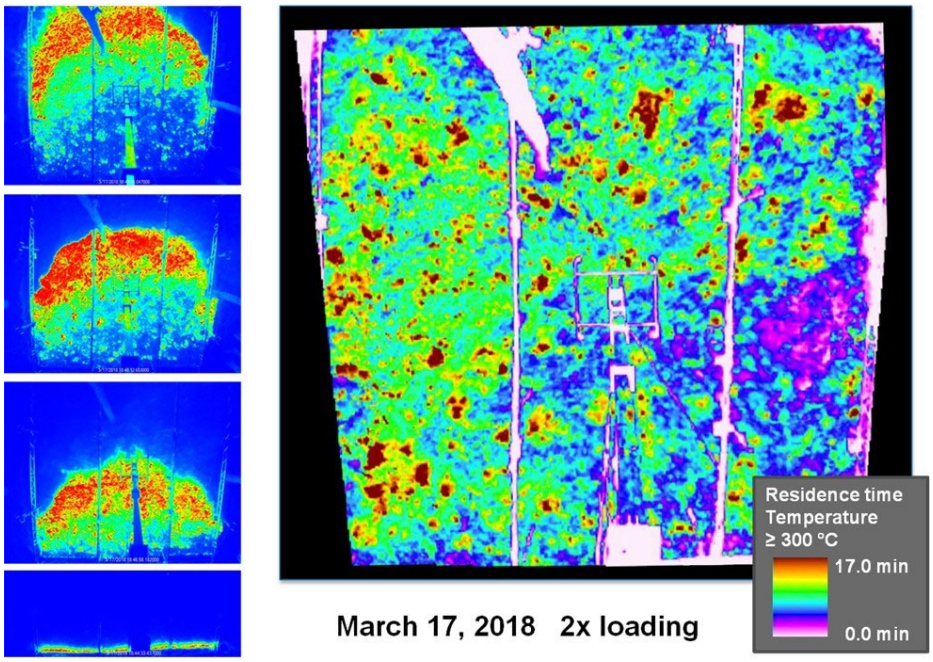


Figure 72. Overhead FLIR camera time series captured at 25 Hz were resampled at 0.1 Hz to estimate residence times of pixel temperatures ≥ 300 °C during the 10 by 10-meter burns. Data are from a fire ignited with the wind using 2x fuel loading on March 17, 2018.

Flow and temperature measurements

Sonic anemometer data provided highly resolved information on wind fields contributing to fire behavior, and the influence of fire fronts on ambient wind speed and direction. Figure 73 shows an example of 1 Hz wind velocity and direction data calculated from 16 sonic anemometers at 2.5 meters above the fuel bed during a 10 by 10-meter burn in March 2018. Overlaying these data layers over ROS data estimated from the overhead FLIR IR camera and thermocouple arrays provided high-resolution information on flow in and above the fire environment as fire fronts progressed across 10 by 10-meter fuel beds.

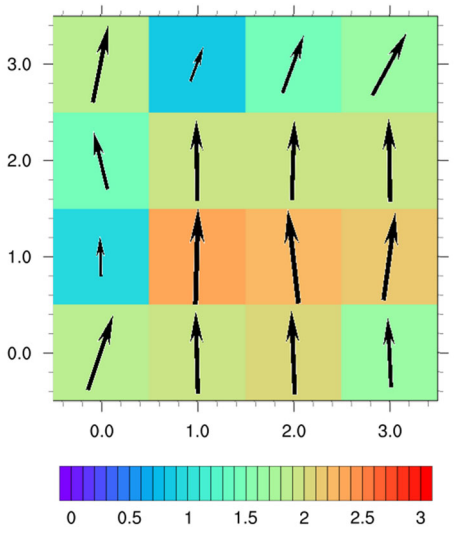


Figure 73. An example of 1 Hz wind velocity and direction calculated from 16 sonic anemometers mounted at 2.5 meters over fuel beds during a 10 by 10-meter burn in March 2018. Size of the arrow and color of the box is proportional to wind velocity (m sec^{-1}), and arrow direction shows direction, with mean wind direction from west to east.

Sonic anemometers and thermocouple arrays also provide high-resolution data documenting inflow of relatively cool air into approaching flame fronts and contrasting tilt directions of buoyant plumes associated with head vs. backing fires. As an example, data from thermocouples at 0 cm and 100 cm heights above fuel beds from seven thermocouple arrays are plotted in Figure 74. Thermocouples at 0.0 cm height remain relatively cool until flame fronts are adjacent to each thermocouple, and then heat rapidly. In contrast, temperatures of thermocouples at 100 cm height increase with convective heating in tilted buoyant plumes well before the fire front arrives. These thermocouple time series patterns contrasted with backing fires, where inflow of cool air into the base of approaching flame fronts occurred, but convective heating in tilted buoyant plumes was much less obvious.

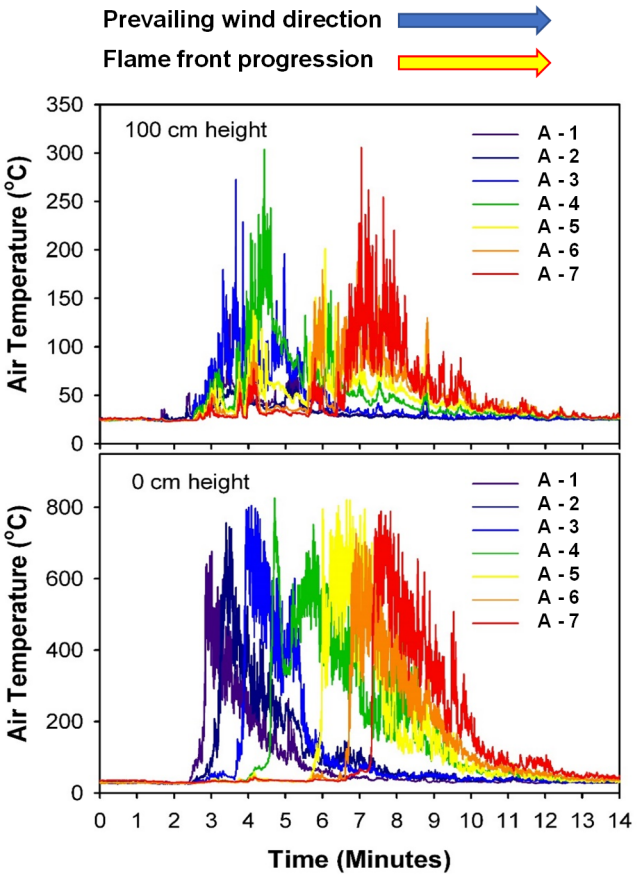
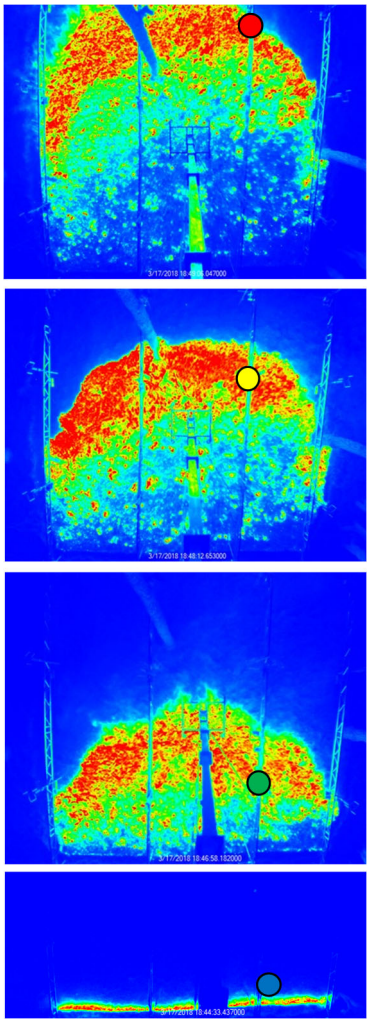


Figure 74. Temperature data from two sets of thermocouples mounted at the 0 cm height (lower panel) and 100 cm height (upper panel) above fuel beds mounted along seven thermocouple arrays on a center truss. The fire was lit with the wind and progressed from west to east along the seven arrays. "A" indicates each array by color. Note the different temperature ranges on the y-axis.

Similar thermocouple temperature profiles and the inflow patterns of cool air into the base of approaching fire fronts were measured during laboratory experiments (Campbell-Lochrie et al. 2018, 2021). Forward tilt of buoyant air masses associated with convective heating was greater during head fires than during backing fires during 10 by 10-meter burns, and was consistent with tower-based measurements made during low and high-intensity prescribed fires (e.g., Heilman et al. 2017, Clark et al. 2020).



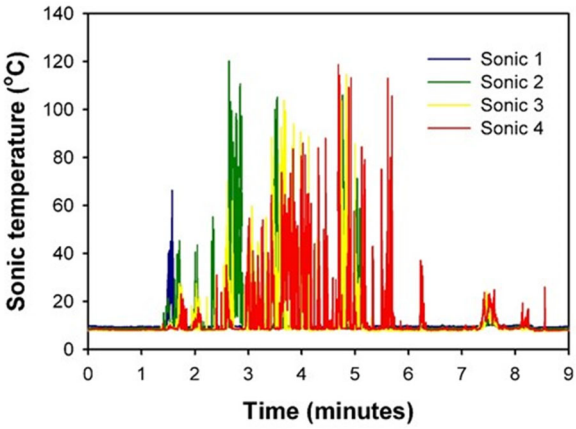


Figure 75. Fire line progression from bottom to top illustrated using the FLIR camera mounted at 10-meter height above a 10 by 10-meter burn conducted on March 17, 2018 (side panel). The first panel (bottom of figure) shows the linear ignition using a line soaked in accelerant. The following panels show a typical behavior where the center of the plot burned more rapidly than the north and south edges. Colored circles indicate sonic anemometer positions along one of the trusses. 10 Hz sonic anemometer air temperature data indicating tilt of the convective plume with the wind (upper panel).

Slopes of the relationships between convective heating and vertical wind speed velocities were a function of height above the flame front. For example, sonic anemometer data from 10 by 10-meter burns 7 and 8 indicate that slopes of the relationships between air temperature and vertical wind velocity in buoyant plumes changed in the predictable manner with height above flame fronts (Figure 76). Relationships between turbulence and heat fluxes in buoyant air above fire fronts measured during the 10 by 10-meter plot experiments reflected patterns of turbulence and temperature profiles measured during large-scale prescribed fires in the field (Clark et al. 2020).

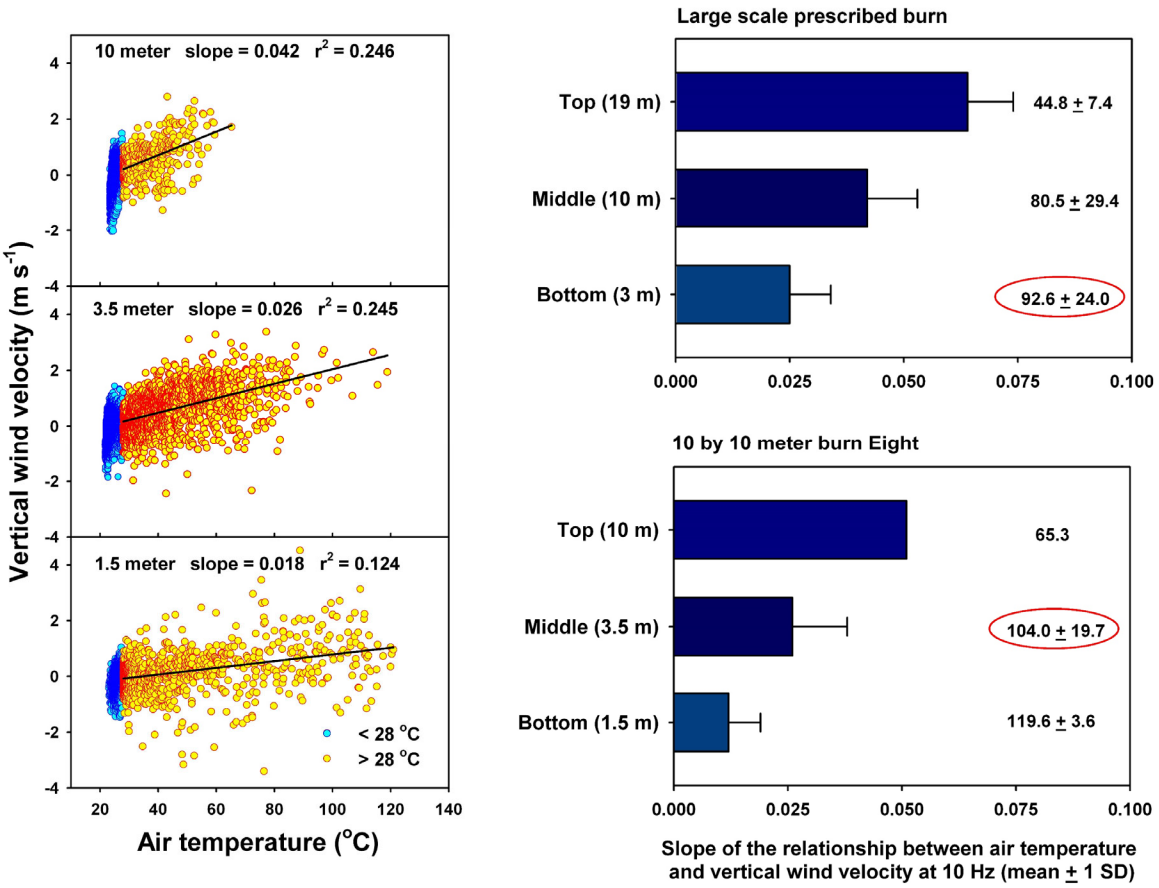


Figure 76**.** (a) The relationship between air temperature and vertical wind velocity at different heights above flame fronts during 10 by 10 m burn 8 conducted in May 2018. Yellow symbols are temperature values ≥ 5 °C above ambient air temperature measured at 10 Hz. (b) Slopes of the relationship between air temperature and vertical wind velocity at different heights above flame fronts during the management-scale burn at Silas Little Experimental Forest in March 2019 (top panel) and 10 by 10 m burn 8 in May 2018 (bottom panel).

Fire spread rates

Spread rates for experiments conducted during warm and dry conditions derived from thermocouple array data averaged 4.0 ± 1.8 cm s^{-1} with maximum average rates of 10.9 ± 4.7 cm s^{-1} (

Table 9). A peak maximum rate of 21.4 cm s^{-1} occurred during experiment #25. Fuel type and condition did influence average and maximum rate of spread of flame fronts; pine needle-only experiments had approximately 3.6 and 1.4 times the ROS of compressed pine needles and pine oak mixes, respectively (

Table 9). When all experiments conducted during warm and dry conditions were compared, there was little relationship between windspeed and rate of spread over this relatively low range of near surface windspeeds ($r^2 = 0.10$, NS;

Table 9). There also was only a weak relationship between fuel loading and rate of spread (r^2 = 0.10, NS).

Combustion and energy release

Convective heat flux generated by flame fronts during 10 by 10-meter burns could be approximated by sensible heat fluxes estimated from sonic anemometer data. Figure 77 illustrates average sensible heat fluxes for a burn lit with the westerly wind on May 20, 2019. Consistent with patterns of buoyant plume tilt measured by the thermocouples, sonic anemometers indicate an increase in both peak 1-minute and total sensible heat fluxes as the fire line progressed from west to east.

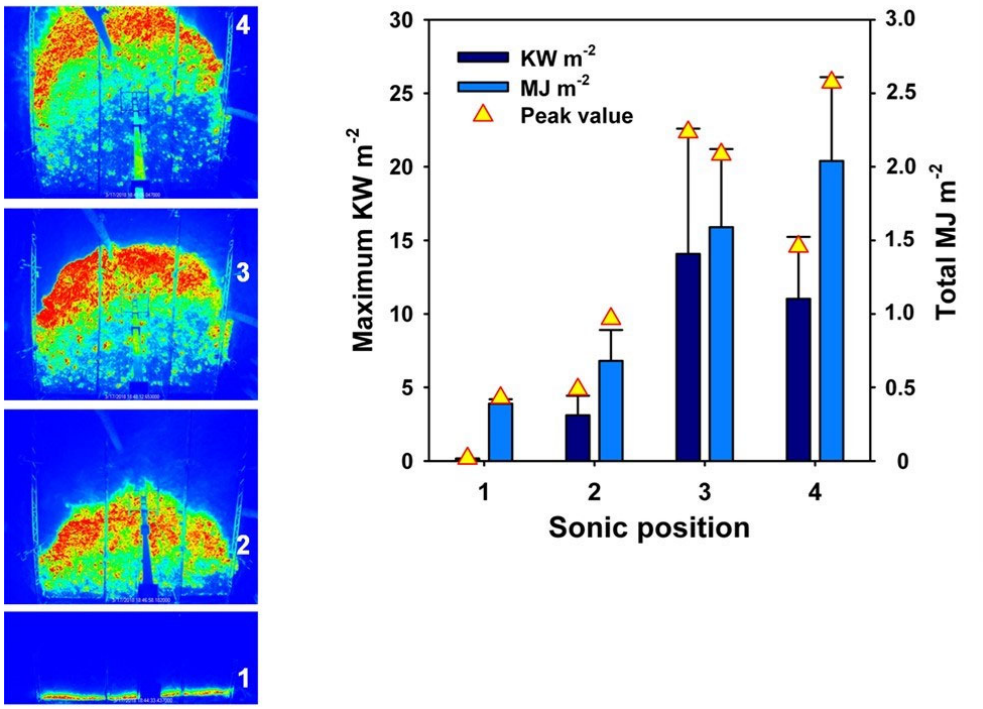


Figure 77. Sensible heat fluxes measured during 10 by 10-meter burn 20 on May 20, 2019 demonstrates patterns of peak 1-minute and integrated sensible heat flux progress with fire line progression. Average maximum 1-minute sensible heat fluxes are shown on the left axis, with peak values for a sonic anemometer at each position indicated with a yellow triangle, and integrated total sensible heat flux is shown on the right axis and approximates total convective heat flux (MJ m^{-2}). The burn was ignited on the western edge with the wind and burned east (side panel).

Spatial variation in convective heat flux was linked with fire behavior, although more intense fire behavior (e.g., occasional fire whirls generated during warm-season fires conducted at 2x and 3x fuel loadings) overwhelmed the ability of sonic anemometers to capture heat flux data (yes, they fried). Figure 77 illustrates variation in fine-scale sensible heat flux measured during a fire ignited with the wind on May 11, 2018 and indicates how variation in ROS and fire intensity can affect both peak 1-minute and integrated convective heat fluxes. Initially, 1-minute peak

sensible heat values were low at all locations except for truss location B1, where enhanced ROS and fire intensity resulted in moderate values (shown in yellow in Figure 78). In the second panel, all sonic anemometers except for sonic D2 show high values (shown in orange in Figure 78), consistent with ROS and fire intensity captured in the FLIR image on the left in Figure 78. ROS then relaxed, and all locations at position 3 showed moderate values for 1-minute peak sensible heat flux. Reacceleration of the fire front resulted in high 1-minute peak sensible heat fluxes at all locations at position 4. Integrated values shown in the right panel of Figure 78 were generally consistent with peak 1-minute values and reflected patterns of buoyant plume tilt during eastward progression of the fire line.

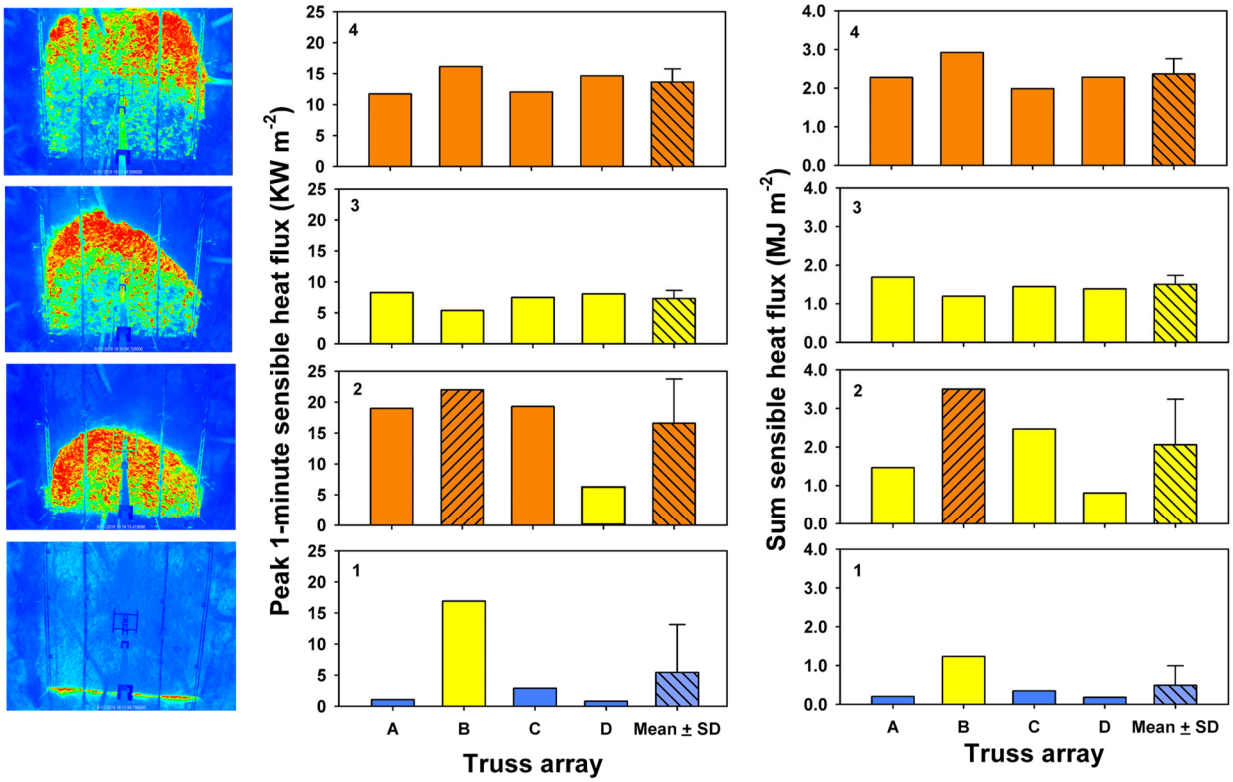


Figure 78**.** Fire line progression and sensible heat fluxes values at each sonic anemometer for 10 by 10-meter burn 13 conducted on May 11, 2018. Fire line progression from bottom (western edge) to top (eastern edge) illustrated using the FLIR camera mounted at 10-meter height above the 3x fuel bed. Peak 1-minute sensible heat flux (KW m^{-2}; middle panel) and integrated total sensible heat flux (MJ m^{-2}; right panel) are shown for each sonic anemometer as the fire line progressed. Average maximum 1-minute sensible heat flux and integrated total sensible heat flux for each row of sonic anemometers along the trusses is shown on the right of each panel. The burn was ignited on the western edge with the wind and burned east.

The effect of differences in ROS on sensible heat fluxes are further illustrated in Figure 79, although perhaps in a non-intuitive manner. Peak 1-minute and integrated sensible heat fluxes were initially higher during a fire with relatively low ROS values than during a second fire with higher ROS. As the fire lines progressed, peak 1-minute values generally corresponded with high ROS, but then decreased after peaking in the fire with low ROS. Integrated sensible heat fluxes

were higher at all sonic anemometer positions during the fire with relatively low ROS compared to that with a higher ROS. It is likely that plume tilt during the fire with higher ROS resulted in heat transfer beyond the footprint of the last row of sonic anemometers (sonic position 4 in Figure 79).

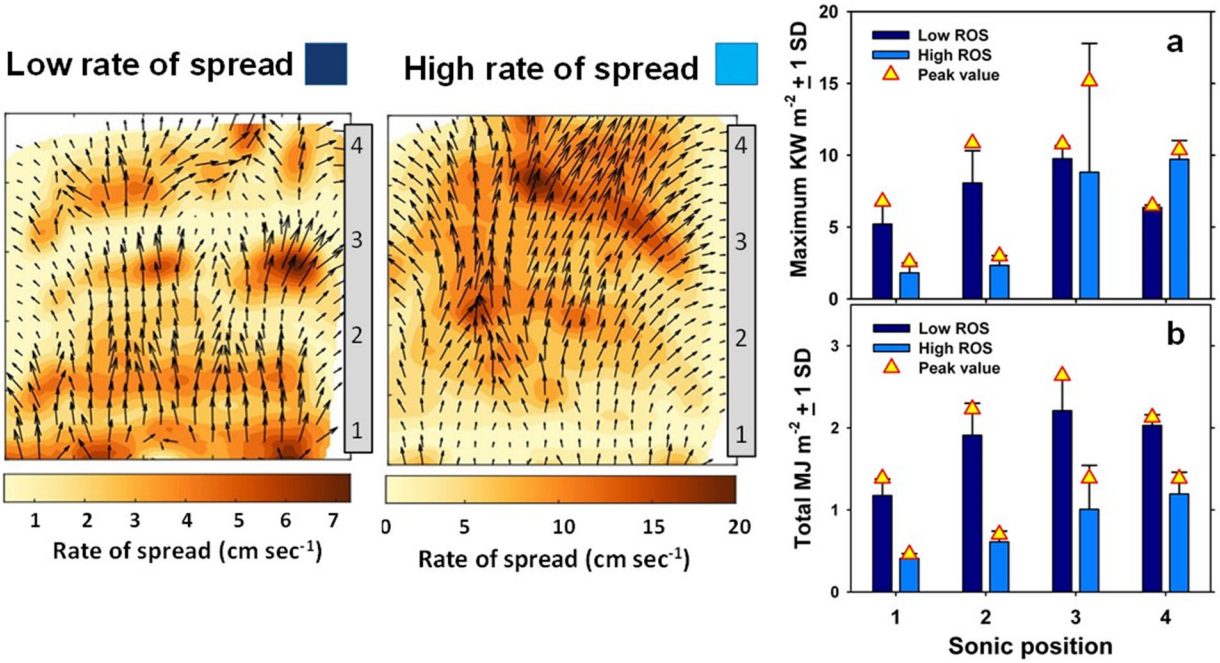


Figure 79**.** Sensible heat fluxes measured during 10 by 10-meter burns 23 and 25 conducted on May 21, 2019 demonstrate how fire behavior (ROS) affects convective heat fluxes at each sonic position. a) Average maximum 1-minute sensible heat flux are shown, with peak values for a sonic anemometer at each position indicated with a yellow triangle. b) Integrated 1-minute sensible heat fluxes during the fire used to estimate total convective heat flux (MJ m^{-2}). Burns were ignited on the western edge and burned east.

Table 10 shows a comparison of total convective heat flux estimated from consumed fuels compared to peak 1-minute and integrated sensible heat flux during burn 7 conducted on May 9, 2018 when sonic anemometers were arranged at 1.5 meter and 3.5 meter heights along two trusses (see Figure 62. Trusses and instrumentation used to quantify fire behavior during 10 x10-meter burns at Silas Little Experimental Forest. (a) tower mounted IR camera and sonic anemometer, trusses with sonic anemometers, thermocouples, pressure gauges, and spectral sensors/digital cameras. (b) closer view of instruments mounted on a single truss for burns 7 and 8 conducted in May 2018.b). Peak and integrated values from sonic anemometers at different heights indicate large differences in sensible heat flux, suggesting that they are sampling different "footprints" associated with fire fronts. While footprint analyses for flux measurements of heat and other scalers have progressed with large-scale flux network analyses (e.g., Cho et al. 2020, in press), we know relatively little about flux footprints during wildland fires. Information to date suggests that both vertical and horizontal footprints can be highly variable. However,

sampling at intermediate heights (e.g., 2.5 to 3.5 meters above fuel beds) captured the largest proportion of estimated convective heat fluxes.

Table 10**.** Comparison of biometric estimates of convective heat flux to sensible heat flux measured at different heights above the flame front during 10 x 10 m burn 7 conducted on May 9, 2018.

Heat flux	Biometric	Sonic anemometer height		
		1.5 meter	3.5 meter	10 meter
1-minute (KW m^{-2})	---	3.91 and 9.39	17.02 and 17.23	6.58
Integrated total (MJ m^{-2})	1.8 to 2.2	0.59 and 0.68	2.98 and 1.09	0.58

Conclusions and implications for future research

10 by 10-meter experiments were designed to "bridge the gap" between small-scale laboratory experiments conducted under controlled conditions and large, management-scale prescribed fire experiments conducted under a finite set of meteorological and fuel loading and moisture contents, yet are essentially uncontrolled experiments. Employing much of the instrumentation and information collected at smaller and larger scales during 10 by 10-meter experiments has contributed to an improved understanding of combustion processes and fire behavior during prescribed fires, but has also identified some limitations to this approach and highlighted a number of areas to be pursued in future research efforts.

Commonalities across scales during our SERDP project included fuel type, loading and fuel moisture levels, which could be manipulated to pre-determined targets that were similar to those in many of the laboratory experiments, and encompassed the much of the range of fine surface fuel loading and consumption measured previously during operational prescribed fires conducted by the NJFFS (Clark et al. 2015, 2020, Gallagher et al. 2017). Sampling of fine-scale pre- and post-fuel structure for consumption utilized both biometric and LiDAR-based approaches (Skowronski et al. 2017, Gallagher et al. 2017). Instrumentation including thermocouple arrays to estimate gas temperatures and arrival times of flame fronts, sonic anemometers to estimate turbulence statistics and sensible heat fluxes, and custom multispectral radiometers to measure radiative heat flux have been used during small-scale laboratory investigations and large-scale prescribed burns (Heilman et al. 2017, in press; Clark et al, 2020).

Consistent fuel sampling and instrumentation employed during small-scale laboratory experiments, 10 by 10-meter burns, and large-scale operational prescribed fires allowed us to ask which key processes contributing to patterns of fire behavior, fuel consumption, and turbulence and heat fluxes were consistent across scales. It also facilitated identification of phenomena that require further study. As examples, fine fuel loading and consumption, flame heights and ROS, and energy fluxes were similar during the 10 by 10-meter experiments and previously conducted low-intensity management-scale burns. Sonic anemometers at various heights above flame fronts

provided valuable data on turbulence and heating in buoyant plumes, but also identified some limitations to this approach, especially in fire whorls generated during experiments with enhanced fuel loads. Although thermocouple arrays demonstrate the occurrence of relatively cool air flowing into the base of approaching flame fronts, the relationship between this phenomena and larger-scale circulations associated with more intense head fires which resulted in downdrafts of cooler air flowing into the back of flame fronts that occurred during some large-scale prescribed fires in forested canopies is unclear. Such phenomena undoubtedly has significance for fire behavior but will require more information to understand and accurately predict during wildland fires. Overall, results obtained during intermediate-scale field experiments are largely consistent with results obtained during small-scale laboratory measurements and large-scale prescribed burns, and contribute to an improved understanding of combustion processes and fire behavior.

Results from intermediate-scale field experiments also suggest some areas that should be investigated further. For example, while footprint analyses for flux measurements of heat and other scalers have progressed with large-scale flux network analyses (e.g., Cho et al. 2020, in press), we know relatively little about flux footprints during wildland fires, which are relevant to the prediction of convective heat flux, pre-heating of fuels, and propagation of flame fronts. Although the presence of flame fronts may invalidate some of the assumptions of both the eddy covariance technique and current footprint models (e.g., stationarity, etc.), an important first step will be simulation of both horizontal and vertical footprints during fires of variable intensity. Further, sensitivity analyses with various parameters associated with eddy covariance calculations, including integration times, sampling heights, roughness length and zero-plane displacement, may be fruitful.

Although we are beginning to understand how turbulence and sensible heat fluxes are related with height above fire lines, we have less information on how radiative heat fluxes change with height above flame fronts. However, integration of sensible (convective), radiative, and other heat flux measurements would provide more complete energy balance measurements for comparison to biometric and TLS measurements of fuel consumption (Clark et al. 2020).

Flame spread analysis

Objective

The objective of this investigation was to work towards a consistent methodology for evaluating the dynamic rate of spread of the replicated fires and to evaluate this rate over potential controlling variables.

Background

Over the course of the 35 small-scale plantation burns for the SERDP project, a range of behavior was observed, anecdotally, when considering the rate of advancement of the flame front. Thus, it is interesting to explore whether this variation can be explained in a systematic and quantitative way. Such an exploration allows us to interrogate our current understanding of flame spread and the relative role of key parameters (related to the fuel and weather).

The first challenge is in quantifying spread rates. This is not necessarily trivial, as there are different avenues (e.g. video analysis, thermocouple data) which offer varying degrees of spatial

and temporal resolution, as well as various data processing challenges. The overhead thermal imaging data are most attractive in that they provide excellent spatial resolution (~4 cm^2 per pixel, covering the entire plot) and temporal resolution (25 Hz, for the entire duration of an experiment). However, these data are in the form of time-temperature histories for individual pixels, and spread rates must be derived, following a series of assumptions and approximations which may introduce uncertainty.

The second challenge is in evaluating spread rate, a highly dynamic trait of a fire (particularly at local scale), against potential controlling variables. It has been well documented that the rate of spread in similar fuel types can be statistically correlated to environmental variables such as wind speed, fuel moisture, and fuel quantity/structure (Fernandes et al. 2009). However, the functional form of these relationships has not been well-established on a purely physical basis, and so the application of previously proposed empirical relationships is dubious (see the summary by (Sullivan 2009) demonstrating the wide range of proposed relationships between wind-speed and spread rate, when following a statistical approach).

In this case, wind speed is chosen as the primary variable of interest. It is known to be important, it is typically a known (and therefore useful) quantity for fire managers, and it is measured in these experiments with a high temporal resolution (10 Hz), which is useful given the highly dynamic spread behavior observed. The hope is that, by isolating the influence of wind-speed, the influence of other relevant parameters can then be explored more readily. Fuel load is a natural comparison point, as this was a controlled variable across the campaign, but quantities such as FMC can also be investigated.

Materials and methods

In this section, the methods used to determine the characteristic wind and the rate of spread for each fire are presented. An overview of the instrumentation layout referenced in this section is shown in Figure 61

Determination of characteristic wind

A characteristic horizontal wind vector, as a function of time, was determined for each experiment. All 17 sonic anemometers were used for this calculation, in order to give an indication of the average direction and magnitude of the wind across the experimental area. Measurements of u and v velocity components were averaged independently, using 10-second moving average, which was sampled at 1 Hz, starting at ignition. All readings with a corresponding diagnostic error code were rejected from this process, as were those where the anemometer recorded a temperature in excess of 50°C (which falls outside the operating range specified by the manufacturer).

The spatial averaging procedure removes any localized features of the wind field, over the plot area, but allows for the fact that at any given moment, individual sensors may be impacted by the fire and not producing reliable data. The temporal averaging procedure removes some high frequency components of the signal in order to focus on the dominant behavior. The choice of a 10-second window was guided by the fact that mean winds were on the order of 1 ms^{-1}, and the plot length was 10m. Thus any significant perturbation is more likely to impact multiple sensors within this window, and be captured in the averaging.

Determination of fire spread

The data from the overhead IR camera was used to determine the progression of the leading edge of the flame front as a function of time. For each pixel in the FOV, the arrival time of the flame front was determined by the corresponding temperature first exceeding 300°C. In order to filter out high frequency fluctuations around this threshold, which are more likely associated with forward tilting of the flame and not the leading edge of the pyrolysis front in the fuel bed, the temperature must have exceeded the threshold continuously for 1 second in order to be considered as 'fire arrival'. Time was determined in seconds from ignition, using the timestamps available in individual frame metadata.

After generating an image of fire arrival times for all pixels in the IR frame, masks are applied to remove regions of spurious data where objects such as the camera support tower, the instrumentation trusses, and any trees may obscure the view of the camera. In particular, reflective surfaces may appear as high temperature regions to the IR camera and be erroneously assigned an arrival time. Once masks were applied, the image was then scaled and rotated so that it could be projected onto a Cartesian coordinate system, with (0,0) defined at the southwest corner of the experimental plot, and x and y increasing to the east and north respectively. This correction was done by aligning reference points in the image with corresponding points in the TLS data, which had been referenced to the same origin.

In order to limit the effects of any highly localized (e.g. single pixel) deviations from the average progression, which may be the result of mis-detection, the 640x480 image was then sub-sampled onto a 100x100 array covering the plot area (i.e. a 10 cm resolution), using linear interpolation. The resulting data was passed through a box filter, obtaining a spatial average from a 3x3 rectangle centered on each point. This process is shown in Figure 80.

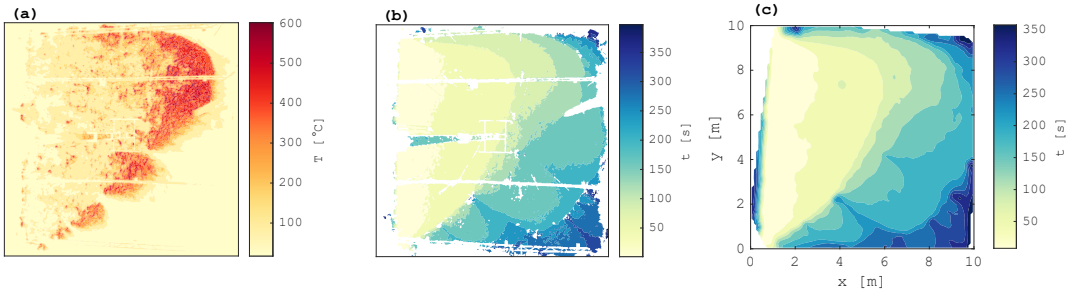


Figure 80. Steps for processing the overhead IR data, for Burn 20. (a) Example of a single frame from the raw IR data. (b) Image of fire arrival times, based on temperature threshold criteria. (c) Arrival time matrix rotated and scaled to match real-world (TLS) coordinates, and sub-sampled at a 10 cm resolution.

The spread rate was then calculated by taking the inverse of the gradient of the arrival time matrix in the x and y directions. The gradient is calculated using a central difference scheme in each direction. Because of the inverse nature of the spread rate calculation, there is a possibility for spurious high values, particularly when complex interactions between segments of fireline are occurring (as opposed to the fire progressing as a clear linear front). Since the focus is on the overall trends, values which fall into the upper 99th percentile of spread rates are removed and

the data is linearly re-interpolated at these points. A second 3x3 spatially averaging box filter is also applied.

As the gradient of arrival time is perpendicular to the fire isochrones, the direction of the gradient vector was also used to obtain independent spread components in the x and y directions. This allows the creation of spatial maps of spread vectors, such as in Figure 81. Because the wind is handled as single, temporally resolved, characteristic vector, it is also useful to apply the same treatment to the spread rate. Taking the same 10-second moving window, spread vectors with relevant corresponding arrival times were averaged to create a plot-average magnitude and direction of spread (cf. Figure 81c). In order to capture the dominant spread characteristics, the analysis ignores 1 meter of data on either flanking edge of the fire (as determined from on the ignition edge).

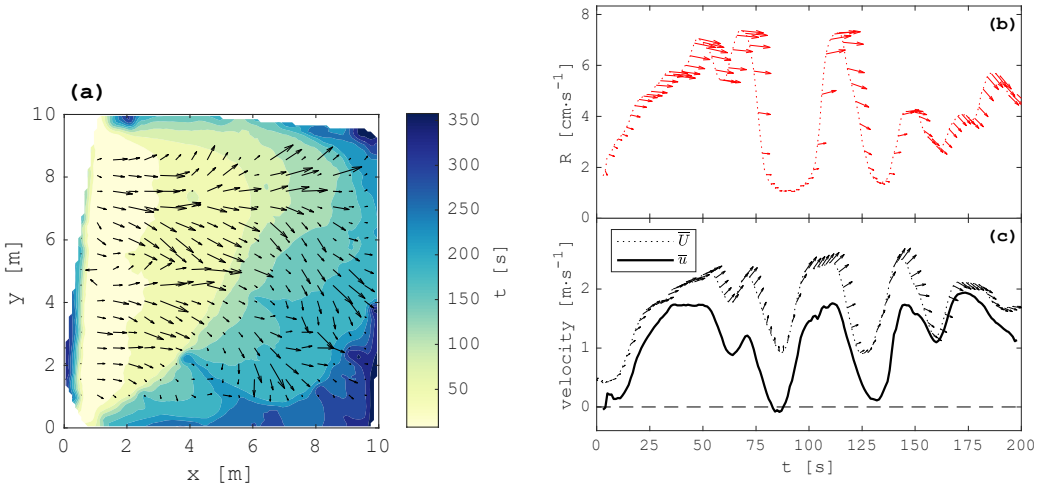


Figure 81. Example of wind and spread rate calculation for Burn 20. (a) The computed vectors of spread rate, overlaid on a contour plot of arrival time, which are used together to create a time-history of plot-average spread. Note that the outer-most meter on either flanking edge is neglected in the analysis, and for clarity, only every 5th vector is shown. (b) The time history of plot-average spread vectors. (c) The 10-second average wind vectors and the total magnitude ($\overline{U}$), as compared with the wind magnitude projected in the direction of average spread ($\overline{u}$).

An example of the moving averages for characteristic wind and characteristic spread rate is given in Figure 81. This approach allows the wind to be decomposed into the component in the direction of spread at a given moment, u, and the component perpendicular, v. In this way, the influence of aligned wind, u, on spread rate is able to be analyzed independent of the specific direction at a given moment. In the example shown, both the wind and the spread are aligned at ~160 s after ignition, and the determination of the u-component allows the behavior to be treated as a head fire, despite the fact that the spread direction has shifted roughly 45° from the direction at ignition.

Results and discussion

An evaluation of the general experimental conditions is given in Table 11. A total of 35 experiments were conducted, of which the first 6 were considered trial runs, and are not included in this analysis. Burn 9 and 12 are omitted due to incomplete IR data, and burn 34 is omitted as it was a trial of an alternative fuel configuration. Of the remaining 26 experiments, 7 did not successfully sustain fire spread in a continuous line across the extent of the plot, due to at least some degree of self-extinguishment (in some cases followed by manual extinguishment).

Table 11. Details of environmental conditions and spread rate for each burn. Ambient temperature and relative humidity come from the 'green tower' data. Wind speed statistics are taken from an average across all sonics during a given burn. Spread rate statistics are taken within a 1m buffer from the plot edges is considered in order to reduce edge effects and the influence of the ignition.

no.	fuel type	m_l [kg·m^{-2}]	T_{amb} [oC]	RH [%]	FMC [%]	$\overline{U}$ [m·s^{-1}]	$\sigma_U/\overline{U}$ [-]	$\overline{u}$ [m·s^{-1}]	$\overline{R}$ [cm·s^{-1}]	$\sigma_R/\overline{R}$ [-]
7	needles (natural)	0.5	22.2	37.0	11.6	0.5	0.57	0.1	5.1	0.26
8	needles (natural)	0.5	23.1	32.5	9.3	1.1	0.44	0.0	2.6	0.62
10	needles	1.0	20.6	54.3	—	0.8	0.17	0.1	—	—
11	needles	1.0	20.8	56.1	14.4	1.0	0.37	0.9	2.6	0.49
13	needles	1.5	23.9	34.3	10.0	1.0	0.61	0.7	3.1	0.68
14*	needles	0.5	21.2	77.9	—	1.0	0.61	—	—	—
15*	needles	1.0	21.2	89.2	—	1.0	0.61	—	—	—
16	needles	1.0	23.1	81.7	—	0.8	0.36	0.7	—	—
17	needles	1.0	22.1	56.5	—	0.8	0.32	-0.1	—	—
18	needles	1.5	22.1	50.3	—	0.6	0.50	0.3	0.5	0.59
19	needles	1.0	19.2	61.6	—	0.5	0.48	0.2	—	—
20	needles	0.5	31.3	38.2	5.5	1.5	0.33	1.1	4.2	0.44
21	needles	1.0	31.2	40.8	7.0	1.1	0.35	1.0	3.4	0.57
22	needles	1.5	29.9	42.1	7.8	1.2	0.35	1.0	3.2	0.50
23	needles	0.5	16.8	39.2	7.2	1.4	0.36	0.9	1.9	0.66
24	needles	1.0	19.0	34.2	5.8	1.0	0.56	0.8	2.9	0.77
25	needles	0.5	20.9	31.6	5.3	1.1	0.60	1.0	5.0	0.67
26	needles	1.5	21.2	31.5	4.9	0.9	0.43	0.6	3.8	0.81
27	needles	1.5	20.1	27.9	7.8	1.0	0.33	0.2	2.6	0.97
28	needles	1.0	21.0	26.9	5.3	0.9	0.44	-0.4	1.0	1.73
29	pine-oak	0.5	22.6	22.1	5.4	0.8	0.42	0.7	3.8	0.48
30	pine-oak	0.5	22.8	24.9	6.4	0.9	0.45	-0.2	0.9	1.13
31	compressed needles	1.5	26.2	64.8	7.0	0.7	0.44	0.3	0.7	0.88
32	compressed needles	1.5	27.6	61.9	8.0	0.9	0.33	-0.9	0.2	0.36
33	compressed needles	1.5	25.2	66.0	9.9	1.3	0.24	0.9	1.1	0.80
35	pine-oak	0.5	25.2	55.5	8.8	0.7	0.58	0.4	—	—

*Sonic anemometer data not available, so average wind was taken from an alternative reference source

In an effort to identify the conditions which are conducive to fire spread in these fuels, Figure 83 shows the success of the burns as a function of relative humidity and wind speed. These are not independent inputs, as they will depend on large scale weather patterns, however, they are the type of variables which will be accessible to a fire manager when planning prescribed burning activities.

It can be seen that increasing humidity leads to an increasing tendency for unsuccessful spread, with the lowest RH for an unsuccessful burn being 54.3%, and the highest RH of a successful burn being 66.0%. The influence of wind is less obvious, though it appears that

successful burns in the marginal region of 55-65% RH require higher winds, as may be expected. The analysis ignores the impact of fuel condition (type, loading, and moisture content), but gives a general indication of when conditions are favourable.

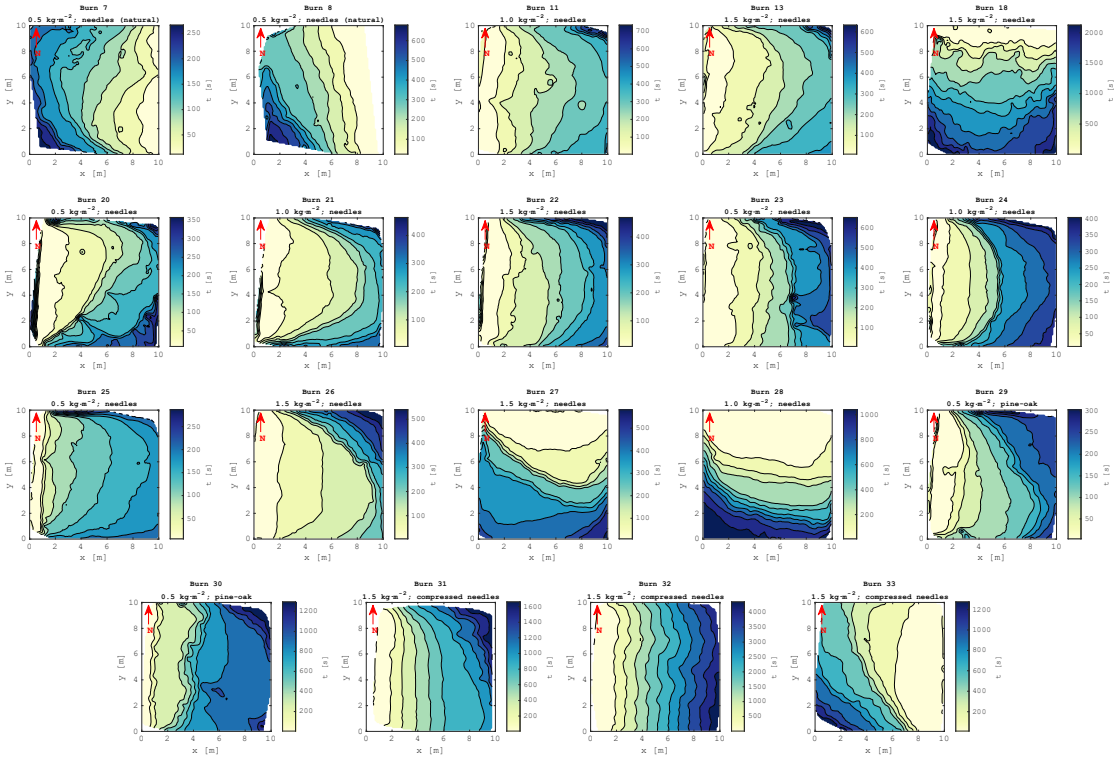


Figure 82. Fire progression for each of the 10x10 fires

Focusing now on the successful burns, Table 11 shows that these were carried out in mild conditions (T_{amb}= 16.7—31.3°C), with dry fuels (FMC= 4.9—14.1%). The average wind speed was relatively consistent, falling between $\overline{U}$=0.5—1.5 m s^{-1}, with relative standard deviations between 0.17—0.61. Note that $\overline{U}$ is the absolute magnitude, so the wind component in the direction of spread, $\bar{u}$, gives a better indication of the alignment of the wind.

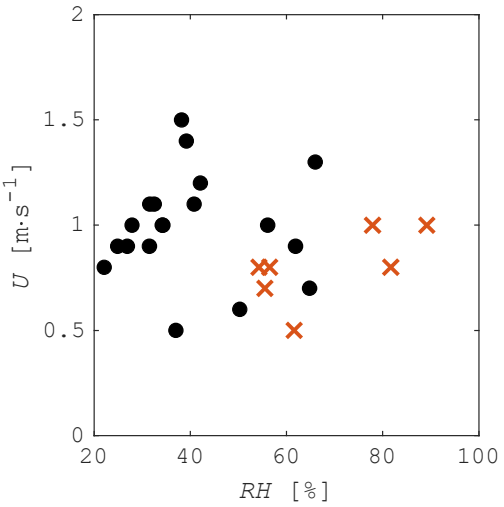


Figure 83. Burn success (spread across the whole plot), as a function of relative humidity and average wind. Filled circles correspond to successful spread and x's to unsuccessful.

Spread rate was more variable, with average values falling between $\bar{R}$= 0.2—5.0 cm s^{-1}, with relative standard deviations between 0.28 -- 1.74. In order to provide a basic assessment of the source of this variation, Table 12 shows Spearman's rank correlation coefficient, r_s, between average spread rate and the various environmental conditions. Values of r_s close to 1 imply an increasing monotonic relationship, and values close to -1 imply a decreasing monotonic relationship. This metric was chosen over Pearson's correlation coefficient, as we do not necessarily assume a linear relationship between spread and any of these variables.

Table 12. Spearman's rank correlation coefficient between spread rate and the selected environmental variables.

Variable	r_s	p-value
T_{amb}	0.02	0.93
RH	-0.35	0.15
FMC	-0.20	0.43
$\bar{U}$	0.22	0.37
$\bar{u}$	0.53	0.02

Rate of spread has the tendency to decrease with increasing relative humidity and fuel moisture content. Rate of spread has the tendency to increase with increasing ambient temperature and wind speed. Of all the tendencies, only the correlation with the wind component in the direction of spread can be considered significant (p-value less than 0.05), though the correlation coefficient is only 0.53. The marginal (r_s=-0.2) and less significant (p-value =0.43) correlation with fuel moisture content is noteworthy, given the acknowledged importance of this parameter. However, this may be linked to the narrow range of moisture content values considered in the experimental campaign. Thus, measurement uncertainty, as well as un-quantified spatial variability, may play a significant role in the finding that mean spread rate was not correlated with moisture content.

Dynamic fire spread

As the analysis of average parameters for individual burns did not reveal strong trends that could be used to understand and predict fire spread rate, a more detailed analysis of the time varying wind and spread rate is warranted. Figure 84a shows all pairs of wind speed (aligned with the direction of spread) and spread rate, obtained from the averaged 1 Hz data for all successful burns.

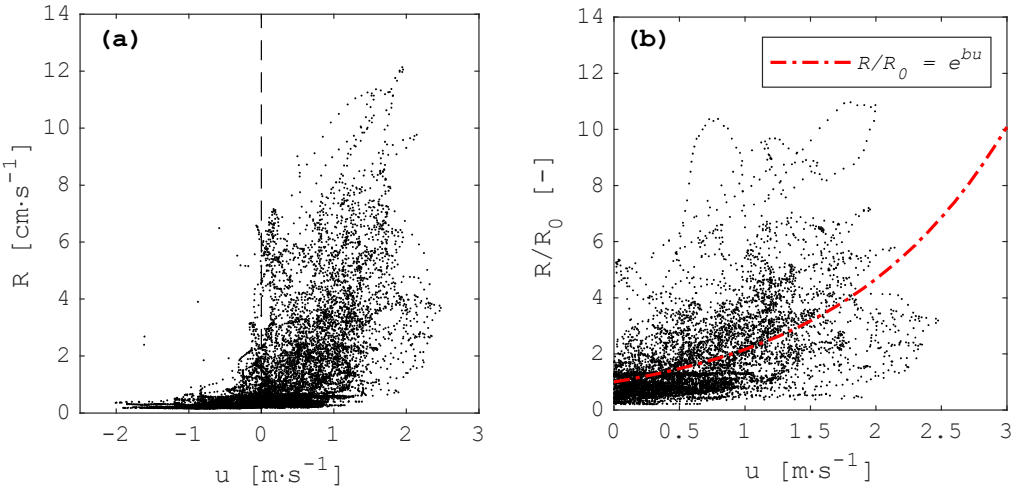


Figure 84. (a) Summary of dynamic spread (R) versus aligned wind (u) for all burns. (b) Data corresponding to concurrent flow ($u > 0$), with spread rate normalized by a zero-wind value, estimated for each burn based on an exponential fit. An exponential best-fit for the entire dataset is shown, where b = 0.77

This figure demonstrates the tendency for an increasing monotonic relationship of spread rate with wind. In opposed flow (backing fire) conditions, the spread rates are constrained to a narrow range. The values increase and become more scattered as the conditions transition to concurrent flow (head fire). If all temporally resolved data is used to calculate r_s, as opposed to just the averages as in Table 12, the correlation coefficient improves to 0.80.

Since the data indicates a clear monotonic relationship, we might propose a function such as the exponential fit shown in Figure 84. An exponential dependence of spread rate on wind speed has been empirically determined in a number of previous experiments. In this case, we focus on only the concurrent flow data (u>0), as opposed flow spread may be dominated by different physical processes, so a single relationship may not be appropriate for both regimes. In an effort to remove the influence of other variables which are nominally constant during a given burn (e.g. m_l, FMC), the data for each burn are normalized by a no-wind spread rate (R_0). This was estimated by first fitting an exponential function to each data set. The normalized data are then plotted in Figure 84b with a cumulative fit. This function appears to capture a general trend, but clearly cannot account for the variability which remains in the data. The maximum under-prediction of a data point is 83% of the observed value, and the maximum over-prediction of a data point is 850% of the observed value.

Conclusions and implications for future research

This analysis has shown the challenge in correlating observed fire behavior with environmental variables. This is due to the time-dependent nature of the fire spread phenomena and in particular challenges associated with accounting for the effects of wind. Despite this, some observations regarding the effects of variables such as relative humidity on the success (or otherwise) of a burn have been identified. The analyses shown here highlight the opportunity to compare multiple types of fire spread drivers and characterize spatial and temporal heterogeneity in fire spread that are often overlooked for net fire outcomes that are exceedingly difficult to predict alone without representing these fire processes. The data sets generated will inform future studies and provide an evidence base for future numerical model development.

Subsequent experimentation using the approaches described in this section can further the connectivity between laboratory and larger-scale field studies and expand upon our understanding of key fire behavior drivers. For instance, future studies that add the complexity of shrubs will serve as an important iteration of this research and enable testing of how observed spread patterns hold up under scenarios of more complex fuels, and how fire burning through simple and complex fuels may interact. This work can also contrast different surface fuels, which have been shown to have varying combustion characteristics either linked to structure or chemistry, and how mixes of fuel particle types behave. Likewise, continued analysis of the scalability between fine-scale and larger-scale fire spread scales and their processes is needed.

Overall, these studies serve to explore the dynamic effects of wind in the field through porous fuels and serve to contrast with the quiescent conditions studied in the laboratory, as well as those observed at the large scale.

Management-scale field investigations

Objectives

The overarching objective of this experiment was to further our understanding of processes controlling fuel consumption and fire behavior and facilitate the opportunity to examine how these processes scale from the laboratory to operational burns, leveraging the laboratory and small-scale field experiments described in previous sections of this report. This objective also translates into the aim of executing an experiment where instrumentation from the small-scale field experiments was embedded in an operational scale burn with more complex fuel conditions, in concert with typical large-scale meteorological and fire spread measurements typical of operational burn experiments. Additional objectives of this experiment were also to collect data necessary for simulation and model testing with WDFS or QUIC-Fire, and to collect turbulence data above canopy necessary to test plume dispersion models.

Background

Our understanding of combustion processes and fire behavior during prescribed fires has benefited from large-scale experimental and operational prescribed burns, because some of the phenomena that occur during large scale burns cannot be replicated in laboratory settings. Management-scale burns, typically on the scale of 15 to 500 ha, provide opportunities to quantify processes controlling fire behavior that are nearly impossible to replicate during smaller-scale experiments. Since 2006, our group has used surface, tower-based and aerial measurements of fuels and atmospheric conditions during wildland fire events across a range of fire intensities to quantify how fire-fuel-atmosphere interactions and atmospheric turbulence (including turbulent heat and momentum fluxes) can influence overall fire behavior, fuel consumption, smoke emissions and dispersion, and ember production (Clark et al. 2020; Heilman et al. 2021; Heilman et al. 2017; Heilman et al. 2019; Heilman et al. 2015; Mueller et al. 2017; Mueller et al. 2021). These efforts have 1) linked spatial patterns of surface and canopy fuel consumption to fire behavior and first-order fire effects (Gallagher 2017; Mueller et al. 2017), 2) quantified patterns of fire-induced turbulent circulations within and above the canopy across a wide range of fire intensities (Clark et al. 2020; Heilman et al. 2021; Heilman et al. 2017; Heilman et al. 2019), and 3) contributed to a better understandings of smoke dispersion (Charney et al. 2019; Kiefer et al. 2014), and ember production, transport and deposition (El Houssami et al. 2016; Thomas et al. 2017b). Further, tower-based measurements of turbulence and sensible / convective heat fluxes before, during, and after the passage of fire fronts have facilitated a better understanding of stand energy exchanges within and above the canopy during fires (Clark et al. 2020; Clark et al. 2012). However, limitations to this approach have been pointed out in previous sections, and are briefly summarized here:

1. Large-scale experiments typically integrate numerous complex phenomena such that disentangling the underlying relationships is difficult, limiting their utility.
2. Because some measurements were made during large-scale operational burns, fine scale fuel consumption measurements were relatively coarse scale, and nearly all large-scale experiments are limited by a lack of comprehensive fire behavior measurements.
3. While these experiments have quantified turbulence and heat and momentum fluxes in the fire environment simultaneously, the small number of towers limits generalizations.

Important questions that have evolved during these investigations revolve, for example, around the development of fire-induced turbulent circulations interacting with vegetation structure. By documenting patterns of vertical and horizontal turbulence associated with buoyant plumes, these efforts have demonstrated the occurrence of horizontal inflow and downdrafts of cooler air behind flame fronts during more intense fires, typically with some torching behavior, but less frequently during low intensity fires (Clark et al. 2020; Heilman et al. 2021; Heilman et al. 2017; Heilman et al. 2015). Fire behavior was observed to "pulse" during these episodic events, with periods of active crown torching and higher rate of spread (ROS) and then a relaxation and lower ROS. When and under what conditions do the more intense fires set up larger-scale circulations, and how do these directly affect fire behavior? More specifically, how are patterns of heating and turbulence related to the propagation of fire fronts, the transition of surface fires to the crown via ladder fuels, and overall fire behavior during prescribed fires?

A second important issue revolves around our ability to synthesize and predict fire propagation during prescribed fires. Despite the development of a number of physics-based fire behavior models (e.g., WFDS, FIRETEC, and QUIC-Fire), their use for prescribed fire planning is just starting to be adopted (Linn et al. 2020). One limitation is the availability of data to initialize, parametrize and evaluate these models, which are also subject to large uncertainties and limited resolution. Thus, we have focused our efforts on developing (archived) data sets that can be used for improving model performance.

Here, we describe a heavily instrumented management-scale fire conducted at the Silas Little Experimental Forest in the Pinelands National Reserve (PNR) on March 13, 2019. We also draw on examples and comparisons to other instrumented management-scale burns conducted over the last two decades in the PNR.

Materials and methods

Overview

Instrumentation consisted of a network of "Firetrackers" and multi-spectral sensors to measure flame arrival times, intensity, and radiative heat flux; dense arrays of thermocouples to measure gas temperatures; and sonic anemometers mounted on towers to measure turbulence and sensible (convective) heat flux at multiple heights above the flame fronts. Fuel loading, moisture contents, and consumption were estimated from a combination of LiDAR and harvest measurements. Our experimental design incorporated much of the same instrumentation and integration times used previously in small-scale laboratory combustion experiments and the intermediate-scale 10 by 10-meter burn experiments conducted in the adjacent pitch pine plantation at the Silas Little Experimental Forest described in previous sections. We also embedded an array of instrumentation that was similar to those employed during the 10 by 10-meter plot experiments conducted in the adjacent pitch pine plantation, including multispectral sensors, pressure sensors, and load cells adjacent to one of the within burn unit towers (see previous sections for details).

Site Description

The management-scale prescribed burn was conducted on 13 March 2019 on a ~12.1-ha area located at the Silas Little Experimental Forest (39°54'56.27" N, 74°35′44.00" W) within the

Brendan T. Byrne State Forest, New Lisbon, New Jersey, USA (Figure 85). The area is a mixed oak – pine stand, with chestnut (*Q. prinus* L.), black (*Q. velutina* Lam.), white (*Q. alba* L.), and scarlet (*Q. coccinea* Münchh.) oaks; and shortleaf (*P. echinata* Mill.) and pitch (*P. rigida* Mill.) pines forming the canopy. Dominant trees in the area were approximately 105 years old, and the maximum height of the overstory vegetation was ~20 m. Basal area was approximately 15.5 m^2 ha^{-1}, with oak trees and saplings and pine trees and saplings accounting for 62% and 38% of the total, respectively (Clark et al. 2018). Understory vegetation consisted of shrubs, primarily huckleberry (*Gaylussacia* spp.) and blueberry (*Vaccinium* spp.). Bear (*Q. ilicifolia* Wangenh.) and blackjack (*Q. marilandica* Münchh.) oak, sedges (*Carex pensylvanica* Lam.), and mosses were also present. The litter layer consisted of mixed fine litter of oaks, pines and understory vegetation, fine stems, and reproductive material, primarily pinecones.

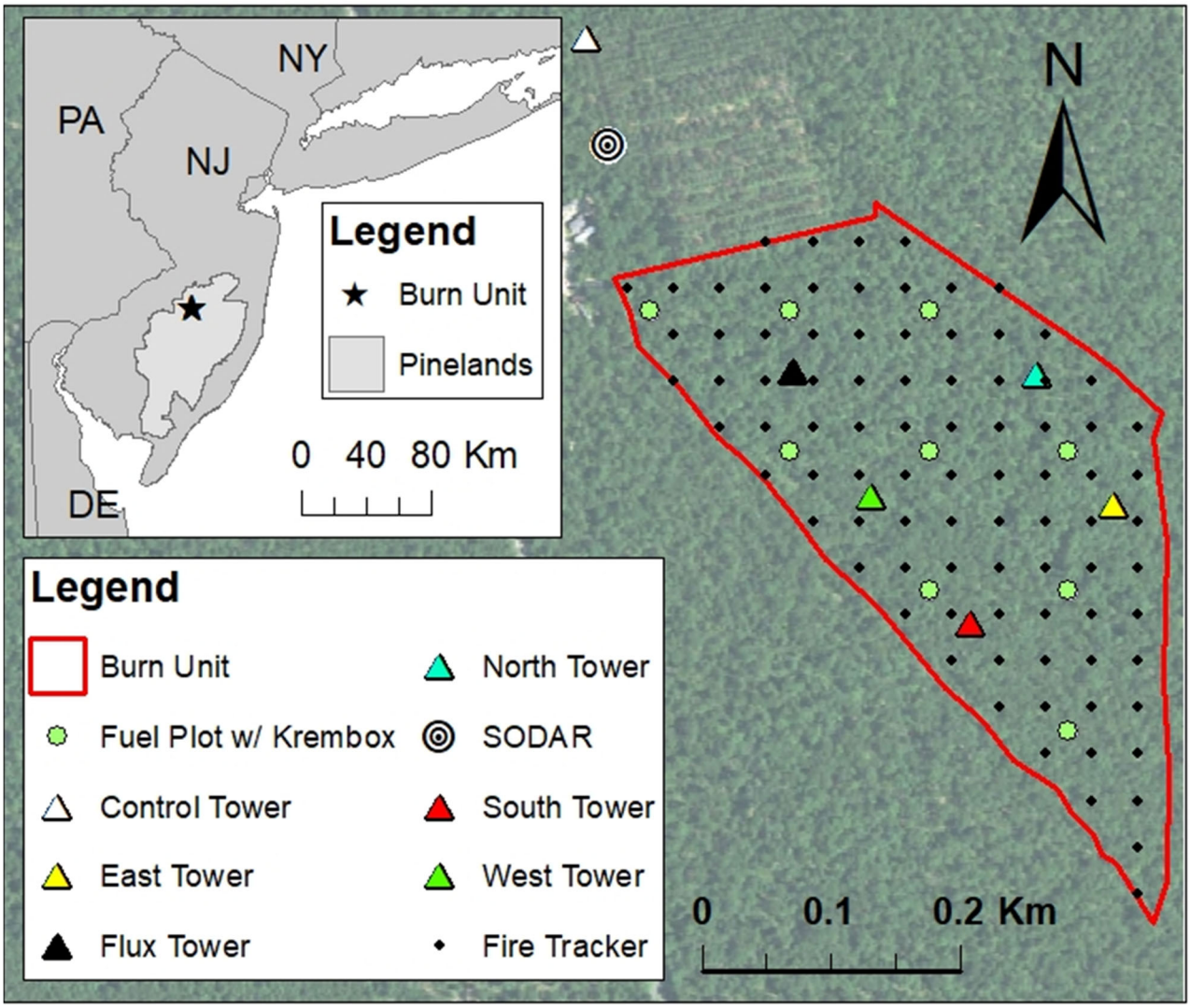


Figure 85. The locations of observed data for the 13 March 2019 SERDP management-scale prescribed burn experiment conducted at the Silas Little Experimental Forest in southern New Jersey.

Fuel loading and consumption

Terrestrial scanning LiDAR (TLS) and biometric measurements were used to estimate forest structure, fuel bed depth and fine-scale variation in fuel consumption and fuel moisture contents. Surface fuels were primarily oak leaves and pine needles, 1-hour and 10-hour stems, understory shrub stems, and oak and pine seedlings and saplings.

Biometric measurements

Pre- and post-burn harvests were used to estimate surface fuel consumption. Circular plots (0.5 m^2) located at 0, 120 and 240 degrees around the perimeter of tree census plots were sampled (n = 12). Additional sampling was conducted around permanent forest census plots (201 m^2) located near the long-term flux tower (Clark et al. 2018). Average fuel moisture content estimated from subsamples collected on site. Fuel moisture samples were stored in separate plastic zip-lock bags and then dried at 70 °C and weighed when dry.

ALS measurements

Airborne laser scanner (ALS) data were collected for the site prior to this experiment in 2009 and has been described in previous studies. The average plant-area-density profile of the overstory vegetation within the experimental area derived from aerial LiDAR measurements was characterized by two maxima; one at approximately 12 m (0.037 m^2 m^{-3}) and the second at 3.5 m (0.029 m^2 m^{-3}) AGL (Skowronski 2011b; Skowronski et al. 2014).

TLS measurements

12 plots located at locations described in Figure 85 as “Fuel Plots”, were scanned immediately before and after each burn was conducted using a Faro Focus 3D X330 HRD (Faro Technologies, Lake Mary, FL). Overstory tower sites, also illustrated in Figure 85, were also scanned pre- and post-burn. TLS data were processed similarly as described in the section of this report on small-scale field experiments, and pre- and post-burn scans were similarly differenced.

Standard meteorology

Standard meteorological measurements were made on one of the five within-plot towers (the flux tower, which also serves as a long-term flux tower in the AmeriFlux network (https://ameriflux.lbl.gov; US-Slt), on the control tower, and on two 3-m towers located to the north of the burn plot within 50 m of the control tower (Figure 85). Incoming shortwave radiation (LI-200, LI-COR, Inc., Lincoln, NE, USA), net radiation (NRLite, Kipp and Zonen, Inc., Delft, the Netherlands), air temperature and relative humidity (HMP45 or HMP50, Vaisala, Inc., Woburn, MA, USA), wind speed and direction (05013-5, R. M. Young Co., Traverse City, MI, USA), and precipitation (TE525, Texas Electronics, Inc., Dallas, TX, USA) were measured at ca. 17 m AGL on the flux and control towers, and at 2 m AGL on the two understory 3-m towers near the burn plot. Soil heat flux was measured using one to three heat flux transducers (#HFT-3.1, Radiation and Energy Balance Systems, Inc., Seattle, WA, USA) buried at 10-cm depth, and soil temperature was measured at a 5-cm depth (CS-107 or CS-109, Campbell Scientific, Inc., Logan, UT, USA) within 20 m of the flux and control towers. Meteorological data were recorded with data loggers (CR10x, CR23x and CR1000, Campbell Scientific, Inc., Logan, UT, USA).

Ambient and fire-induced meteorology

Within the 12.1-ha prescribed burn area, a network of four additional 19-m meteorological towers was set up to monitor atmospheric conditions inside the burn area before the prescribed fire ignition, during the spread of the fire through the area, and after the active burning period (Figure 85). On the long-term flux tower and the four additional towers, sonic anemometers (Model 81000V, R. M. Young, Inc., Traverse City, MI, USA) were mounted at the 3-, 10-, and 19-m levels and aligned in the true-north direction to measure variations in the three-dimensional wind velocity components (U,V,W) and air temperature (T). Data were recorded at 10 Hz using Campbell Scientific CR3000 data loggers (Campbell Scientific, Inc., Logan, UT, USA). Additional temperature measurements were made using thermocouples (Omega SSRTC-GG-K-36, Omega Engineering, Inc., Stamford, CT, USA) mounted at the 0.25-m, 0.5-m, 1.0-m, 2.5-m, 5.0-m, 10.0-m, and 15.0-m levels on each tower. All thermocouples were logged at 10 Hz using CR-3000 data loggers. High-frequency (10 Hz) atmospheric pressure variations were measured at approximately 2.6 m, 8.6 m, and 16.0 m AGL on the west tower.

The control tower was also instrumented with sonic anemometers and thermocouples at the same vertical levels as the sonic anemometers mounted on the within-plot towers to characterize the general ambient wind velocities and temperatures during the experiment. Sonic anemometer and thermocouple data were logged at 10 Hz using CR3000 data loggers.

For better comparison with the 10 by 10-meter experiments conducted in the adjacent plantation, a 100 m^2 subplot surrounding the west tower was instrumented with sonic anemometers mounted at approximately 3 m AGL on four towers located at each corner of the plot. Pressure sensors (BMP180 or BMP280, Sunnyvale, CA, USA) were paired with each sonic anemometer to measure high-frequency (10 Hz) pressure variations. The TACO and a single load cell were also installed near the west tower.

A DOPPLER SOnic Detection and Ranging (SODAR) wind profiler (Remtech PA0, The Villages, FL, USA) was set up near the control tower and within 100 m of the northern edge of the plot to measure lower atmospheric boundary-layer wind speeds and directions (0 – ~400 m above ground level (AGL)) at 20-m intervals every five minutes for the duration of the fire experiment.

Fire Spread

In order to spatially characterize the spread of the prescribed fire through the burn area, an array of 68 FireTracker sensors was installed at ground level throughout the plot in a grid with approximately 40-m spacing between sensors. The sensors consisted of 1.5-mm diameter K-type thermocouples attached to Arduino Feather® data loggers (2796, Adafruit, New York, NY, USA) with thermocouple amplifiers (269, Adafruit) and GPS antennas (746, Adafruit) to time stamp and provide location for each sensor. FireTrackers were placed at a nominal spacing of 25 and were buried such that the tip of the thermocouple protruded through the surface fuels. All FireTracker data were logged at a frequency of 2 Hz.

Fire ignition and general characteristics

At approximately 1500 LT on 13 March 2019, the New Jersey Forest Fire Service ignited a line fire using drip torches along the westernmost boundary of the plot, proceeding from south to north. The line fire was allowed to spread with the wind (i.e., a head fire) from the southwestern

plot boundary through the plot and through the *in situ* towers in a generally northeastward direction until reaching the eastern plot boundary. Burning was confined to the surface and understory fuels; very little overstory vegetation was burned. The southern portions of the line fire reached the eastern plot boundary by approximately 1630 LT, and active burning was completed by approximately 1730 LT.

Data processing and analyses

Fuel loading and consumption

Average consumption was estimated from biometric samples by subtracting post-burn mass from pre-burn mass for each fuel component. Fuel consumption data were expressed as g m^{-2}. To calculate energy partitioning, estimated consumption was multiplied by averaged fuel moisture content for each fuel component.

TLS data around towers were used primarily for the purposes of recording equipment locations within burned areas. Pre- and post-burn TLS data at the radiometer locations were differenced to estimate the change in surface fuel volume.

Fire spread

Arrival at a FireTracker was determined by a temperature rise of greater than 2°C and processed to estimate progression between trackers using the process described in Thomas et al. (In Review). Arrival times were linearly interpolated onto a 5 m x 5 m grid. The inverse of the resultant gradient was used to calculate spread rate vectors. We additionally smoothed these with a box filter, owing to regions of complex fireline interactions resulting in spuriously large values of spread. In this smoothing process, each point filter takes the average of the nearest surrounding grid points (i.e. over a 10 m x 10 m area).

Ambient and fire-induced meteorology

The sonic anemometer data collected during the experiment were subjected to a quality-control procedure that involved the removal of wind-velocity and temperature values that exceeded 6 standard deviations from the running 1-hr velocity component and temperature means. A tilt-correction routine (Wilczak et al. 2001) was applied to the vertical wind-velocity-component data (W) to minimize measurement errors associated with sonic anemometers that were not mounted exactly level on the towers.

Using the quality-controlled sonic anemometer temperature (T) data at the 3-m level on each within-plot tower, individual fire-front-passage (FFP) periods were subjectively determined for each tower based on when the 10 Hz temperature time series from the sonic anemometers at 3 m height and thermocouples at the base of each tower began to clearly display an increasing trend from ambient conditions and when temperatures then returned approximately to ambient conditions. The subjective analysis yielded FFP periods lasting 15 min at the flux and east towers and 20 min at the south, west, and north towers (see

Table 14). 30-minute-long periods before (pre-FFP) and after (post-FFP) the FFP periods were delineated at each tower based on the defined FFP periods.

Following the tilt-correction, data despiking, and fire-period delineation procedures, horizontal streamwise velocities ($S = (U^2 + V^2)^{0.5}$) at each 0.1 s were computed. Mean horizontal streamwise velocities (S); mean zonal ($\bar{U}$), meridional (V), and vertical (W) velocities; and mean

temperatures (T) for the 30-minute-long pre-FFP and post-FFP periods were then computed at each measurement level on each tower and used as the basis for calculating perturbation horizontal streamwise velocities (s' = S - S); perturbation zonal (u' = U - Ū), meridional (v' = V - V) and vertical (w' = W - W) velocities; perturbation temperatures (t' = T - T); turbulent kinetic energy (TKE = 0.5 ($u'^2 + v'^2 + w'^2$)); kinematic heat fluxes (u' t', v' t', w' t'); and kinematic momentum fluxes (u'v', u'w', v'w', s'w') at each 0.1 s within the different periods. Note that perturbation velocities and temperatures computed during the defined FFP periods at each tower were computed using the pre-FFP mean velocities and temperatures to allow for a better representation of the turbulence generated by the fire, a procedure consistent with the methodology of Seto et al. (2013) and Heilman et al. (2015).

The kinematic momentum (s'w') and heat (w't') fluxes that describe the vertical turbulent transport of horizontal (streamwise) momentum and the vertical turbulent transport of heat, respectively, were further analyzed to assess how sweep-ejection dynamics (Wallace 2016) affected the fluxes. The individual s'w' and w't' values at each 0.1 s were classified as sweep events (downward flux of high horizontal momentum air from above: $s' > 0$ and $w' < 0$; downward flux of cool air from above: $w' < 0$ and $t' < 0$), ejection events (upward flux of low horizontal momentum air from below: $s' < 0$ and $w' > 0$; upward flux of warm air from below: $w' > 0$ and $t' > 0$), outward interaction events (upward flux of high horizontal momentum air from below: $s' > 0$ and $w' > 0$; upward flux of cool air from below: $w' > 0$ and $t' < 0$), or inward interaction events (downward flux of low horizontal momentum air from above: $s' < 0$ and $w' < 0$; downward flux of warm air from above: $w' < 0$ and $t' > 0$). Momentum-flux (heat-flux) sweep and ejection events contribute to negative (positive) momentum- (heat-) flux values, whereas momentum-flux (heat-flux) outward and inward interaction events contribute to positive (negative) momentum- (heat-) flux values. The frequency of occurrence of each type of event and the contribution of each type of event to the overall momentum and heat fluxes within the defined pre-FFP, FFP, and post-FFP periods were determined. Frequencies and contributions were assessed at each *in situ* tower location and monitoring level (3, 10, and 19 m AGL).

Friction velocity (u_*, m s^{-1}) and sensible heat fluxes (H, W m^{-2}) were calculated from coordinate-rotated wind velocities and sonic temperature data using instantaneous (10 Hz) deviations from 1-minute block averages using EdiRe software (Clement 2012). Maximum differences in sensible heat flux between burn area and control towers were then calculated for each 1-minute period. Differences in sensible heat fluxes (in MJ m^{-2}) between burn area and control towers were then integrated over the period of each burn and compared to estimates calculated for the sum of consumed fuels.

Results and discussion

Fuel loading and consumption

The pre-burn mean surface fuel loading, which included understory stems, sedges, fine litter, 1-hr and 10-hr wood, and reproductive material averaged was 1.35 ± 0.34 kg m^{-2} (mean ± 1 SD; Table 13, Figure 86). Pre-ignition mean fuel moisture contents for the understory stems, 1-hr fine fuel, 1-hr plus 10-hr wood, and 10-hr fuel moisture sticks near meteorological towers were 53.0 ± 8.0%, 25.6 ± 6.8%, 21.5 ± 9.0%, and 12.1 ± 1.5%, respectively.

Biometric estimates of consumption indicated that consumed fuel was primarily fine litter and herbs, representing > 95% of total consumption, while little consumption of understory stems and woody fuels occurred. Total fuel consumption was averaged 0.34 kg m^{-2} and represented 25% of pre-burn surface fuel loading (Table 13, Figure 86).

Table 13. Pre-burn and post-burn surface and understory fuel loading in the prescribed burn area and estimated fuel consumption.

Fuel type	Pre-Burn ($g\ m^{-2}$)	Post-Burn ($g\ m^{-2}$)	Consumption ($g\ m^{-2}$)
Understory stems	281.5 ± 96.3	260.9 ± 124.5	20.6
Sedges	5.4 ± 9.8	0.0 ± 0.0	5.4
Fine litter	929.3 ± 604.8	604.8 ± 116.2	324.5
1-Hour wood	84.7 ± 85.0	85.0 ± 25.6	-0.3
10-Hour wood	29.4 ± 32.6	32.6 ± 21.9	-3.2
Reproductive	16.7 ± 26.0	26.0 ± 19.0	-9.3
Total	1347.0 ± 338.1	1009.2 ± 119.1	337.8

Following Kremens et al. (2012), consumption and moisture content of fuels were used to calculate energy partitioning during combustion (Figure 86).

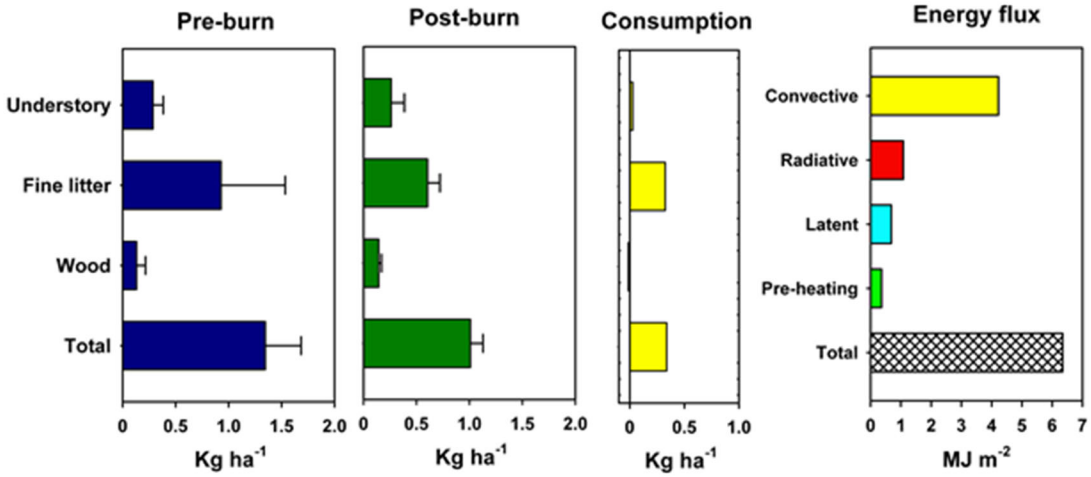


Figure 86. Pre- and post-burn fuel loading and estimated consumption from 24 0.5 m^{-2} plots at the March 13, 2019 management scale burn. Additional sampling was conducted in forest census plots within 100 m of the main flux tower (see Clark et al. (2018)for details). Energy partitioning was calculated from consumed fuels and moisture contents, following Kremens et al. (2012).

Standard meteorology

Above canopy (19 m) wind speed and direction averaged 2.87 ± 0.05 m s^{-1} and 185 ± 27 ° (south-southwesterly winds) during the prescribed burn, with peak gusts of 6.26 ± 0.32 m s^{-1}. Air temperature and relative humidity above canopy averaged 12.09 ± 1.95 °C and 33.8 ± 9.5 % over the course of the fire. 10-hour fuel temperature averaged 18.10 ± 4.61 °C. The near-surface (3 m AGL) ambient mean wind speed, wind direction, temperature and relative humidity in the plot during the 30-min period before ignition was 0.41 m s^{-1}, 228° (southwesterly winds), 11.28 °C, and 24.9 %, respectively.

Fire Spread

After ignition of the line-fire along the western boundary of the burn plot beginning at approximately 1500 LT, the fire front moved in a general southwest to northeast direction with the wind and passed through all of the tower locations. Estimated fireline position as a function of time derived from the Firetracker network is shown in Figure 87.

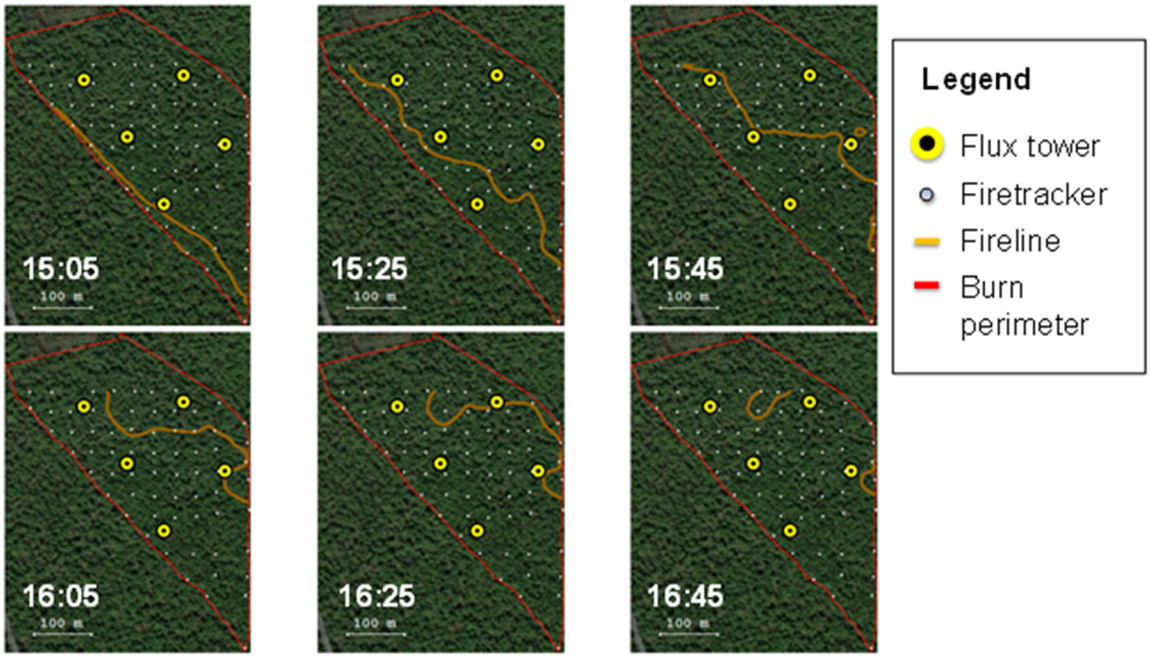


Figure 87. Fireline progression for the management scale burn conducted on March 13, 2019. The fireline is shown in orange, and timestamps for each image are shown in white in the lower left corner of each image.

The spreading line-fire induced temperature, wind velocity, and turbulence variations near the fire front and extending from the surface upward through the top of the forest overstory vegetation.

Table 14 shows time periods in local time when flame fronts were in the vicinity of each tower, as measured by sonic anemometers at 3 m height and thermocouples at the base of each tower.

Table 14. Time periods (LT) for the delineated pre-FFP, FFP, and post-FFP periods at each tower located in the interior of the prescribed burn plot.

Tower	Pre-FFP	FFP	Post-FFP
South	14:25 - 14:55	14:55 – 15:15	15:15 – 15:45
West	14:55 – 15:25	15:25 - 15:45	15:45 – 16:15
Flux	14:55 – 15:25	15:25 – 15:40	15:40 – 16:10
East	15:08 – 15:38	15:38 – 15:53	15:53 – 16:23
North	15:43 - 16:13	16:13 – 16:33	16:33 - 17:03

Ambient and fire-induced meteorology

Time series of the 10 Hz temperature (T); zonal, meridional, and vertical velocity components (U,V,W); and turbulent kinetic energy (TKE) at the 3-, 10-, and 19-m levels on the west tower during the experiment are shown in Figure 88. The time series are representative of the general impact the advancing line fire had on atmospheric conditions at all the tower locations.

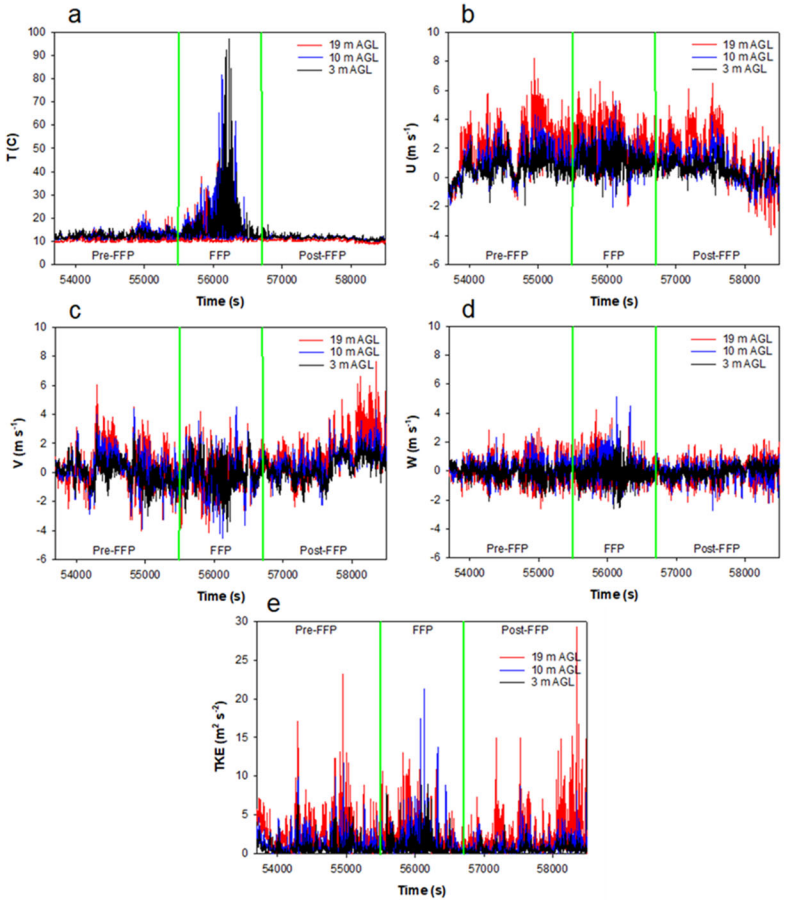


Figure 88. Time series of (a) temperature (T), (b) zonal wind velocity (U), (c) meridional wind velocity (V), (d) vertical wind velocity (W), and (e) turbulent kinetic energy (TKE) at 3 m, 10 m, and 19 m AGL before, during, and after fire-front-passage at the west tower.

During much of the 30-min pre-FFP period at the west tower (1455-1524 LT), instantaneous temperatures ranged from ~10-15°C, generally decreasing with height from the 3-m to the 19-m level (Figure 88a). About 15 min before the beginning of the FFP period, some instantaneous temperatures at the 10- and 19-m levels reached ~20°C due to the downwind transport of the convective plume generated by the upwind fire front. During the 20-min FFP period, instantaneous temperatures above 90°C were observed at the 3-m level. Temperatures generally returned to pre-FFP values during the 30-min post-FFP period, although the variability in the post-FFP temperatures was noticeably less than the pre-FFP variability. For example, at 3 m AGL, the temperature standard deviation decreased from 1.17°C during the pre-FFP period to 0.76°C during the post-FFP period. The zonal (Figure 88b) and meridional (Figure 88c) velocity component time series indicate northwesterly to southwesterly wind-direction fluctuations over most of the pre-FFP to post-FFP period, with wind speeds increasing with height through the overstory vegetation and most of the horizontal velocity response to the line fire during the FFP period occurring at the 3-m and 10-m levels. The FFP period was characterized by enhanced updrafts of up to 6 m s^{-1} leading up to and during the time when the fire front passed through the

west tower location, and enhanced downdrafts of half the magnitude of the updrafts for a short period of time after the front passed the tower (Figure 88d). Finally, although the average energy of the turbulent circulations (TKE) during the FFP period was higher near the canopy top (19 m AGL) than at levels below, episodes of very high TKE values at the 10-m mid-canopy level were prominent; a maximum TKE value exceeding 20 $m^2 s^{-2}$ occurred there (Figure 88e). Also noteworthy is the more quiescent turbulence regime at the 3- and 10-m levels during the post-FFP period compared to the pre-FFP period; TKE standard deviations at the 3-m and 10-m levels decreased from 0.66 $m^2 s^{-2}$ and 1.00 $m^2 s^{-1}$ to 0.47 $m^2 s^{-2}$ and 0.78 $m^2 s^{-2}$, respectively.

Mean pre-FFP, FFP, and post-FFP temperatures, wind velocity components, and values at the three monitoring levels computed from all the *in situ* towers are shown in Figure 89. Features of the period means include (1) the tendency for post-FFP temperatures to fall below pre-FFP temperatures (Figure 89a) due in part to downdrafts behind the fire front (Figure 89d); (2) a general shift toward more southerly winds in moving from the pre-FFP periods through the FFP periods and into the post-FFP periods, particularly at the 3- and 10-m levels Figure 89 and Figure 89c); (3) the tendency for values to increase with height, even during FFP periods when atmospheric temperature perturbations are at a maximum near the surface (Figure 89e); and (4) the substantial weakening of the turbulence regime in moving from the FFP environment to the post-FFP environment, with post-FFP mean values dropping below pre-FFP means at all monitoring levels (Figure 89e).

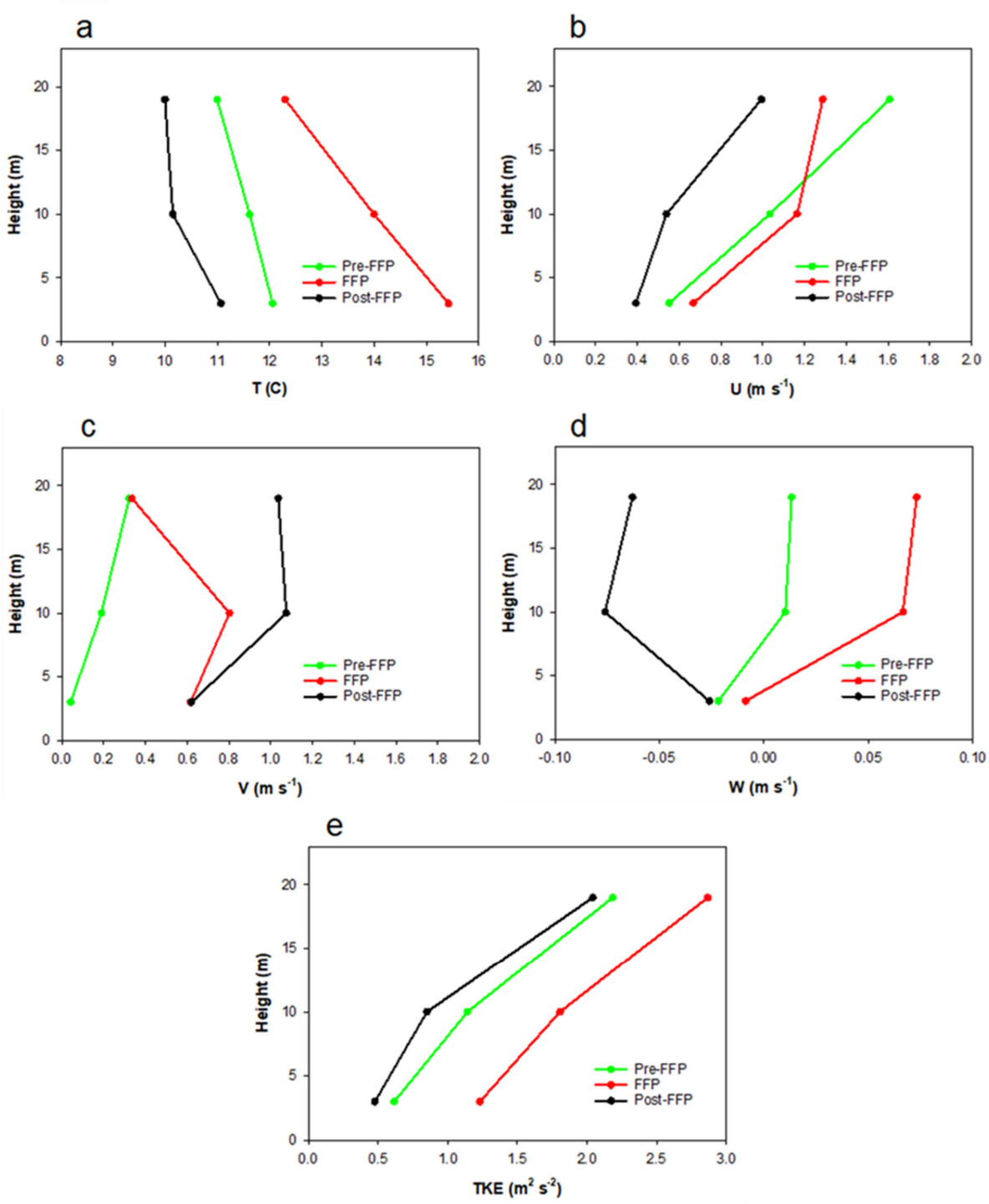


Figure 89. Mean (a) temperatures (T), (b) zonal wind velocities (U), (c) meridional wind velocities (V), (d) vertical wind velocities (W), and (e) turbulent kinetic energy (TKE) at 3 m, 10 m, and 19 m AGL during the pre-FFP, FFP, and post-FFP periods, computed from all five in situ towers.

Additional turbulence statistics are shown in Table 15 and provide a general summary (averages across all the *in situ* towers) of the height-dependent impacts of the spreading surface line fire on the temporal means of the TKE components (u'^2,v'^2,w'^2), turbulence anisotropy ($w'^2(2 * TKE)^{-1}$), the kinematic horizontal and vertical momentum fluxes ($u'v'$,$u'w'$,$v'w'$), and the kinematic horizontal and vertical heat fluxes ($u't'$,$v't'$,$w't'$) during the pre-FFP, FFP, and post-FFP periods. The TKE component and anisotropy statistics clearly show that most of the energy of the turbulent circulations at all height levels during the fire experiment was associated with the horizontal velocity perturbations as opposed to the vertical velocity perturbations, even during the highly buoyant FFP periods; average anisotropy values were always less than the 0.33 isotropic value. Averaged anisotropy was always most pronounced at the 3-m level. The kinematic momentum-flux magnitudes almost always increased with height within the overstory vegetation layer. It is noteworthy that during the FFP and post-FFP periods, horizontal momentum-flux ($u'v'$) magnitudes tended to exceed the vertical momentum-flux ($u'w'$,$v'w'$) magnitudes at all height levels. The observed horizontal ($u't'$,$v't'$) and vertical ($w't'$) kinematic heat-flux magnitudes did not always increase with height. At the 3-m level during FFP periods and at the 3- and 10-m levels during the post-FFP periods, horizontal heat-flux magnitudes tended to exceed vertical heat-flux magnitudes.

Also included in Table 15 are the height-dependent, tower-averaged, horizontal and vertical velocity distribution skewness values ($Sk_u = u'^3\sigma_u^{-3}$, $Sk_v = v'^3\sigma_v^{-3}$, $Sk_w = w'^3\sigma_w^{-3}$; where σ_u, σ_v, and σ_w are the standard deviations of the U, V, and W velocities, respectively) for the three periods. The skewness values underscore the impacts a wildland fire in a forested environment can have on inducing non-Gaussian turbulence regimes. During the pre-FFP periods, Sk_u and SK_v values at all height levels tended to be positive, with tower-averaged values ranging from 0.10 to 0.42. Sk_w values tended to be negative within the forest overstory vegetation layer at the 3- and 10-m levels and slightly positive near the canopy top at 19 m AGL. Tower-averaged Sk_w values were -0.46, -0.16, and 0.08 at the 3-, 10- and 19-m levels, respectively. The highly buoyant FFP periods were characterized by positively skewed horizontal and vertical velocity distributions at all height levels. During the post-FFP periods, vertical velocity distributions tended to be even more negatively skewed than during the pre-FFP periods, as indicated by the tower-averaged Sk_w value of -0.76 at the mid-canopy 10-m level.

The general temperature, wind velocity, and turbulence regimes that characterized the pre-FFP, FFP, and post-FFP periods at the *in situ* towers, as described in the previous section, sets the context for an analysis of the momentum-flux sweep-ejection dynamics that occurred during the fire experiment. Associated with the ambient and/or fire-induced wind-velocity variations during the three periods were variations in the vertical turbulent fluxes of horizontal momentum throughout the vertical extent of the forest overstory vegetation. Sweep, ejection, outward interaction, and inward interaction events all contributed to the mean momentum fluxes that characterized the pre-FFP, FFP, and post-FFP periods. However, the relative number of occurrences of the different types of events and their relative contributions to the period-specific mean momentum fluxes varied substantially from one period to another.

Table 15. Turbulence statistics at the 3-m, 10-m, and 19-m levels within the pre-FFP, FFP, and post-FFP periods. Brackets indicate an average across all the in situ towers. Overbars indicate temporal means within each period. Units for the tower-averaged temporal mean TKE components (u'^2, v'^2, w'^2), kinematic momentum fluxes ($u'v'$, $u'w'$, $v'w'$), and kinematic heat fluxes ($u't'$, $v't'$, $w't'$) are $m^2\ s^{-2}$, $m^2\ s^{-2}$, and $m\ s^{-1}$ °C, respectively. Anisotropy values ($w'^2\ (2 * TKE)^{-1}$) and skewness values for the horizontal and vertical velocity distributions (Sk_u, Sk_v, Sk_w) are unitless.

Variable	Pre-FFP			FFP			Post-FFP		
	3 m	10 m	19 m	3 m	10 m	19 m	3 m	10 m	19 m
$[w'^2]$	0.53	0.9	2.12	0.8	1.14	2.63	0.44	0.81	1.67
$[w'^2(2*TKE)^{-1}]$	0.59	1.09	1.69	1.36	1.82	2.2	0.42	0.66	1.94
$[u'v']$	0.11	0.29	0.56	0.31	0.66	0.91	0.09	0.23	0.47
$[u'w']$	0.14	0.18	0.19	0.16	0.23	0.21	0.15	0.19	0.17
$[u't']$	-0.05	-0.01	-0.1	-0.13	-0.23	-0.58	-0.09	-0.12	-0.4
$[u'w']$	-0.07	-0.14	-0.3	-0.03	-0.18	-0.29	-0.03	-0.07	-0.15
$[v'w']$	-0.01	-0.09	-0.06	-0.01	-0.04	0.01	0	-0.1	-0.17
$[u't']$	-0.02	-0.02	-0.14	1.15	0.12	-0.56	0.01	0.05	-0.02
$[v't']$	0.07	0.17	0.11	2.4	0.94	-0.23	-0.13	-0.24	-0.31
$[w't']$	0.12	0.26	0.43	1.85	2.93	2.75	0.09	0.08	0.16
$[SK_u]$	0.1	0.18	0.23	0.72	0.55	0.02	-0.03	0.09	-0.09
$[SK_v]$	0.32	0.42	0.29	0.9	0.68	0.19	0.09	0.39	0.49
$[SK_w]$	-0.46	-0.16	0.08	0.31	0.74	0.86	-0.4	-0.72	-0.21

Figure 90 shows the mean fractional number of sweep, ejection, outward interaction, and inward interaction events at the three monitoring heights on the *in situ* towers during the pre-FFP, FFP, and post-FFP periods based on the 10 Hz sonic anemometer measurements. The pre-FFP and post-FFP periods (Figure 90a and Figure 90c) at all the monitoring heights were dominated by ejection (upward flux of lower horizontal momentum air from below) and sweep (downward flux of higher horizontal momentum air from above) events. Both types of events contributed to negative vertical momentum fluxes ($s'w' < 0$). The frequencies of occurrence of outward interaction (upward flux of higher horizontal momentum air from below) and inward interaction (downward flux of lower horizontal momentum air from above) events during these periods were much lower, with both of those events contributing to positive vertical momentum fluxes ($s'w' > 0$). In contrast to the pre- and post-FFP periods, the FFP periods at the tower locations were dominated by sweep events at all height levels, with outward interaction events also being relatively frequent at the 3-m height level (Figure 90b). The increases in the number

of sweep and outward interaction events primarily came at the expense of ejection events. The number of inward interaction events were also at a minimum during the FFP periods compared to the pre- and post-FFP periods.

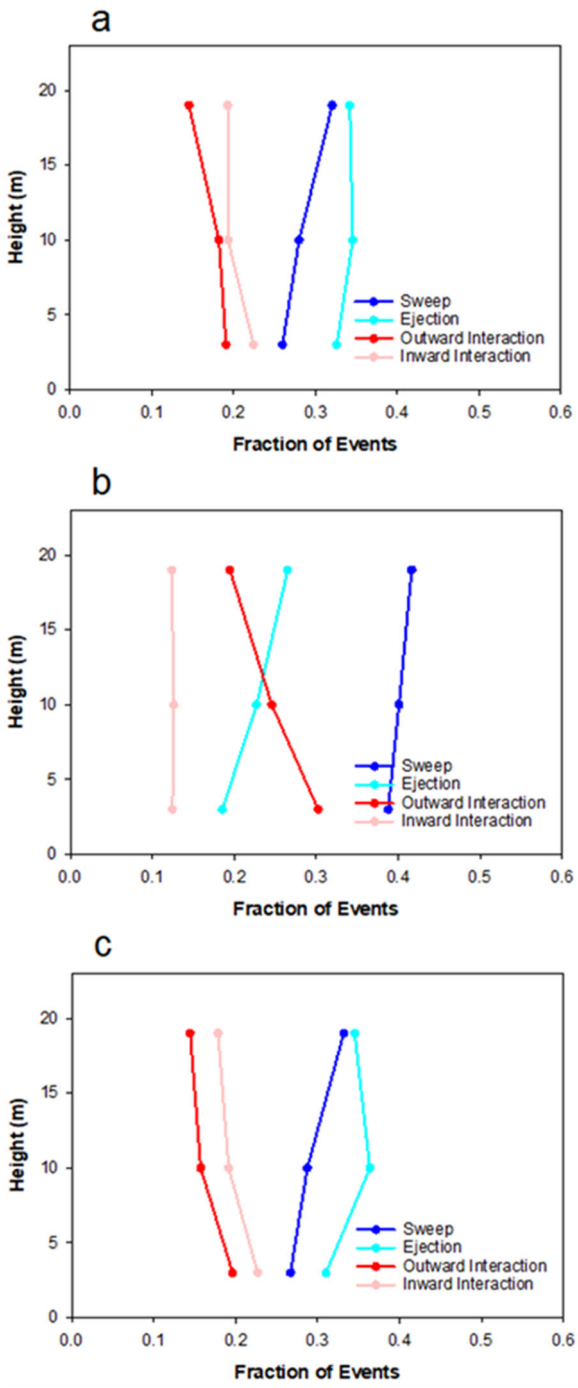


Figure 90. Mean fractional number of sweep, ejection, outward interaction, and inward interaction events during the (a) pre-FFP, (b) FFP, and (c) post-FFP periods at 3 m, 10 m, and 19 m AGL, computed from all five in situ towers.

The individual sweep, ejection, outward interaction, and inward interaction events with their varying levels of occurrence collectively contributed to the average vertical turbulent momentum fluxes that characterized each period at the different tower locations. As with the occurrence analyses shown in Figure 90, the relative flux contributions of the different types of events varied from one period to another (Figure 91). Although ejection events were the most common type of event during the pre- and post-FFP periods at all height levels (Figure 90a and Figure 90c), sweep events actually made the largest contributions to the mean momentum fluxes at all levels in those periods (Figure 91a and Figure 91c). Even during the highly buoyant FFP periods, sweep events were usually of sufficient strength throughout the vertical extent of the forest overstory vegetation layer to maintain negative vertical momentum fluxes at all levels (Figure 91b). The more frequent outward interaction events during the FFP periods, particularly at the 3- and 10-m levels (Figure 90b), mitigated the flux contribution effects of the sweep events and reduced the magnitudes of the negative vertical momentum fluxes in the FFP periods. At one of the towers (south tower), outward interaction events during the FFP period were actually strong enough to lead to an overall positive mean momentum flux (0.091 m^2 s^{-2}) at the 3-m level for the period.

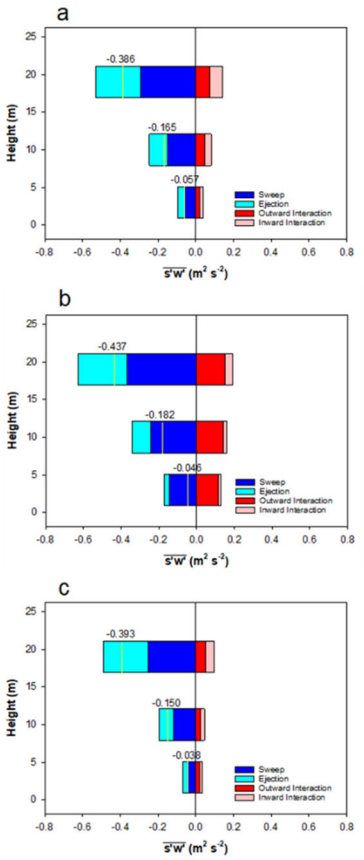


Figure 91. Mean contributions of sweep, ejection, outward interaction, and inward interaction events to the average vertical turbulent momentum fluxes during the (a) pre-FFP, (b) FFP, and (c) post-FFP periods at 3 m, 10 m, and 19 m AGL, computed from all five in situ towers. Average vertical turbulent momentum flux values (m^2 s^{-2}) at each height level are indicated with labeled yellow vertical lines.

Similar to the discussion above, the quadrant analysis technique was also applied to the turbulent heat fluxes observed at the three levels on each of the five towers in the burn plot to delineate the contributions of different types of events to turbulent vertical heat transfer throughout the vertical extent of the forest overstory vegetation during the pre-FFP, FFP, and post-FFP periods. Figure 92 shows the mean fractional number and the contribution of sweep, ejection, outward interaction, and inward interaction events during the pre-FFP, FFP, and post-FFP periods at 3 m, 10 m, and 19 m AGL, computed from the flux tower within the burn plot. The results from the other four towers within the burn plot are similar to those of the flux tower. Also shown in Figure 92 are results from the control tower located north of the burn plot. Because the control tower was unaffected by the fire, results from the control tower turbulent heat flux sweep-ejection analysis serve as indicators for the distribution and time evolution of ambient vertical turbulent heat fluxes. Comparisons of the results between the control tower and the flux tower help elucidate the influence of fire on turbulent vertical heat transfer through the canopy layer. For comparison, the time series for the control tower was also divided into three periods corresponding to the pre-FFP, FFP and post-FFP periods at the flux tower, although the control tower was not influenced by the fire.

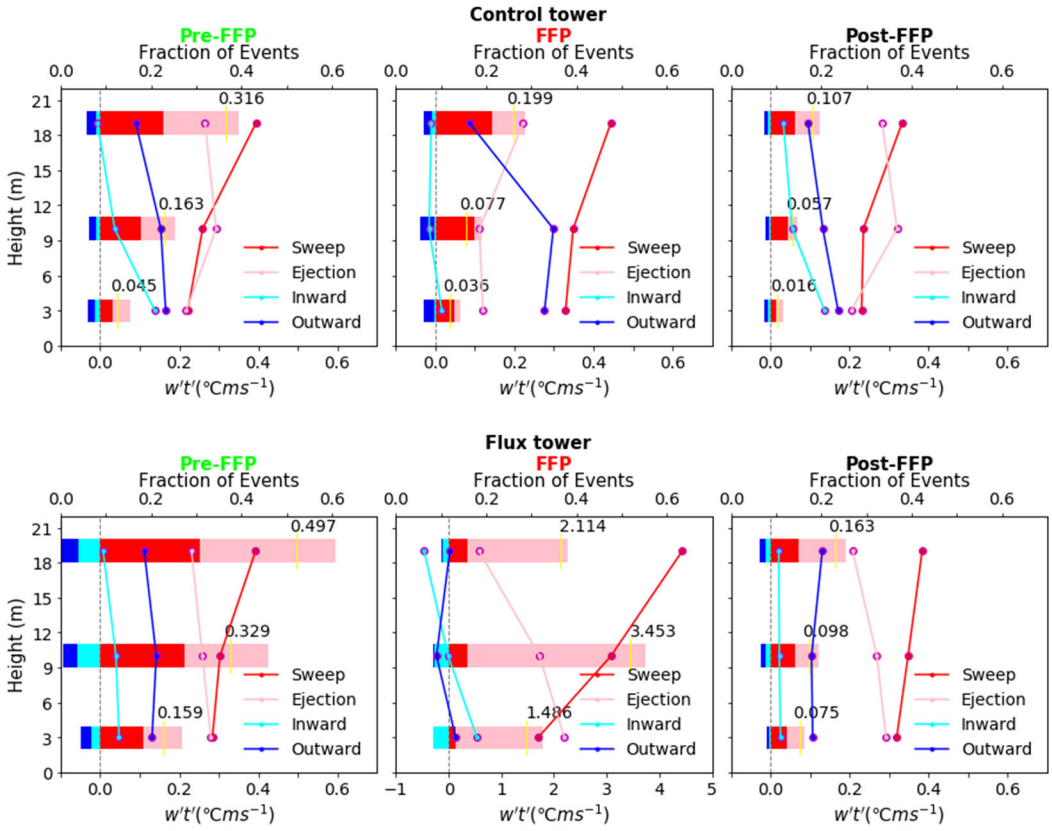


Figure 92. Mean fractional number (lines) and contributions (bars) of sweep, ejection, outward interaction, and inward interaction events to the average vertical turbulent momentum fluxes during the (a) pre-FFP, (b) FFP, and (c) post-FFP periods at 3 m, 10 m, and 19 m AGL at the control tower and the flux tower. Average vertical turbulent momentum flux values (m^2 s^{-2}) at each height level are indicated with labeled yellow vertical lines.

During the pre-FFP period, the sweep (downward flux of cool air from above) and ejection (upward flux of warm air from below) events (vertical profiles) generally comprised 60-70% of all the events from the 3-m level up to the canopy top near 19-m AGL. Sweep events were comparable in numbers to those of ejection events at the 3- and 10-m levels, but were 10-15% more frequent than ejection events at the 19-m level. Despite being less frequent, ejection events made larger contributions to the total vertical turbulent heat flux than sweep events at the 19-m level. At the two lower levels, the contributions from ejection and sweep events were comparable. At all three levels, outward interaction events (upward flux of cool air from below) outnumbered the inward interaction events (downward flux of warm air from above), but their contribution to the total vertical heat flux was similar. The relative frequency and contribution results for the four types of events were consistent between the flux and control tower, which is expected during the pre-FFP period. There were, however, some differences in the values of the frequencies and especially the contributions. The positive contributions to the heat flux from sweep and ejection events, the negative contributions from inward and outward interaction events, and the resulting total heat fluxes were considerably larger at all three levels on the flux tower than on the control tower, indicating the influence of local vegetation and meteorological conditions on the vertical turbulent heat flux.

Moving from pre-FFP period to the FFP period, there was a decrease in the heat flux at all three levels on the control tower, resulting primarily from a decrease in ejection events and their contributions associated with the diurnal variation in local meteorological conditions. Compared to the control tower, the event-frequency and heat-flux contribution changes that occurred from the pre-FFP period to the FFP period at the flux tower were substantial. The total vertical turbulent heat fluxes increased by nearly 10 times at the 3- and 10-m levels and about 5 times at the 19-m level. These dramatic increases resulted primarily from the substantial increases in the contributions of ejection events, although the contributions from sweep events to the upward heat flux and from inward and outward interaction events to the downward flux also increased. The drastic increases in the contributions from ejection events were, however, not matched by similar increases in their frequencies of occurrence. In fact, the frequency of ejection events decreased by more than 10% from the pre-FFP period to the FFP period at the 19-m level, while the frequencies of sweep events increased by more than 10% at both the 10- and 19-m levels. This mismatch between the frequency of occurrence and contribution behavior indicates that the fire significantly enhanced the upward transfer of warm air from the surface and inside the forest canopy but did not increase the frequency of upward heat-transfer events. The enhanced upward heat transfer during the FFP period was accompanied by an increase in the number of sweep events that brought cooler air from above into the canopy layer toward the surface, but the actual contributions of the sweep events to the overall heat fluxes at each level were small compared to the ejection-event contributions.

The post-FFP period was marked by a return to the pre-FFP conditions. The overall heat fluxes at all three levels on the control tower were smaller during the post-FFP period than during the pre-FFP period, reflecting the cooling and stabilization of the ambient atmosphere as a sea-breeze front passed through the area. The relative values of the frequencies and contributions at all three levels were similar between the pre-FFP and post-FFP periods at both towers. The

sea-breeze passage may have also played an important role in reducing local effects and making the ambient atmosphere more homogenous, as seen by the much smaller difference between the flux tower and the control tower during the post-FFP period compared to the pre-FFP period.

"Energy release during management-scale burns": As buoyant plumes rose above flame fronts, they cooled but also accelerated. This is indicated in Figure 93, where although maximum temperatures decreased with height above flame fronts, the slopes of the relationship between air temperature and vertical windspeeds increased with height.

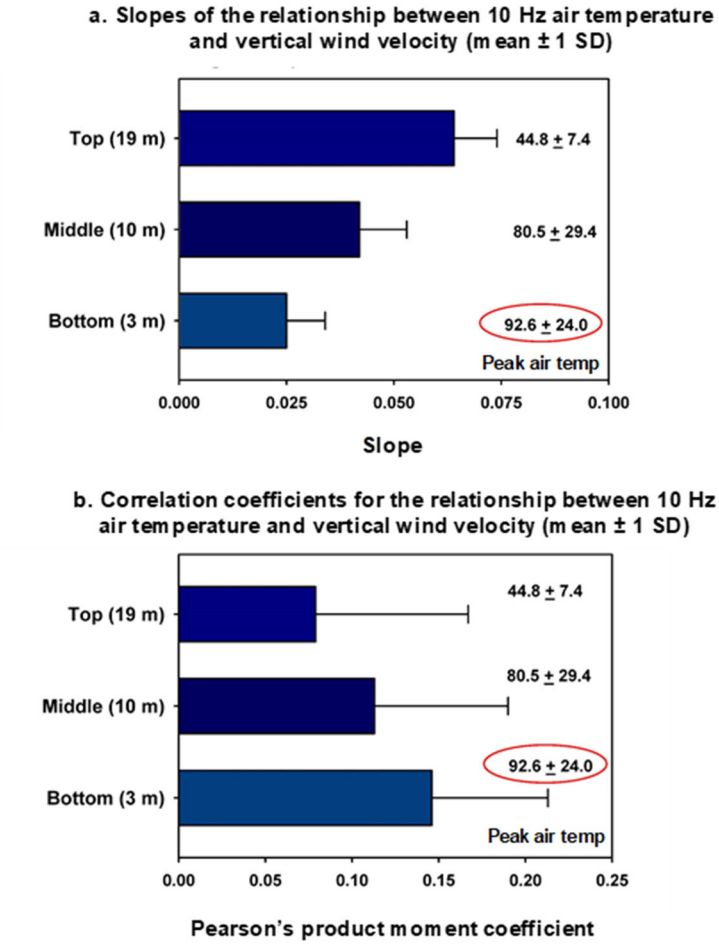


Figure 93. (a) Average slopes and (b) correlation coefficients for the relationship between air temperature and vertical wind velocity at different heights above flame fronts during the large-scale burn at Silas Little Experimental Forest conducted on March 13, 2019. Average maximum 10 Hz air temperatures (mean ± 1 SD) at each height are indicated to the right of each bar.

Correlations are strongest at the lowest level (3-meter height), consistent with profile measurements made during 10 by 10-meter burns 7 and 8 (see previous section, Figure 76a and b). As a result of temperature (decreasing with height) and vertical wind velocity (increasing with height) profiles generated above flame fronts, peak 1-minute sensible heat flux values (which approximate convective heat flux) are conserved through the canopy, as shown in Figure 94a.

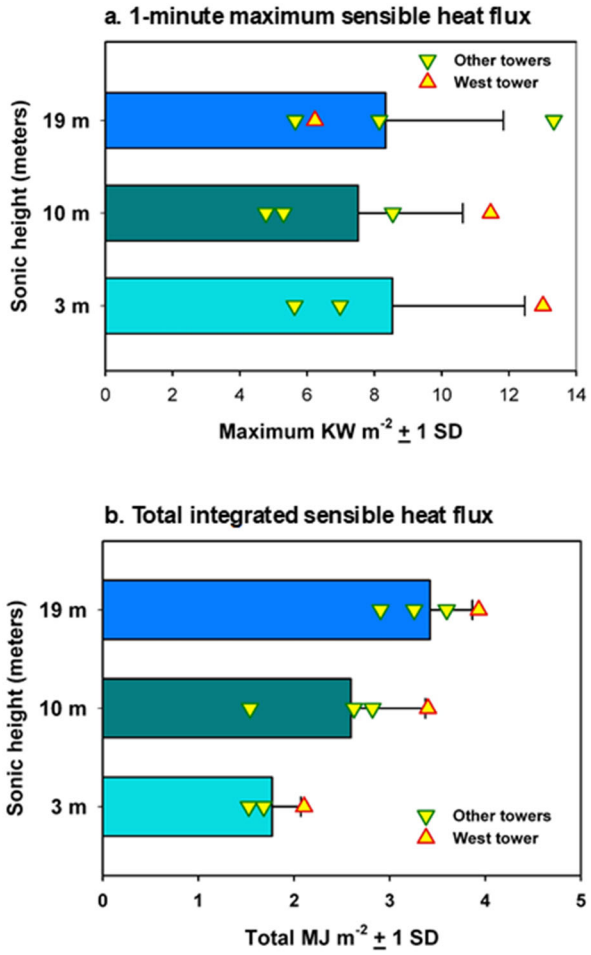


Figure 94. (a) 1-minute peak sensible heat flux and (b) integrated total `sensible heat flux measured at different heights above flame fronts during the large-scale burn at Silas Little Experimental Forest conducted on March 13, 2019. Red lined triangles indicated values for the west tower, and green lined triangles indicated values for the other towers in the burn area.

Total integrated heat flux increased with height through the canopy at nearly all locations (Figure 94b). Similar profiles have been observed in other instrumented management-scale prescribed fires (Figure 95), as well as during some of the 10 by 10-meter experiments. Exposure of canopy fuels to relatively warm, high vertical velocity plumes warms and potentially dries ladder and canopy fuels, contributing to flame propagation and crown torching.

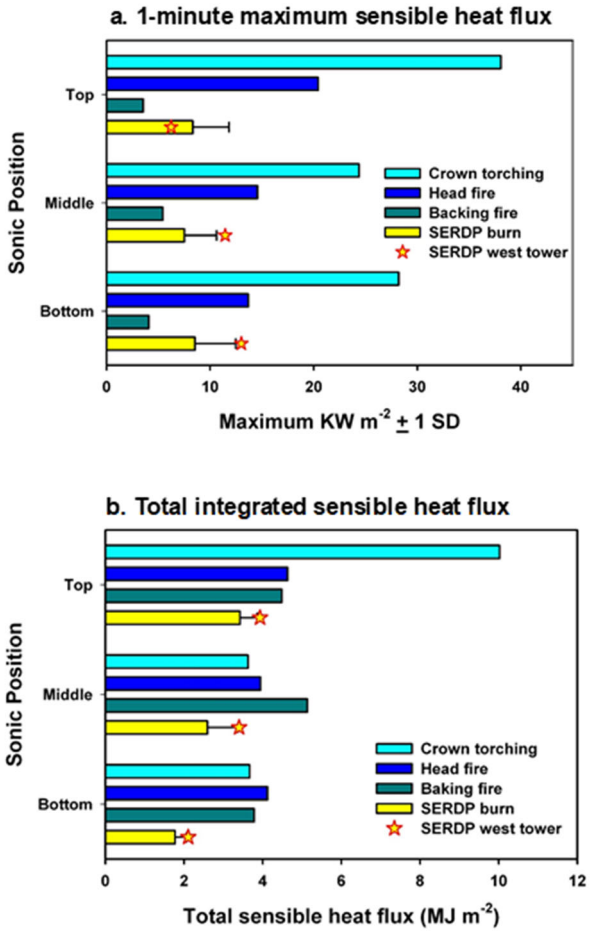


Figure 95. (a) Maximum 1-minute sensible heat flux and (b) total sensible heat flux at different heights above flame fronts during four instrumented burns in the New Jersey Pinelands. Values are means ± 1 SD, and values from the west tower at the SERDP management scale burn are indicated with yellow stars.

Figure 95 indicates that peak 1-minute sensible flux values measured at each tower during the management scale burn ("SERDP burn" in Figure 95) are intermediate compared to backing and head surface fires, and considerably lower than a fire characterized by pitch pine crown scorching conducted in the New Jersey Pinelands. Total integrated sensible heat flux during the management scale burn is also similar to somewhat lower than values measured during other surface fires (Figure 95b).

Sensible heat measured at each height during the management scale burn conducted in 2019 accounted for 81 ± 11%, 62 ± 18% and 42 ± 7% of estimated convective heat flux calculated from fuel consumption shown in Figure 86. On average, sensible heat fluxes measured above canopy accounted for approximately 70% of estimated convective heat flux calculated for consumed fuels (Figure 95b). Across all experiments in (Clark et al. 2020) and an additional instrumented prescribed fire conducted in February 2020, sensible heat flux measured at the top of the canopy was approximately 90% of calculated convective heat fluxes (Figure 96). It should

be noted that heat storage in unconsumed fuels, the forest floor and soil layers are not accounted for in these comparisons (e.g., Kremens et al. (2012)).

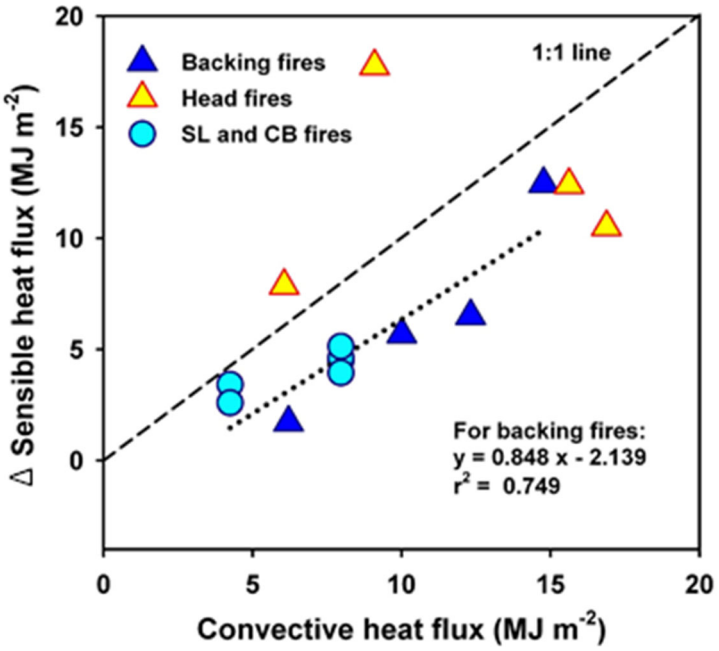


Figure 96. Convective heat flux calculated from fuel consumption measurements and above-canopy Δ sensible heat flux for low-intensity backing fires (blue symbols) and high-intensity head fires (yellow symbols).

Conclusions and implications for future research

Highly instrumented management scale prescribed fires integrate a myriad of processes, but well-designed experiments that focus on specific questions can improve our understanding of fire behavior during prescribed fires. We found that the use of consistent instrumentation and integration times across scales and building on previous research efforts has facilitated progress at this larger scale. Dense arrays of thermocouples and relatively inexpensive sonic anemometers to measure turbulence and sensible heat fluxes at multiple heights above the flame fronts has provided reasonably well-resolved turbulence and energy flux data, at least during lower intensity fires. The use of newly designed networks such as the "Firetrackers" and multispectral sensors to estimate arrival times, intensity, and radiative heat fluxes improved our ability to track fire fronts, their energy release, and overall energy balance during management scale fires.

One of our key finding suggests that even in the buoyant atmospheric layers above fire fronts within forested areas, the downward turbulent flux of higher horizontal momentum air from aloft can still occur throughout the vertical extent of the overstory vegetation and thereby potentially introduce high momentum air (i.e., wind gusts) into combustion zones and affect fire spread. The extent to which this downward turbulent momentum transfer can occur, of course, is partially dependent on fire intensity, but also related to the plant-area-density characteristics of the overstory vegetation, with denser overstory vegetation leading to enhanced dissipation of turbulence energy via the breakdown of large turbulent eddies to smaller turbulent eddies by

forest structural elements. Convective heat flux calculated from fuel consumption and sensible heat flux calculated from sonic anemometer data during the passage of fire fronts compared favorably, as has been demonstrated in previous large-scale prescribed fires.

Management-scale atmospheric modeling

Objective

The overall goal of the management-scale numerical modeling component of this project was to explore the complex interactions of ambient, fire, and forest overstory-induced mean and turbulent flows, across spatial scales of 100 m to 1000 m and time scales of minutes to one hour, with applicability to fire spread and energy transfer through forest canopies. The field measurements from the management-scale component of the project were used to guide the development of and improve the accuracy of numerical simulations of the ambient, fire, and forest overstory-perturbed atmosphere during the 2019 management-scale prescribed fire in the Silas Little Experimental Forest (SLEF). All management-scale numerical simulations were performed using a version of the Advanced Regional Prediction System (ARPS) model (Xue et al. 2000; Xue et al. 2001) capable of simulating mean and turbulent flows within and above forest vegetation layers (ARPS-CANOPY; (Kiefer et al. 2013; Kiefer et al. 2014)). The management-scale modeling component of the project took place in three phases:

- Pre-burn guidance simulations intended to help guide the placement of instrumentation prior to the management-scale field experiment. A series of simulations were conducted in late 2018 and early 2019 to characterize the ambient, fire, and forest overstory-induced mean and turbulent flows in a burn plot in the Franklin Parker Preserve (FPP) in south-central New Jersey. Due to the federal government partial shutdown in early 2019, the FPP burn was not conducted, and a field experiment was instead conducted in SLEF in March 2019. The last-minute change to the burn block location precluded the development of pre-burn guidance simulations for the SLEF burn.
- *Post-burn validation exercise to identify the strengths and weaknesses of the model, informing future model development.* Observations collected during the SLEF field experiment were used to validate the model and identify where and when the model captured the ambient, fire, and forest overstory-induced mean and turbulent flows, and conversely, where and when it did not.
- Sensitivity tests performed to characterize the response of ambient, fire, and forest overstory-induced mean and turbulent flows to lower-confidence aspects of the model and experiment design. Tests conducted include (1) the method used to represent the fire sensible heat source in the model (exponentially decaying vertical turbulent heat flux profile and soil temperature perturbation), (2) characteristics of the exponentially decaying vertical turbulent heat flux profile (surface heat flux value and e-folding depth), (3) the model vertical grid structure, and (4) the canopy drag coefficient.

Background

Numerical models are used to study ambient, fire, and forest overstory-induced flows to fill in gaps in our knowledge of fire-atmosphere-canopy interactions and to help answer questions that field experiments alone are unable to address (due to, for example, gaps in space and time between data points, degrees of freedom that are difficult if not impossible to control, and limits on repeatability). Possible applications of modelling efforts at the management scale include improvements to predictions of smoke dispersion, tree mortality, and fire behaviour.

Perturbation of the atmosphere within and above forests by wildland fires has primarily focused on the effects of sensible heat flux from the fire, and has been the subject of field experiments (Clark et al. 2020; Heilman et al. 2015; Hiers et al. 2009) and high-resolution atmospheric modelling studies (Hoffman et al. 2015; Kiefer et al. 2015, 2016; Kiefer et al. 2014; Kiefer et al. 2018; Pimont et al. 2011). Numerical modelling studies have shown that *low-intensity* fire-induced atmospheric perturbations are sensitive to various aspects of the ambient atmosphere, fire, and forest canopy. For example, Kiefer et al. (2015) found that the fireline-normal component of wind and maximum vertical velocity were sensitive to the presence of a forest canopy and to the strength of the ambient wind. Kiefer et al. (2016) examined fire-induced atmospheric perturbations in the presence of forest gaps and concluded that the impact of the fire on the atmosphere was greatest in the case with the gap centered on the fire and weakest in the case with the gap upstream of the fire. They also found that gaps in forest canopies had the potential to play a role in the vertical as well as horizontal transport of heat away from the fire. Kiefer et al. (2018) found that perturbation of the atmosphere by the sensible heat released from a surface fire, both in terms of pattern and magnitude, was sensitive to both the vertical canopy structure and the magnitude of the fire sensible heat source.

As pointed out by Kiefer et al. (2016), an improved understanding of atmospheric perturbations within and above a forest during a low-intensity wildland fire has relevance to many aspects of wildland fires including fire spread, smoke transport and dispersion, tree mortality, transport of fire embers, and seed dispersal. Note that as in (2015, 2016); Kiefer et al. (2014); (2018), the term *canopy* is used herein to describe the entire vegetation layer including, but not limited to, the overstory and crown.

Materials and Methods

Model summary

For numerical simulations of the management-scale fire experiments, ARPS (Xue et al. 2000; Xue et al. 2001) and ARPS-CANOPY were utilized. ARPS is a three-dimensional, compressible, nonhydrostatic atmospheric model with a terrain-following coordinate system. ARPS has been applied across a range of spatial scales, from studies of turbulent flows, using grid spacing as fine as O(1) m (Dupont and Brunet 2008), to studies of mesoscale and synoptic-scale phenomena, utilizing grid spacing of O(1–10) km (e.g., Michioka and Chow (2008); Parker and Johnson (2004); Xue et al. (2001)). Hereafter, this model is referred to as *original ARPS* to distinguish it from *ARPS-CANOPY*.

ARPS-CANOPY (Kiefer et al. 2013) is a version of the ARPS model with a canopy submodel in which the effects of vegetation elements (e.g., branches and leaves) on drag, turbulence production/dissipation, radiation transfer, and the surface energy budget are accounted for through modifications to the ARPS model equations. Such changes allow for explicit simulation of airflow through a multi-level forest canopy, as opposed to representing the bulk effect of a vegetation canopy on the atmosphere within a single layer, beneath the lowest model grid point (as in, e.g., the original ARPS model and the Weather Research and Forecasting model, Powers et al. 2017). Although various metrics may be used to describe how vegetation is vertically distributed in a column (e.g., the vertical profile of canopy bulk density or the vertical profile of biomass), the vertical profile of plant area density (Ap), defined as the one-sided area

of plant material per unit volume, is utilized in ARPS-CANOPY to represent the bulk effects of the canopy on various atmospheric processes (e.g., drag and radiative heating/cooling).

Model physics

A 1.5-order subgrid-scale turbulence parameterization with a prognostic equation for turbulent kinetic energy (TKE) is utilized in original ARPS and ARPS-CANOPY, with the addition of canopy source and sink terms in ARPS-CANOPY (*Model summary* section). In all simulations, the original ARPS anisotropic turbulence option is used in which both horizontal and vertical components of eddy viscosity are computed; this option is recommended when vertical grid spacing is considerably smaller than horizontal grid spacing (Xue et al. 2000). This turbulence parameterization has been tested extensively and has been found to produce the correct vertical structure of mean variables and turbulent statistics with and without a forest canopy (e.g., Dupont and Brunet (2008); Kiefer et al. (2013)). Furthermore, a land surface model based on Noilhan and Planton (1989) and Pleim and Xiu (1995), and radiation physics following Chou (1990, 1992) and Chou and Suarez (1994) are utilized [with the addition of a canopy heat source term and with canopy shading effects on the ground energy budget accounted for (ARPS-CANOPY only)]. Lastly, for simulations with horizontal grid spacing larger than 100 m, a non-local turbulence closure scheme based on Sun and Chang (1986) is also utilized, in addition to the 1.5-order subgrid-scale (local) turbulence scheme.

The vegetation canopy is represented in ARPS-CANOPY as a height-varying Ap profile specified at each grid point. Whereas a meaningful estimation of Ap is challenging at even the scale of single tree stands, it has been demonstrated that LiDAR-derived canopy height profiles can be utilized to characterize the three-dimensional canopy structure (e.g., canopy bulk density, kg m^{-3}) at high horizontal and vertical resolutions on spatial scales O (10 km) (Kiefer et al. 2014; Skowronski 2011a; Skowronski et al. 2014). Here, we have derived Ap on a grid with 30-m (horizontal) and 2-m (vertical) grid spacing from aerial LiDAR data. The resulting canopy profiles at the nearest ARPS-CANOPY grid points to the six SLEF flux towers are displayed in Figure 97. A similar Ap dataset was developed for the FPP pre-burn guidance simulations (not shown).

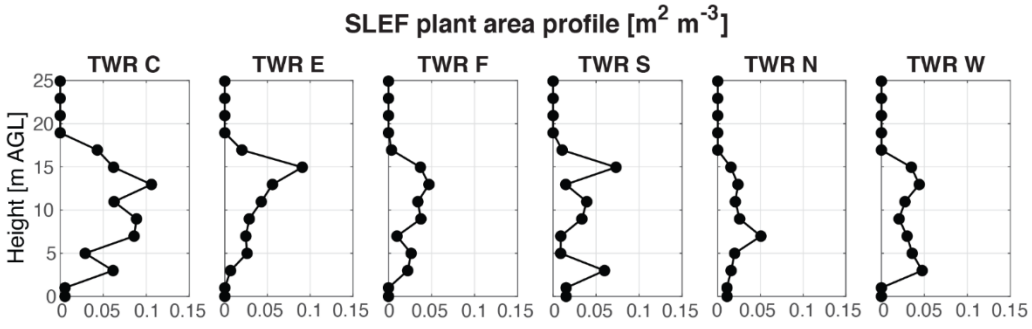


Figure 97. Plant area density profiles at the nearest grid point to the six SLEF flux towers: TWR C (control), TWR E (east), TWR F (flux), TWR S (south), TWR N (north), and TWR W (west).

One of the primary challenges encountered during this project is the representation of the fire sensible heat source in the model. There are three ways in which the fire sensible heat source has been represented in original ARPS and ARPS-CANOPY in previous studies:

- Exponentially decaying vertical turbulent heat flux profile (Kiefer et al. 2014)
- Soil temperature perturbation (Kiefer et al. 2008)
- Surface turbulent heat flux (Kiefer et al. 2015, 2016; Kiefer et al. 2009, 2010; Kiefer et al. 2018)

The first two approaches to parameterizing the fire sensible heat release have been pursued during this study.

An exponentially decaying heat flux profile approach was utilized for the FPP pre-burn guidance simulations and was initially used in the SLEF simulations due to the successful application of the approach to a 2011 Joint Fire Science Program (JFSP)-funded prescribed fire study in the New Jersey Pine Barrens (Charney et al. 2019; Heilman et al. 2015; Kiefer et al. 2014)(Kiefer et al. 2014; Heilman et al. 2015; Charney et al. 2019).(Charney et al. 2019; Heilman et al. 2015; Kiefer et al. 2014). This approach was recommended by Sun et al. (2006) based on a comparison of model simulations to data collected during the Meteotron experiment (Benech 1976). However, in the SLEF case there was no support in the tower heat flux measurements for implementation of an exponentially decaying profile of vertical turbulent heat flux in ARPS-CANOPY (Figure 98). Except for the south tower, which has no 10-m sonic, the heat fluxes at the in-situ towers increase with height from 3 m to 10 m above ground level (AGL). At the north and west towers, the maximum heat flux occurs at 10 m AGL, whereas at the east and flux towers, the maximum heat flux occurs at 20 m AGL. At the south tower, the maximum heat flux occurs at 3 m AGL, but again, there is no 10-m sonic on that tower. An additional challenge in designing a turbulent heat flux profile to represent the fire sensible heat source is extrapolation of the heat flux profiles above 20 m and below 3 m, where there are no heat flux measurements.

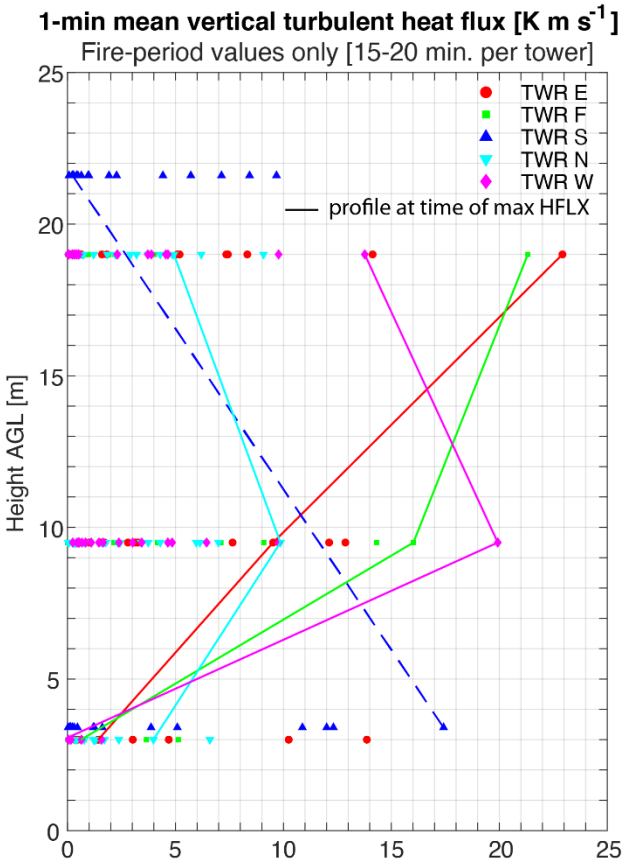


Figure 98. One-minute mean vertical turbulent heat fluxes during 15–20-minute fire period at each tower (markers), and profiles at time of peak heat flux (lines): TWR C (control), TWR E (east), TWR F (flux), TWR S (south), TWR N (north), and TWR W (west). At TWR S there was no 10-m sonic anemometer; a dashed line is used to indicate the heat flux profile there.

Because of the challenges encountered in specifying a vertical turbulent heat flux profile in ARPS-CANOPY, an alternate approach was pursued in which a soil temperature perturbation is implemented to represent the fire sensible heat source (i.e., *hotplate*). This approach was applied previously in an ARPS study of fire-induced buoyant plumes (Kiefer et al. 2008). With a soil temperature perturbation, conduction between the ground surface and overlying atmosphere is represented in the model, as well as convective and radiative vertical heat transfer (via upward longwave radiation from the heated surface). One challenge in implementing a hotplate heat source is choosing an appropriate soil temperature perturbation. A 400 K perturbation was used in (Kiefer et al. 2008) to represent a moderate-intensity fire. Based on a review of FireTracker instantaneous temperatures (Figure 99), it appears that a 400 K skin temperature perturbation is reasonable for the SLEF burn. The median peak FireTracker temperature across the 70 thermocouples is 699 K (p50 in Figure 99), corresponding to about a 400 K perturbation from ambient (background FireTracker temperatures were about 27 ºC or 300 K).

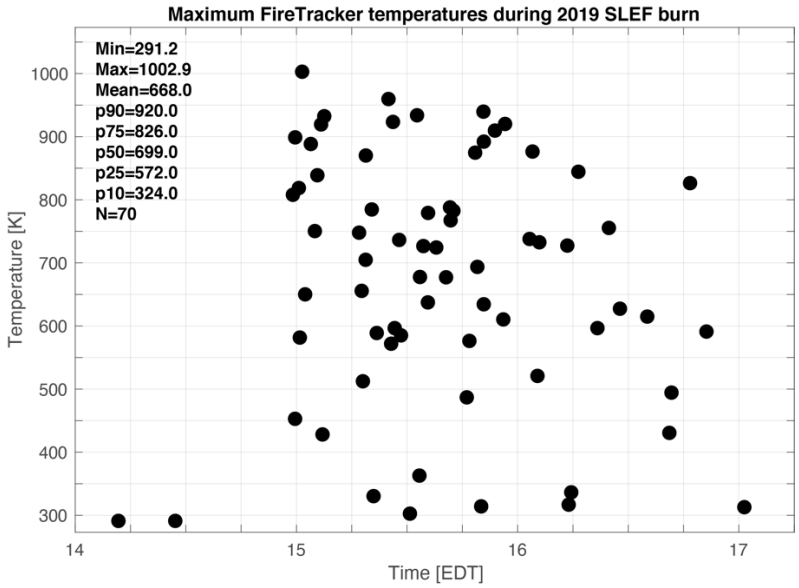


Figure 99. Maximum FireTracker temperatures observed during the SLEF 2019 prescribed fire.

For both the vertical heat flux profile and soil temperature perturbation (hotplate) approaches, the timing and location of the heat source within the SLEF burn block was informed by data from the FireTracker thermocouple array. Data from the array was processed, yielding contoured maps of fire front position every 30 seconds (Eric Mueller, personal communication). Using GIS software, the period of fire presence within each ARPS-CANOPY grid cell was determined. The heat source was applied in a particular burn block grid cell if the fire front was located anywhere within the grid cell. The heat source was applied steadily during the grid-cell fire window, with the heat source ramped up and down at the beginning and end of the fire window. For an example of the relationship between FireTracker fire front position and the representation of the fire in ARPS-CANOPY, see Figure 100.

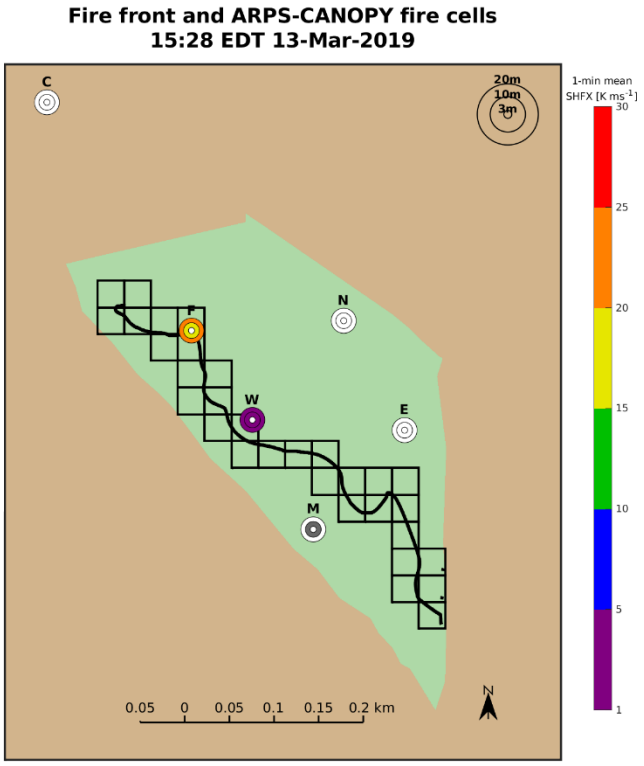


Figure 100. FireTracker fire front position (thick line), ARPS-CANOPY grid cells in which the heat source is applied (black squares), and 1-min mean vertical turbulent heat flux at the six flux towers [see legend for height above ground level (AGL) of observations; heat flux values less than 1 K ms^{-1} are unshaded], at 15:28 EDT 13 Mar 2019. Towers are named as follows: TWR C (control), TWR E (east), TWR F (flux), TWR S (south), TWR N (north), and TWR W (west). At TWR S there was no 10-m sonic anemometer; gray shading is used to denote the absence of heat fluxes at this level.

Experimental design – FPP

The ARPS-CANOPY model was configured to simulate ambient, fire, and forest overstory-induced mean and turbulent flows for a hypothetical low-intensity backing fire through the FPP burn block. The model was configured as follows:

- A two-domain idealized framework was chosen to (i) simplify analysis of fire and forest overstory-induced turbulent flows by minimizing complicating factors (e.g., larger-scale flows) and (ii) more readily refine the model grid to resolve the turbulent flows. Horizontal grid spacing was 90 m for the outer domain and 30 m for the inner domain; identical vertical grid structure was used for both domains, with 2-m minimum vertical grid spacing at the surface.
- The outer domain simulation was initialized with a sounding designed to represent plausible early-morning weather conditions in the New Jersey Pine Barrens in mid-March. At the initial time (08:00 EDT), temperature, wind speed, and wind direction at 1 m AGL were 1.1 ºC (34 ºF), 1.4 m s^{-1} (3.1 mph), and 236.5 deg. (west-southwest).
- To account for the influence of the forest canopy on atmospheric heat, momentum, and moisture, LiDAR-derived Ap data were interpolated to the two ARPS-CANOPY grids (Nick

Skowronski, personal communication). Analysis of the vertical and horizontal heterogeneity of the vegetation inside and outside of the burn block was conducted prior to implementing the fire parameterization.

- It was assumed that ignition would occur along the eastern perimeter of the burn block, with a backing fire spreading west-southwest, opposite the ambient wind direction (236.5 deg.). Sensible heat release from the fire to the atmosphere was parameterized as an exponentially decaying turbulent heat flux profile (*Model Physics* section). The rate of spread (1 m min^{-1}) and surface heat flux magnitude (5 kW m^{-2}) were chosen to be representative of a low-intensity fire spreading through a forest understory and were based on two JFSP prescribed fires conducted in the New Jersey Pine Barrens in 2011 and 2012. The time of ignition was 10:00 EDT, two hours after model initialization, and the fire was applied during a six-hour period, in the inner domain only.
- Sensitivity experiments were conducted with the fire sensible heat flux magnitude varied between 0 kW m^{-2} (no fire) and 25 kW m^{-2}.

In developing instrument deployment recommendations, areas of the burn block exhibiting the following characteristics were identified:

- Stronger gradients in simulated variables
- Less sensitivity of simulated variables to changes in fire heat source magnitude
- Simulated phenomena of interest (e.g., vortices)

Experiment design – SLEF

A multiscale modeling strategy was utilized to capture a range of atmospheric scales of motion, from synoptic (>2000 km) to mesoscale (2-2000 km) to microscale (<2 km). A series of one-way nested simulations were performed using ARPS/ARPS-CANOPY, with horizontal grid spacing ranging from 4 km in the outermost domain to 30 m in the innermost domain (Table 16). Initial and lateral boundary conditions for the outermost domain were obtained from the 12-km North American Mesoscale (NAM) model (Rogers et al. 2009). As shown in Figure 101, the outermost domain (D1) covered the northeastern United States, while the innermost domain (D5) covered only the area within about five kilometers of the SLEF burn block. A distinction needs to be made here between D1-D3, in which the original ARPS model was employed, and D4 and D5, in which ARPS-CANOPY was applied; note that the fire parameterization was only introduced in D5. Because of this one-way nesting strategy, D1–D3 simulated synoptic- to mesoscale processes and provided boundary conditions for D4, the domain with the canopy submodel but no fire parameterization, which in turn provided boundary conditions for D5, the domain with both the canopy submodel and fire parameterization.

Table 16. Overview of model simulations for SLEF case, where Dx, Dy, and Dz are the grid spacing in the west-east, south-north, and vertical dimensions.

Domain	Grid size	Physical Domain [km]	Dx, Dy [m]	Dz min [m]	Init. time [EST 13 Mar 2019]	Duration [hr]	Model
D1	300x300	1200.0 x	4000	50.0	08:00	12	AR
D2	200x200	266.6 x	1333	25.0	08:00	12	AR
D3	125x125	55.5 x	444	12.5	08:00	12	AR
D4	250x250	22.5 x	90	2.0	10:00	10	AR
D5	250x250	7.5 x 7.5	30	2.0	12:00	6	AR

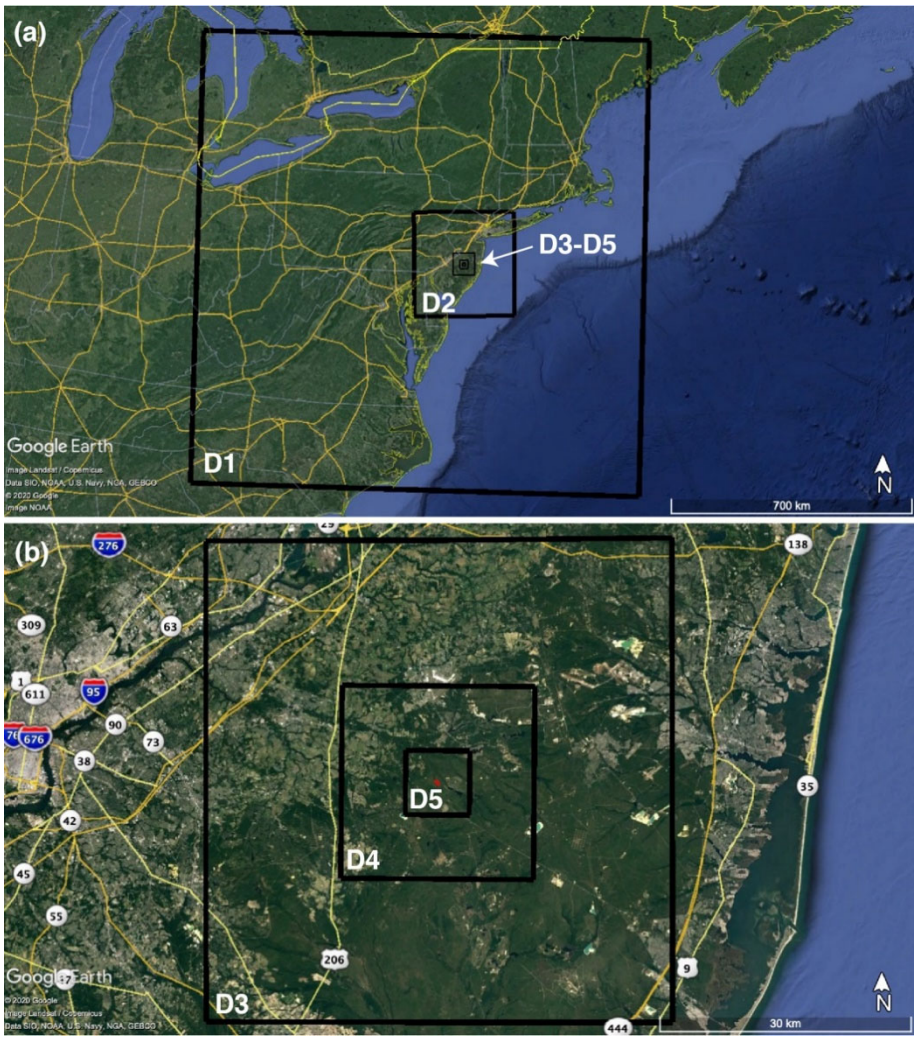


Figure 101. Google Earth images depicting nesting strategy for SLEF case, at two zoom levels: (a) outer zoom with domains D1-D5, (b) inner zoom with domains D3-D5. See Table 16 for details of each domain. Burn block denoted by red polygon in center of domain D5.

For the model validation exercise, vertical profiles, timeseries, and three-dimensional surface plots of simulated variables from D5, with observed values overlaid, were generated in order to assess the ability of ARPS-CANOPY to capture the spatial and temporal variability of mean and turbulent flows during the SLEF prescribed fire. This multi-dimensional approach allowed for a more comprehensive comparison of simulated and observed variables than a comparison of point observations to the simulated values at the closest grid point to each tower.

In addition to the model validation step, the following sensitivity experiments with D5 were conducted in an effort to explore the sensitivity of the model-observation comparison to lower-confidence aspects of the model and experiment design, by varying (1) the method used to represent the fire sensible heat source in the model (exponentially-decaying vertical turbulent heat flux profile and soil temperature perturbation), (2) characteristics of the exponentially-decaying vertical turbulent heat flux profile (surface heat flux value and e-folding depth), (3) the model vertical grid structure, and (4) the canopy drag coefficient (Table 17). For each sensitivity experiment, mean profiles of temperature, wind speed, wind direction, and TKE were examined.

The first sensitivity experiment was conducted to examine which sensible heat source approach, exponentially decaying vertical turbulent heat flux profile or soil temperature perturbation (i.e., hotplate), yielded the best comparison between simulated and observed mean profiles of temperature, wind speed, wind direction, and TKE. It was hypothesized that the hotplate approach is more physically sound, as all three forms of fire-atmosphere heat transport [conduction, convection, and radiation (via upward longwave radiation from the heated surface)] are represented in the model, unlike the vertical turbulent heat flux approach in which convection is the sole transport method.

The second sensitivity experiment was designed to address the sensitivity of mean profiles inside and outside of the forest canopy to the magnitude and vertical distribution of the turbulent heat flux profile. In this experiment, the surface value of vertical turbulent heat flux was varied between 2.4 and 24 kW m^{-2} (i.e., 10% and 100% of the peak 1-min mean observed heat flux averaged across the flux towers inside the burn block); and the e-folding extinction depth (a measure of how sharply the heat flux decays with height) was varied between 4.4 and 18 m (25% and 100% of the average canopy height in the burn block); the larger the e-folding depth, the more slowly the heat flux decays away from the surface.

The third sensitivity experiment was designed to help clarify how sensitive the model-observation agreement was to the number of vertical grid levels in the forest canopy and overlying atmosphere. Vertical grid stretching, a technique used in numerical models to maximize vertical resolution at the surface (or in other atmospheric layers), was applied from the ground upward in preliminary SLEF simulations. Since constant 2-m vertical grid spacing was utilized across the lowest 84 m in ARPS-CANOPY simulations of the 2011 JFSP prescribed fire (Kiefer et al. 2014), it was deemed important to examine the impact of near-surface vertical grid spacing on the model-observation agreement. This is especially true since the vertical grid spacing determines the number of grid points within the forest canopy layer.

The fourth and final sensitivity experiment was performed to explore the impact of the canopy drag coefficient in ARPS-CANOPY on the agreement between observed and simulated

mean wind speed and TKE inside the forest canopy. Preliminary model simulations were found to overestimate these variables in the lower canopy, and it was posited that an increase in canopy drag might improve the model-observation comparison by reducing momentum in the lower canopy. It is worth noting that canopy drag coefficients vary considerably between canopy models and the parameterization of canopy drag is a source of model uncertainty (Kiefer et al. 2013).

Table 17. Summary of sensitivity experiments. VG refers to the vertical grid structure [0: grid stretching beginning at 0 m AGL; 84: grid stretching beginning at 84 m AGL], CD is the canopy drag coefficient (0.2 or 0.3), the heat source is either a vertical profile of vertical turbulent heat flux (HF) [with an e-folding depth of 4.4 m (Low) or 18 m (High)] or a hotplate (HP), also known as a soil temperature perturbation. No-fire (NF_0) simulation included at bottom of table.

Simulation	Heat source: **H**eat **F**lux / **H**ot **P**late	Heat source magnitude: flux [kW m-2] or skin temp. pert. [K]	Heat flux e-folding depth [m] (**L**ow/**H**igh)	Height where **V**ertical **G**rid stretching begins [m]	**C**anopy **D**rag coefficient
$HF_{2.4L}VG_0CD_{0.2}$	HF	2.4	4.4 (L)	0	0.2
$HF_{24L}VG_0CD_{0.2}$	HF	24.0	4.4 (L)	0	0.2
$HF_{24H}VG_0CD_{0.2}$	HF	24.0	18.0 (H)	0	0.2
$HF_{24L}VG_{84}CD_{0.2}$	HF	24.0	4.4 (L)	84	0.2
$HF_{24L}VG_{84}CD_{0.3}$	HF	24.0	4.4 (L)	84	0.3
$HP_{400}VG_{84}CD_{0.2}$	HP	400	---	84	0.2
$NF_0VG_{84}CD_{0.2}$	--	--	--	84	0.2

Results and discussion

FPP - Spatial heterogeneity analysis

A series of figures depicting contours of the 90th percentile values of 1-min mean temperature, wind speed, and turbulent kinetic energy (TKE) were generated to identify the near-peak value associated with the fire passage (values that might lead to fire effects like tree damage or mortality), and to look at how that near-peak value varied spatially across the burn block. The wind speed gradient was found to be strongest near the western perimeter, with the magnitude of the gradient weakening with increasing heat source magnitude (Figure 102). The temperature gradient was found to be strongest near the southern and western perimeter, with little change to the location of the gradient maximum with increasing heat source magnitude

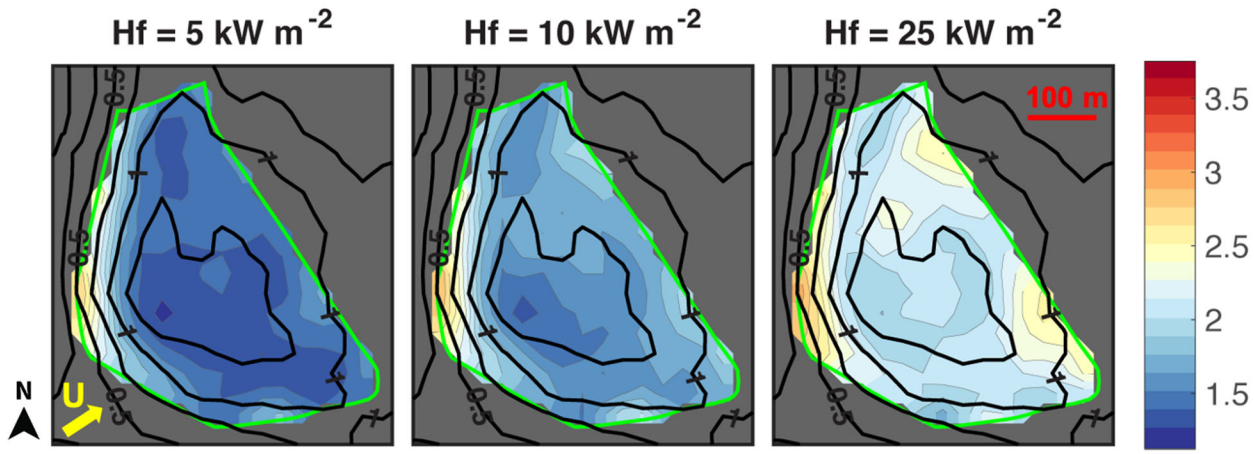


Figure 102. 90th percentile values of 1-min mean wind speed [m s^{-1}] during each FPP simulation, at 9.8 m AGL, where Hf refers to the surface value of the vertical turbulent heat flux profile representing the fire sensible heat source. Contours of Ap [m^2 m^{-3}] are overlaid on each panel, and the ambient wind direction (236.5 deg) is indicated in the left panel.

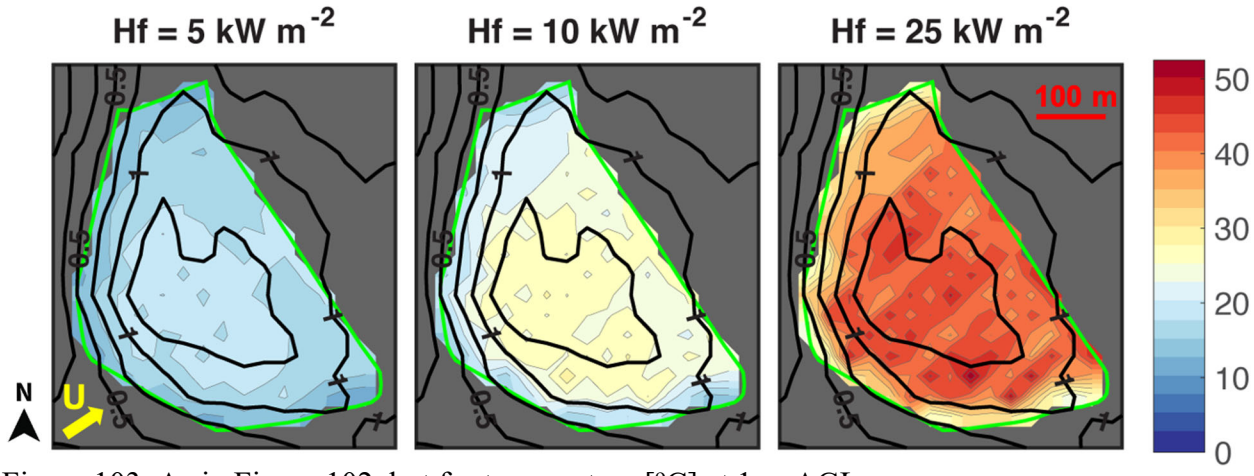


Figure 103. As in Figure 102, but for temperature [°C] at 1 m AGL.

FPP - Instrument deployment recommendations

Preliminary results suggested one or more linear arrangements, with clustering where simulated gradients were overall strongest and results were least sensitive to fire heat source magnitude (i.e., western perimeter of burn block) (Figure 104). The actual orientation of the linear arrangement would be subject to the forecast wind direction (e.g., westerly vs. southwesterly). Use of such a strategy would allow for an examination of spatial heterogeneity via analysis of horizontal profiles perpendicular to the backing fireline.

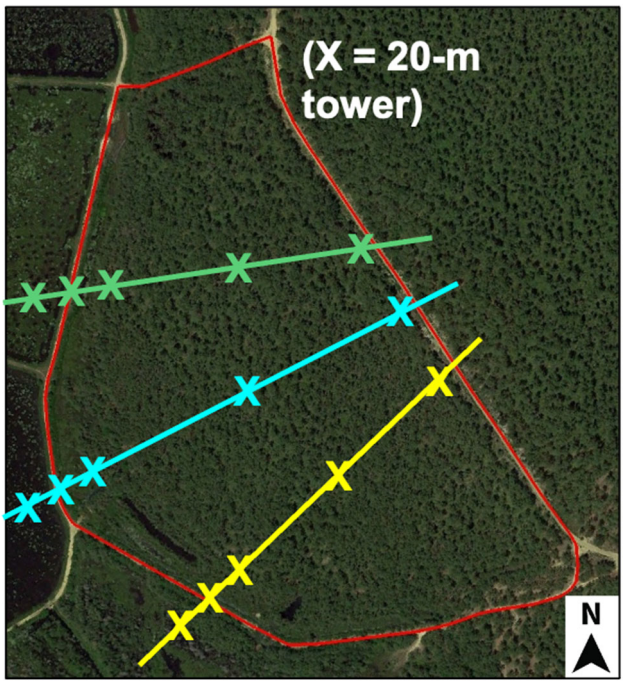


Figure 104. Schematic depicting possible configuration of 20-m flux towers for hypothetical FPP case, based on ARPS-CANOPY simulations, overlaid on Google Earth image.

SLEF - Model validation

The simulation $\mathbf{HP_{400}VG_{84}CD_{0.2}}$ (Table 2; 400 K soil temperature perturbation, constant grid spacing up to 84 m, and 0.2 canopy drag coefficient) was validated against flux tower observations. Time-averaged vertical profiles of ARPS-CANOPY simulated temperature, wind speed, and wind direction were found to compare favorably with observations at all six instrumented towers, as was TKE at the 3 and 10 m levels within the canopy (Figure 105). The TKE profile shape was captured by ARPS-CANOPY at all six towers, with largest TKE at and above the canopy top and smallest TKE in the lower canopy. At the control, north, and south towers, the mean TKE at 20 m AGL exhibited good agreement with observations, whereas at the east, flux, and west towers, TKE within and above the canopy overstory was considerably underestimated (recall from Fig. 1 that canopy height at all six towers was approximately 18 m).

Timeseries of 1-min mean variables at the 3, 10, and 20 m heights shed further light on the strengths and weaknesses of the ARPS-CANOPY simulation (Figure 106). The magnitude and temporal evolution of temperature during the period from 14:45-17:45 EDT was captured at all towers. At the control tower, a notable cold bias was evident during the first half of the timeseries and a sharp drop in temperature at about 16:15 EDT (evidence of a sea breeze passage) was absent in the model simulation; such model error also occurred at the other towers but was obscured using much larger y-axis limits to accommodate the high temperatures associated with fire frontal passage. For wind speed and direction, the magnitude and temporal evolution was well captured by the model simulation, including the transition from west/northwesterly winds to southerly winds during the afternoon. Comparison of the simulated and observed TKE time series clarified the lack of agreement in the vertical profile plot: outside of the fire window, the simulated and observed TKE were in reasonable agreement. Furthermore,

although the TKE values of 5-10 m^2s^{-2} observed during the fire period (magenta lines) were greatly underestimated by ARPS-CANOPY, values of a similar magnitude were simulated by the model outside of that period.

Third, three-dimensional surface plots of simulated variables (e.g., TKE; Figure 107) were generated to provide additional context for the model errors identified in the vertical profile and timeseries plots. 1-min mean TKE at all grid points within a 33x33 grid point subset of the full domain, centered on the burn block, was plotted at the 3, 10, and 20 m AGL grid levels, along with corresponding observations at the six flux towers. This visualization helped provide context for the underestimation of TKE at 20 m AGL at the east, flux, and west towers. The model simulation depicted an area of mean TKE of 4-6 m^2s^{-2} across the northwestern half of the burn block at 15:36 EDT (Figure 107a). This area of enhanced TKE was a transient feature in the planetary boundary layer transported by the ambient flow from south-southwest to north-northeast. The magnitude of 20 m AGL mean TKE differed from that of the no-fire simulation $NF_0VG_{84}CD_{0.2}$ by about 0.5-1 m^2s^{-2}, mainly downwind of the fireline (Figure 107b), suggesting that the low-intensity fire as implemented in $HP_{400}VG_{84}CD_{0.2}$ had a small (but non-negligible) effect on turbulence in and above the forest canopy.

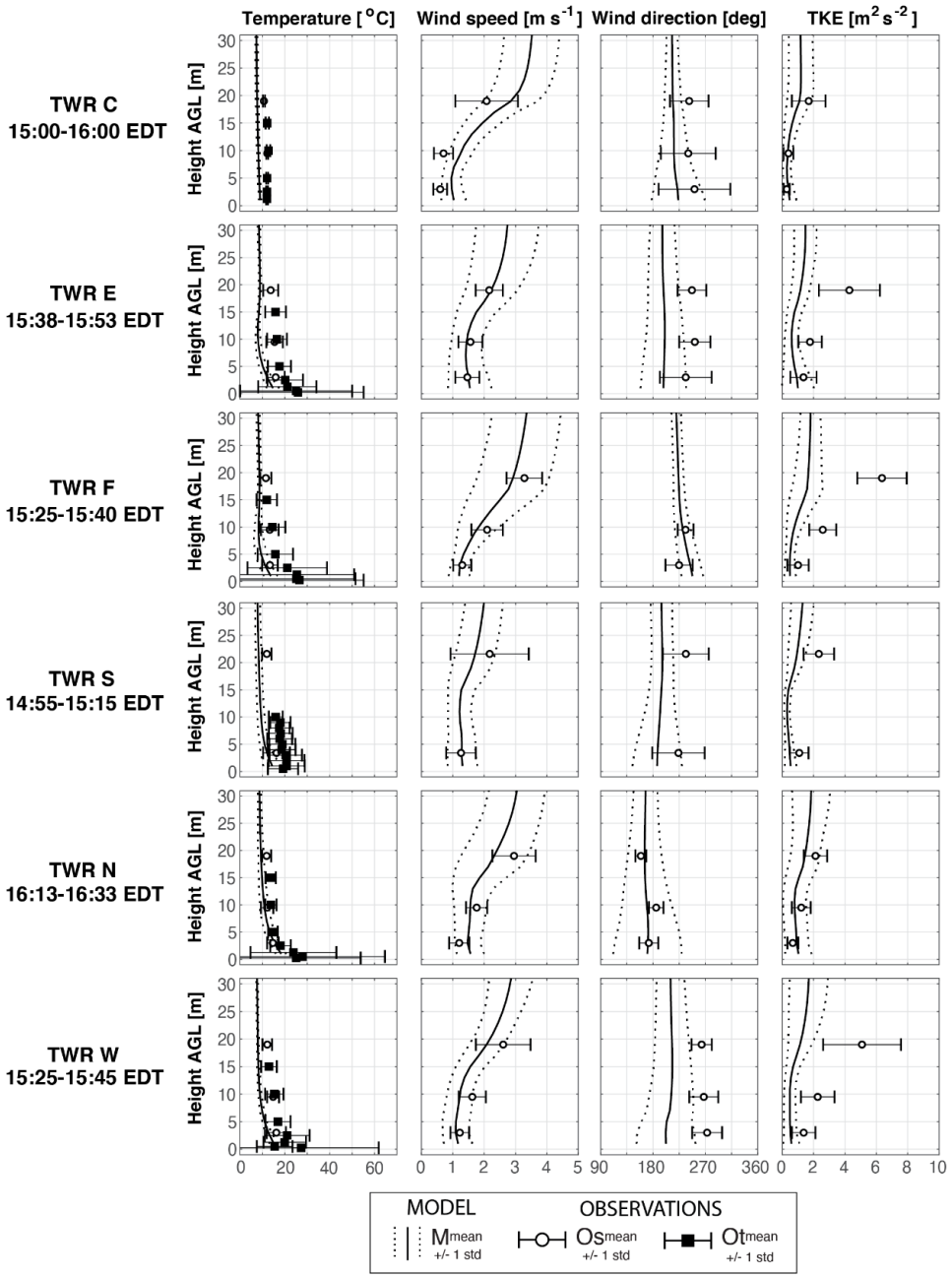


Figure 105. Vertical profiles of time-averaged simulated variables interpolated to tower coordinates, for the ARPS-CANOPY simulation $HP_{400}VG_{84}CD_{0.2}$ (Table 16). Towers are named as follows: TWR C (control), TWR E (east), TWR F (flux), TWR S (south), TWR N (north), and TWR W (west). Averaging period is indicated below tower name; for all towers except TWR C, this period corresponds to the fire period subjectively determined from time series of observed vertical turbulent heat flux; for TWR C, this period corresponds to the one-hour period immediately prior to sea breeze passage. Lines denote the model simulation and markers denote the tower observations; see legend below figure [M: model; Os: observation (sonic anemometer); Ot: observation (thermocouple)].

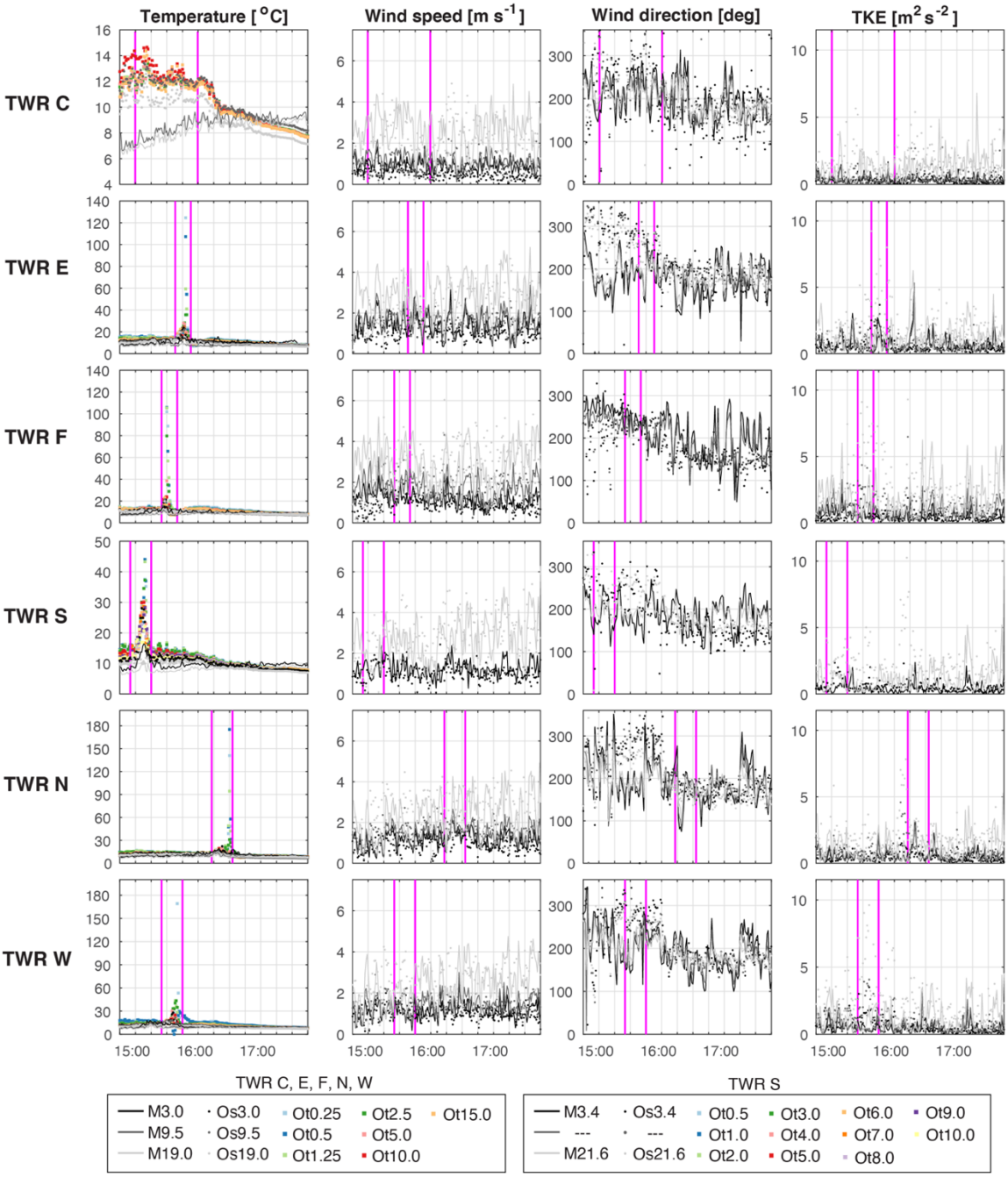


Figure 106. Timeseries of 1-min mean simulated variables interpolated to tower coordinates, for the ARPS-CANOPY simulation $HP_{400}VG_{84}CD_{0.2}$ (Table 16). Towers are named as follows: TWR C (control), TWR E (east), TWR F (flux), TWR S (south), TWR N (north), and TWR W (west). For all towers except TWR C, the magenta lines denote the beginning and end of the fire period subjectively determined from time series of observed vertical turbulent heat flux; for TWR C, the magenta lines denote the one-hour period immediately prior to sea breeze passage. Lines denote the model simulation and markers denote the tower observations; see legend below figure [M: model; Os: observation (sonic anemometer); Ot: observation (thermocouple)].

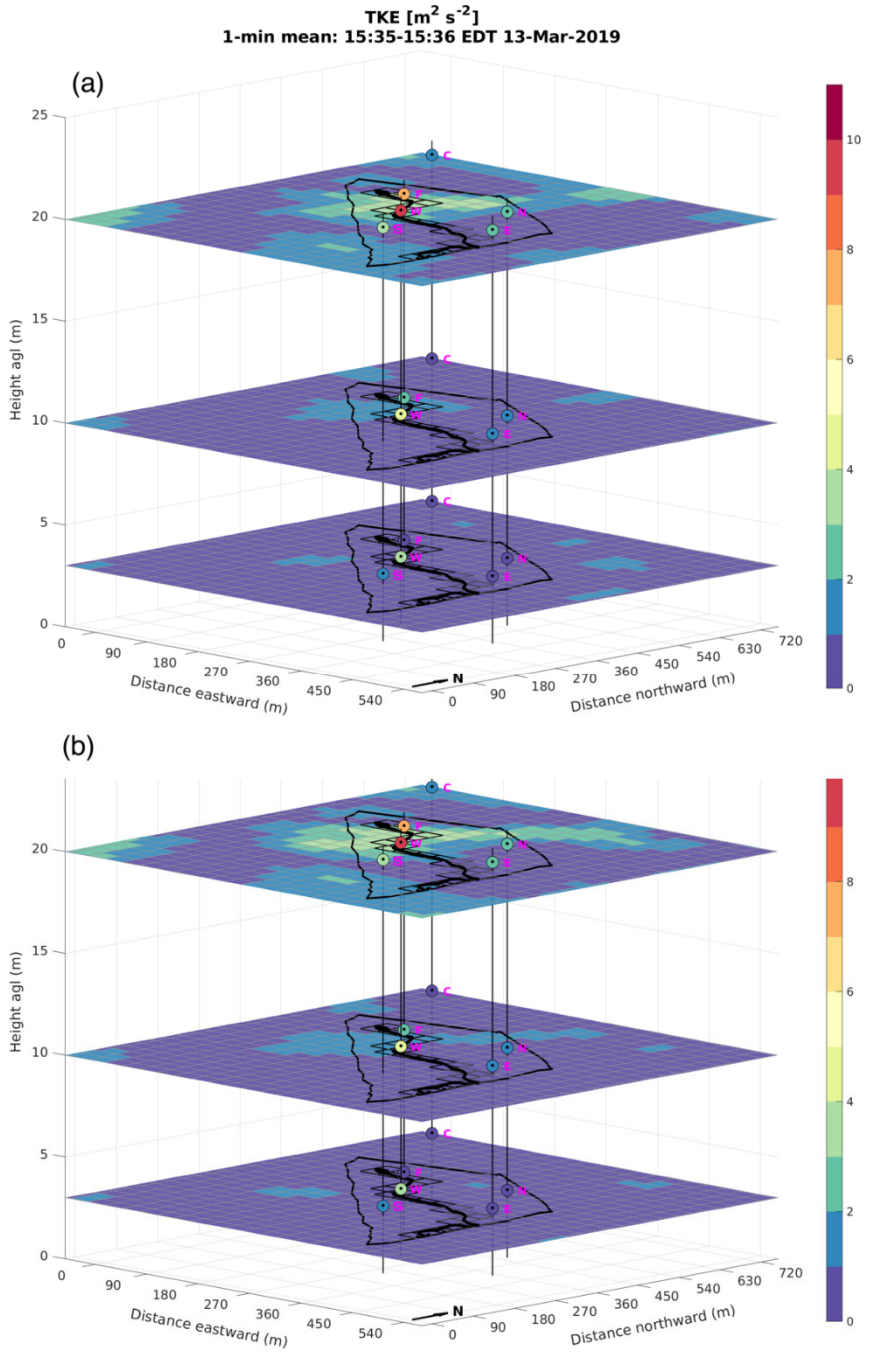


Figure 107. Three-dimensional model surface plot of 1-min mean TKE at 3, 10, and 20 m AGL, for the ARPS-CANOPY simulations (a) $HP_{400}VG_{84}CD_{0.2}$ and (b) $NF_0VG_{84}CD_{0.2}$ (no-fire) (Table 17). Towers are named as follows: TWR C (control), TWR E (east), TWR F (flux), TWR S (south), TWR N (north), and TWR W (west). For TWR S the 10-m marker is omitted since there was no 10-m sonic anemometer on that tower.

SLEF - Model sensitivity experiments

Sensitivity experiments were conducted to assess the sensitivity of the model-observation agreement to lower-confidence aspects of the model and experiment design (Table 17). As in Figure 105, time-averaged vertical profiles of temperature, wind speed, wind direction, and TKE were examined.

Regarding mean profile sensitivity to the choice of fire heat source method (Figure 108; simulations $HF_{24L}VG_{84}CD_{0.2}$ and $HP_{400}VG_{84}CD_{0.2}$), differences in mean profiles between the two methods were considerable (except for wind direction). Overall, the best comparison to observations was found with the 400 K soil temperature perturbation (i.e., hotplate) approach. Although neither method yielded the overstory TKE maximum observed at the flux tower, the vertical turbulent heat flux profile method yielded a bottom-heavy profile indicating a vertical distribution of turbulence that runs counter to reality. The vertical turbulent heat flux profile approach also yielded substantially larger mean wind speeds in the lower canopy than indicated by the flux tower observations, whereas the soil temperature method captured the vertical structure of the wind profile. Lastly, it is worth noting that unlike the vertical turbulent heat flux profile method, the soil temperature perturbation method yielded increasing standard deviation of wind speed and TKE with height, in agreement with the tower observations.

Concerning sensitivity of the mean profiles to the vertical turbulent heat flux profile characteristics (Figure 109), increasing the surface heat flux by an order of magnitude from 2.4 kW m^{-2} to 24 kW m^{-2}, but keeping the e-folding depth constant (compare $HF_{2.4L}VG_{0}CD_{0.2}$ and $HF_{24L}VG_{0}CD_{0.2}$), had a considerable effect on the profiles below about 15 m AGL, but limited impact above 15 m AGL. Increasing the surface heat flux led to weaker vertical wind shear inside the canopy and a bottom-heavy TKE profile that was not supported by the flux tower observations. Furthermore, fixing the 24 kW m^{-2} surface heat flux but increasing the e-folding depth by a factor of four from 4.5 m to 18 m (compare $HF_{24L}VG_{0}CD_{0.2}$ and $HF_{24H}VG_{0}CD_{0.2}$) had a notable effect on the temperature profile but little effect on the wind speed, wind direction, and TKE profiles.

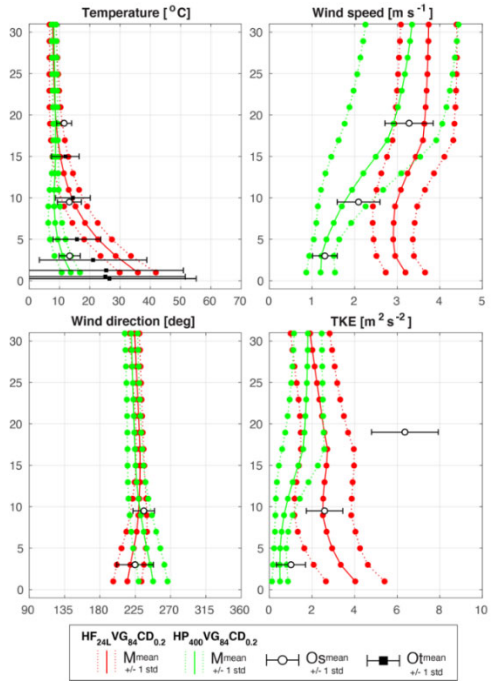


Figure 108. Fire-period average profiles of temperature, wind speed, wind direction, and TKE, for heat source sensitivity tests, at the flux tower (TWR F). Averaging period is 15:25-15:40 EDT. See Table 17 for experiment details. Lines denote the model simulation and markers denote the tower observations; see legend below figure [M: model; Os: observation (sonic anemometer); Ot: observation (thermocouple)].

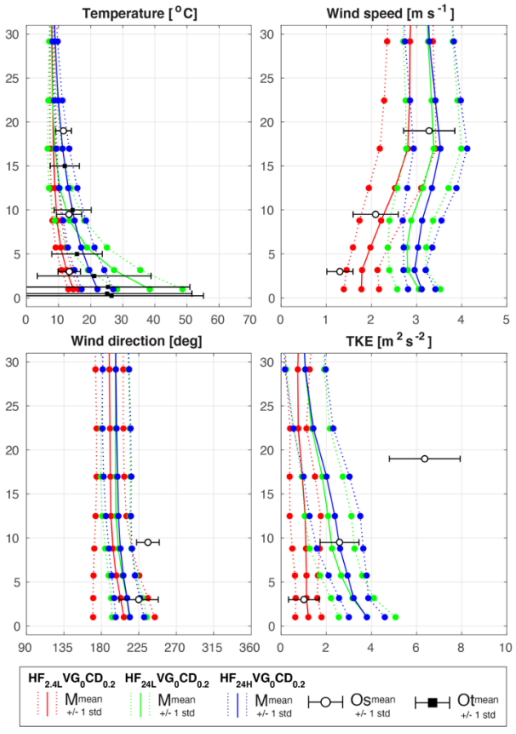


Figure 109. As in Fig. 107, but for vertical turbulent heat flux profile sensitivity tests.

Third, regarding mean profile sensitivity to vertical grid structure within and above the canopy (Figure 110; simulations $HF_{24L}VG_0CD_{0.2}$ and $HF_{24L}VG_{84}CD_{0.2}$), minimal changes to temperature and wind speed are noted, with wind direction and TKE exhibiting small but non-negligible sensitivity. In the case with constant 2-m grid spacing up to 84 m ($HF_{24L}VG_{84}CD_{0.2}$), the simulated wind direction profile achieves better agreement with observations, as does the TKE profile at 20 m AGL. It appears that the use of nine vertical grid levels at or below 18 m AGL (approximate canopy height) ($HF_{24L}VG_{84}CD_{0.2}$), rather than six ($HF_{24L}VG_0CD_{0.2}$), yields better representation of the atmospheric processes controlling the wind direction and TKE profiles within the canopy.

Fourth, concerning mean profile sensitivity to the canopy drag coefficient (Figure 111; simulations $HF_{24L}VG_{84}CD_{0.2}$ and $HF_{24L}VG_{84}CD_{0.3}$), differences in mean profiles between cases with canopy drag coefficients of 0.2 and 0.3 are generally small. Wind speed and TKE below about 10 m AGL (where they are overestimated by ARPS-CANOPY) are little changed, a reflection of the small plant area density values in the lower canopy Figure 97. In other words, when the exponentially decaying turbulent heat flux profile is used to represent the fire heat source, the TKE profile is bottom-heavy regardless of the canopy drag coefficient.

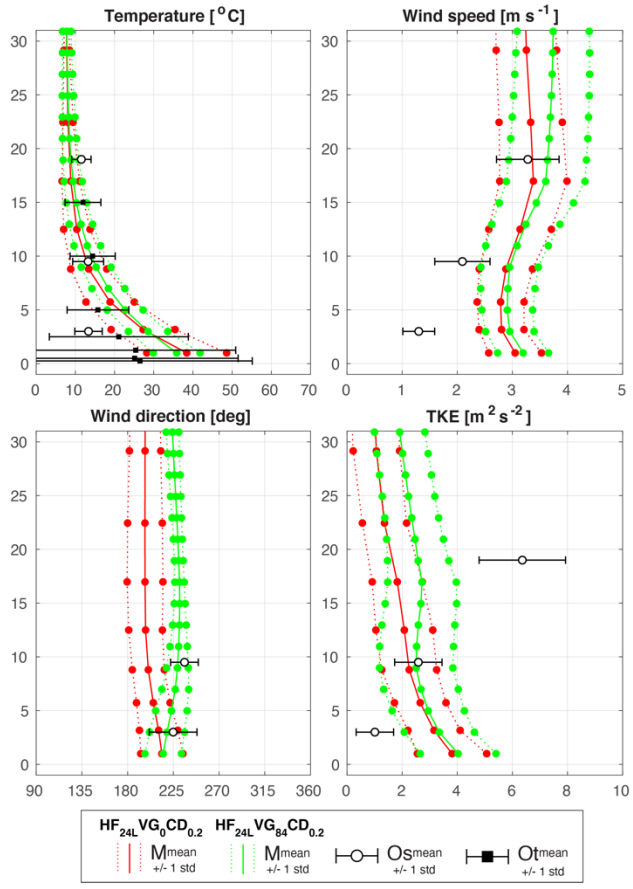


Figure 110. As in Fig. 107, but for vertical grid structure sensitivity tests.

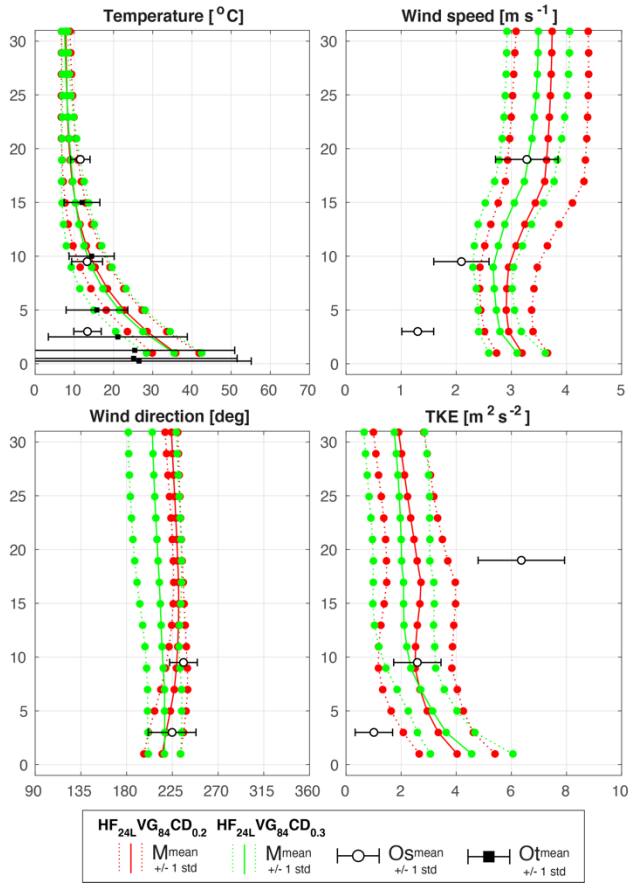


Figure 111. As in Fig. 107, but for canopy drag coefficient sensitivity tests.

Taken as a whole, the tests revealed the challenges involved in representing the sensible heat source in the model. Sensitivity of the mean vertical profiles to the vertical grid structure (Figure 110) and canopy drag coefficient (Figure 111) were small relative to the sensitivity to the fire heat source representation (Figure 108) and vertical turbulent heat flux profile parameters (Figure 109). As seen in Figure 108, the turbulent heat flux profile method yielded a less satisfactory comparison to observations than the soil temperature perturbation (i.e., hotplate) approach.

Conclusions and implications for future research

The modeling framework developed for the FPP case shows promise for informing instrumentation deployment strategy for future prescribed fires. Preliminary results suggest one or more linear arrangements, with clustering where simulated gradients are overall strongest. However, deployment recommendations may depend on the specific variables of interest (e.g., wind speed, TKE, relative humidity). Furthermore, the actual deployment strategy is subject to late adjustments based on weather forecasts, and above all, on-the-ground expertise.

It is anticipated that the pre-burn simulations conducted for the cancelled 2019 FPP burn will be distilled during spring/summer 2021 into pre-burn guidance for a planned 2022 FPP burn (post-project).

The model validation exercise and sensitivity experiments conducted for the SLEF case have provided useful insights into the strengths and weaknesses of ARPS-CANOPY and the fire sensible heat source representation in the model. At the control, north, and south towers, the model was able to reproduce the vertical distribution of temperature, wind speed, wind direction, and TKE. The favorable comparison at these three towers confirms the finding of previous studies (e.g., Kiefer et al. (2014)) that ARPS-CANOPY is capable of accurately simulating ambient, fire, and forest overstory-induced mean and turbulent flows during low-intensity management-scale fires in forested environments. However, at the east, flux, and west towers, although the model was able to reproduce the temperature, wind speed, and wind direction profiles, and the overall shape of the TKE profile, ARPS-CANOPY was found to grossly underestimate overstory TKE. None of the fire heat source approaches used in ARPS/ARPS-CANOPY appears capable of yielding the quantity of TKE observed just above canopy top at those three towers. Possible reasons for the overstory TKE underestimation by ARPS-CANOPY at some towers include (1) orientation of the ambient wind normal to the fireline as it passed beneath the east, flux, and west towers, yielding a relatively short residence time for air parcels crossing the one-grid-point-wide ARPS-CANOPY fireline, compared to other periods during the burn when the ambient wind was oriented at an oblique angle to the fireline; and (2) the absence in ARPS-CANOPY of smoldering heat release behind the fireline that may have contributed to the larger TKE values observed at the towers.

An important outcome of this effort is the knowledge gained regarding the fire heat source representation in ARPS-CANOPY. The turbulent heat flux profile approach used successfully in Kiefer et al. (2014) performed poorly in this study. It is critical to note that none of the one-way heat source approaches applied in previous ARPS and ARPS-CANOPY studies (exponentially decaying vertical turbulent heat flux profile, surface turbulent heat flux, or soil temperature perturbation) has been adequately validated. Furthermore, the need for a fire behavior submodel in ARPS-CANOPY is underscored by the shortcoming of the one-way heat source representation used in this study. Efforts are ongoing external to this project to implement the wildland fire spread model DEVS-FIRE in ARPS-CANOPY, as was done with ARPS in Dahl et al. (2015).

Because capturing the spatial and temporal distribution of ambient, fire, and forest overstory-induced mean and turbulent flows has relevance to prediction of, for example, fire behavior, smoke dispersion, and tree mortality, the remainder of this project will focus on (1) identifying turbulence processes present during the SLEF fire but not captured by the model, and (2) improving the representation of the fire sensible heat source in the model. Regarding (1), a resolved TKE budget will allow us to examine production, transport, and dissipation terms that control the evolution of TKE inside and outside of the forest canopy. Regarding (2), work will center around further examination of the model's inability to generate the observed TKE maximum just above the canopy top, and will include additional sensitivity experiments (e.g., imposing a vertical turbulent heat flux profile with the largest magnitude in the canopy overstory, rather than at the surface, and representing the sensible heat release from smoldering behind the fireline). Lastly, a manuscript will be prepared during spring 2021 detailing the successes and challenges encountered in simulating the ambient, fire, and forest overstory-induced mean and turbulent flows during the 2019 management-scale prescribed fire.

Conclusions and Implications for Future Research

This work has provided an immense amount of information regarding combustion process and fire behavior but has also indicated that there are significant gaps in our understanding of the effects of fuel bed structure on the combustion process driving flame spread. The complex and coupled nature of fluid mechanics and heat transfer within structured fuels requires further investigation, particularly when considering understory and canopy fuels in addition to the surface fuels that we focused on here. For example, it has been shown that flow in porous fuels can lead to cooling due to convection but also increased combustion due to the enhanced flow of oxygen. These sensitivities require further investigation to allow improved prediction of fire phenomena, and this type of tradeoff creates uncertainties that will require further investigation. Overall, an improved understanding of combustion processes and the interactions between environmental variables and fuel attributes have resulted from our project, and this will improve our ability to predict the fire spread and fuel consumption in the future.

Our findings have highlighted the role of fuel structure in the burning of fuel layers. The structure cannot be adequately described by commonly used terms of fuel load and bulk density. Investigations of fuel flammability suggest that an optimal fuel structure exists for a given fuel type due to the controlling (and competing) processes which govern burning. Future assessments of wildland fuel flammability should seek to quantify these effects in more detail.

In addition, the effects of fuel structure on the mean entrainment flow and radiative heat transfer through the fuel bed require further investigation. Resolving the flow will allow better evaluation of the convective heat transfer ahead of the flame region and the oxygen mass flux available for combustion in the flaming and smoldering regions. The heat transfer from this trailing, smoldering region, and the factors on which it depends, also needs to be better quantified. Understanding these processes will allow for improved understanding of low-intensity fire spread. region and the overall flame spread process.

An important outcome of the modeling effort of the management-scale fire experiment is the knowledge gained regarding the fire heat source representation in ARPS-CANOPY. The turbulent heat flux profile approach used successfully in Kiefer et al (2014) performed poorly in this study. It is critical to note that none of the one-way heat source approaches applied in previous ARPS and ARPS-CANOPY studies (exponentially decaying vertical turbulent heat flux profile, surface turbulent heat flux, or soil temperature perturbation) has been adequately validated. Furthermore, the need for a fire behavior sub model in ARPS-CANOPY is underscored by the shortcoming of the one-way heat source representation used in this study. Efforts are ongoing external to this project to implement the wildland fire spread model DEVS-FIRE in ARPS-CANOPY, as was done with ARPS in Dahl et al. (2015).

Because capturing the spatial and temporal distribution of ambient, fire, and forest overstory-induced mean and turbulent flows has relevance to prediction of, for example, fire behavior, smoke dispersion, and tree mortality, the analyses of the model results have been focused on (1) identifying turbulence processes present during management-scale fire but not captured by the model, and (2) improving the representation of the fire sensible heat source in the model. Overall, these studies serve to explore the dynamic effects of wind in the field and serve to

contrast with the quiescent conditions studied in the laboratory. The data sets generated will inform future studies and provide an evidence base for future numerical model development.

An important benefit of the work completed in this project is the vast amount of data that will be available for future modeling. We have paid particular attention to experimental design, replication, and data consistency in the outdoor 10x10 fire spread experiments. Meta-data and carefully quality-checked data files for these experiments will be available as citable data products housed at the USDA Forest Service Research Data Archive. In addition, our data has been selected as pilot data for the ESS-Dive demonstration project.

Appendices

Appendix 1. Supporting technical data:

Nomenclature

A_{char} pre-exponential factor for char oxidation
A_{pyr} pre-exponential factor for pyrolysis
$c_{p,s}$ specific heat of solid at constant pressure
c_d vegetation drag coefficient
c_s vegetation shape factor
D mass diffusivity
E_{char} activation energy for char oxidation
E_{pyr} activation energy for pyrolysis
$\boldsymbol{F}_D$ drag term in momentum equation
g acceleration of gravity
h_c convection coefficient
$\mathcal{H}$ pressure term in momentum equation
h gas mixture enthalpy
h_i enthalpy of species *i*
J total irradiance
L_{pyr} heat of pyrolysis
$\dot{m}_i'''$ chemical mass consumption of gas species *i*
p_0 thermodynamic pressure
$\dot{\boldsymbol{q}}_r''$ radiative heat flux vector
$\dot{q}_{sr}''$ radiative heat flux of solid
$\dot{q}_{sc}''$ convective heat flux of solid
$\dot{Q}_{s,vap}''$ heat of vaporization of fuel
$\dot{Q}_{s,kin}''$ heat of pyrolysis of solid
R universal gas constant
t time
T gas temperature
T_s solid temperature
u velocity vector
Y_i mass fraction of species *i*
β_s packing ratio
ΔH_{char} heat of combustion of char residue
κ fuel bed radiation attenuation factor
λ_{LES} thermal conductivity (from the LES model)
ρ gas density
ρ_s solid density
ρ_∞ gas density at ambient temperature
σ Stefan-Boltzmann constant
σ_s vegetation surface-to-volume ratio
$\boldsymbol{\tau}$ viscous stress tensor

Appendix 2- List of Scientific/Technical Publications

Peer Reviewed Publications

Campbell-Lochrie, Z., Walker-Ravena, C., Gallagher, M., Skowronski, N., Mueller, E.V., & Hadden, R.M. (2021). Investigation of the role of bulk properties and in-bed structure in the flow regime of buoyancy-dominated flame spread in porous fuel beds. *Fire Safety Journal, 120*, 103035

Campbell-Lochrie, Z., Walker-Ravena, C., Gallagher, M., Skowronski, N., Mueller, E.V., & Hadden, R.M. Effect of Fuel Bed Structure on the Controlling Heat Transfer Mechanisms in Quiescent Porous Flame Spread. In preparation.

Clark, K.L., Heilman, W.E., Skowronski, N.S., Gallagher, M.R., Mueller, E., Hadden, R., & Simeoni, A. (2020). Fire Behavior, Fuel Consumption, and Turbulence and Energy Exchange during Prescribed Fires in Pitch Pine Forests. *Atmosphere, 11*, 242

Clark, K. L. Gallagher, M.; Skowronski, N.; Heilman, W. Fuel Consumption and Particulate Emissions During Prescribed Fires in the Pinelands National Reserve, New Jersey. Submitted.

Clark, K. L., Gallagher, M., Skowronski, N., & Heilman, W. Fuel Consumption and Particulate Emissions During Prescribed Fires in the Pinelands National Reserve, New Jersey. In Preparation.

Di Cristina, G., Skowronski, N.S., Simeoni, A., Rangwala, A.S., & Im, S.K. (2021). Flame spread behavior characterization of discrete fuel array under a forced flow. *Proceedings of the Combustion Institute*. https://doi.org/10.1016/j.proci.2020.05.035

Di Cristina, G., Kozhumal, S., Skowronski, N.S., Simeoni, A., Rangwala, A.S., & Im, S.K. (2021). Forced convection fire spread along wooden dowel array. *Fire Safety Journal*, *120*, 103090.

Di Cristina, G., Skowronski, N.S., Simeoni, A., Rangwala, A.S., & Im, S.K. Flame spread predictions using an empirical B-number model and stagnation point flow. *Combustion and Flame*. Submitted.

Di Cristina, G., Skowronski, N.S., Simeoni, A., Rangwala, A.S., & Im, S.K. A large-scale, portable, wind tunnel for wildland fire research. *Experimental Thermal and Fluid Science*. Submitted.

Heilman, W.E., Clark, K.L., Bian, X., Charney, J.J., Zhong, S., Skowronski, N.S., Gallagher, M.R. & Patterson, M. Turbulent momentum flux behavior above a fire front in an open-canopied forest. *Atmosphere*. Submitted

Heilman, W. E. (2021. Atmospheric turbulence in wildland fire environments: Implications for fire behavior and smoke dispersion. Fire Management Today 79:24-29.

Kiefer, M. T., Heilman, W.E., Zhong, S., Charney, J.J., Bian, X., Skowronski, N.S., Clark, K.L., Gallagher, M.R., Hom, J.L., & Patterson, M. Representing low-intensity fire sensible heat output in a mesoscale atmospheric model with a canopy sub-model: A case study with ARPS-CANOPY (version 5.2.12). Geoscientific Model Development. Submitted.

Mueller E.V., Gallagher M.R., Skowronski N.S., & Hadden R.M. Approaches to modeling bed drag in pine forest litter for wildland fire applications, *Transport in Porous Media*. In Press.

Mueller E.V., Gallagher M.R., Skowronski N.S., & Hadden R.M. Convective heat transfer in pine forest litter beds for wildland fire applications. In preparation.

Mueller E.V., Gallagher M.R., Skowronski N.S., & Hadden R.M. Role of unsteady wind on fire spread and combustion dynamics in pine forest litter fuels. In preparation.

Wang, D., Heilman, W. E., Bian, X., Zhong, S., Charney, J.J., Kiefer, M.T., Clark, K.L., Skowronski, N.S., Gallagher, M.R., & Patterson, M. Turbulent heat transfer during a prescribed fire in an open-canopied forest. *Atmosphere.* Submitted.

Conference or symposium proceedings scientifically recognized and referenced

Campbell-Lochrie, Z.,Walker-Rávena, C., Mueller, E.V., & Hadden, R.M. "The effect of interstitial flow on the burning dynamics of porous fuel beds," in *Advances in forest fire research*, D. X. Viegas, Ed. Coimbra: Imprensa da Universidade de Coimbra, 2018, pp. 650–660.

Clark, K., Gallagher, M., Skowronski, N., Patterson, M., Heilman, W.E., Bian, X., Charney, J.J., Hom, J., Mueller, E., Hadden, R., Campbell-Lochrie, Z., Walker-Ravena, C., & Kremens, R. 2019.Intermediate-scale fire behavior measurements in the field: Bridging the gap between laboratory experiments and management-scale prescribed fires. In: Proceedings of the 6th Fire Behavior and Fuels Conference, April 29 - May 3, 2019, Albuquerque, New Mexico USA. Missoula, MT: International Association of Wildland Fire: 615-620.

Mueller, E.V., Skowronski, N.S., Clark, K.L., Gallagher, M.R., Mell, W.E., Simeoni, A., & Hadden, R.M. Detailed physical modeling of wildland fire dynamics at field scale – an experimentally informed evaluation. *Int. Assoc. for Fire Safety Sciences Symposium*, 27 Apr – 1 May 2020, Waterloo, Ontario, CA.

Mueller, E.V., Campbell-Lochrie, Z., Mell, W.E., & Hadden, R.M. "Numerical simulation of low-intensity fire spread in pine litter," in *Advances in forest fire research*, D. X. Viegas, Ed. Imprensa da Universidade de Coimbra, 2018, pp. 1296–1299.

Conference or symposium abstracts

Walker-Rávena, E., Campbell-Lochrie, Z., & Hadden, R.M. "The Influence of Structure on the Flammability of Wildland Fuels under Radiative Heating," 2019. 6th International Fire Behaviour and Fuels Conference, Marseille, France, April 2019

Walker-Ravena, C., Gallagher, M.R., Skowronski, N.S., Hadden, R.M. The role of local and global geometry on the flammability of porous fuel beds. Poster. 13th International Symposium on Fire Safety Science. 27 April – 1 May 2020, Waterloo, Ontario, CAN.

Campbell-Lochrie, Z., Walker-Ravena, C., Gallagher, M., Skowronski, N.S., Mueller, E.V., & Hadden, R.M. The Role of Bulk Properties and In-Bed Structure in the flow regime of buoyancy driven flame spread in natural porous fuel beds. 13th International Symposium on Fire Safety Science. 27 April – 1 May 2020, Waterloo, Ontario, CAN. [Online] April 2021

Campbell-Lochrie, Z., Walker-Ravena, C., Gallagher, M., Skowronski, N.S., Mueller, E.V., &

Hadden, R.M. The role of fuel loading and structure on the physical phenomena that control the flame spread process in wildland fuels. England and Wales Wildfire Forum Wildfire Conference 2019. Cardiff, Wales, Nov 2019

Campbell-Lochrie, Z.,Walker-Rávena, C., Mueller, E.V., & Hadden, R.M. "The effect of interstitial flow on the burning dynamics of porous fuel beds," *8th International Conference on Forest Fire Research*, 12-16 Nov 2018, Coimbra, Portugal.

Charney, J., Skowronski, N.S., Heilman, W., & Gallagher, M. Multi-scale analyses of wildland fire combustion processes in open-canopied forests using coupled and iteratively informed laboratory -, field-, and model-based approaches. Poster presentation. American Meteorological Society 12th Fire and Forest Meteorology Symposium. 15 – 18 May 2018, Boise, ID.

Clark, K.L., Heilman, W.E., Skowronski, N.S., Gallagher, M.R., Mueller, E.V., Hadden, R.M, & Simeoni, A. Turbulence and Energy Exchange during Wildland Fires in the New Jersey Pinelands. American Geophysical Union, 9-13 Dec. 2019. San Francisco, CA, USA.

Clark, K.L., Skowronski, N.S., Gallagher, M.R., Mueller, E.V., Hadden, R., Campbell-Lochrie, Z., Walker-Ravena, C., Heilman, W., Bian, X., Kremens, R., Hom, J. & Patterson, M. Intermediate-scale fire behavior measurements in the field: Bridging the gap between laboratory experiments and management-scale prescribed fires. International Association for Wildland Fire 6th International Fire Behavior and Fuels Conference, 29 – 04 May 2019, Albuquerque, NM, USA.

Clark, K.L., Skowronski, N.S., Gallagher, M.R., Mueller, E.V., Hadden, R., Campbell-Lochrie, Z., Walker-Ravena, C., Heilman, W., Bian, X., Kremens, R., Hom, J. & Patterson, M. Intermediate-scale fire behavior measurements in the field: Bridging the gap between the laboratory experiments and management-scale prescribed fires. Poster. United States Department of Defense SERDP and ESTCP Symposium, 27-29 November 2018, Washington, D.C.

Everland, L., Gallagher, M.R., Pokswinski, S., Hiers, K., Wilson, A., Defeo, J., & Skowronski, N.S. Environmentally Driven Dynamics of Bark Flakes: A Primary Driver of Spotfires During Wildland Fires. Rutgers Climate Symposium, 20 November 2019, Piscataway, NJ, USA

Gallagher, M.R., S. Pokswinski, S., Rhone, M., Soriano, N., Bell, S., Loudermilk, L., O'Brien, J.J., Skowronski, N.S., & Hiers, K. Dynamism of bark roughness as a possible factor in firebrand production. International Association for Wildland Fire 6th International Fire Behavior and Fuels Conference, 29 – 04 April 2019, Albuquerque, NM, USA.

Gallagher, M.R., Skowronski, N.S., Heilman, W., Clark, K., Patterson, M., Cole, J., Hadden, R., Mueller, E., Thomas, J.C., Campbell-Lochrie, Z., Walker-Ravena, C., Simeoni, A., McLaughlin, G., Webber, J., Achey, M., Judy, S., Gerber, T., Brick, B., Moore, S., Earlin, J., Knaurer, S., Corvinus,, B., & House, A. Invited Oral Presentation: Differential Impacts of Quality and Seasonality of Fire in Pitch Pine Forests. American Association for Geography Annual Meeting, 1 – 5 April 2019, Washington, D.C., USA.

Gallagher, M., Skowronski, N.S., Clark, K.L., Heilman, W.E., Charney, J., Bian, X., Cole, J., Patterson,M., Hom, J., Hadden, R., Mueller, E., Campbell-Lochrie, Z., Walker- Ravena, C.,

Thomas, J., Yuill, C., Rhone, M., Kremens, R., Simeoni, A., Rangwala, A., Im, S., DiCristina, G., Zhong, S., & Kiefer, M. Fine scale remote sensing of fuel loading, temperature, fire spread, and consumption to test numerical physics-based fire spread models. Poster. United States Department of Defense SERDP and ESTCP Symposium, 27-29 November 2018, Washington, D.C.

R.M. Hadden, Campbell-Lochrie, Z., Walker-Ravena, C., Mueller, E.V., Zen, S., Gallagher, M., Skowronski, N.S., & Clark, K.L. Experimental investigation of the role of fuel load, fuel structure, and environmental conditions on low-intensity prescribed fires. England and Wales Wildfire Forum Wildfire Conference 2019. Nov 2019

Heilman, W.E., Charney, J.J., Bian, X., Zhong, S., Skowronski, N.S., Clark, K.L., Gallagher, M.R., Patterson, M., Hom, J.L., & Seitz, J. Observed Vertical Momentum Flux Characteristics during a Management-Scale Prescribed Fire in a Forested Environment. 13th Fire and Forest Meteorology Symposium. 12-14 May 2020 Palm Springs, CA, USA.

Heilman, W. E., Clark, K.L., Bian, X., Charney, J.J., Zhong, S., Skowronski, N.S., Gallagher, M.R., & Patterson, M. 2021. Observed turbulent momentum flux characteristics during a management-scale prescribed fire in a forested environment. 13th Fire and Forest Meteorology Symposium, American Meteorological Society, Virtual.

Hoehler, M., Gallagher, M., & Hadden, R. The Eye of Sauron. *Proc. Int. Assoc. for Fire Safety Sciences Symposium*, 27 Apr – 1 May 2020, Waterloo, Ontario, CA.

Kiefer, M.T., Heilman, W.E., Zhong, S., Charney, J.J., Bian, X., Skowronski, N.S., Clark, K.L., Gallagher, M.R., Hom, J.L., & Patterson, M. Use of a High-Resolution Atmospheric Model for Pre-Burn Instrumentation Deployment Guidance. International Association for Wildland Fire 6th International Fire Behavior and Fuels Conference, 29 – 04 May 2019, Albuquerque, NM, USA.

Kiefer, M.T., Heilman, W.E., Zhong, S., Charney, J.J., Bian, X., Skowronski, N.S., Clark, K.L., Gallagher, M.R., Hom, J.L., & Patterson, M. 2021. A numerical study of fire- and forest canopy-induced turbulence during a management-scale prescribed fire in the New Jersey Pine Barrens. 13th Fire and Forest Meteorology Symposium, American Meteorological Society, Virtual.

Mueller E.V., Campbell-Lochrie Z., Mell W., Hadden R.M. (2018) Numerical simulation of low-intensity fire spread in pine litter, *8th International Conference on Forest Fire Research*, 12-16 Nov 2018, Coimbra, Portugal.

Mueller E.V., Mell W., Simeoni A., Hadden R.M. (2017) A multi-scale approach to the development of robust physics-based models of wildland fire behavior, Invited workshop, *21st International Congress on Modelling and Simulation (MODSIM)*, 3-8 Dec 2017, Tasmania, AU.

Mueller E.V., Skowronski N., Clark K., Gallagher M.R., Campbell-Lochrie Z., Walker-Ravena C., Kremens R., Mell W., Simeoni A., Hadden R.M. (2018) Use of a detailed physics-based modeling approach for evaluating the impact of low-intensity operational burning activities, Invited talk, EP31B-05, *AGU Fall Meeting*, 10-14 Dec 2018, Washington, DC, USA.

Mueller, E.V., N. Skowronski, K. Clark, M. Gallagher, Z. Campbell-Lochrie, C. Walker-Ravena, R. Kremens, W. Mell, A. Simeoni, and R. Hadden. Use of a detailed physics-based modeling

approach for evaluating the impact of low-intensity operational burning activities. American Geophysical Union Fall Meeting. 10-14 Dec 2018, Washington, D.C., USA.

Skowronski, N.S. 2017. A new look at backing fire and effects. Association for Wildland Fire 7th International Fire Ecology and Management Congress, Orlando, FL. 1-2 December 2017.

Skowronski, N.S. 2018. Combustion Physics of Wildland Fire: What is SERDP Research Telling Us? SERDP Annual Meeting. Washington, DC. 3 December 2019.

Skowronski, N.S., Simeoni, A., Heilman, W.E., Clark, K.L., Mell, W., Hom, J., Charney, J.J., Im, S.K., Rangwala, A., Zhong, S., Kremens, R., & *Gallagher, M.R.* 2016. Multi-scale analyses of wildland fire combustion processes in open-canopied forests using coupled and iteratively informed laboratory-, field-, and model-based approaches. 5th Fire and Fuels Conference, Portland, OR. 11-15 April 2016.

Skowronski, N.S., Gallagher, M., Clark, K., Heilman, W.E., Charney, J.J., Bian, X., Cole, J., Hom, J., Patterson, M., Hadden, R., Mueller, E., Thomas, J., Campbell-Lochrie, Z., Ravena-Walker, C., Kremens, R., Simeoni, A., Rangwala, A., Im, S., DiCristina, G., Yuill, C., Rhone, M., Zhong, S., & Kiefer, M. 2018. Fine-scale remote sensing of fuels, consumption, fire spread, and heat flux. Strategic Environmental Research and Development Program (SERDP) and Environmental Security Technology Certification Program (ESTCP) Symposium, Washington, DC.

Literature Cited

Albini, F.A. (1981). A model for the wind-blown flame from a line fire. *Combustion and Flame, 43*, 155-174

Anderson, H.E. (1990). *Relationship of fuel size and spacing to combustion characteristics of laboratory fuel cribs*. US Department of Agriculture, Forest Service, Intermountain Forest and Range …

Anderson, W.R., Catchpole, E., & Butler, B. (2010). Convective heat transfer in fire spread through fine fuel beds. *International Journal of Wildland Fire, 19*, 284-298

Andrews, P.L. (2014). Current status and future needs of the BehavePlus Fire Modeling System. *International Journal of Wildland Fire, 23*, 21-33

Bao, Y., Wu, Q., & Zhou, D. (2012). Numerical investigation of flow around an inline square cylinder array with different spacing ratios. *Computers & Fluids, 55*, 118-131

Bartoli, P., Santoni, P., Simeoni, A., & Torero, J. (2011a). Feux de forêt: amélioration de la connaissance du couplage combustible-flamme. In: Thèse de Doctorat, Université de Corse, Corte

Bartoli, P., Simeoni, A., Biteau, H., Torero, J.L., & Santoni, P.-A. (2011b). Determination of the main parameters influencing forest fuel combustion dynamics. *Fire Safety Journal, 46*, 27-33

Beer, T. (1995). Fire propagation in vertical stick arrays-the effects of wind. *International Journal of Wildland Fire, 5*, 43-49

Benech, B. (1976). Experimental study of an artificial convective plume initiated from the ground. *Journal of Applied Meteorology and Climatology, 15*, 127-137

Campbell-Lochrie, Z., Walker-Ravena, C., Gallagher, M., Skowronski, N., Mueller, E.V., & Hadden, R.M. (2021). Investigation of the role of bulk properties and in-bed structure in the flow regime of buoyancy-dominated flame spread in porous fuel beds. *Fire Safety Journal, 120*, 103035

Campbell-Lochrie, Z., Walker-Rávena, C., Mueller, E.V., & Hadden, R.M. (2018). The effect of interstitial flow on the burning dynamics of porous fuel beds. *Parte: http://hdl. handle. net/10316.2/44517*

Cao, J., Tamura, Y., & Yoshida, A. (2012). Wind tunnel study on aerodynamic characteristics of shrubby specimens of three tree species. *Urban forestry & urban greening, 11*, 465-476

Carmo, B., Meneghini, J., & Sherwin, S. (2010a). Possible states in the flow around two circular cylinders in tandem with separations in the vicinity of the drag inversion spacing. *Physics of Fluids, 22*, 054101

Carmo, B.S., Meneghini, J.R., & Sherwin, S.J. (2010b). Secondary instabilities in the flow around two circular cylinders in tandem. *Journal of Fluid Mechanics, 644*, 395-431

Catchpole, W., Catchpole, E., Butler, B., Rothermel, R., Morris, G., & Latham, D. (1998). Rate of spread of free-burning fires in woody fuels in a wind tunnel. *Combustion Science and Technology, 131*, 1-37

Cattafesta, L., Bahr, C., & Mathew, J. (2010). Fundamentals of wind-tunnel design. *Encyclopedia of Aerospace Engineering*

Charney, J.J., Kiefer, M.T., Zhong, S., Heilman, W.E., Nikolic, J., Bian, X., Hom, J.L., Clark, K.L., Skowronski, N.S., & Gallagher, M.R. (2019). Assessing Forest Canopy Impacts on Smoke Concentrations Using a Coupled Numerical Model. *Atmosphere, 10*, 273

Chou, M.-D. (1990). Parameterizations for the absorption of solar radiation by O2 and CO2 with application to climate studies. *Journal of Climate, 3*, 209-217

Chou, M.-D. (1992). A solar radiation model for use in climate studies. *Journal of Atmospheric Sciences, 49*, 762-772

Chou, M.-D., & Suarez, M.J. (1994). An efficient thermal infrared radiation parameterization for use in general circulation models

Clark, K., Renninger, H., Skowronski, N., Gallagher, M., & Schäfer, K. (2018). Decadal-scale reduction in forest net ecosystem production following insect defoliation contrasts with short-term impacts of prescribed fires. *Forests, 9*, 145

Clark, K.L., Heilman, W.E., Skowronski, N.S., Gallagher, M.R., Mueller, E., Hadden, R., & Simeoni, A. (2020). Fire Behavior, Fuel Consumption, and Turbulence and Energy Exchange during Prescribed Fires in Pitch Pine Forests. *Atmosphere, 11*, 242

Clark, K.L., Skowronski, N., & Gallagher, M. (2014). The fire research program at the Silas Little Experimental Forest, New Lisbon, New Jersey. *USDA Forest Service experimental forests and ranges* (pp. 515-534): Springer

Clark, K.L., Skowronski, N., Gallagher, M., Renninger, H., & Schäfer, K. (2012). Effects of invasive insects and fire on forest energy exchange and evapotranspiration in the New Jersey pinelands. *Agricultural and Forest Meteorology, 166*, 50-61

Clement, R. (2012). EdiRe Data Software, version 1.5. 0.32. *University of Edinburgh: Edinburgh, UK*

Comte-Bellot, G., & Corrsin, S. (1966). The use of a contraction to improve the isotropy of grid-generated turbulence. *Journal of Fluid Mechanics, 25*, 657-682

Cruz, M.G., Alexander, M.E., & Sullivan, A.L. (2017). Mantras of wildland fire behaviour modelling: facts or fallacies? *International Journal of Wildland Fire, 26*, 973-981

Curry, J.R., & Fons, W.L. (1940). Forest-fire behavior studies. *Mechanical Engineering. 62: 219-225, 62*, 219-225

Di Cristina, G., Kozhumal, S., Simeoni, A., Skowronski, N., Rangwala, A., & Im, S.-k. (2021). Forced convection fire spread along wooden dowel array. *Fire Safety Journal, 120*, 103090

Dupont, S., & Brunet, Y. (2008). Influence of foliar density profile on canopy flow: a large-eddy simulation study. *Agricultural and Forest Meteorology, 148*, 976-990

Dupuy, J.-L. (1995). Slope and fuel load effects on fire behavior: laboratory experiments in pine needles fuel beds. *International Journal of Wildland Fire, 5*, 153-164

Dupuy, J.-L., & Maréchal, J. (2011). Slope effect on laboratory fire spread: contribution of radiation and convection to fuel bed preheating. *International Journal of Wildland Fire, 20*, 289-307

El Houssami, M. (2016). Development of a numerical and experimental framework to understand and predict the burning dynamics of porous fuel beds. University of Edinburgh

El Houssami, M., Lamorlette, A., Morvan, D., Hadden, R.M., & Simeoni, A. (2018). Framework for submodel improvement in wildfire modeling. *Combustion and Flame, 190*, 12-24

El Houssami, M., Mueller, E., Filkov, A., Thomas, J.C., Skowronski, N., Gallagher, M.R., Clark, K., Kremens, R., & Simeoni, A. (2016). Experimental procedures characterising firebrand generation in wildland fires. *Fire technology, 52*, 731-751

Emmons, H.W. (1965). Fundamental problems of the free burning fire. In, *Symposium (International) on Combustion* (pp. 951-964): Elsevier

Emmons, H.W., & Shen, T. (1971). Fire spread in paper arrays. In, *Symposium (international) on Combustion* (pp. 917-926): Elsevier

Fang, J., & Steward, F. (1969). Flame spread through randomly packed fuel particles. *Combustion and Flame, 13*, 392-398

Fehrmann, S., Jahn, W., & de Dios Rivera, J. (2017). Permeability comparison of natural and artificial pinus radiata forest litters. *Fire technology, 53*, 1291-1308

Fernandes, P.M., Botelho, H.S., Rego, F.C., & Loureiro, C. (2009). Empirical modelling of surface fire behaviour in maritime pine stands. *International Journal of Wildland Fire, 18*, 698-710

Fernandez-Pello, A., & Law, C. (1982). On the mixed-convective flame structure in the stagnation point of a fuel particle. In, *Symposium (International) on Combustion* (pp. 1037-1044): Elsevier

Finney, M.A., Cohen, J.D., Forthofer, J.M., McAllister, S.S., Gollner, M.J., Gorham, D.J., Saito, K., Akafuah, N.K., Adam, B.A., & English, J.D. (2015). Role of buoyant flame dynamics in wildfire spread. *Proceedings of the National Academy of Sciences, 112*, 9833-9838

Finney, M.A., Cohen, J.D., McAllister, S.S., & Jolly, W.M. (2013). On the need for a theory of wildland fire spread. *International Journal of Wildland Fire, 22*, 25-36

Finnigan, J. (2000). Turbulence in plant canopies. *Annual Review of Fluid Mechanics, 32*, 519-571

Fons, W.L. (1946). Analysis of fire spread in light forest fuels. *Journal of Agricultural Research, 72*, 93-121

Gallagher, M.R. (2017). Monitoring fire effects in the New Jersey Pine Barrens with burn severity indices. In: Rutgers University-School of Graduate Studies

Gallagher, M.R., Clark, K., Thomas, J.C., Mell, W., Hadden, R.M., Mueller, E.V., Kremens, R.L., El Houssami, M., Filkov, A.I., Simeoni, A.A., & Skowronski, N.S. (2017). New Jersey fuel treatment effects: Pre- and post-burn biometric data. In. Fort Collins, CO: Forest Service Research Data Archive

Gollner, M.J., Xie, Y., Lee, M., Nakamura, Y., & Rangwala, A.S. (2012). Burning behavior of vertical matchstick arrays. *Combustion Science and Technology, 184*, 585-607

Harimi, I., & Saghafian, M. (2012). Numerical simulation of fluid flow and forced convection heat transfer from tandem circular cylinders using overset grid method. *Journal of fluids and structures, 28*, 309-327

Heilman, W.E., Banerjee, T., Clements, C.B., Clark, K.L., Zhong, S., & Bian, X. (2021). Observations of Sweep–Ejection Dynamics for Heat and Momentum Fluxes during Wildland Fires in Forested and Grassland Environments. *Journal of Applied Meteorology and Climatology, 60*, 185-199

Heilman, W.E., Bian, X., Clark, K.L., Skowronski, N.S., Hom, J.L., & Gallagher, M.R. (2017). Atmospheric turbulence observations in the vicinity of surface fires in forested environments. *Journal of Applied Meteorology and Climatology, 56*, 3133-3150

Heilman, W.E., Bian, X., Clark, K.L., & Zhong, S. (2019). Observations of Turbulent Heat and Momentum Fluxes during Wildland Fires in Forested Environments. *Journal of Applied Meteorology and Climatology, 58*, 813-829

Heilman, W.E., Clements, C.B., Seto, D., Bian, X., Clark, K.L., Skowronski, N.S., & Hom, J.L. (2015). Observations of fire-induced turbulence regimes during low-intensity wildland fires in forested environments: implications for smoke dispersion. *Atmospheric Science Letters, 16*, 453-460

Hiers, J., Ottmar, R., Butler, B., Clements, C., Vihnanek, R., Dickinson, M., & O'Brien, J. (2009). An overview of the prescribed fire combustion and atmospheric dynamics research experiment (Rx-CADRE). In, *4th International Fire Ecology and Management Congress: Fire as a Global Process, Savannah, Georgia, USA*

Hoffman, C.M., Linn, R., Parsons, R., Sieg, C., & Winterkamp, J. (2015). Modeling spatial and temporal dynamics of wind flow and potential fire behavior following a mountain pine beetle outbreak in a lodgepole pine forest. *Agricultural and Forest Meteorology, 204*, 79-93

Holdich, R. (2020). *Fundamentals of particle technology*. MidlandIT

Janssens, M.L. (1991). Measuring rate of heat release by oxygen consumption. *Fire technology, 27*, 234-249

Jiang, L., Zhao, Z., Tang, W., Miller, C., Sun, J.-H., & Gollner, M.J. (2019). Flame spread and burning rates through vertical arrays of wooden dowels. *Proceedings of the Combustion Institute, 37*, 3767-3774

Khan, W., Culham, J., & Yovanovich, M. (2005). Fluid flow around and heat transfer from an infinite circular cylinder

Kiefer, M., Zhong, S., Heilman, W., Charney, J., & Bian, X. (2013). Evaluation of an ARPS-based canopy flow modeling system for use in future operational smoke prediction efforts. *Journal of Geophysical Research: Atmospheres, 118*, 6175-6188

Kiefer, M.T., Heilman, W.E., Zhong, S., Charney, J.J., & Bian, X. (2015). Mean and turbulent flow downstream of a low-intensity fire: Influence of canopy and background atmospheric conditions. *Journal of Applied Meteorology and Climatology, 54*, 42-57

Kiefer, M.T., Heilman, W.E., Zhong, S., Charney, J.J., & Bian, X. (2016). A study of the influence of forest gaps on fire–atmosphere interactions. *Atmospheric Chemistry and Physics, 16*, 8499-8509

Kiefer, M.T., Heilman, W.E., Zhong, S., Charney, J.J., Bian, X., Skowronski, N.S., Hom, J.L., Clark, K.L., Patterson, M., & Gallagher, M.R. (2014). Multiscale simulation of a prescribed fire event in the New Jersey Pine Barrens using ARPS-CANOPY. *Journal of Applied Meteorology and Climatology, 53*, 793-812

Kiefer, M.T., Lin, Y.-L., & Charney, J.J. (2008). A study of two-dimensional dry convective plume modes with variable critical level height. *Journal of Atmospheric Sciences, 65*, 448-469

Kiefer, M.T., Parker, M.D., & Charney, J.J. (2009). Regimes of dry convection above wildfires: Idealized numerical simulations and dimensional analysis. *Journal of the Atmospheric Sciences, 66*, 806-836

Kiefer, M.T., Parker, M.D., & Charney, J.J. (2010). Regimes of dry convection above wildfires: Sensitivity to fire line details. *Journal of the Atmospheric Sciences, 67*, 611-632

Kiefer, M.T., Zhong, S., Heilman, W.E., Charney, J.J., & Bian, X. (2018). A numerical study of atmospheric perturbations induced by heat from a wildland fire: Sensitivity to vertical canopy structure and heat source strength. *Journal of Geophysical Research: Atmospheres, 123*, 2555-2572

Koo, E., Pagni, P.J., Weise, D.R., & Woycheese, J.P. (2010). Firebrands and spotting ignition in large-scale fires. *International Journal of Wildland Fire, 19*, 818-843

Kosdon, F.J., Williams, F., & Buman, C. (1969). Combustion of vertical cellulosic cylinders in air. In, *Symposium (International) on Combustion* (pp. 253-264): Elsevier

Kremens, R., Dickinson, M., & Bova, A. (2012). Radiant flux density, energy density and fuel consumption in mixed-oak forest surface fires. *International Journal of Wildland Fire, 21*, 722-730

Kremens, R.L., Skowronski, N.S., Simeoni, A.A., Clark, K.L., Mell, W.E., Hadden, R.M., Gallagher, M.R., Mueller, E.V., El Houssami, M., & Filkov, A.I. (2017). New Jersey fuel treatment effects: Wildfire Airborne Sensor Program-orthorectified long-wave infrared and visible data images

Kyan, C.P., Wasan, D.T., & Kintner, R.C. (1970). Flow of single-phase fluids through fibrous beds. *Industrial & Engineering Chemistry Fundamentals, 9*, 596-603

Linn, R.R., Goodrick, S., Brambilla, S., Brown, M.J., Middleton, R.S., O'Brien, J.J., & Hiers, J.K. (2020). QUIC-fire: A fast-running simulation tool for prescribed fire planning. *Environmental Modelling & Software, 125*, 104616

Little, S., & Trew, I.F. (1979). Pitch X loblolly pine hybrids: Loblollies for the North? *Journal of Forestry, 77*, 709-716

Marcelli, T., Santoni, P.A., Simeoni, A., Leoni, E., & Porterie, B. (2004). Fire spread across pine needle fuel beds: characterization of temperature and velocity distributions within the fire plume. *International Journal of Wildland Fire, 13*, 37-48

McAllister, S., & Finney, M. (2016). The effect of wind on burning rate of wood cribs. *Fire technology, 52*, 1035-1050

McCaffrey, B., & Heskestad, G. (1976). A robust bidirectional low-velocity probe for flame and fire application. *Combustion and Flame, 26*, 125-127

McDermott, R., McGrattan, K., & Hostikka, S. (2008). Fire dynamics simulator (version 5) technical reference guide. *NIST Special Publication, 1018*

McGuire, J. (1952). The calculation of heat transfer by radiation. *Fire Safety Science, 20*, -1--1

Mehta, R.D., & Bradshaw, P. (1979). Design rules for small low speed wind tunnels. *Aeronautical Journal, 83*, 443-449

Mell, W., Maranghides, A., McDermott, R., & Manzello, S.L. (2009). Numerical simulation and experiments of burning douglas fir trees. *Combustion and Flame, 156*, 2023-2041

Mell, W.E., Manzello, S.L., Maranghides, A., Butry, D., & Rehm, R.G. (2010). The wildland–urban interface fire problem–current approaches and research needs. *International Journal of Wildland Fire, 19*, 238-251

Michioka, T., & Chow, F.K. (2008). High-resolution large-eddy simulations of scalar transport in atmospheric boundary layer flow over complex terrain. *Journal of Applied Meteorology and Climatology, 47*, 3150-3169

Miller, C.H., & Gollner, M.J. (2015). Upward flame spread over discrete fuels. *Fire Safety Journal, 77*, 36-45

Morandini, F., Perez-Ramirez, Y., Tihay, V., Santoni, P.-A., & Barboni, T. (2013). Radiant, convective and heat release characterization of vegetation fire. *International Journal of Thermal Sciences, 70*, 83-91

Morandini, F., Silvani, X., Rossi, L., Santoni, P.-A., Simeoni, A., Balbi, J.-H., Rossi, J.L., & Marcelli, T. (2006). Fire spread experiment across Mediterranean shrub: influence of wind on flame front properties. *Fire Safety Journal, 41*, 229-235

Morel, T. (1975). Comprehensive design of axisymmetric wind tunnel contractions

Mueller, E., Mell, W., & Simeoni, A. (2014). Large eddy simulation of forest canopy flow for wildland fire modeling. *Canadian Journal of forest research, 44*, 1534-1544

Mueller, E.V., Skowronski, N., Clark, K., Gallagher, M., Kremens, R., Thomas, J.C., El Houssami, M., Filkov, A., Hadden, R.M., & Mell, W. (2017). Utilization of remote sensing techniques for the quantification of fire behavior in two pine stands. *Fire Safety Journal, 91*, 845-854

Mueller, E.V., Skowronski, N., Clark, K.L., Gallagher, M.R., Campbell-Lochrie, Z., Walker-Ravena, C., Kremens, R., Mell, W., Simeoni, A., & Hadden, R.M. (2018). Use of a detailed physics-based modeling approach for evaluating the impact of low-intensity operational burning activities. In, *AGU Fall Meeting Abstracts*

Mueller, E.V., Skowronski, N.S., Clark, K.L., Gallagher, M.R., Mell, W.E., Simeoni, A., & Hadden, R.M. (2021). Detailed physical modeling of wildland fire dynamics at field scale-An experimentally informed evaluation. *Fire Safety Journal, 120*, 103051

Noilhan, J., & Planton, S. (1989). A Simple Parameterization of Land Surface Processes for Meteorological Models, Monthly Weather Re-35 view, 117, 536–549. In

Palmer, K. (1957). Smouldering combustion in dusts and fibrous materials. *Combustion and Flame, 1*, 129-154

Papaioannou, G.V., Yue, D.K., Triantafyllou, M.S., & Karniadakis, G.E. (2006). Three-dimensionality effects in flow around two tandem cylinders. *Journal of Fluid Mechanics, 558*, 387

Parker, M.D., & Johnson, R.H. (2004). Structures and dynamics of quasi-2D mesoscale convective systems. *Journal of the Atmospheric Sciences, 61*, 545-567

Pimont, F., Dupuy, J.-L., Linn, R.R., & Dupont, S. (2011). Impacts of tree canopy structure on wind flows and fire propagation simulated with FIRETEC. *Annals of Forest Science, 68*, 523

Pleim, J.E., & Xiu, A. (1995). Development and testing of a surface flux and planetary boundary layer model for application in mesoscale models. *Journal of Applied Meteorology, 34*, 16-32

Pope, S.B. (2001). Turbulent flows. In: IOP Publishing

Prahl, J.M., & Tien, J.S. (1973). Preliminary investigations of forced convection on flame propagation along paper and matchstick arrays. *Combustion Science and Technology, 7*, 271-282

Quintiere, J.G. (2006). Fundamentals of fire phenomena

Raghavan, V., Babu, V., & Sundararajan, T. (2009). Investigation of interaction between methanol fed tandem porous spheres burning in a mixed convective environment. *Combustion Theory and Modelling, 13*, 461-485

Rogers, E., DiMego, G., Black, T., Ek, M., Ferrier, B., Gayno, G., Janjic, Z., Lin, Y., Pyle, M., & Wong, V. (2009). The NCEP North American mesoscale modeling system: Recent changes and future plans. In, *Preprints, 23rd Conference on Weather Analysis and Forecasting/19th Conference on Numerical Weather Prediction*

Rossa, C.G. (2017). The effect of fuel moisture content on the spread rate of forest fires in the absence of wind or slope. *International Journal of Wildland Fire, 26*, 24-31

Rossa, C.G., & Fernandes, P.M. (2018). Empirical modeling of fire spread rate in no-wind and no-slope conditions. *Forest Science, 64*, 358-370

Rothermel, R. (1972). A mathematical model for predicting fire spread in wildland fuels. *USDA Forest Service Research Paper INT (USA)*

Rothermel, R.C., & Anderson, H.E. (1966). *Fire spread characteristics determined in the laboratory*. Intermountain Forest & Range Experiment Station, Forest Service, US …

Rudnicki, M., Mitchell, S.J., & Novak, M.D. (2004). Wind tunnel measurements of crown streamlining and drag relationships for three conifer species. *Canadian Journal of forest research, 34*, 666-676

Rumpf, H. (1990). The characteristics of systems and their changes of state disperse. *Part. Technol., Chapman and Hall*, 8-54

Santoni, P., Bartoli, P., Simeoni, A., & Torero, J. (2014). Bulk and particle properties of pine needle fuel beds–influence on combustion. *International Journal of Wildland Fire, 23*, 1076-1086

Schlichting, H., & Gersten, K. (2016). *Boundary-layer theory*. Springer

Schlichting, H., Gersten, K., Krause, E., Oertel, H., & Mayes, K. (1955). 574 Boundary-layer theory. In: Springer

Seto, D., Clements, C.B., & Heilman, W.E. (2013). Turbulence spectra measured during fire front passage. *Agricultural and Forest Meteorology, 169*, 195-210

Sewatkar, C., Patel, R., Sharma, A., & Agrawal, A. (2012). Flow around six in-line square cylinders. *Journal of Fluid Mechanics, 710*, 195-233

Silvani, X., & Morandini, F. (2009). Fire spread experiments in the field: temperature and heat fluxes measurements. *Fire Safety Journal, 44*, 279-285

Silvani, X., Morandini, F., Dupuy, J., Susset, A., Vernet, R., & Lambert, O. (2018). Measuring velocity field and heat transfer during natural fire spread over large inclinable bench. *Experimental thermal and fluid science, 92*, 184-201

Simeoni, A., Salinesi, P., & Morandini, F. (2011). Physical modelling of forest fire spreading through heterogeneous fuel beds. *International Journal of Wildland Fire, 20*, 625-632

Simeoni, A., Thomas, J., Bartoli, P., Borowieck, P., Reszka, P., Colella, F., Santoni, P.-A., & Torero, J.L. (2012). Flammability studies for wildland and wildland–urban interface fires applied to pine needles and solid polymers. *Fire Safety Journal, 54*, 203-217

Skowronski, N.S. (2011a). Quantifying three-dimensional vegetation structure and its responses to disturbances using laser altimetry in the New Jersey Pinelands. In: Rutgers The State University of New Jersey-New Brunswick

Skowronski, N.S. (2011b). Quantifying three-dimensional vegetation structure and itsresponses to disturbances using laser altimetry in the New Jersey Pinelands. In: Rutgers The State University of New Jersey-New Brunswick

Skowronski, N.S., Clark, K.L., Gallagher, M., Birdsey, R.A., & Hom, J.L. (2014). Airborne laser scanner-assisted estimation of aboveground biomass change in a temperate oak–pine forest. *Remote sensing of Environment, 151*, 166-174

Steward, F., Wuest, L., & Waibel, R. (1977). Some characteristics of fires within uniform fuel matrices. *Heat Transfer Division Paper*

Stocks, B., Alexander, M., Wotton, B., Stefner, C., Flannigan, M., Taylor, S., Lavoie, N., Mason, J., Hartley, G., & Maffey, M. (2004). Crown fire behaviour in a northern jack pine black spruce forest. *Canadian Journal of forest research, 34*, 1548-1560

Su, Y.-x. (1991). Flow analysis and design of three-dimensional wind tunnel contractions. *AIAA journal, 29*, 1912-1920

Sullivan, A., Knight, I., Hurley, R., & Webber, C. (2013). A contractionless, low-turbulence wind tunnel for the study of free-burning fires. *Experimental thermal and fluid science, 44*, 264-274

Sullivan, A., Surawski, N., Crawford, D., Hurley, R., Volkova, L., Weston, C., & Meyer, C. (2018). Effect of woody debris on the rate of spread of surface fires in forest fuels in a combustion wind tunnel. *Forest ecology and management, 424*, 236-245

Sullivan, A.L. (2009). Wildland surface fire spread modelling, 1990–2007. 3: Simulation and mathematical analogue models. *International Journal of Wildland Fire, 18*, 387-403

Sumner, D. (2010). Two circular cylinders in cross-flow: a review. *Journal of fluids and structures, 26*, 849-899

Sun, R., Jenkins, M.A., Krueger, S.K., Mell, W., & Charney, J.J. (2006). An evaluation of fire-plume properties simulated with the Fire Dynamics Simulator (FDS) and the Clark coupled wildfire model. *Canadian Journal of forest research, 36*, 2894-2908

Sun, W.-Y., & Chang, C.-Z. (1986). Diffusion model for a convective layer. Part I: Numerical simulation of convective boundary layer. *Journal of Applied Meteorology and Climatology, 25*, 1445-1453

Thomas, J.C. (Ed.) (2016). *Improving the understand of the fundamental mechanism that influence the ignition and burning dynamics of porous wildland fuels*: University of Edinburgh, School of Engineering, Edinburgh, UK, 2016

Thomas, J.C., Hadden, R.M., & Simeoni, A. (2017a). Experimental investigation of the impact of oxygen flux on the burning dynamics of forest fuel beds. *Fire Safety Journal, 91*, 855-863

Thomas, J.C., Mueller, E.V., Santamaria, S., Gallagher, M., El Houssami, M., Filkov, A., Clark, K., Skowronski, N., Hadden, R.M., & Mell, W. (2017b). Investigation of firebrand generation from an experimental fire: Development of a reliable data collection methodology. *Fire Safety Journal, 91*, 864-871

Thomas, P. (1967). Some aspects of the growth and spread of fire in the open. *Forestry: An International Journal of Forest Research, 40*, 139-164

Varner, J.M., Kane, J.M., Kreye, J.K., & Engber, E. (2015). The flammability of forest and woodland litter: a synthesis. *Current Forestry Reports, 1*, 91-99

Viegas, D.X., Pinto, C., & Raposo, J. (2018). Burning Rate. In S.L. Manzello (Ed.), *Encyclopedia of Wildfires and Wildland-Urban Interface (WUI) Fires* (pp. 1-8). Cham: Springer International Publishing

Vogel, M., & Williams, F. (1970). Flame propagation along matchstick arrays. *Combustion Science and Technology, 1*, 429-436

Vollsinger, S., Mitchell, S.J., Byrne, K.E., Novak, M.D., & Rudnicki, M. (2005). Wind tunnel measurements of crown streamlining and drag relationships for several hardwood species. *Canadian Journal of forest research, 35*, 1238-1249

Weise, D.R., & Biging, G.S. (1994). Effects of wind velocity and slope on fire behavior. In, *In: Takashi Kashiwagi, ed. 1994. Fire Safety Science Proceedings of the Fourth International Symposium. Intl. Assoc. for Fire Safety Science, Boston, MA: pp: 1041-1051* (pp. 1041-1051)

Werner, H., & Wengle, H. (1993). Large-eddy simulation of turbulent flow over and around a cube in a plate channel. *Turbulent shear flows 8* (pp. 155-168): Springer

Wilczak, J.M., Oncley, S.P., & Stage, S.A. (2001). Sonic anemometer tilt correction algorithms. *Boundary-Layer Meteorology, 99*, 127-150

Wilson, R.A. (1990). *Reexamination of Rothermel's fire spread equations in no-wind and no-slope conditions*. US Department of Agriculture, Forest Service, Intermountain Forest and Range …

Wolff, M., Carrier, G., & Fendell, F. (1991). Wind-aided firespread across arrays of discrete fuel elements. II. Experiment. *Combustion Science and Technology, 77*, 261-289

Xue, M., Droegemeier, K.K., & Wong, V. (2000). The Advanced Regional Prediction System (ARPS)–A multi-scale nonhydrostatic atmospheric simulation and prediction model. Part I: Model dynamics and verification. *Meteorology and atmospheric physics, 75*, 161-193

Xue, M., Droegemeier, K.K., Wong, V., Shapiro, A., Brewster, K., Carr, F., Weber, D., Liu, Y., & Wang, D. (2001). The Advanced Regional Prediction System (ARPS)–A multi-scale nonhydrostatic atmospheric simulation and prediction tool. Part II: Model physics and applications. *Meteorology and atmospheric physics, 76*, 143-165

Yang, C.T., & T'ien, J. (1998). Numerical simulation of combustion and extinction of a solid cylinder in low-speed cross flow

Zhang, Y., Sun, J., Huang, X., & Chen, X. (2013). Heat transfer mechanisms in horizontal flame spread over wood and extruded polystyrene surfaces. *International journal of heat and mass transfer, 61*, 28-34

Zhou, Y., & Yiu, M. (2006). Flow structure, momentum and heat transport in a two-tandem-cylinder wake